Investigations of the Physics Potential and Detector Development for the ILC

Von der Fakultät für Mathematik, Naturwissenschaften und Informatik
der Brandenburgischen Technischen Universität Cottbus

zur Erlangung des akademischen Grades

Doktor der Naturwissenschaften
(Dr. rer. nat.)

genehmigte Dissertation

vorgelegt von

Diplom-Physiker
Martin Ohlerich

geboren am 2. September 1977 in Cottbus

Gutachter: Prof. Dr. Wolfgang Lohmann

Gutachter: Prof. Dr. Joachim Mnich

Gutachter: Prof. Dr. Jürgen Reif

Tag der mündlichen Prüfung: 2. Februar 2010

Selbständigkeitserklärung

Hiermit versichere ich, dass ich die vorliegende Arbeit selbständig und nur unter Verwendung der angegebenen Quellen und Hilfsmittel angefertigt habe.

München, den 02.08.2009

Martin Ohlerich

Erklärung über frühere Promotionsanträge

Hiermit versichere ich, dass ich bisher noch keinen Antrag für ein Promotionsverfahren eingereicht habe.

München, den 02.08.2009

Martin Ohlerich

Contents

Abbreviations

ADC	Analog-to-Digital Converter
BeamCal	Beam Calorimeter
CCD	Charge Collection Distance
CCE	Charge Collection Efficiency
cms	Center-of-Mass System
CVD	Chemical Vapor Deposition
DALINAC	Darmstadt Linear Accelerator
ECAL	Electromagnetic Calorimeter
FSR	Final State Radiation
FTD	Forward Tracking Discs
Geant	Geometry and Tracking Software Package
HCAL	Hadronic Calorimeter
ILC	International Linear Collider
IP	Interaction Point
ISR	Initial State Radiation
LC	Linear Collider
LCIO	Linear Collider Input/Output
LDC	Large Detector Concept
LEP	Large Electron Positron Collider
LHC	Large Hadron Collider
LumiCal	Luminosity Calorimeter
Marlin	Modular Analysis and Reconstruction for the Linear Collider
MC	Monte-Carlo
MIP	Minimal Ionizing Particle
MPV	Most Probably Value
MVA	Multivariate Analysis
pcCVD	Polycrystalline CVD
PDF	Probability Density Function
scCVD	single crystal CVD
SIT	Silicon Intermediate Tracker
SNR	Signal-to-Noise Ratio
TPC	Time Projection Chamber
UV	Ultra-violet

Symbols

Physical Constants

c	Speed of light, $c = 299792458$ m/s
e	Elementary charge, $e = 1.602 \cdot 10^{-19}$ C
$\hbar$	Planck constant divided by 2π, $\hbar = 1.055 \cdot 10^{-34}$ Js
k_B	Boltzmann constant, $k_\mathrm{B} = 1.381 \cdot 10^{-23}$ J/K
m_e	Electron mass, $m_\mathrm{e} = 511$ keV
r_e	Classical electron radius, $r_\mathrm{e} = 2.818 \cdot 10^{-15}$ m
G_F	Fermi coupling constant, $G_F = 1.166 \cdot 10^{-5}$ GeV^{-2}
N_A	Avogadro constant, $N_A = 6.022 \cdot 10^{23}$ mole^{-1}
ε_0	Vacuum permittivity, $\varepsilon_0 = 8.854 \cdot 10^{-12}$ F/m
α	Fine-structure constant, $\alpha = \frac{e^2}{4\pi\varepsilon_0\hbar c} \approx \frac{1}{137}$
ϑ_W	Weak mixing angle, $\sin^2\vartheta_W = 0.231$
M_Z	pole Mass of the Z boson, $M_Z = 91.2$ GeV
Γ_Z	Decay width of the Z boson, $\Gamma_Z = 2.4952$ GeV
M_W	pole Mass of the W boson, $M_W = 80.4$ GeV
M_h	pole Mass of the Higgs boson, e.g. $M_h = 120$ GeV
Γ_h	Decay width of the Higgs boson

Elementary Particles

$\mathrm{e}^\pm$	electron, positron
$\mu^\pm$	muon, antimuon
$\tau^\pm$	tauon, antitauon
$\nu_{\mathrm{e},\mu,\tau}$	neutrinos
u, d, s, c, b, t	quarks: up, down, strange, charm, bottom, top
$W^\pm, Z$	weak gauge bosons
γ	photon
$\widetilde{\tau}^\pm$	stau (SUSY particle)
χ_0	neutralino (SUSY particle)

General Symbols

c_e	Trapping speed
$d_\mathrm{hit-track}$	Shortest distance between a hit and a track
d_s	Sensor thickness
d_0	Radial impact parameter (track parameter)
f	General function
g, g'	Coupling constants
$j_\mathrm{e,h}$	Current densities for electrons and holes
m	Rest mass
m_eff	Effective mass
m_h, m_Z	Higgs and Z boson Lorentz invariant mass, Breit-Wigner distributed around the pole mass
m_ℓ	Lepton mass
$m_\mathrm{di-lepton}$	reconstructed di-lepton mass
m_recoil	reconstructed recoil mass
n	Density of electrons in the conduction band
n_i	Intrinsic free charge carrier density in the solid
n_A	Atom density
n_S, n_S^i	Scattering center densities
n_T	Density of filled traps
n_0	Stationary density of free charge carriers
p	Density of holes in the valence band, Energy-momentum vector (p_Z, p_h, ...)
$p_\perp$	Transverse momentum
q	general charge
r	Recombination speed
r_S	Interaction rate per unit volume
$\sqrt{s}$	Center-of-mass energy
t_drift	Drift time
v	Speed; Vacuum amplitude of the Higgs field, Chapter 1
v_drift	Drift speed
$v_\mathrm{th}^\mathrm{e,h}$	Thermal speed for electrons and holes
y	Normalized mean drift length, $y = \lambda/d_\mathrm{s}$
z_0	Longitudinal impact parameter (track parameter)
A	Atomic mass
A_beam	Beam spot area
A_s	Electrode area of a sensor
A_μ, B_μ, W_μ^i	Vector fields (Spin 1)
B	Magnetic field
$B(X)$	Branching fraction for decay X
D	Dose
$\mathcal{D}$	Density of states
$D_\mathrm{e,h}$	Diffusion constants for electrons and holes

E	Energy
E_{F}	Fermi energy level
E_{C}, E_{V}	Conduction and valence band edges
E_{dep}	Deposited energy
E_{gap}	Energy band gap
E_{total}	Total cluster energy
E_{ECAL}	ECAL cluster energy
E_{HCAL}	HCAL cluster energy
E_{T}	Trap energy level
E_Z	Z boson energy
$\mathcal{E}$	Electric field
F	Force
G	Gaussian distribution
$G_{\mathrm{e,h}}$	Generation rates for electrons and holes
GL	Gauss-Landau convolution
I	Ionization potential
I_{beam}	Beam current
I_{dark}	Dark current
I_{s}	Sensor current
I_{FC}	Faraday cup current
I_{TSC}	Thermally stimulated current
$\mathcal{L}$	Luminosity
L	Integrated luminosity; Landau distribution
L_h	Likelihood function
$\mathcal{L}_0$, $\mathcal{L}_\phi$	Lagrangian
N	number, e.g. number of bunch particles
N_{eh}	Averaged number of electron-hole pairs created per μm and per particle
N_B, N_B^a	Total and accepted number of background events
N_{C}, N_{V}	Effective density of states in the conduction and valence band, respectively
N_S, N_S^a	Total and accepted number of signal events
N_{T}	Defect/Trap density
P	Probability
Q	electric Charge
Q_{coll}	Collected charge
Q_{ind}	Induced charge
R	Radius of curvature
R_c	Correction factor for dose calculation
$R_{\mathrm{e,h}}$	Recombination rates for electrons and holes
R_M	Moliére radius
S	Action functional, Chapter 1; Significance, Chapter 4
T	transferred energy in a single collision; Temperature, Chapter 5
U	Externally applied voltage
$V(\phi)$	Spin-zero field potential

X_0	Radiation length
Z	Atomic number

Greek letters

α_{acoll}	acollinearity
β	Speed normalized to the speed of light, $\beta = v/c$
γ	Relativistic factor, $\gamma^2 = (1-\beta^2)^{-1}$
ε	Relative permittivity
ε^S	Signal selection efficiency
$\epsilon_{\text{cluster}}$	$\epsilon_{\text{cluster}} = (1 - ex)$, where ex is excentricity of an ellipsoid
ε_{dep}	Energy deposited per particle
ε_{eh}	Electron-hole pair creation energy
η_{eh}	Most probable number of electron-hole pairs created per μm and per particle
$\eta_{\mu\nu}$	Metric tensor
ϑ	Polar angle
λ	Higgs self-coupling strength, Chapter 1 and 4; Mean drift length, Chapter 5
μ	Mean value of a Gaussian distribution; Mobility; Mass parameter in the Higgs potential, Chapter 1
μ_{p}	Pedestal mean value
μ_0	Low-field mobility
$\mu_{\text{e,h}}$	Mobility for electrons or holes
$\pi(x)$	Probability density function of quantity x
ρ	Mass density
ϱ	Charge of an empty trap
σ	Cross-section (general)
σ_{cond}	Conductivity
σ_{eh}	Cross-section for electron-hole pair creation
σ_{e}	Cross-section for exciting an electron from a trap to the conduction band
σ_{G}, σ_{p}	Noise and pedestal standard deviation
σ_{hZ}	Higgs-strahlung cross-section
σ_{L}	Scale parameter for a Landau distribution
σ_{T}	Cross-section for trap creation
τ_{relax}	Characteristic time constant of relaxation of electrons from conduction band
τ_{R}, τ_{T}	Time constant for recombination and trapping of electrons from conduction band
τ_c, τ_e	Time constants for electron capture in and emission from traps
$\tau_{\text{T}}^{N_{\text{T}}}$	Characteristic time constant for trap filling and emptying
ϕ	Spin-0 field (e.g. Higgs); Particle flux
Φ	Higgs doublet field
φ	Intrinsic Landau distribution
ϕ_0	Azimuthal angle (track parameter)
ψ	Spinor field

$\langle x \rangle$	mean value of quantity x
δx	Deviation of x from its mean value, $\langle x \rangle$, or from stationary state, x_0
Δx	Standard deviation of a Gaussian distributed quantity x, uncertainty or resolution of quantity x, $(\Delta x)^2 = \langle (\delta x)^2 \rangle$
$\Delta_N x$	Standard deviation of the estimate of the mean value from a statistical sample with N events, $\Delta_N x = \Delta x / \sqrt{N}$, measurement uncertainty
∇	Spatial gradient

Abstract

The International Linear Collider offers a lot of different interesting challenges concerning the physics of elementary particles as well as the development of accelerator and detector technologies. In this thesis, we investigate two rather separate topics – the precision measurement of the Higgs boson mass and of its coupling to the neutral gauge boson Z and the research and development of sensors for BeamCal, which is a sub-detector system of the ILC detector.

After the Higgs boson has been found, it is important to determine its properties with high precision. We employ the Higgs-strahlung process for this purpose. A virtual Z boson is created in the e^+e^- collisions, which emits a Higgs-boson while becoming on-shell. Using the so-called recoil technique, we determine the Higgs boson mass by reconstructing the Z boson momentum and using the center-of-mass energy of the colliding leptons. This technique allows to measure the Higgs boson mass without considering the Higgs boson decay, i.e. it can be applied even to a Higgs boson invisibly decaying.
Monte-Carlo studies including a full detector simulation and a full event reconstruction were performed to simulate the impact of a realistic detector model on the precision of the Higgs boson mass and production cross-section measurement. Also, an analytical estimate of the influence of a given detector performance on the Higgs boson mass measurement uncertainty is given. We included a complete sample of background events predicted by the Standard Model, which may have a detector response similar to the signal events. A probabilistic method is used for the signal-background separation. Several other probabilistic methods were used to investigate and improve the measurement of the Higgs-strahlung cross-section and the Higgs boson mass from the recoil mass spectrum obtained after the signal-background separation. For a Higgs boson mass of 120 GeV, a center-of-mass energy of $\sqrt{s} = 250$ GeV and an integrated luminosity of $L = 50$ fb^{-1}, a relative uncertainty of 10 % is obtained for the cross-section measurement, and a precision of 118 MeV for the Higgs boson mass.
The original motivation to use the recoil technique for a Higgs boson mass measurement independent on its decay modes could not be completely confirmed.
For a Higgs boson mass of 180 GeV and $\sqrt{s} = 350$ GeV, a statistics corresponding to $L = 50$ fb^{-1} is not sufficient to achieve the necessary significance of the recoil mass peak above the background.

The BeamCal is a calorimeter in the very forward region, about 3 m away from the nominal interaction point and surrounding the beam pipe. Due to its location, a lot of beamstrahlung pair particles will hit this calorimeter, representing a challenge for the operational reliability of the sensors under such harsh radiation conditions. We investigated single-crystal and polycrystalline CVD diamond, gallium arsenide and radiation-hard silicon as sensor candidates for their radiation hardness and found that diamond and gallium arsenide are promising. We used a 10 MeV electron beam of few nA to irradiate the samples under investigation up to doses of 5 MGy for diamond, up to about 1.5 MGy for gallium

arsenide and up to about 90 kGy for silicon. We measured in regular periods the CCD to characterize the impact of the absorbed dose on the size of the signal, which is generated by electrons of a ^{90}Sr source crossing the sensor. Additional measurements such as the dark current and the CCD as functions of the voltage completed the characterization of the sensor candidates.
For the single-crystal CVD diamond, also the thermally stimulated current was measured to determine amongst others the defect density created by irradiation. In the diamond samples, evidence for strong polarization effects inside the material was found and investigated in more detail.
A phenomenological model based on semi-conductor physics was developed to describe the sensor properties as a function of the applied electric field, the dose and the dose rate. Its predictions were compared with the results of the measurements. Several parameters such as time scales and cross-sections were determined using this model, which led to ongoing investigations.

Kurzfassung

Der Internationale Linear Collider (ILC) bietet eine Vielfalt an interessanten Herausforderungen für die Elementarteilchenphysik, die Beschleuniger- und die Detektortechnologie. In der vorliegenden Arbeit untersuchen wir je ein Kernthema aus der Physik und der Detektortechnologie – zum einen die Präzisionsmessung der Higgs-Bosonenmasse und der Kopplung des Higgs-Bosons an das neutrale schwere Eichboson, Z, und zum anderen die Untersuchung und Entwicklung von Sensoren für BeamCal, einem Teildetektorsystem des ILC-Detektors.

Das Higgs-Boson ist ein bisher nicht entdecktes fundamentales Teilchen, welches vom elektroschwachen Standardmodell vorhergesagt wird. Sehr wahrscheinlich wird es am LHC gefunden. Danach ist es wichtig, seine Eigenschaften mit hoher Präzision zu bestimmen. Wir benutzen dafür den Higgs-Strahlungsprozess. Ein virtuelles Z-Boson wird in einer e^+e^--Kollision erzeugt, welches ein Higgs-Boson emittiert und dabei auf die Massenschale übergeht. Mit Hilfe der sogenannten Rückstosstechnik bestimmen wir die Higgs-Bosonmasse durch Rekonstruktion des Impules des Z-Bosons und mittels der Schwerpunktsenergie der kollidierenden Leptonen. Diese Technik erlaubt es, die Higgs-Bosonmasse und die Kopplung an das Z-Boson zu messen ohne die Higgs-Zerfallsmoden zu betrachten, d.h. sie kann auch angewendet werden, wenn das Higgs-Boson in nicht detektierbare Teilchen zerfällt.
Monte-Carlo Studien, die eine volle Detektorsimulation und eine volle Ereignisrekonstruktion enthalten, wurden durchgeführt, um den Einfluss eines realistischen Detektormodells auf die Präzision der Messgrößen abzuschätzen. Dazu wird analytisch sowie numerisch die Auswirkung der Impulsmessungspräzision auf die Messung der Higgs-Bosonmasse bestimmt. Wir fügten eine vollständige Menge an Hintergrundereignissen hinzu, wie sie vom Standardmodell vorausgesagt werden und welche eine Signatur im Detektor aufweisen, die der der Signalereignisse sehr ähnlich ist. Für die Unterscheidung von Signal- und Hintergrundereignissen wurde eine wahrscheinlichkeitsbasierte Methode benutzt. Weitere wahrscheinlichkeitstheoretische Methoden wurden verwendet, um die Messung des Higgs-Strahlungsprozesses und der Higgs-Bosonmasse aus dem Rückstossmassenspektrum nach der Signal-Hintergrund-Trennung zu untersuchen und zu verbessern. Für eine Higgs-Bosonmasse von 120 GeV, eine Schwerpunktenergie von $\sqrt{s} = 250$ GeV und eine integrierte Luminosität von $L = 50$ fb^{-1} wurde eine relative Unsicherheit von 10 % für die Streuqueschnittmessung und eine Unsicherheit von 118 MeV für die Messung der Higgs-Bosonmasse erhalten.
Die ursprüngliche Motivation für die Verwendung der Rückstosstechnik war die Bestimmung der Higgs-Bosonmasse unabhängig von seinen Zerfallskanälen. Diese Unabhängigkeit kann nicht vollständig bestätigt werden.
Für eine Higgs-Bosonmasse von 180 GeV und für $\sqrt{s} = 350$ GeV ist die notwendige Anzahl von Ereignissen bei $L = 50$ fb^{-1} nicht ausreichend, um ein signifikantes Signal über dem Hintergrund zu erhalten.

Das BeamCal ist ein Kalorimeter in der Vorwärtsregion des ILC-Detektors, etwa 3 m vom nominalen Wechselwirkungspunkt entfernt, und umgibt das Strahlrohr. Durch seine Position wird es einer großen Anzahl von e^+e^--Paaren aus der Beamstrahlung ausgesetzt sein, was eine enorme Herausforderung für die Funktionstüchtigkeit und Zuverlässigkeit der Sensoren bei exterm hoher Strahlendosis bzw. -dosisrate darstellt. Wir untersuchten ein- und polykristalline CVD Diamant-, Galliumarsenid- und strahlenharte Siliziumsensormatrialen auf ihre Strahlenhärte und fanden vielversprechende Ergebnisse für Diamant und Galliumarsenid. Wir benutzten einen 10 MeV Elektronenstrahl von einigen nA, um die zu untersuchenden Sensorproben bis zu Dosen von 5 MGy für Diamant, bis etwa 1,5 MGy für Galliumarsenid und bis zu 90 kGy für Silizium zu bestrahlen. In regelmäßigen Abständen wurde die CCD mit relativistischen Elektronen aus einer ^{90}Sr-Quelle gemessen, um den Einfluss der vom Sensor absorbierten Dosis auf die Größe des MIP-Signals zu bestimmen. Zusätzliche Messungen u.a. des Dunkelstromes und der CCD als Funktionen der angelegten Spannung vervollständigen die Charakterisierung der Sensormaterialkandidaten.
Für den einkristallinen CVD Diamanten wurde auch der thermisch stimulierte Strom gemessen zur Bestimmung u.a. der Dichte der Defekte, die durch die Bestrahlung erzeugt wurden. Es wurden Hinweise auf starke Polarisationseffekte in den Diamantproben gefunden und detailierter untersucht.
Um die Sensoreigenschaften als Funktion des angelegten elektrischen Feldes, der Dosis und der Dosisrate zu beschreiben, wurde ein phänomenologisches Modell entwickelt. Die Voraussagen dieses Modells wurden mit den Ergebnissen der Messungen verglichen und mehrere Parameter wie etwa Zeitkonstanten und Streuquerschnitte wurden mit Hilfe dieses Modells bestimmt. Das durch dieses Modell gewonnene Verständnis induzierte weiterführende Untersuchungen.

Chapter 1

Introduction to High-Energy Physics

1.1 The Standard Model of Elementary Particles

1.1.1 Historical Flashback

In the ancient Greece, people believed that matter, i.e. all things in our world, is composed of very small, fundamental, non-divisible particles. They called them *atoms*. According to their imagination, the properties of a subject depend on the shape of the atoms from which this subject is made of. Except for the notion of plastic and geometric properties of the atoms, the idea of the elementary building blocks survived till now, though in a modified version. Until the 19th century the atomic structure of the matter was manifested by means of chemistry. D. Mendeleev and L. Meyer sorted the elements in a periodic table according to their properties, though they even did not divine the reason for this regular pattern in this table. The attempt to understand why the chemical elements can be arranged in the periodic table of elements led to a lot of new experiments.
Throughout the 19th century, scientists investigated the cathode rays, which finally led to the discovery of the electron by J.J. Thomson. He found out that the electron is a negatively charged subatomic particle. The consequent question for what is else inside the atom – which was initially posed to explain the structure and the behavior of atoms – opened the gates to the nuclear and elementary particle physics of today.
At the end of the 19th century the x-rays and radioactivity were discovered by W. K. Röntgen and A. H. Becquerel and P. and M. Curie, respectively. E. Rutherford characterized the types of radioactivity and started at the beginning of the 20th century the investigations of matter in scattering experiments using α-particles from nuclear fissions as projectile [1]. He could demonstrate that the largest fraction of the atom mass is concentrated in positively charged nuclei. The scattering experiments performed by the group around Rutherford comprised the prototype for the following and also modern high-energy collision experiments. In collision experiments of α-particles with gases till 1920, Rutherford was sure to knock-out every time the same particles, namely the nuclei of hydrogen, which were known since 1886. He identified them as elementary particles, called them protons and stated that the nuclei of more complex atoms than hydrogen consist of protons.

In the 1930s J. Chadwick, and independently W. Bothe and his apprentice H. Becker, found the neutron as another subatomic particle. It was discovered that also neutrons are contained in the nuclei additionally to the protons and that the radioactive β-decay can be understood as the decay of a neutron, which are bound in a nucleus, into a proton, an electron and an electron antineutrino. The latter one is another elementary particle and was postulated by W. Pauli to ensure energy conservation in the neutron decay. In this decade also the positron - the antiparticle of the electron - and the muon were discovered. A. Einstein [2, 3] postulated in his theory of special relativity the equivalence of energy and mass. Therefore, it became obvious that in high-energy collision experiments new particles with a larger mass can be created. In the second half of the 20th century powerful accelerators were build to generate high-energetic particles that are brought to collision. However, more and more new particles were discovered – particles with different masses, charges, spins, and other properties. Suddenly, it was not so clear how to understand the label "elementary particle", since to many seemed to exist. In the attempt to resolve more details, i.e. going to higher and higher energies, even more "elementary" particles were created. To find the "real" elementary particles, one started to search for a pattern in this *particle zoo*, and one employed symmetry considerations, which led to a scheme we call the particle content of the Standard Model of elementary particles.
One important condition for the success of the modern picture of elementary particles was the development of the quantum mechanics by M. Planck, N. Bohr, E. Schrödinger, W. Heisenberg and many others, and the relativistic extension of it - the quantum field theories – by P. Dirac, E. Fermi, W. Pauli, R. Feynman, and many others, respectively. I. Newton introduced in the 17th century forces as the reason of motion. However, in quantum field theories, forces in Newton's sense lose their meaning and are replaced by interactions via exchange of particles. It is a great success of the theoretical physics to identify exchanged particles as force mediating particles. In this concept, Newton's third law of motion – the interaction law – is reincarnated to some extend. Furthermore, the dispute lasting for centuries about the nature of light - particle or wave - was eventually decided by the quantum mechanical picture. Although due to the clarification of the photo-electric effect by Einstein it seemed that photons are particles, it was fast recognized that all quantum mechanical particles, specifically all elementary particles, exhibit both a particle and a wave nature – depending on the characteristic energy or length scale of an experiment. The reason is that in quantum mechanics certain quantities such as position and momentum of a particle cannot be measured simultaneously with an arbitrary precision due to the so-called Heisenberg's uncertainty principle [4]. On a microscopic scale quantum mechanical interference occurs due to the probabilistic character of the world on this scale causing wave-like properties.
However, quantum mechanics bear even more interesting features of particles by which they can be classified, for instance the spin. The spin-statistics theorem, worked out and proven by M. Fierz, W. Pauli, J. Schwinger, R. P. Feynman, A. Einstein, S. Bose and others, determines the relation of the quantum mechanical many-particle behavior of the particles and their spin. The statements are: There exist only integer spin (bosons) or half-integer spin (fermions) particles. Fermions underlie the Fermi-Dirac statistics. They

are specifically subject to the Pauli exclusion principle. Bosons underlie the Bose-Einstein statistics.
Interestingly, certain aforementioned abstract symmetries, which were used to explain the diversity of particles using only few basic modules, proved to be the reason for the interactions. In the so-called gauge theories each degree of freedom of a symmetry group introduces a force mediating exchange particle. These exchange particles are bosons, whilst the elementary particles that build the matter and that interact via the exchange bosons are fermions.
From the epistemological point of view it is important to understand that from few basic but mostly abstract principles the entire theory should follow. In the next subsections the attempt is made to illuminate this statement more detailed.

1.1.2 The Basic Constituents of Matter

The historical overview above is far from being complete. It just should sketch the historical way the elementary particle physics has gone so far. We now start to describe the basic particle content of the Standard Model of elementary particles.
The fundamental fermions are six quarks and six leptons as well as their corresponding antiparticles. An antiparticle has exactly the same properties as the corresponding particle, but carries inverse charges (also abstract ones). The spin of fermions is one-half. They are considered to be really fundamental, point-like particles in the Standard Model, and the experiments do not veto this, yet.
The six quarks can be distinguished by their flavor – up, down, charm, strange, bottom and top – and they have electric and color charge degrees of freedom. They are subject to all fundamental forces – the electromagnetic, the weak, and the strong interaction and the gravity. The electric charge of quarks is either one-third or two-third of the electron charge. Quarks are massive, and they are components of hadrons, i.e. compound particles bound via the strong interaction. Quarks do not exist as free single particles. Hadrons are composed of quarks in such a way that the total electric charge is an integer multiple of the electron charge, and that they are color singlets, i.e. they are colorless or white. The two basic possibilities to meet this requirement are a quark-antiquark pair with color-anticolor quantum numbers or three quarks, where each carries a different color of either red, green or blue, what gives in total white. The former particles are called *mesons* and the latter *baryons*. Proton and neutron are baryons. The antibaryons consist of three antiquarks carrying accordingly anticolor charges, which must give in total white, i.e. antired (cyan), antigreen (magenta) and antiblue (yellow). Baryons and mesons, i.e. all quark compounds, are called *hadrons*, and these constitute the major part of the particle zoo, mentioned above.
The leptons also exist in six flavors and can be subdivided into electrically charged and neutral leptons. They do not carry color charges and hence do not interact strongly. The three charged leptons are the electron, the muon and the tauon. They are massive. The three neutral leptons are the neutrinos associated with the charged leptons. In the Standard Model they are considered to be massless, although recent experimental results contradict this assumption. Nevertheless, their masses are very small and still beyond the

Particle	Gen.	Electric Charge [e]	Mass [GeV]	Spin	EM	weak	strong
Leptons							
electron, e	1^{st}	-1	5.11×10^{-4}	1/2	yes	yes	no
muon, μ	2^{nd}	-1	0.1057	1/2	yes	yes	no
tauon, τ	3^{rd}	-1	1.777	1/2	yes	yes	no
electron neutrino, ν_e	1^{st}	0	$< 2.0 \times 10^{-9}$	1/2	no	yes	no
muon neutrino, ν_μ	2^{nd}	0	$< 1.7 \times 10^{-4}$	1/2	no	yes	no
tau neutrino, ν_τ	3^{rd}	0	$< 1.55 \times 10^{-2}$	1/2	no	yes	no
Quarks							
up, u	1^{st}	2/3	$1.5 - 3 \times 10^{-3}$	1/2	yes	yes	yes
charm, c	2^{nd}	2/3	1.25	1/2	yes	yes	yes
top, t	3^{rd}	2/3	174.2	1/2	yes	yes	yes
down, d	1^{st}	-1/3	$3 - 7 \times 10^{-3}$	1/2	yes	yes	yes
strange, s	2^{nd}	-1/3	0.095	1/2	yes	yes	yes
bottom, b	3^{rd}	-1/3	4.2	1/2	yes	yes	yes
+ the according antiparticles							

Table 1.1: Fermions of the Standard Model and some of their properties [5]. (EM=electromagnetic)

current precision of measurement. All leptons undergo weak interactions, and the charged leptons additionally interact electromagnetically.

Table 1.1 shows the today known leptons and quarks. They are arranged in three families or generations. The reason for this pattern is not known, yet, and as far as we know most of the matter of our current universe is mainly composed of the particles of the first generation – up and down quarks, and electrons. Since the neutrinos are stable, the whole universe is also filled with neutrinos. They interact only weakly and, therefore, do not contribute to the condensed matter. The particles of the other families are generated either in natural processes such as muon creation in the atmosphere by scattering of cosmic rays, or in high-energy colliders, but they decay quite fast into lighter particles. Conserved quantities such as the lepton and baryon number or the electric charge protect the lightest particles from decaying. This, together with a not yet explained dominance of matter over anti-matter, might be the reason why our universe almost exclusively consists of baryons made from up and down quarks – building the *nucleons* proton and neutron – and electrons. Nucleons and electrons are forming the atoms.

The fundamental bosons, which are experimentally verified, are spin-one particles. They are the force-mediating particles. Table 1.2 summarizes the known force-mediating bosons of the Standard Model. The photon, mediator of the electromagnetic interaction, is massless, and electrically and color neutral. There are eight types of gluons, mediators of the strong interaction. They are massless and electrically neutral as well, but possess color charges. The latter fact is the reason for the self-coupling of gluons and has important im-

Boson	Electric Charge [e]	Spin	Mass [GeV]	Represents the interaction	stable
photon, γ	$< 5 \times 10^{-30}$	1	$< 6 \times 10^{-26}$	electromagnetism	yes
W boson, $W^{\pm}$	± 1	1	80.4	weak	no
Z boson, Z	0	1	91.2	weak	no
gluon, g	0	1	0	strong	–

Table 1.2: Bosons of the Standard Model and their properties [5].

plications. For example, the masses of the hadrons originate mainly from binding energy, i.e. gluons that are exchanged. The above mentioned color-confinement, which makes the proton a stable particle in the current universe[1], is another consequence, which in turn leads to the fact that only free hadrons with an integer elementary charge occur, which are exactly balanced with negative charges of the electrons, so that our universe is electrically neutral – in agreement with our experience. The strong force has the additional feature of asymptotic freedom [6, 7]. That is, at high energies the strong force becomes weaker and the quarks start to behave as if they were free. This is the reason why the strong force can be investigated in high-energy collision experiments, because at high energies the strong force effects can be calculated perturbatively. At low energies the strong force causes compound states, which are complicated multi-particle systems. The quark compound states can be treated in the lattice QCD, which consists essentially of the discretization of the QCD field equations on a grid, which are then solved by means of numerics.

The force-mediators of the weak interaction are the W and Z bosons. They are massive. W bosons possess an elementary charge of either sign. However, they have no color degrees of freedom. Bound states of fermions, as are possible for the electromagnetic and the strong interaction, such as protons (strong interaction) and atoms (electromagnetic interaction), do not exist for the weak interaction. Weak interactions cause decays, e.g. radioactive decay, and are studied in certain scattering processes.

The fact that the weak interaction bosons possess masses reveals a complication in the theory. The latter is solved by the so-called *Higgs mechanism*, which is explained in the next sections. This mechanism explains how the weak interaction bosons get masses. However, it introduces an additional particle into the particle content of the Standard Model: the *Higgs boson*. It is a spin-zero particle, which is not yet detected at the moment of writing this thesis. Using the Higgs mechanism one can predict the mass ratio of the W and Z bosons. However, it also introduces new parameters into the theory, which must be determined from the experiment. There is also a way to use the Higgs mechanism for giving masses to the fundamental fermions in a consistent way.

[1] A free neutron has a slightly larger mass than the proton due to a different quark content. Therefore, by weak interactions a free neutron decays into a proton, an electron and an electron-antineutrino. Neutrons bound in stable nuclei are considered to be stable.

1.1.3 The Dynamics of the Elementary Particles

The detailed picture is more abstract and, thus, more difficult than the one outlined above. From the theoretical point of view one can start with a Lagrangian, $\mathcal{L}_0$, which describes the free particles listed in Table 1.1, i.e. a Lagrangian which only contains terms of spin-one-half matter fields, the four-component spinors $\psi(x)$, and has no interaction terms.

$$\mathcal{L}_0 = \bar{\psi}(i\gamma_\mu \partial^\mu)\psi \ , \tag{1.1}$$

where γ_μ are four matrices fulfilling the equation,

$$\gamma^\mu\gamma^\nu + \gamma^\nu\gamma^\mu = 2\eta^{\mu\nu} \ , \tag{1.2}$$

which defines the Clifford-algebra. Herein are $\eta^{00} = 1$, $\eta^{11} = \eta^{22} = \eta^{33} = -1$ and $\eta^{\mu\nu} = 0$ for $\mu \neq \nu$. ∂^μ is the covariant space-time gradient, and $\bar{\psi} = \psi^\dagger\gamma^0$, where $\psi^\dagger$ is the complex-conjugated and transposed spinor of ψ. ψ stands here for any possible spin-one-half fermion.
Using the Lagrangian, $\mathcal{L}_0$, representing the energy terms of a system, the action functional, S [8, 9, 10, 11], can be defined as

$$S = \int d^4x \, \mathcal{L}_0 \ . \tag{1.3}$$

From the requirement of a stationary action,

$$\delta S = 0 \ , \tag{1.4}$$

the equations of motion for the particle fields follow.
For spin-one-half fermions the equation of motion is the Dirac equation,

$$i\gamma_\mu \partial^\mu \psi = 0 \ . \tag{1.5}$$

A possible mass term in the Lagrangian, which would have the form of $m\bar{\psi}\psi$, is neglected for the moment, and we introduce it later for reasons becoming obvious.
Spin-one bosons obey the Maxwell equations of the electrodynamics as equation of motion,

$$\partial_\mu \partial^\mu A^\nu = 0 \ , \tag{1.6}$$

where A^ν is a four-component vector field. A massless spin-one boson has actually only two degrees of freedom – the two transverse spin polarization states. Thus, an auxiliary condition must be fulfilled for real photons represented by A^μ, e.g. the Lorentz gauge $\partial_\mu A^\mu = 0$. This condition, however, is no longer necessary as soon as a mass term of the shape $\frac{M^2}{2}A^\nu A_\nu$ is present in the Lagrangian, or the photon is virtual, i.e. its energy-momentum relation leads to a non-zero photon mass. Then three polarization states are possible – two transversal and one longitudinal.

Spin-zero particles fulfill the Klein-Gordon equation,

$$\partial_\mu \partial^\mu \phi = 0 \ , \tag{1.7}$$

where ϕ is a scalar function, real for neutral particles or complex for charged particles. If the mass is non-zero there is a mass term $\frac{M^2}{2}\phi^\dagger\phi$ in the Lagrangian.
Mathematically spoken, the fields are considered to be representations of the Lorentz group. The algebraic structure of these fields reflects the geometrical properties of the space-time [11].

Gauge Theory

Noether's theorem [12, 13] states that there is a conserved current and eventually a conserved quantity if the action function S is invariant under some symmetry transformation of the fields, from which the action is constructed, i.e. specifically if $\mathcal{L}_0$ is invariant under such a transformation. For example, from Poincaré-invariance, i.e. invariance under space-time translations and rotations, we obtain conservation of energy, momentum and angular momentum. The theorem holds also for invariance under more abstract symmetries. In quantum mechanics a solution of the Schroedinger equation is still a solution, if one multiplies it by a phase factor, $e^{i\delta}$, where δ is a constant. This operation is called a *global phase transformation*. In the non-relativistic case, the invariance under such global phase transformations gives rise to the conservation of the probability.
In quantum field theories such as quantum electrodynamics[2], $\mathcal{L}_0$ is invariant under the global phase transformation,

$$\psi \longrightarrow e^{i\delta}\psi \ . \tag{1.8}$$

The consequence is the conservation of the total electric charge. However, we can demand a much more strict requirement. There is no reason why we should have only invariance under global phase transformations, since the experiments show also local conservation of charges, i.e. in finite volumes. We can, thus, also demand invariance under local phase transformations,

$$\psi \longrightarrow e^{i\delta(x)}\psi \ , \tag{1.9}$$

where $\delta(x)$ is now a function of the space-time coordinates. The free Lagrangian is, however, not invariant under this local phase transformation, which is often also called *local gauge transformation*,

$$\mathcal{L}_0 = \bar{\psi} i\gamma_\mu \partial^\mu \psi \longrightarrow \underbrace{\bar{\psi} i\gamma_\mu \partial^\mu \psi}_{\mathcal{L}_0} - \bar{\psi}\gamma_\mu(\partial^\mu \delta(x))\psi \neq \mathcal{L}_0 \ . \tag{1.10}$$

To obtain invariance under local gauge transformations, one can introduce an additional, so-called *gauge field*, A^μ, which transforms in a very specific way to cancel the extra term above. The Lagrangian $\mathcal{L}_0$ is rewritten by replacing $\partial^\mu \rightarrow \partial^\mu + iqA^\mu(x)$,

$$\mathcal{L}_0 = \bar{\psi}\big(i\gamma_\mu(\partial^\mu + iqA^\mu)\big)\psi \ , \tag{1.11}$$

[2] Quantum electrodynamics (QED) is the quantum field theory of the electromagnetic interaction.

where q is the coupling constant of the interaction. We demand that A^μ transforms as

$$A^\mu \longrightarrow A^\mu + \frac{1}{q}\partial^\mu \delta(x) \ , \tag{1.12}$$

and $\delta(x)$ can be an arbitrary function of the space-time coordinates. The Lagrangian (1.11) is now invariant under local gauge transformations. A^μ is a four-component vector field representing a spin-one boson.
Hence, the requirement of invariance of the Lagrangian under local phase transformation of the matter fields, introduces terms into the Lagrangian that describe the interactions of these matter fields with a boson field. Mathematically, terms such as $e^{i\delta}$ are representations of elements of the group $U(1)$, and δ is the parameter of this group. Thus one can state that the invariance of the action function under local $U(1)$-transformations of matter fields introduces interaction terms with spin-one particles.
In quantum electrodynamics one demands local conservation of the electric charge. This corresponds to the requirement of invariance with respect to local phase transformations of the type $e^{i\delta(x)}$, which is an element of the group $U_{\mathrm{EM}}(1)$.[3] The invariance requirement introduces the coupling of the charged matter fields with a spin-one boson, which is identified with the photon. The above defined coupling constant q is chosen to be the charge of the particle under consideration. It is zero for neutral particles, i.e. there is no electromagnetic interaction with electrically neutral particles. For the electron is $q = e$, the elementary charge.
This is the prototype of the so-called *gauge theories*. It is assumed that each interaction corresponds to the invariance of the action (i.e. the Lagrangian) under local phase transformations of the matter fields. These transformations form so-called *gauge groups*. The quantum chromodynamics, i.e. the theory of the strong interaction, is another successful example of a gauge theory. The gauge group of the quantum chromodynamics is the $SU_C(3)$, the color group, and has elements of the type $e^{i\lambda_a}$, where λ_a are now matrices – the eight Gell-Mann matrices. The $SU_C(3)$ has some special properties. It is non-abelian, i.e. its elements do not generally commute. This implicates the above mentioned properties of the strong interaction such as the self-coupling of the gluons, color-confinement and asymptotic freedom.
It should be noted that only local symmetries lead to gauge couplings, i.e. interactions. Of course, there are a lot of experimentally supported global symmetries such as baryon and lepton number conservation. They, however, do not introduce interactions.

Higgs Mechanism and Symmetry Breaking

The exact symmetry under local gauge group phase transformations has another important consequence. The gauge bosons, i.e. the boson fields introduced by the invariance requirement, are massless. Mass terms for spin-one bosons would look like

$$\frac{M_A^2}{2} A_\mu A^\mu \ , \tag{1.13}$$

[3] The index EM denotes the electromagnetism.

where M_A is the mass of the boson represented by the field $A_\mu(x)$. Such a term violates the local gauge invariance under transformations (1.12). As the photon and the gluons are massless, we know that the $U_{\mathrm{EM}}(1)$- and $SU_C(3)$-symmetries are exact. The weak interaction gauge bosons, W and Z, are massive. We, thus, are forced to conclude that the symmetry for this interaction is broken.
It is a more technical issue, but the symmetry breaking is assumed to be spontaneous rather than explicit. The reason for this is to keep the theory renormalizable, which is not the case if the symmetry is explicitly broken. Renormalization ensures the self-consistency and the predictive power of a field theory. In the case of a non-renormalizable theory one has to introduce an infinite number of parameters to be consistent, which, of course, spoils the predictive power.
The idea of spontaneous symmetry breaking works as follows [14, 15]. One introduces a complex spin-zero field, ϕ. The Lagrangian for this field contains a potential

$$V(\phi) = -\frac{\mu^2}{2}|\phi|^2 + \frac{\lambda}{4}|\phi|^4 \,, \tag{1.14}$$

where λ and μ^2 are parameters. For stability of the ground state, the condition $\lambda > 0$ must hold. This potential is obviously invariant for $\phi \to e^{i\delta(x)}\phi$. The total Lagrangian for this field, however,

$$\mathcal{L}_\phi = (\partial_\mu\phi)^\dagger(\partial^\mu\phi) - V(\phi) \tag{1.15}$$

is not invariant for the same reasons as explained above. One has to introduce a gauge field A_μ and replace $\partial^\mu \to \partial^\mu + iqA^\mu(x)$. By this operation the coupling of ϕ to A_μ is introduced. The Lagrangian then reads

$$\mathcal{L}_\phi = \big((\partial_\mu + iqA_\mu)\phi\big)^\dagger\big((\partial^\mu + iqA^\mu)\phi\big) - V(\phi) \,, \tag{1.16}$$

which is invariant under the $U(1)$ local phase transformation.
If $\mu^2 < 0$ the potential $V(\phi)$ has the ground state, i.e. its minimum, at $\phi_0 = 0$. For $\mu^2 > 0$, the minimum is at $\phi_0 = \sqrt{\frac{\mu^2}{\lambda}}e^{i\delta} \equiv ve^{i\delta}$ $(0 < \delta < 2\pi)$. $v = \sqrt{\frac{\mu^2}{\lambda}}$ is called the *vacuum amplitude*. The first remark is that there is an infinite number of equivalent minima, parametrized by δ, i.e. the system has to decide to which minimum it goes. The second remark is that, although the potential $V(\phi)$ has the full symmetry, the ground state, ϕ_0, has not: $ve^{i\delta_1} \neq ve^{i\delta_2}$ for $\delta_1 \neq \delta_2$. Note that the previous ground state $\phi_0 = 0$ in the case $\mu^2 > 0$ still exhibits this symmetry! The third remark: Since ϕ gets a space-independent, non-zero vacuum amplitude, the whole universe is filled with this field. The ground-state of ϕ, which is the constant vacuum amplitude, leads to an angular momentum of the universe of zero, which is in agreement with observed isotropy in the cosmic microwave background and in the velocity distribution of the galaxies [16, 17].
If we substitute the vacuum amplitude into (1.16) we obtain a term of the following kind

$$q^2v^2A_\mu A^\mu = \frac{q^2\mu^2}{\lambda}A_\mu A^\mu \,. \tag{1.17}$$

This is a mass term of the type (1.13), and a comparison yields the mass

$$M_A = \sqrt{\frac{2q^2\mu^2}{\lambda}} \ . \tag{1.18}$$

This way of breaking a symmetry via introducing a spin-zero field is called the *Higgs mechanism*. ϕ is called the Higgs field. The Higgs mechanism gives an elegant possibility to introduce gauge boson masses without breaking the gauge symmetry explicitly.
By expanding ϕ around the ground state, $\phi = \phi_0 + h(x)$, we introduce the basic excitations of the Higgs field – the Higgs boson field. $h(x)$ also fulfills the Klein-Gordon equation (1.7). There appear additional terms in Equation (1.16), for example, a mass term,

$$\left(-\frac{\mu^2}{2} + \frac{6}{4}\lambda v^2\right) h^\dagger h = \mu^2 h^\dagger h \equiv \frac{M_h^2}{2} h^\dagger h \ , \tag{1.19}$$

is obtained. The Higgs boson mass, $M_h = \sqrt{2}\mu$, is positive if $\mu > 0$. There are several terms of self-couplings of the Higgs boson field proportional to h^3 and h^4. Last but not least there are couplings of the Higgs boson field with the gauge boson field such as $\phi_0 h A^\mu A_\mu$ and $h^2 A_\mu A^\mu$. Possible physics processes due to these terms can be exploited to measure e.g. the mass of the Higgs boson as demonstrated in Chapter 4 using the hZZ-coupling.

1.1.4 The Standard Model and the Combination of Weak and Electromagnetic Interaction

The goal of the elementary particle physics is to construct as few as possible fundamental particle multiplets (in the ideal case just one), into which the known particles can be arranged, and to find the correct gauge group to get the interactions. At the moment, for each type of interaction there is one gauge group and one corresponding coupling constant. It is desirable to find one minimal group that incorporates all the fundamental interactions and also explains all the properties found by the experiments. There are a lot of ideas and theories, some of which are mentioned in one of the following subsections. However, we want to sketch first the Standard Model, which is the current theory of the elementary particles favored by the experiments. It is more complex than indicated in the previous subsection. The mechanism of symmetry breaking has to be embedded in the structure of the gauge group, which is the $U_Y(1) \times SU_L(2) \times SU_C(3)$ for the Standard Model. All of the aforementioned elements such as matter fields, gauge invariance and the introduction of gauge fields, and the Higgs field are present.
The group $SU_C(3)$ describes the phenomena of the strong interaction, which is an important part of the Standard Model. However, the relevant mechanisms for the electroweak symmetry breaking and the fermion mass creation are acting in the subgroup $U_Y(1) \times SU_L(2)$, the electroweak gauge group, which is independent of the $SU_C(3)$ part to some extend. We therefore describe only the electroweak part of the Standard Model.
Let's start with an introduction of notations and a completion of the properties of the particles of the Standard Model. We demonstrate everything with the leptons of the first

generation. For the leptons of the other generations and for the quarks one can proceed in the same way. For the quarks just some complications due to the strong interaction need to be taken into account. Henceforth, unless otherwise specified, a neutrino denotes the electron neutrino.
To account for the structure of the electroweak interaction, which involves maximum parity violation [18, 19], we have to introduce some new properties of particles. The first is the *chirality* or *handedness*. A left-handed electron is defined as

$$\mathrm{e}_L = P_L \mathrm{e} = \frac{1-\gamma_5}{2}\mathrm{e}\ , \tag{1.20}$$

where e denotes the spinor for the electron, P_L is the projection operator, and $\gamma_5 = i\gamma_0\gamma_1\gamma_2\gamma_3$ is constructed from the Dirac matrices in Equation (1.2). Accordingly, right-handed electrons are

$$\mathrm{e}_R = P_R \mathrm{e} = \frac{1+\gamma_5}{2}\mathrm{e} \quad \text{and} \quad \mathrm{e} = \mathrm{e}_L + \mathrm{e}_R\ .$$

This also holds for the neutrino. It turns out that the weak interactions due to W bosons act only on left-handed particles (or right-handed anti-particles). In the Standard Model right-handed neutrinos do not exist.
In the weak interaction, transitions from left-handed electrons to left-handed neutrinos are possible. It is then reasonable to consider both particles as two different states of one fundamental particle represented by a left-handed doublet

$$\begin{pmatrix} \nu_L \\ \mathrm{e}_L \end{pmatrix}\ .$$

Right-handed particles are singlets. One can assign to the doublet a quantum number, called *weak isospin*, T, analogous to the normal spin. The doublet has weak isospin $T = 1/2$, and the singlet has weak isospin $T = 0$. The third component of this isospin is either $T_3 = \pm\frac{1}{2}$ for the components of the doublet and $T_3 = 0$ for the singlet.
Furthermore we introduce the *hypercharge* Y. The reason for this will become obvious soon. The electric charge Q, hypercharge Y, and the third weak isospin component T_3 are connected via the Gell-Mann-Nishijima-Relation [20, 21],

$$Q = T_3 + \frac{1}{2}Y\ . \tag{1.21}$$

The hypercharge Y is the generator of the gauge group $U_Y(1)$. The values of the isospin and the hypercharge for all Standard Model fermions are summarized in Table 1.3.
At first one remark: In table 1.3 also the quantum numbers for the quarks are given. The second (down-like) components of the left-handed quark doublets are primed. Indeed, the quark mass eigenstates are not the eigenstates of the weak interaction. The down-like quarks are transformed via a 3×3 unitary matrix – the so-called Cabibbo-Kobayashi-Maskawa (CKM) matrix [23, 24]. Although very interesting physics underlies it, such as

			T	T_3	Y	Q
$\begin{pmatrix}\nu_{eL}\\ \mathrm{e}_L\end{pmatrix}$	$\begin{pmatrix}\nu_{\mu L}\\ \mu_L\end{pmatrix}$	$\begin{pmatrix}\nu_{\tau L}\\ \tau_L\end{pmatrix}$	1/2 1/2	1/2 -1/2	-1 -1	0 -1
e_R	μ_R	τ_R	0	0	-2	-1
$\begin{pmatrix}u_L\\ d'_L\end{pmatrix}$	$\begin{pmatrix}c_L\\ s'_L\end{pmatrix}$	$\begin{pmatrix}t_L\\ b'_L\end{pmatrix}$	1/2 1/2	1/2 -1/2	1/3 1/3	2/3 -1/3
u_R	c_R	t_R	0	0	4/3	2/3
d_R	s_R	b_R	0	0	-2/3	-1/3

Table 1.3: The properties of the Standard Model fermions [22]. The left-handed neutrinos carry the index of their associated lepton. Q is in units of e.

the reason for the CP-violation in K- and B-meson decays, we just mention it here without pursuing details.

We are now ready to formulate the Standard Model. We choose as gauge group the $U_Y(1) \times SU_L(2) \times SU_C(3)$, one group for the hypercharge (coupling g'), one for the weak isospin (coupling g), and one for the color charge (coupling α_s). The $U_Y(1)$ has one generator and, thus, creates one gauge boson – the B_μ. $SU_L(2)$ has three generators and contributes three gauge bosons – we denote them W^1_μ, W^2_μ, and W^3_μ. The $SU_C(3)$ has eight generators and gives, consequently, eight gauge bosons, G^a_μ ($a = 1, \ldots, 8$), summarized under the label *gluon*.

However, the electroweak gauge bosons are not the physical boson states, the properties of which can be measured in an experiment. They mix if they have equal quantum numbers, as it may usually happen in quantum mechanics. $W^\pm_\mu = (W^1_\mu \mp iW^2_\mu)/\sqrt{2}$ constitute the positively and negatively charged W bosons, respectively. They are particle and antiparticle in the sense that they can annihilate each other into photons. B_μ and W^3_μ carry the same quantum numbers and mix to give

$$\begin{pmatrix}A_\mu\\ Z_\mu\end{pmatrix} = \begin{pmatrix}\cos\theta_W & \sin\theta_W\\ -\sin\theta_W & \cos\theta_W\end{pmatrix}\begin{pmatrix}B_\mu\\ W^3_\mu\end{pmatrix} \ . \tag{1.22}$$

Herein, A_μ is the photon field, Z_μ the Z boson field, and θ_W is the so-called *weak mixing angle* or *Weinberg angle*.

The transformation (1.22) must ensure that the photon, A_μ, couples only to the charged leptons and quarks, but not to the neutrinos. As a result, we obtain the relations between the original coupling constants g and g' of the $U_Y(1)$ and $SU_L(2)$, respectively, and the elementary charge, e, and θ_W, both measurable in the experiment,

$$e = g\sin\theta_W \ , \qquad \text{and} \qquad \cos\theta_W = \frac{g}{\sqrt{g'^2 + g^2}} \ . \tag{1.23}$$

Several authors [25, 26, 27, 28, 29, 30, 31, 32, 33, 34, 35] contributed to the development of the electroweak Standard Model, also known as Glashow-Salam-Weinberg (GSW) theory of electroweak interaction.

To introduce masses for the weak gauge bosons $W^{\pm}$ and Z, we employ the Higgs mechanism sketched in the previous section. We introduce a spin-zero field that must be a $SU_L(2)$ doublet to perform the breaking the electroweak symmetry in the correct way,

$$\Phi = \begin{pmatrix} \phi^+ \\ \phi^0 \end{pmatrix} = \begin{pmatrix} \phi_1 + i\phi_2 \\ \phi_3 + i\phi_4 \end{pmatrix} . \tag{1.24}$$

It has four degrees of freedom. The potential for the Higgs field is chosen to be

$$V(\Phi) = -\frac{\mu^2}{2}\Phi^\dagger\Phi + \frac{\lambda}{4}(\Phi^\dagger\Phi)^2 , \tag{1.25}$$

and the ground state as

$$\Phi = \begin{pmatrix} 0 \\ v \end{pmatrix} .$$

The ground state is unique up to weak isospin rotations, i.e. $SU_L(2)$ phase transformations. The vacuum amplitude is $v = \sqrt{\mu^2/\lambda}$, as in the previous section. By acquiring this vacuum amplitude the $U_Y(1) \times SU_L(2)$ symmetry is spontaneously broken down to the remaining $U_{\mathrm{EM}}(1)$ symmetry of electromagnetism. The three broken symmetry degrees of freedom create Goldstone bosons [36], which become the longitudinal polarization degrees of freedom for the W and Z bosons, which get the masses

$$M_W = \frac{1}{\sqrt{2}}vg \qquad \text{and} \qquad M_Z = \frac{1}{\sqrt{2}}v\sqrt{g^2 + g'^2} . \tag{1.26}$$

The photon mass M_A remains zero!
By the Higgs mechanism the W and Z boson masses are related to each other by

$$\frac{M_W}{M_Z} = \cos\theta_W .$$

Furthermore, the vacuum amplitude v can be expressed by the Fermi constant, G_F, by

$$v^2 = \frac{1}{\sqrt{8}G_F} . \tag{1.27}$$

The Higgs mechanism, hence, introduces some interesting relations, which have been tested in the experiment. Except the fact that the Higgs boson, i.e. the elementary excitation of the Higgs field from ground state, has not been found, yet, the electroweak theory, together with the Higgs mechanism, has been experimentally confirmed up to very high precision [37, 38].
The Higgs mechanism can be also used to introduce masses for the fermions, without violating the gauge invariance, via so-called *Yukawa couplings*, e.g. for the electron

$$\mathcal{L}_{\mathrm{Yuk}} = -y_{\mathrm{e}}\bar{\mathrm{e}}_R\Phi^\dagger\begin{pmatrix} \nu_{\mathrm{e}L} \\ \mathrm{e}_L \end{pmatrix} + h.c. ,$$

where y_{e} is a free parameter. *h.c.* stands for the *Hermitian conjugate*. Inserting the Higgs field vacuum amplitude, a mass term is obtained

$$\mathcal{L}_{\mathrm{Yuk}} = -y_{\mathrm{e}}v(\bar{\mathrm{e}}_R\mathrm{e}_L + \bar{\mathrm{e}}_L\mathrm{e}_R) = -y_{\mathrm{e}}v\bar{\mathrm{e}}\mathrm{e} \equiv -m_{\mathrm{e}}\bar{\mathrm{e}}\mathrm{e} .$$

Event Rates and Cross-Section

What is the reason for all the effort done so far? What can one do with the knowledge above? What is the connection to our experience or the experiment? It is important to identify the interaction terms because they give the so-called *tree-level* couplings, i.e. the couplings that are intrinsically allowed. From them one can construct more complicated processes with a lot of intermediate vertices. However, the more interactions contribute to one process, the less probable is this process if the coupling constants are small. One can then construct perturbation expansions.
In the perturbation theory the interaction terms of the Lagrangian are used to calculate the transition amplitude from one initial state, $|i\rangle$, to a specific final state, $|f\rangle$,

$$\langle f|\mathcal{L}_{\text{interaction}}|i\rangle \ .$$

The square of the absolute value of this amplitude gives the transition probability for this process. The natural quantity in high energy experiments is the so-called *interaction cross-section*, σ. It is equal to this transition probability, integrated over the momenta of the final state particles, and normalized to the flux of the incoming initial state particles. This normalization seems to be arbitrary but is advantageous for high-energy experiments, in which many particles in bunches are accelerated and collided at the same time. In the cross-section then only the physics is encoded, but not the accelerator operation parameters. The latter are merged into a quantity called *luminosity*, $\mathcal{L}$. The event rate for a process X, i.e. the number of events of process X per unit time, is equal to the cross-section for this process times the impinging particle flux, which is here equal to the luminosity,

$$R_X = \mathcal{L}\sigma_X \ . \tag{1.28}$$

Since the cross-section is not time-dependent one can simply integrate this equation. The quantity

$$L = \int_{t_0}^{t_1} \mathcal{L}\, dt \tag{1.29}$$

is called the *integrated luminosity*, and $\int_{t_0}^{t_1} R_X\, dt = N_X$ is the number of the events of the process X occurred in the time interval. In this way one can measure the cross-section of a process, identified in the detector of an experiment, just by counting the events in a given time interval,

$$\sigma_X = \frac{N_X}{L} \ . \tag{1.30}$$

In Chapter 4 this is exploited in a simulation study for the so-called Higgs-strahlung process.

1.1.5 The Profile of the Higgs Boson and Limits on its Mass

As already pointed out in the previous section, the Higgs mechanism leads to an additional fundamental particle – a spin zero Higgs boson. It is a prediction of the Standard Model

that one electrically and color neutral, massive Higgs boson with even parity and zero spin exists. There are more Higgs doublets introduced in some other models causing a larger number of Higgs particles. However, a Higgs boson with the same properties as that in the Standard Model should always exist, if the corresponding spin-zero field causes the spontaneous breaking of a gauge symmetry.

The mass of the Standard Model Higgs boson, M_h, is a free parameter. From theoretical considerations such as the requirement of vacuum stability, the Higgs boson mass is expected to be between few MeV and about 1 TeV. At the time of writing this thesis, experiments at the Large Electron-Positron Collider (LEP) at CERN have excluded a Higgs boson, as predicted by the Standard Model, in the mass range of $M_h < 114$ GeV [37, 39]. In addition, the mass range from 160 to 170 GeV is excluded by the Tevatron experiments [40]. The comparison of other electroweak parameters measured at the SLC, the LEP and the Tevatron with the Standard Model leads to an upper mass limit, $M_h \leq 200$ GeV. For larger values of M_h, contributions from higher order diagramms containing virtual Higgs-boson loops would create discrepancy between measurements and the theory predictions.

In the Standard Model the Higgs boson couples to the fermions via the Yukawa-couplings, which are proportional to the corresponding fermion masses. Also the couplings of the gauge bosons to the Higgs boson are proportional to the gauge boson masses. Therefore, the dominant decay mode of the Higgs boson is that into the heaviest, kinematically allowed particle-antiparticle pair, and depends, therefore, on the mass of the Higgs boson.

In the mass region up to 140 GeV, the Standard Model Higgs boson will decay mostly into $b\bar{b}$ quark pairs. For a Higgs boson mass larger than about 140 GeV the dominant decay mode will be into a W^+W^- boson pair. There are many other decay modes, as shown in Figure 1.1. Their branching fractions (left) and the decay width of the Higgs boson (right) are plotted as functions of the Higgs boson mass between 100 GeV and 200 GeV.

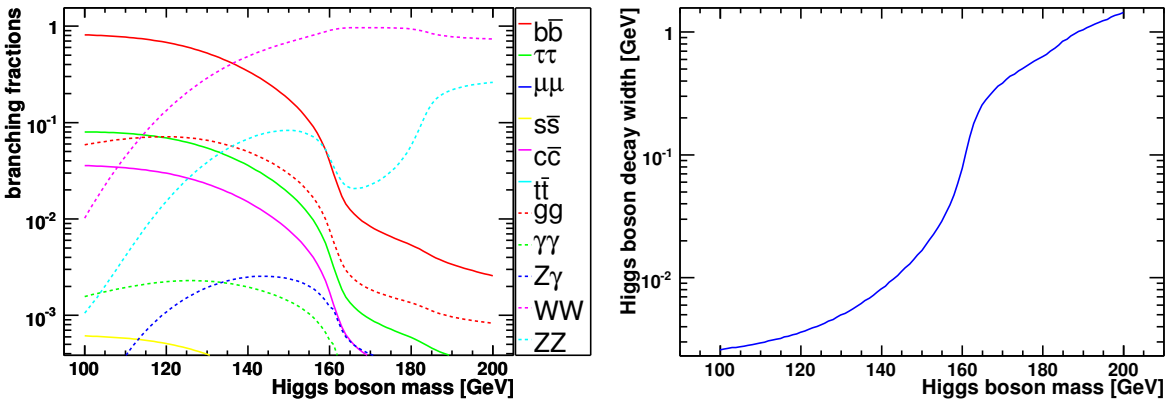

Figure 1.1: Branching fraction (left) and decay width (right) of the Standard Model Higgs boson as function of the Higgs boson mass using the HDECAY program [41].

1.1.6 The Mass and the Limits of the Standard Model

The Mass

Physicists have all the time been thinking about the mass. I. Newton defined this property in two ways – the ability to resist the change of the momentum by outer forces, the inertial mass, and the ability to attract another massive object, the heavy mass. Both were found to be proportional to each other, which is reflected by the fact that all objects fall with the same acceleration in the gravitation field of the earth as was demonstrated by G. Galilei. This was, however, just a curiosity. Einstein postulated the intrinsic equivalence of heavy and inertial mass, and took as basic assumption for the theory of general relativity. Already from the theory of special relativity was shown that mass is also equivalent to energy.
Mass can be binding energy in complex bound states as is the case for hadrons. The largest fraction of the hadron masses is originated by the binding energy in form of gluons exchanged by the quarks constituting the hadron. On the other hand, the fundamental fermions are assumed to be point-like particles, i.e. no bound states. Their masses are much smaller than the hadron masses, and must be explained in another way.
There are models such as the Technicolor Model, which assume that the particles that are currently considered as fundamental are also bound states of more fundamental, massless particles. Then the masses of the currently known fundamental fermions are again due to binding energy, but from another, currently unknown force. In this way one would get rid of the question of the fundamental particle masses – there are none. However, the gauge boson masses are not easy to include into this picture.

Already the classical electrodynamics predict a mass. An electron, for example, is charged and exhibits an electric field. If the electron moves, also its electric field moves and changes into an electromagnetic field. This field contains energy and has a momentum proportional to the velocity of the electron, which can be considered as contribution of the total electron momentum. Due to the equivalence of energy and mass, the electromagnetic energy can be interpreted as mass. Its value is proportional to

$$m_{\mathrm{e}}^{\mathrm{EM}} = \frac{2}{3}\frac{e^2}{4\pi\varepsilon_0 a c^2} \ ,$$

where a is the radius of the electron, if the electron is assumed to be a sphere (the other constants are of minor interest at the moment) [42]. For different shapes, factors other than 2/3 may occur. This formula shows already the inherent problem. We currently assume that the electron is a point-like particle, i.e. it has a radius $a = 0$. The result would be an infinite electron mass. The problem lies in the self-interaction of the electron with its electromagnetic field, and is even not solved in quantum electrodynamics, where the bare masses of the particles are infinite. However, these infinities can be removed by means of renormalization. The result are the finite, physical masses, which, however, are still free parameters. This destroys the hope that the electromagnetic mass is completely determined by the charge of the particle.

The differences of the masses of the electron and the electron neutrino could be understood in this model (except the problem that electrons are point-like particles and have a zero radius). The neutrino is electrically neutral and should not have a mass. However, why has the muon a larger mass than the electron, and why about 200 times larger? It has else the same properties. It is not simply an excited electron, – as some models propose – otherwise we would be able to detect decays of a muon into an electron and a photon as occur for excited nuclei or atoms.
The electromagnetic mass can be at most a contribution to the total mass. The difference of the masses of charged and neutral π-meson can be explained by the electromagnetic contribution. However, mesons are complex compounds that have many contributions to their masses, and the electromagnetic contribution is small in comparison to that of the binding energy, for instance. In any case, the masses of the fundamental point-like fermions cannot be explained by an electromagnetic mass. Also the mass of the neutral Z boson cannot be explained in this model.

As seen in the previous section, the Higgs mechanism can introduce rest masses for the fundamental fermions by breaking a symmetry spontaneously. The mass is obtained from the strength of the coupling of a fermion to the Higgs field. The gauge bosons get a masses automatically as result of this mechanism. However, the Higgs mechanism keeps the fermion masses as free parameters.
Therefore the mass spectrum of the Standard Model particle content is not understood, yet, and also the possible mechanisms for the mass generation are still under ambitious investigations.

Extensions of the Standard Model

The many free mass parameters in the Standard Model are not very satisfying for a real fundamental theory. Also the fact that there are four fundamental forces (if there are not even more still undiscovered) is not explained, and gravity is actually not included in the Standard Model. There are more issues, some of more technical aspect. For instance, the Higgs boson mass would diverge with the increasing renormalization scale, unless the values of the fermion masses are such exactly arranged that the divergent mass term cancels. This fine-tuning of the fermion masses to solve the so-called *hierarchy problem* [43] is considered to be rather unnatural. Similarly, it is a riddle why the coupling strengths of the different fundamental forces differ by order of magnitudes.
It is often said that electromagnetism and weak interaction are *unified* by the GSW theory. However, there are still two different coupling constants, i.e. two different free parameters of the theory. A unification happens in the following sense. The couplings are not constants, they are different at different energy scales. The reason for this so-called renormalization behavior, i.e. the running of couplings with the energy scale, is the violation of the scale invariance. The physical behavior of a system is not reproduced if the system is just scaled. Nevertheless, the electromagnetic, weak, and strong couplings approach each other at high energies or short length scales by this running of the couplings. We assume that

at energies of about 10^{15} GeV, the GUT (grand unified theory) scale, indeed the three couplings reach at one value. If the Standard Model is considered to be a low-energy effective theory, an approach of a more complete model with a higher gauge symmetry than that of the Standard Model, then in this more complete model the different currently known forces might be generated out of a single force by some mechanism. This complete model represents then a real unification of the forces. However, within the current precision of the experiment, from which the coupling evolutions are extrapolated, the three couplings of the electromagnetic, the weak and the strong interaction in the Standard Model do not merge in exactly one point.
Furthermore, there is experimental evidence that neutrinos have a mass. As a consequence there can be also right-handed neutrinos. If neutrinos are represented by Dirac spinors then right-handed neutrinos must exist to keep the Standard Model including the mass generation via the Higgs mechanism consistent. This would require to extend the Standard Model particle content as experimental requirement.
A theory is desirable which covers all these issues. It might have a very high gauge symmetry, which contains only one single object that splits into the currently known fermions and force-mediating bosons by some mechanism, thereby creating the particle mass spectrum and the giving the forces their strengths. How this is to accomplish is unknown. This concept, however, is motivated by the success of the quantum chromodynamics. Herein, particles are arranged in multiplets in which the numerous hadrons could be led back to the six quarks. This, in turn, led to the establishment of the quantum chromodynamics (the quantum field theory of the strong interaction). Modern efforts deal with the extension of the Standard Model gauge group to groups of higher symmetry, which contain the Standard Model. Thereby, the attempt is made to introduce only one coupling. The minimal extensions of the Standard Model gauge group lead, unfortunately, to experimentally vetoed results such as the decay of the proton. Extensions to a higher symmetry become more and more complex and introduce furthermore new fermions and/or gauge bosons, which are not observed in the experiments, yet.

One currently highly favored model is the supersymmetric extension of the Standard Model [44, 45, 46, 47, 48]. The basic idea is the introduction of a fundamental symmetry between fermions and bosons. Thereby, the hierarchy problem in the Standard Model is solved in a natural way because the divergent contributions cancel each other exactly due to the fermion-boson symmetry. In the supersymmetry, also the gauge couplings are unified precisely at the GUT scale. The minimal supersymmetric extension of the Standard Model contains two Higgs doublets, and one of the Higgs bosons has similar properties as the Standard Model Higgs boson – the branching fractions of the Higgs boson decay may differ.
However, there are some new issues in the supersymmetry, which have to be clarified in the next collider experiments. The Standard Model particle content is doubled, and no supersymmetric partners of the known Standard Model particles is found, yet. Hence, the supersymmetric partners must be rather heavy. This and other reasons suggest that the supersymmetry is broken, if it is realized at all. The mechanism of breaking supersymmetry

is not understood, yet, although several scenarios are proposed, by which even the gravity can be included. The intrinsic supersymmetric model contains much more free parameters than the Standard Model, the number of which can be reduced considerably by symmetry breaking, but depends on the specific scenario.
Furthermore, supersymmetry cannot explain the fermion mass spectrum of the Standard Model. It must be included by hand, but with the help of it, one can predict at least the mass pattern of the supersymmetric partners.

The theoreticians do not become tired to create new ideas and models. The current status, short before the start of the LHC (Large Hadron Collider) [49] operation, is that there are many different models – some more preferred at the moment than others – that have to be discriminated by the experiment. They need not only cover the requirements of elementary particle physics but also those of astrophysics and cosmology. Satisfying models for elementary particles do not only have to be self-consistent and in agreement with the collider experiments but must also be in agreement with astrophysical and cosmological observations. They must provide mechanisms that explain the processes in stars, galaxies, and galaxy clusters. Specifically there are indications for matter and energy of unknown type – the so-called dark matter and dark energy. The radial velocity distributions of stars in the galaxies contradict Newton's law of gravity, and there exists a structure in the fluctuations of the 2.7 Kelvin microwave background radiation. Dark matter is a possibility to explain these effects. A model of elementary particles must provide a candidate for a dark matter particle. The Standard Model does not so. In the supersymmetric models there are candidates, such as the neutralino or the gravitino. Such a particle must be massive, rather stable, electrically and color neutral, and only very rarely interacting with the baryonic matter [5, 50]. Such particles, or effects from their existence, should be visible also in running and upcoming collider experiments.

1.2 Detection of Elementary Particles and Measurement of their Properties

Particles created in high-energy scattering experiments escape from the collision center. Several of these particles have a short lifetime and decay. Others are stable, such as electrons, protons, and photons or, at least, decay slowly enough to cover a substantial distance inside the detector material, such as muons, charged pions, neutrons and long-lived kaons.
To reconstruct the process that happened in the collision it is necessary to detect and identify the particles stemming from the interaction region – we call them *final state particles*. One needs to measure their properties such as the energy, the momentum, the charge, the spin, and other quantum numbers.
Devices build for this purpose are called *detectors*. An ideal detector detects particles and measures all properties without changing the particle properties. Real detectors interact with the particles to be detected, and the properties of both the detector and the particle are changed in this process. Furthermore, the detector response is often not linear with the measured properties of the detected particles. Careful calibrations must be performed to interpret the detector signals and translate them into the quantities to be determined.

1.2.1 Interaction of High-Energetic Particles with Matter

Each detection principle is based on interactions. In the previous section we listed the three known fundamental interactions (gravity plays no role in experiments of elementary particle physics) – electromagnetic, strong, and weak. Only via these particles interact with matter and deposit a part of their energy that is partly visible as signal. Depending on the properties of the particles traversing through the matter such as mass, energy, and the ability to interact via one or more of the aforementioned interactions, the energy loss of the traversing particle happens essentially by recoiling the nuclei or electrons bound in the matter, by excitation of inner degrees of freedom such as higher electronic or nuclear levels, by absorption of the impinging particle, or by emission of secondary particles and radiation. We summarize the most important facts about the possible interactions of high-energetic particles with matter.

Charged Particles

The electromagnetic interaction, which acts on all charged particles and photons, is the dominant one due to its wide range. Charged particles can lose their energy when traversing through matter by ionization, by emission of bremsstrahlung, and by direct electron-positron pair production.
Ionization is actually defined as the release of an electron from the bound state in atom such that the electron becomes free and leaves behind the ionized - i.e. positively charged - atomic cores. Of course, also the simple excitation of atomic electrons to higher bound energy levels requires energy, which reduces the kinetic energy of the particle that traverses

the matter. Not regarding these details, the essential mechanism of energy loss in ionization is the energy transfer when recoiling the electrons, which are bound in the atoms of the material. The probability for this process to occur is proportional to $\alpha^2 \propto e^4$. Ionization is the dominant energy loss mechanism for charged particles at lower energies. Stable particles would finally lose all of its kinetic energy and stop inside the material if the material volume is sufficiently large.
The impinging particle can also interact with the Coulomb field of the nuclei in the matter. Depending on the mass of the nucleus and on the mass and the energy of the impinging particle, the nucleus can be recoiled as well, and, if bound in a solid state lattice, is either excited to swing around its lattice position (phonon excitation) or knocked out from its lattice position, resulting in a highly ionized state. The latter case represents the creation of *radiation damages* in solids. Also in such a process energy is transfered from the impinging particle to the material. Strictly speaking, however, this does not belong to ionization, although the basic mechanism of energy loss is the same. The probability for knocking out nuclei is proportional to Z^2, since the nucleus charge is Ze. This process is the more suppressed the smaller the ratio of the mass of the impinging particles to the nucleus mass is and plays usually no role for the energy loss. It might be, however, important for the following.

Another important aspect of the electromagnetic interaction with the material is the deflection by small angles in the Coloumb field of the nuclei when the energy loss is small. In the simplest approach the distribution of the scattering angle for a short distance of particle transport can be described by a Gaussian distribution. This process is called *multiple Coulomb scattering* and has an impact on the momentum reconstruction for particles with a smaller momentum or light particles, i.e. the electrons.

Bremsstrahlung involves the emission of photons when the impinging particle is deflected by the Coulomb field of a nucleus. This process is dominant at higher energies, and has more impact on particles with smaller masses, since the radiated energy is related to the acceleration of the particle. The acceleration, in turn, is larger for a particle with a smaller mass (for a given force in Newton's law). The bremsstrahlung cross-section is inversely proportional to the square of the mass of the impinging particle. Therefore, the bremsstrahlung losses for muons are about 40000 times smaller than for electrons. The bremsstrahlung cross-section increases also with Z^2, and is proportional to $\alpha^3 \propto e^6$.

In *direct pair production* an electron-positron pair is created when the impinging particle is deflected in the Coulomb field of a nucleus. It occurs only above the threshold of about 1.2 MeV, the energy corresponding to twice the rest mass of an electron. Pair production becomes dominant at high energies, and the cross-section is proportional to Z^2 and to $\alpha^4 \propto e^8$.

Positrons also lose permanently energy by the same processes as for electrons. Additionally, they can also annihilate with a material electron, in the process of which two photons are

created.

Photons

The most important ways for high-energy photons[4] to interact with matter are the photo-electric effect, Compton scattering and electron-positron pair production. In all processes the original photon is destroyed. While the photo-electric effect is dominant for relatively small photon energies (less than about 0.5 MeV in lead), electron-positron pair production is dominant at high energies (above about 5 MeV for lead). To be able to create an electron-positron pair, the energy of a photon must be at least as high as the energy corresponding to twice the electron rest mass. Compton scattering plays the dominant role for energies in the range between 0.5 and 5 MeV.
With the photo-electric effect, material electrons are excited to higher energy levels or knocked out, and might be able to excite or ionize further atoms. The cross-sections for the photo-electric effect, Compton scattering and electron-positron pair production can be calculated by means of perturbation theory in quantum electrodynamics. While Compton scattering and pair production are rather simple processes, the photo-electric effect can be quite complicated, because a photon can only be absorbed if there is an allowed energy level for the excited electron.[5] In single atoms there are discrete energy levels, and also in solid states there are allowed energy ranges, in which electrons can exist. Thus, the photo-electric effect cross-section at low photon energies is a complicated function of the energy and the material under consideration. Only at higher energies, electrons can be released from the bound state, and are even able to leave the solid as so-called δ-electrons. In the range of several MeV photons can also excite nuclei to higher energy levels by photo nuclear absorption followed usually by the emission of a neutron or another particle from the nucleus.
Low energy Photons with energies up to few 100 keV can also undergo elastic scattering with the material electrons - Rayleigh scattering. In this energy range, though, the photon absorption due to the photo-electric effect dominates largely.

Neutral Hadrons

The energy loss of neutral, relatively stable hadrons, e.g. neutrons and kaons, traversing a material is accomplished by elastic and inelastic scattering on the nuclei. In the former case, energy is transferred by recoiling the nucleus, which may be then highly ionized. In the latter case, a lot of pions or nucleus fragments can be created.
The ionized recoiled nuclei, nucleus fragments and pions traverse the matter subsequently as charged particles, mainly loosing their energy by electromagnetic interactions. The neutral pions decay almost instantaneously mainly into two photons.
The energy loss due to elastic scattering is the larger the more similar the masses of projectile and target are. Since calorimeter absorbers are usually made from material

[4] Here of major interest.
[5] This plays an important role at smaller energies (several eV to few 100 keV).

with a large atomic number, the deceleration by elastic scattering is less effective than that by inelastic scattering. Therefore, neutrons can travel a substantial distance without depositing a significant energy in a hard collision with a nucleus. If the neutrons are slow enough or pass a resonance in the absorption cross-section of the material, they can be captured by the nucleus causing maybe subsequent nuclear reactions.

Neutrinos

Neutrinos interact only via weak interactions, and are, therefore, hard to detect. A high-energetic neutrino that actually scatters on an electron can transfer its energy to the electron via W boson exchange. This electron can then be an indicator for a neutrino incident. In other scattering processes further particles might be created, such as muons, tauons, and quark pairs by virtue of the structure of the weak interaction. If neutrinos interact with quarks inside a nucleons they can change the type of this nucleon and therefore that of the atomic number of the nucleus, or they even induce fission of a nucleus. In this way, neutrino incidents can be verified chemically by extracting the transformed atoms.
However, in collider experiment the detector volume and the neutrino fluxes are too small. In such experiments neutrinos are registered due to missing energy and momentum, i.e. by the difference between the sum of the energies and momenta of all initial state and found final state particles.

1.2.2 Stopping Power and Energy Loss Straggling

General Considerations

For the detector design, it is necessary to estimate how much energy a particle deposits inside the traversed detector material. We therefore start with the estimation of the energy loss of a particle traversing a certain material. Energy loss and energy deposition are closely related to each other, although the relation might be rather complex.
We denote with σ the cross-section of the process in which the impinging particle loses a part of its energy, with n_S the density of scatterers in the detector material, and with ϕ the flux of the impinging particles not having undergone scattering, yet. Then the number of collision events per unit time and volume is given by

$$r_S = \phi \sigma n_S \ . \tag{1.31}$$

If the atoms are the scattering centers, for instance, then n_S is the atom density,

$$n_{\mathrm{A}} = \frac{N_A \rho}{A} \ , \tag{1.32}$$

where N_A is the Avogadro constant and A the atomic mass (mass of one mole). ρ is the mass density.
If several scattering processes are involved with cross-sections σ_i and corresponding densities of the scattering centers, n_S^i, then the single and total rates of scattering events per

unit volume are

$$r_S^i = \phi\sigma_i n_S^i \quad \text{and} \qquad r_S = \sum_i r_S^i = \phi \sum_i \sigma_i n_S^i \equiv \phi\sigma n_S \; . \tag{1.33}$$

Let the flux ϕ of incident particles without any interaction be directed into the positive x-direction, and it enters a material block at $x = 0$. ϕ will decrease with the penetration depth x. The decreasing rate of ϕ with respect to x is the negative scattering rate,

$$\frac{d\phi}{dx} = -r_S = -\sigma n_S \phi \; ,$$

the solution of which is

$$\phi(x) = \phi_0 e^{-\sigma n_S x} \; ,$$

where ϕ_0 is the initial flux of incident particles at $x = 0$. For photons, ϕ is the intensity if the only considered energy loss process is absorption. The quantity

$$\lambda = (\sigma n_S)^{-1} = \left(\sum_i \sigma_i n_S^i \right)^{-1} \equiv \left(\sum_i \lambda_i^{-1} \right)^{-1} \tag{1.34}$$

is the *mean free path*[6] for obvious reasons. The quantities $\lambda_i = (\sigma_i n_S^i)^{-1}$ are the mean free paths for the single processes. The probability that the interaction processes i happened under the condition that a single interaction occurred at all is given by

$$P(i|\text{single interaction occurred}) = \frac{r_S^i}{r_S} = \frac{\sigma_i n_S^i}{\sum_j \sigma_j n_S^j} \; ,$$

which is completely determined by the properties of the material and scattering processes. If the detector material has the thickness d_s, then the average number of scattering events is approximately given by

$$\langle M \rangle = \frac{d_\mathrm{s}}{\lambda} \; , \tag{1.35}$$

where M denotes the corresponding random number. M is in first order Poissonian distributed if the energy of the traversing particle does not change too much due to the interactions, that is

$$P(M = k) = \frac{\langle M \rangle^k e^{-\langle M \rangle}}{k!} = \left(\frac{d}{\lambda} \right)^k \frac{e^{-d/\lambda}}{k!} \; . \tag{1.36}$$

This is specifically fulfilled for the penetration of thin material layers.
We denote by T the energy transferred in a single collision from the penetrating particle to the material. The differential cross-section normalized to the total cross-section,

$$\pi(T) = \frac{1}{\sigma} \frac{d\sigma}{dT} \; ,$$

[6] Also called *interaction length*, *attenuation length* or (for photon absorption) *absorption length*.

represents the probability for a specific value of T in a single interaction. The cross-section σ is defined such that

$$\int_{T_{\min}}^{T_{\max}} \pi(T)\, dT \equiv \frac{1}{\sigma} \int_{T_{\min}}^{T_{\max}} \frac{d\sigma}{dT}\, dT = 1 \ ,$$

where $T_{\min}$ and $T_{\max}$ were introduced to be either physical limits or cut-offs e.g. in order to make the integral convergent. The average energy loss in a single scattering process is then

$$\langle T \rangle = \int_{T_{\min}}^{T_{\max}} T\, \pi(T)\, dT = \frac{1}{\sigma} \int_{T_{\min}}^{T_{\max}} T\, \frac{d\sigma}{dT}\, dT \ . \tag{1.37}$$

The averaged energy lost by the impinging particle of energy E_0, $\delta E = E_0 - E(d_{\mathrm{s}})$, after traversing the distance d_{s} of the material is then given as the product of Equations (1.35) and (1.37),

$$\begin{aligned} \delta E = E_0 - E(d_{\mathrm{s}}) = \langle M \rangle \cdot \langle T \rangle &= \frac{d_{\mathrm{s}}}{\lambda} \frac{1}{\sigma} \int_{T_{\min}}^{T_{\max}} T\, \frac{d\sigma}{dT}\, dT \\ &= \frac{d_{\mathrm{s}} n_S \sigma}{\sigma} \int_{T_{\min}}^{T_{\max}} T\, \frac{d\sigma}{dT}\, dT \ , \end{aligned}$$

where also Equation (1.34) has been used. We obtain therefore

$$\frac{\delta E}{d_{\mathrm{s}}} = \frac{E_0 - E(d_{\mathrm{s}})}{d_{\mathrm{s}}} = n_S \int_{T_{\min}}^{T_{\max}} T\, \frac{d\sigma}{dT}\, dT \ .$$

For $d_{\mathrm{s}} \to 0$ we finally arrive at

$$\frac{dE}{dx} = -n_S \int_{T_{\min}}^{T_{\max}} T\, \frac{d\sigma}{dT}\, dT = -\sum_i n_S^i \int_{T_{\min}}^{T_{\max}} T\, \frac{d\sigma_i}{dT}\, dT \equiv \sum_i \frac{dE_i}{dx} \ . \tag{1.38}$$

In the last equality we exploited Equation (1.33) and that n_S and the n_S^i are independent of T, and we obtain that the energy loss rate is a sum of the individual energy loss rates by the single processes, as it must be. $S = -dE/dx$ is called the *stopping power*. It describes the ability of a material to decelerate a particle of a certain type exhibiting a certain momentum.

Ionization Stopping Power

We want to sketch the derivation of the stopping power due to ionization of a heavy particle other than an electron, say a muon, i.e. the impinging particle mass $M \gg m_{\mathrm{e}}$. Since the ionization process is the collision of the impinging muon with the material electrons, the number of scatterers per unit volume is the density of the material electrons, $\frac{\rho N_A}{A} Z$. The calculation of the cross-section is conveniently accomplished in the rest frame of the impinging muon, i.e. we consider the scattering of an incoming electron on the fixed

Coulomb field of the resting muon. We use for this process the differential Mott scattering cross-section [10, 9], which accounts for the spin-1/2 nature of the electrons[7], in terms of the energy transfer T,

$$\frac{d\sigma}{dT} = \frac{z^2 e^4}{8\pi\varepsilon_0^2 m_\mathrm{e} c^2 \beta^2} \frac{1}{T^2} \left(1 - \beta^2 \frac{T}{T_\mathrm{max}}\right) . \tag{1.39}$$

Herein, z is the charge of the heavy particle (1 for the muon) in units of e, $\beta = v/c$ its speed (which equal to the speed of the electron in the muon rest frame), and c is the speed of light.
We insert Equation (1.39) into Equation (1.38). The limits of the integral are as follows. T_min is the minimum energy to be transferred to ionize an atom, i.e. the mean ionization potential, I. It is a material property. Values are given for instance in Reference [5]. T_max is the maximum transferable energy, which is reached in head-on collisions, i.e. $T_\mathrm{max} = 2m_\mathrm{e}c^2\beta^2(\gamma^2-1)/\big(1+2\gamma(m_\mathrm{e}/M)+(m_\mathrm{e}/M)^2\big)$ ($T_\mathrm{max} \approx 2m_\mathrm{e}c^2\beta^2\gamma^2$ for $m_\mathrm{e} \ll M$ and $\gamma \gg 1$), where $\gamma^2 = 1/(1-\beta^2)$. After the integration under the assumption $I \ll T_\mathrm{max}$, we obtain

$$\begin{aligned} \frac{dE}{dx} &= -\rho\frac{N_A}{A} Z \frac{e^4 z^2}{8\pi\varepsilon_0^2 m_\mathrm{e} c^2 \beta^2} \left(\ln\frac{T_\mathrm{max}}{I} - \beta^2\right) \\ &\approx -\rho\frac{N_A}{A} Z \frac{e^4 z^2}{8\pi\varepsilon_0^2 m_\mathrm{e} c^2 \beta^2} \left(\ln\frac{2m_\mathrm{e}c^2\beta^2\gamma^2}{I} - \beta^2\right) . \end{aligned} \tag{1.40}$$

This is just the half of the result found by Bethe and Bloch [51, 52, 5]. The reason might be that inelastic scattering, i.e. the pure excitation of the atoms, is not considered here since we start to integrate over T from the ionization potential. These excitations, however, can be a significant contribution to the energy loss due to the favored low energy transfer by the Rutherford cross-section and are accounted for in the derivation by Bethe and Bloch, which is based on the quantum mechanical scattering theory of heavy particles on atoms. Several other corrections were also included such as shell (C/Z) and density ($\delta(\beta\gamma)/2$) corrections accounting for the inner atomic structure of the material (playing a role at lower energies) and the screening effect due to a higher density of target electrons with higher Z (important at higher energies). The result is the Bethe-Bloch formula [5] for a particle being not an electron

$$\frac{dE}{dx} = -\rho\frac{N_A}{A} Z \frac{e^4 z^2}{4\pi\varepsilon_0^2 m_\mathrm{e}^2 c^2 \beta^2} \left[\frac{1}{2}\ln\frac{2m_\mathrm{e}c^2\beta^2\gamma^2 T_\mathrm{max}}{I^2} - \beta^2 - \frac{\delta(\beta\gamma)}{2} - \frac{C}{Z}\right] . \tag{1.41}$$

The energy loss as a function of the particle momentum, dE/dx, exhibits a minimum at $\beta\gamma \approx 3.5$. This minimum corresponds to a certain momentum for different particle types. It represents the minimum possible averaged energy loss of the particle traversing the material due to ionization or atomic excitation. Such *minimum ionizing particles* (MIP) are often used to investigate and determine detector properties.

[7] This cross-section is often also referred to as *modified Rutherford cross-section*.

The stopping power for electrons is a bit more complicated due to the quantum mechanical interference of the final state electrons[8] [53], but exhibits the same general properties as that for other particles. For illustration, Figure 1.2 shows the total stopping power (red solid line) of an electron in graphite. Shown are also the stopping powers mainly contributing

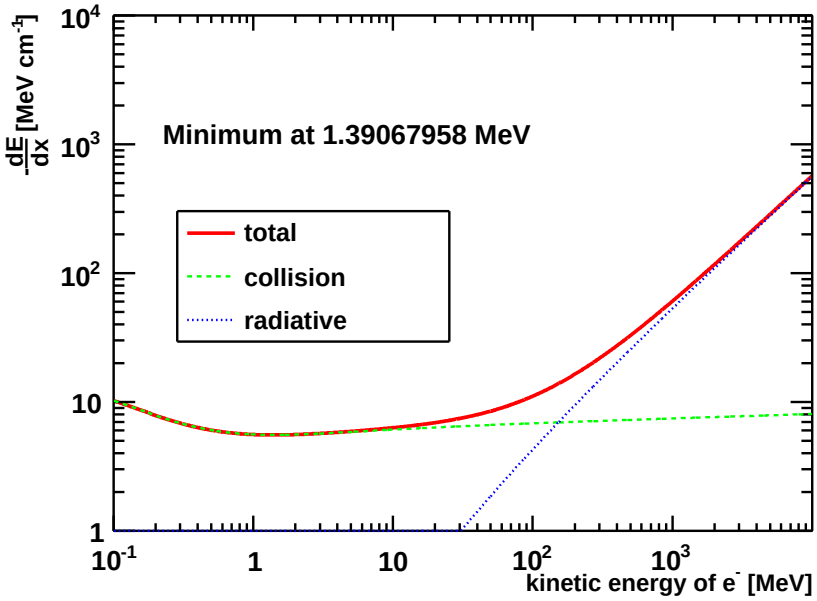

Figure 1.2: The theoretical stopping power of an electron in graphite. The minimum at about 1.4 MeV corresponds to $\beta\gamma \approx 3.5$. Electrons of this kinetic energy in graphite are called MIPs.

to the total stopping power due to ionization and excitation (green dashed line) and due to bremsstrahlung losses (blue dotted line), which play a dominant role for electrons already at moderate electron momenta.

Fluctuations of the Energy Loss

We are now posing the following question. For an impinging particle with energy E_0, what is the probability to lose the energy $\delta E = E_0 - E(d_\mathrm{s})$ when passing through a material block of thickness d_s? Related to this is the question of how does δE fluctuate [54]. The probability density function $f(\delta E, d_\mathrm{s})$ gives the probability for a certain energy loss, δE, in a event when a single particle with energy E_0 crosses the material block. f depends parametric on the thickness, d_s, and also on the sensor material.
The Boltzmann transport equation is used to determine f,

$$\frac{\partial f(\delta E, d_\mathrm{s})}{\partial d_\mathrm{s}} = \int_{T_\mathrm{min}}^{T_\mathrm{max}} w(T)\, f(\delta E - T, d_\mathrm{s})\, dT - f(\delta E, d_\mathrm{s}) \int_{T_\mathrm{min}}^{T_\mathrm{max}} w(T)\, dT\ . \tag{1.42}$$

[8] The Møller scattering cross-section can be used.

The change of f within an interval d_s is equal to the *collision integral*, i.e. the number of particles that experience a certain energy loss, δE, along d_s due to ionization losses, minus the number of particles that leave this energy interval. One can consider them as generation and loss terms, and the Equation (1.42) as a rate equation for f. The Mott cross-section, Equation (1.39), multiplied by the density of electrons can be used to determine the probability for a particle to undergo a certain energy loss, $w(T) = \rho\frac{N_A Z}{A}\frac{d\sigma}{dT}$. Equation (1.42) can be approximately solved using the method of Laplace transformation. After some further approximations such as $T_\mathrm{min} = 0$ and $T_\mathrm{max} = \infty$,[9] which are the minimum and maximum transferable energies in one collision, and some algebraic transformations one obtains

$$f(\delta E, d_\mathrm{s}) = \frac{1}{\xi}\varphi(\lambda) \qquad \text{where } \varphi(\lambda) = \frac{1}{2\pi i}\int_{c-i\infty}^{c+i\infty} e^{u\ln u+\lambda u}\,du\ , \quad (c>0)$$
$$\xi = \frac{z^2e^4}{8\pi\varepsilon_0^2 m_\mathrm{e}c^2\beta^2}\frac{N_A}{A}\rho Z d_\mathrm{s} \qquad \text{and } \lambda = \frac{\delta E - \xi\left(\ln\frac{\xi}{\varepsilon'} + 1 - \gamma_E\right)}{\xi}\ . \tag{1.43}$$

Herein, ξ is the average energy loss of a particle of energy E_0 penetrating an absorber of thickness d_s as estimated from the Bethe-Bloch equation (1.41). Furthermore, $\ln\varepsilon' = \ln\frac{I^2}{2m_\mathrm{e}c^2\beta^2\gamma^2} + \beta^2$, and $\gamma_E \approx 0.577215665$ is the Euler constant.
$\varphi(\lambda)$ is the intrinsic *Landau probability density function* and has no free parameters. Its most probable value is located at $\lambda_\mathrm{MPV} = -0.22278299$. The quantity φ, depicted in Figure 1.3, is normalized to one but does not possess any of its moments such as the mean value and the standard deviation. There is a long right-hand side tail to take account of the finite probability for the loss of a large energy fraction of the particle crossing the material block.
$f(\delta E, d_\mathrm{s})$ is obtained from $\varphi(\lambda)$ by scaling φ and λ, whereby the parameter dependence of f is introduced. The most probable value for f is therefore found using that of φ and by scaling at

$$\delta E_\mathrm{MPV} = \xi\left(\ln\frac{\xi}{\varepsilon'} + 0.2\right)\ . \tag{1.44}$$

It is the characteristic value of the distribution f and behaves as a function of the material block thickness like $\delta E_\mathrm{MPV}/x \sim (a\ln x + b)$. For comparison, the mean energy loss per unit length using the Bethe-Bloch formula (1.40) is constant with respect to x. Several corrections such as shell and density corrections were introduced into Equation (1.43), such as for the Bethe-Bloch formula. δE_MPV can also be used to estimate the deposited energy since the latter is not that different from δE_MPV. Specifically, it does not fluctuate as the mean value does in experiments and can therefore be measured more reliably.

The reason for the non-existence of the mean value of $\varphi(\lambda)$ is the approximation $T_\mathrm{max} = \infty$, which was convenient to solve Equation (1.42). Therefore, for a given T_max, the Landau

[9] This is necessary for the applicability of the Laplace transformation. In the final step the lower limit is again replaced by the ionization energy. Otherwise the result would be infinite.

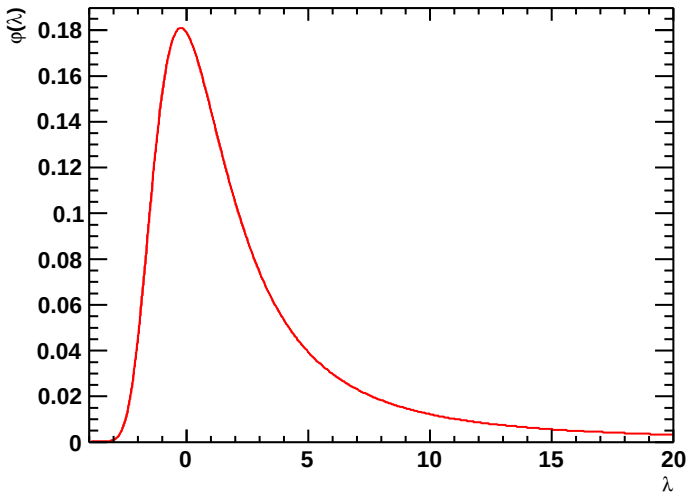

Figure 1.3: The Landau probability density function for energy loss straggling, $\varphi(\lambda)$.

theory is applicable for $\xi/T_{\max} < 0.01$. The Vavilov theory [55] avoids this approximation, and a somewhat more complicated function than φ is obtained. The Vavilov theory is valid for $0.01 < \xi/T_{\max} < 10$. Above the upper limit, i.e. for thick absorbers, a Gaussian distribution [53] can be used to describe the fluctuations of δE.

For very thin absorbers or material with a very low density (gas absorbers), Bichsel [56, 57, 58] pointed out larger discrepancies of the analytically found energy loss straggling functions (i.e. the probability density functions for the energy loss) to those measured, because of the more and more dominant role of the Poisson statistics for the number of interactions on the path through the material as shown in Equation (1.36). The theoretical description of energy loss straggling functions can be done best numerically, via Monte-Carlo simulation programs such as e.g. GEANT4 [59, 60]. In this way also the energy deposition could be in principle included into the considerations.

The energy deposited by a particle passing through a material is usually smaller than the energy lost by this particle. By interactions with the material e.g. bremsstrahlung photons and δ-electrons generated by the impinging particle, which in turn can leave the material block carrying a sizable amount of energy. The δ-electrons also traverse a certain path through the material loosing and depositing energy and the photons could be re-absorbed if the sensor is thick enough. All these primary and secondary particles will move furthermore in almost each direction, not only along the direction of the impinging particle. This represents a very complex scenario of interactions, which can be described best using Monte-Carlo simulations giving more realistic results than the analytical estimations above. The energy deposition is, however, still not easy to include correctly due to the dependence of the energy dissipation processes on the microscopic and macroscopic material properties. This will be discussed in part in Chapter 5.

1.2.3 Showers

Electromagnetic Showers

When high-energetic electrons or photons hit a sufficiently thick and dense material block, electromagnetic cascades are initiated. The situation for initial electrons and photons is comparable since bremsstrahlung and pair production are almost equal by cross-sections. The electron loses its energy dominantly by ionization, where secondary electrons might be released, and emits bremsstrahlung photons or creates electron-positron pairs with lower energies by direct pair production. A lot of these secondary particles have enough energy to excite further atoms or release electrons by ionization or to create further high-energetic photons. The bremsstrahlung photons can produce electron-positron pairs, either partner of which carries in average half of the photon energy, and undergoes again bremsstrahlung. The multiplication process continues until the energy of the photons is not sufficient to create further electron-positron pairs, and for the electrons and positrons ionization becomes the dominant energy loss process. This avalanche process is called *showering*, and the generated particles distributed in a certain are called a *shower*.
Such a shower evolves with the penetration depth into the direction of the impinging primary particle, but also in lateral direction. For electromagnetic showers, the shower shape can be parametrized. The main parameters for the electromagnetic shower are the depth at the shower maximum, i.e. the depth where the maximum of energy is dissipated, and the transversal shower extension, expressed as *Moliére radius*. These parameters depend on the detector material properties.
The longitudinal extension, i.e. the scale along the initial direction of the primary particle, is determined by the *radiation length*, X_0. It is defined as the mean distance over which the high-energetic primary electron loses its initial energy down to the 1/e-fraction due to bremsstrahlung. This is the same as 7/9 of the mean free path for a high-energy photon until it converts to an electron-positron pair. One can use the phenomenological Dahl parametrization [5], to estimate X_0 in different materials,

$$X_0 = \frac{716.4A}{Z(Z+1)\ln\frac{287}{\sqrt{Z}}}\,\mathrm{g\,cm^{-2}}\,, \tag{1.45}$$

which is precise up to 2.5 % (except for helium, where the precision is about 5 %). It is usually given in g/cm^2, so that the division by the mass density of the material gives a length.
The longitudinal shower profile is conveniently expressed by the scaled variable $t = x/X_0$, where x in the longitudinal spatial shower evolution coordinate. The mean longitudinal profile of the energy deposition in the electromagnetic shower can be described as [61],

$$\frac{dE_{\mathrm{dep}}}{dt} = E_{\mathrm{sh}} b \frac{(bt)^{a-1}e^{-bt}}{\Gamma(a)}\,. \tag{1.46}$$

The quantities a and b are functions of Z and of the type and the energy of the incident particle. $\Gamma(x)$ denotes the Γ function. E_{sh} is the energy contained in the shower.

Then the shower maximum is at the penetration depth

$$t_{\max} = (a-1)/b = \ln(E_0/\varepsilon_{\rm cr}) + c \ \text{ in units of } X_0 \ , \tag{1.47}$$

where E_0 is the energy of the incident primary particle, $c = -0.5$ for electrons, and $c = +0.5$ for photons. $\varepsilon_{\rm cr}$ is the critical energy at which the energy losses by bremsstrahlung and ionization are equal. It is approximately

$$\varepsilon_{\rm cr} = \frac{610 \text{ MeV}}{Z + 1.24} \text{ for solids and liquids and} \quad \varepsilon_{\rm cr} = \frac{710 \text{ MeV}}{Z + 0.92} \text{ for gases .} \tag{1.48}$$

The shower depth (in terms of X_0) of 95 % longitudinal containment is about [62],

$$t_{95\%} \approx t_{\max} + 0.08Z + 9.6 \ . \tag{1.49}$$

The Moliére radius is defined as the radius of the cylinder enveloping the shower axis in which on average 90 % of the particle energy is deposited. The Moliére radius can be parametrized as [63, 64, 65],

$$R_M = X_0 E_s/\varepsilon_{\rm cr} \ , \tag{1.50}$$

where $E_s = \sqrt{\frac{4\pi}{\alpha}} m_{\rm e} c^2 \approx 21.2$ MeV.

Hadron Showers

The energy deposition of hadrons consists of an electromagnetic and a hadronic part. In processes of inelastic interactions with the nuclei mostly neutral and charged pions, neutrons, protons and nuclear fragments are created. The neutral pions decay immediately almost exclusively into photons, which in turn cause electromagnetic showers. The neutrons, protons and nucleus fragments are rather stable and can carry a substantial amount of energy away from the center of the incidence. They deposit their energy by elastic and inelastic scattering with the atoms and the nuclei.
One difficulty of the description of hadronic cascades is the fluctuation of the number of created neutral pions. These are reflected in strong event-to-event fluctuations of the fraction of the energy deposition in the electromagnetic part of the shower. Another issue is the irregular shape of hadron showers due to travelling neutrons. In the hadronic processes also neutrinos and muons might be produced leaving the material volume without any significant energy deposition, and also the release of binding energy of the nuclear fragments contribute to the fluctuations of the deposited energy. Therefore, hadron showers are not as compact as electromagnetic showers. They have an irregular shape and exhibit strong fluctuations of the fractional energy deposited electromagnetically.
The characteristic length for the hadronic multiplication process is the *interaction length*, λ_I [5, 53], i.e. the mean free path for inelastic hadronic interactions, which is essentially energy-independent. In a simple parametrization [66], the shower maximum is located at

$$t_{\max} \approx (0.6 \ln E_0 - 0.2) \ ,$$

and the shower depth for a 95 % longitudinal containment of the shower energy is

$$t_{95\ \%} \approx t_{\max} + 4E_0^{0.15} \ .$$

Herein, the energy of the incident particle, E_0, is given in GeV, and $t_{\max}$ and $t_{95\ \%}$ are in units of λ_I. The shower radius for 95 % radial conftainment can be estimated as

$$R_{95\ \%} \approx \lambda_I \ ,$$

which is usually larger than that for an electromagnetic shower, since the cross-sections for hadronic processes are smaller than that for electromagnetic ones.

1.2.4 Detector Technologies

Any material that reacts to an impinging particle can be used as detector. Most detector materials get excited or ionized by charged particles. The energy deposited by electromagnetic processes, which are dominant, can be read out as electrical, optical, chemical, etc. signals, whereas detectors based on electrical and optical signals have prevailed in high-energy collider experiments.
We consider here detectors relevant for high-energy collider experiments and list the detector types mostly used in such experients. Particles accelerated to high energies collide close to the so-called *nominal interaction point* (IP), i.e. the intended point of collisions. The real point of collision is called the *primary vertex*. Depending on the scattering process under investigation a lot of particles producted in the collision fly radially away from the primary vertex. The detectors are, therefore, more or less concentrically arranged arround the IP.
One can subdivide the detectors in *trackers* and *calorimeters*. Calorimeters measure the energy of the impinging particle. To do this the detector material must be dense (high Z material) and the detector volume sufficiently large, so that all the particle energy is dissipated inside this volume and nothing escapes from the detector. Trackers, in contrast, just measure the path of a particle. In an ideal case the tracker traces the path of the particle without affecting the particles momentum. Therefore, trackers should be transparent (low Z material).

Tracking Detectors

Trackers are made to measure track points of the three-dimensional (3D) trajectory of a charged particle. This can be accomplished with several technologies. Silicon tracking detectors, for example, are made of silicon planes, with a fine lateral (2D) segmentation each – called *pixels* in case of very small area segments, *pads* for larger, almost quadratic segments or *strips* if the segmentation in one lateral direction is finer. A particle passing through such a plane deposits energy at the point of penetration. Thereby, excess charge carriers are generated originating by their drift in an electric field an electronic signal in this point, which can be identified by the tracker plane and the 2D position of the pixel on this plane. Several consecutive such planes then trace the particle trajectory.

In time projection chambers (TPC) [67] the electrons, stemming from the ionization along the trajectory of the high-energy particle, drift along an electric field to an end plane, which is perpendicular to this field. These end planes comprise finely segmented sensors that provide the projection of the trajectory. The drift time measurement gives the third coordinate of each trajectory point. Figure 1.4 shows a scheme of a TPC.

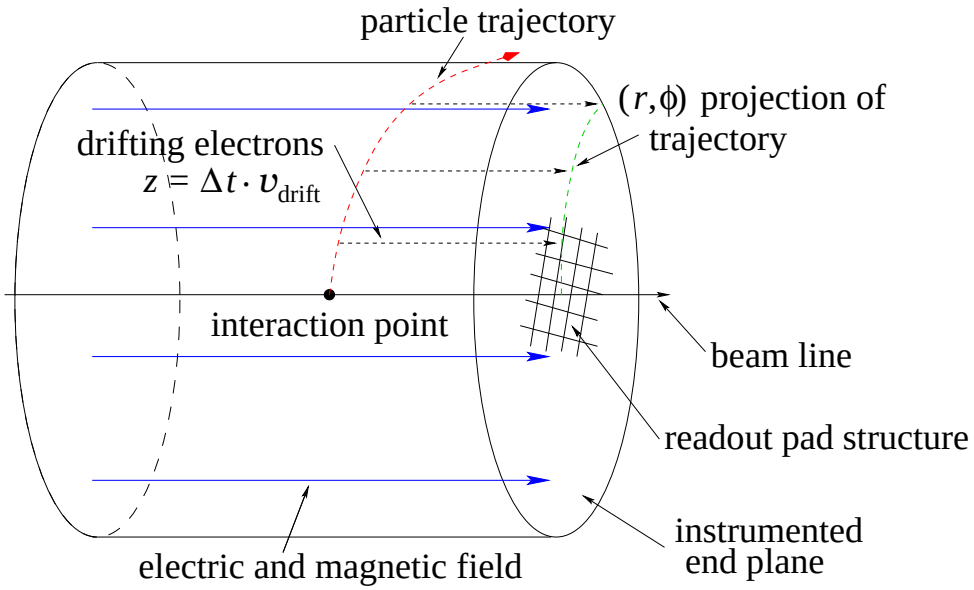

Figure 1.4: Working scheme of a TPC. The electric field is directed parallel to the beam line. The electrons released by ionization along the particle trajectory drift in this field to the end plane, which consists of finely segmented sensors that register and enhance the signals from electrons.

The signals from the segmented tracker sensors are converted into 3D points (called *hits*) that trace the particle trajectory. A curve can be fitted to these points to obtain a *reconstructed trajectory*, i.e. an approximated path of the particle. The parametrization of the curve depends on the model used for the transport of the high-energetic particle through the detector. The tangent of this curve gives the reconstructed momentum direction in each point of the reconstructed trajectory.
In order to measure also the value of the momentum, one applies a magnetic field parallel to the beam line such that a charged particle having a velocitiy component perpendicular to the magnetic field direction, $v_\perp$, is deflected by the Lorentz force, F_L, according to

$$F_L = qv_\perp B \ . \tag{1.51}$$

Herein, B is the magnetic field, and q is the particle charge. In a constant magnetic field, for a particle with transverse momentum $p_\perp = \gamma m v_\perp$, the Lorentz force is compensated by the centrifugal force. The trajectory of the particle is bend with a radius of curvature R, which is related to the transverse momentum by

$$R = \frac{p_\perp}{qB} \ . \tag{1.52}$$

For a given positive magnetic field, R is negative for a negatively charged particle, and positive for a positively charged particle. Therefore, the charge sign can be obtained from the direction of curvature of the particle trajectory with respect to the magnetic field direction.
The absolute value of the charge must be measured separately. This can be accomplished by measuring the amount of energy loss by the high-energetic particle inside the tracker per path length, i.e. dE/dx. Due to the Bethe-Bloch formula (1.41) the energy loss is proportional to z^2, where z is the particle charge in terms of an electron charge. A doubly charged particle loses four times more energy by ionization than e.g. a muon.
For particles of unit charge and by determining the value of dE/dx, also a particle identification can be performed for relatively low particle momenta [56]. From this, the mass and, eventually, the energy can be determined.

Calorimeters

Calorimeters shall provide a measurement of the energy of a particle and also its impact point into the calorimeter. The calorimeter stops the particle so that tracking detectors must be put in front of calorimeters. Calorimeters are useful especially for the energy measurement of neutral particles, since they do not leave tracks inside the tracker.
Calorimeters made from a single block just give the energy information. The signal can be provided in different ways. Scintillator crystals transform the dissipated energy into a light pulse, which can be registered at the edges of the crystal. A calorimeter can also be segmented and consist of high-Z absorber layers, which enhance the shower development, interspersed by sensor layers, which register the signals from charged particles in the shower. Such a calorimeter is called a *sampling calorimeter*. The sensors can be similar to those of the silicon tracking detectors. They absorb only a small part of the dissipated energy, and by calibration one can determine the energy totally deposited by the incident particle. There is another advantage of a sampling calorimeter: one obtains information about the longitudinal shower profile, described by Equation (1.46). By a lateral segmentation of the sensor planes into pads, one additionally obtains a sampling of the transversal spatial shower distribution. This information can be used to determine the shower position, i.e. the entrance point of the impinging particle into the calorimeter and the shower direction, which can give indications of the momentum direction of the incoming particle. The shower shape can also be used for the particle identification, since it differs for different particle types.
Specifically, calorimeters are again subdivided into electromagnetic and hadron calorimeters. The first one can be sampling calorimeters, which must be able to stop electrons and photons in front of an hadron calorimeter by inducing an electromagnetic cascade. Neutral and charged hadrons may start to shower in the electromagnetic calorimeter, but the hadron shower extends into the hadron calorimeter, where the primary particle is eventually stopped. Therefore, electrons and photons leave almost their total energy only in the electromagnetic calorimeter, while hadrons have the larger fraction of energy deposited inside the hadron calorimeter.

Hadron calorimeters can be designed in a specific way to account for the fluctuations in the creation of neutral pions. By a clever choice or design of the absorber material, one can achieve that electrons and charged pions of the same energy cause the same response of the hadron calorimeter - or in the commonly used terminology – the e/π ratio is close to one. Calorimeters fulfilling this requirement are *compensating*. Compensation ensures a linear response of the calorimeter to the hadron shower energy deposition and an improvement of the accuracy of the energy measurement with increasing incident energy [68].
For electromagnetic calorimeters, the accuracy of the measurement of the shower position is limited by the Moliére radius of the absorber and the lateral segmentation of the sensor layers. The energy measurement uncertainty can be parametrized as ([5] and references quoted therein)

$$\frac{\Delta E_{\text{dep}}}{E_{\text{dep}}} = \frac{a}{\sqrt{E_{\text{dep}}}} \oplus b \oplus \frac{c}{E_{\text{dep}}} \, . \tag{1.53}$$

Here, E_{dep} is the mean deposited energy in GeV and ΔE_{dep} the standard deviation of the E_{dep} measurement. The symbol $\oplus$ means addition in quadrature ($x \oplus y \equiv \sqrt{x^2 + y^2}$). The stochastic term a takes into account fluctuations of the shower, of the sampling fraction, photoelectron statistics, etc. The term b represents detector non-uniformity and calibration uncertainties, i.e. systematic effects. The term c represents electronic noise.
For hadron calorimeters, the above parametrization can be used as well for the energy measurement uncertainty [68].
These are essentially the detector technologies used in this thesis. A lot of other interesting detector technologies are described e.g. in references [5, 67], but are beyond the scope of this work.

Sensor Technologies

Sensors translate the signals from the energy deposited by traversing particles inside the detector into e.g. electric signals, which can be read out and converted into quantities to be measured. There is a huge variety of sensor technologies based on many possible sensor materials and depending on the specific requirements of a tracker or a calorimeter.
For example, the energy deposited by a traversing particle causes the excitation of atoms or molecules in a scintillator crystal. When relaxing to the ground state, the photons emitted is the detector response in this case. These light signals are converted into electric signals employing e.g. the photo-electric effect by a sensor outside the crystal.
The excess electrons generated in a solid by ionization can be the detector response as well, and the detector volume that contains these excited electrons can be part of the sensitive element, which generates the final signal to be read out. A clear separation of detector volume and sensor element does not exist. In a sampling calorimeter, the absorber layers are actually insensitive material enhancing the showering process. Sensor elements are interspersed as sensor layers. Each sensor element in turn can be considered as single detector.
In the recent decades solid state ionization chamber sensors based on semiconductor technology have commonly prevailed in high-energy experiments due to their reliability, avail-

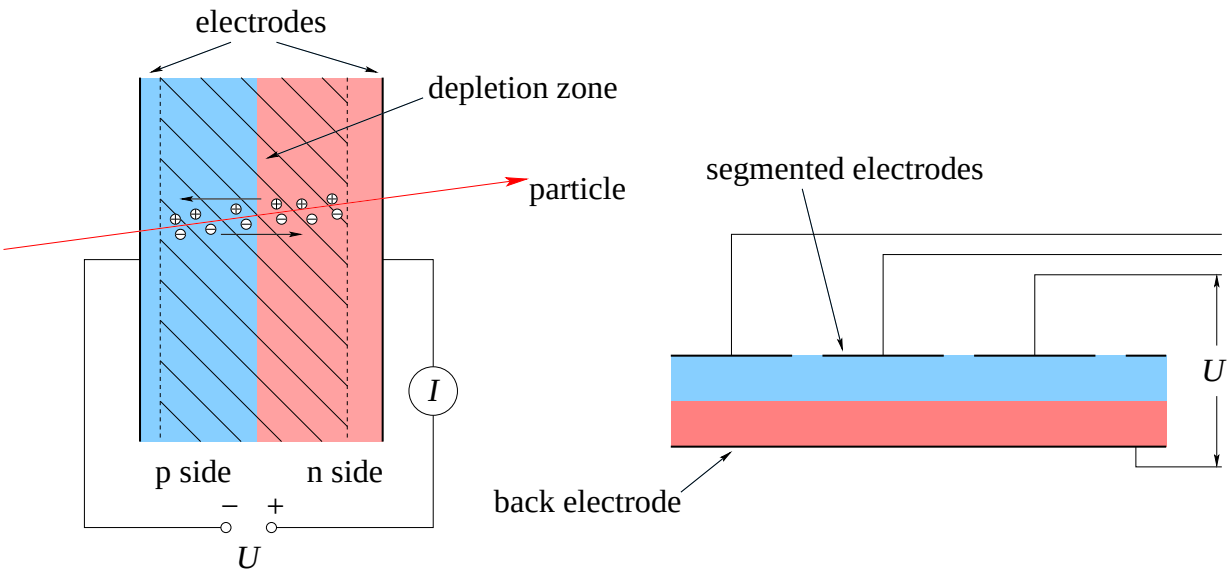

Figure 1.5: Schematics and working principle of a silicon diode as a sensor - with and without electrode segmentation.

ability and flexible application. The simplest setup of a semiconductor sensor, for instance, is a silicon diode as depicted in Figure 1.5. The diode is reversely biased such that the depletion zone – the sensitive volume – is enlarged to the complete diode volume. A particle traversing through this volume generates electron-hole pairs by energy loss due to ionization. These electrons and holes drift in the electric field towards the respective electrodes causing a signal current that flows in the outer circuit. Such silicon diodes can be made very thin, and the electrodes can be realized as metalization segmented laterally as indicated in the Figure 1.5 to provide also the information about the lateral position of the penetration point of the impinging particle. Very good spatial resolutions can be achieved by such sensors. Depending on the size and the geometry of the segmentation, a single sensor element on the plane is called a pixel, a pad or strip. They are used as tracking detectors and as sensor planes for calorimeters.

The advantages of silicon diodes are their good availability, low costs, the precision and homogeneity, with which pixels, pads and strips can be positioned, and their signal generation and transport properties such as large signal charge yield and mobility. On the other hand, for the currently used silicon technology a change of the performance of the sensors with increasing radiation load is observed making the operation of silicon sensors at room temperture under harsh radiation impossible. Therefore, insulators such as diamond had been and still are under investigation for applications, where the radiation hardness is an issue. They are not operated as a diode, but are a homogeneous material block and the externally applied field performs the electron-hole separation and drift towards the electrodes. Chapter 5 reports on the ongoing investigations of materials for such sensors in more detail.

The sensors of a TPC on the end plane can be simple pad anodes made from e.g. copper,

which pick up the incoming drift charge. However, the amount of electrons, which is generated by a traversing particle in the TPC volume and which drift towards the end plate, is too small to provide a significant signal current when hitting the surface of the electrodes. Therefore, signal enhancing devices such as GEMs (Gas Electron Multiplier) are introduced. The GEM foil is a thin sheet of plastics coated with metal on both sides, which are set to a high voltage difference against each other causing strong electric fields in the holes of the GEM foil. The incoming drift electrons from the TPC volume are accelerated in this field causing avalanches of secondary electrons, which eventually hit the pad electrodes on the end plane. Figure 1.6 shows a schematics of the working principle of a GEM, the secret of which is the shape of the holes of the GEM foil, which are obtained by chemically piercing.

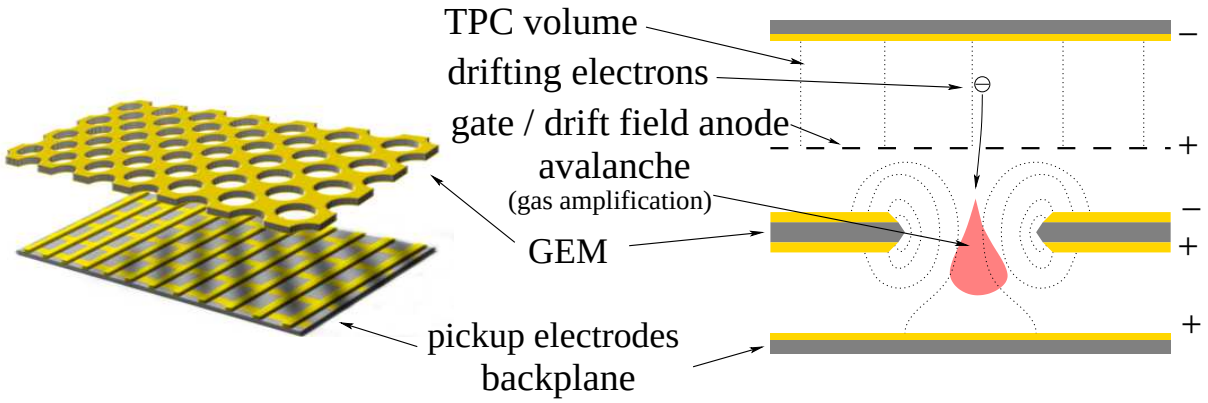

Figure 1.6: Schematics and working principle of a GEM.

Fluctuations in the Signal Charge and the Fano Factor

The current picture of a sensor based on ionization such as the silicon diode is as follows. The energy loss of the impinging particle is distributed according to some distribution f (of Landau type for example). The deposited energy is again a continuous random variable with its own probability density function, which is translated into the discrete number of collisions, i.e. eventually into the number of electron-hole pairs excited by ionization. Only a fraction of these charges are registered as signal, again in a random way. To estimate the signal yield of a detector from a particle of a certain energy, one needs to know all these probability density functions. Conversely, from the signal amount one usually wishes to know the energy deposited initially.
We shortly discuss, which precision of the energy measurement can be achieved. In semiconductors, the amount of signal charges fluctuates for a fixed total deposited energy, E_0, according to [69]

$$\Delta N_Q = \sqrt{F N_Q} \,,$$

where N_Q is the average number of electron-hole pairs, and ΔN_Q its standard deviation. The factor F is called the Fano factor [70, 71, 72, 73] and can be calculated e.g. for a

semiconductor detector according to [69]

$$F = \frac{E_x}{E_{\text{gap}}} \left(\frac{\varepsilon_{\text{eh}}}{E_{\text{gap}}} - 1 \right) .$$

Herein, E_x is the average energy for an excitation of a phonon, i.e. an excitation of lattice vibrations. The band gap energy, E_{gap}, is assumed to be the energy minimally required for an ionization, and ε_{eh} is the average electron-hole pair creation energy. The latter one is larger than the band gap because the conservation of momentum in a single collision requires phonon excitation and because many modes for an energy transfer with an excitation energy larger than the band gap are available.
For silicon is $E_x = 0.037$ eV, $E_{\text{gap}} = 1.1$ eV and $\varepsilon_{\text{eh}} = 3.6$ eV leading to $F = 0.08$ [69]. The Fano factor is a material dependent quantity, which is usually smaller than one. It accounts for the correlations between consecutive excitation and ionization events. Theoretical values are available for several materials, e.g. for diamond $F = 0.08$, in reference [74].
For the application as sensor material, a small Fano factor is preferable, since it enhances the precision of the signal measurement and, therefore, also the precision of the measurement of the deposited energy.

1.2.5 Collider Experiments

General Setup

In experiments at high-energy colliders such as the International Linear Collider (Chapter 2) or the Large Hadron Collider a certain detector configuration has proved of value, which is called *multi purpose detector*. Around the interaction point (and the beam pipe) concentrically several sub-detectors are positioned consecutively.
The idea for this design is the following. In the collisions at the interaction point a lot of particles might be created. Some of them will decay in very short time after the collision and create secondary vertices, from which new particles start and pass through the detector. The decay products and all particles entering and penetrating the detectors are either stable or have a lifetime above a certain threshold.
If these particles are charged they will ionize the atoms of the tracker detector volume, i.e. they will create electron-hole pairs in the silicon tracker volume or electron-ion pairs in the gas of the TPC. Neutral particles are not registered inside the trackers. Photons and electrons create an electromagnetic shower in the electromagnetic calorimeter, thereby, depositing all of their energy in this calorimeter. Hadrons will additionally and dominantly deposit their energy inside the hadron calorimeter. Muons of sufficient energy penetrate almost all the detectors, leaving only MIP signals. In an ideal case they are the only particles passing through the muon spectrometer. The different particles can be identified by their energy depositions inside the different sub-detectors.
The task in an collider experiment is to reconstruct the trajectories and the showers of the particles using the tracker and calorimeter signals. From them the energy, the momentum

and the charge sign can be determined. Once the trajectories are reconstructed, they can be assigned to one or more vertices, to reconstruct the processes happened in the interaction point region.

Reconstruction Terminology

Trackers and calorimeters are segmented in pixels, strips or pads, i.e. small sensitive detector elements. To each of these detector elements a position can be assigned. If a particle traverses such an element a signal is generated the size of which is proportional to the number of electrons released inside the detector volume by ionization. The detector elements giving a signal if particles traverse them trace the trajectory of the particle or the energy deposited inside the shower. A *hit* is defined as a four-tuple consisting of the position of the center point of such a detector element and the energy deposit inside this element volume.
The reconstruction of trajectories and showers is carried out on the set of hits for each event[10]. In a first step tracker hits are assigned to a *track*, which approximates the trajectory of the particle causing these hits. Similarly, hits in a calorimeter belonging to one shower are summarized to a *cluster*. This treatment of the detector information is called *pattern recognition*. For each track, the momentum and the charge sign is determined by fitting a trajectory model, which gives the reconstructed trajectory. From the reconstructed cluster the energy of the particle causing it is determined.
In a second step tracks and clusters are assigned to each other. If this is correctly done, there should remain clusters only from neutral particles. Track-cluster pairs and single clusters are called *particle flow objects* containing reconstructed momenta, energies and charges.
According to the presence of a track and to the energy distribution of a cluster in the electromagnetic and hadron calorimeters and the muon spectrometer, a particle type is assigned to each particle flow object. A particle flow object with a particle type is called a *reconstructed particle*.
The trajectory model has usually several parameters. Except the curvature and the tangent direction, which are related to the momentum vector, there is also the distance of the trajectory from the nominal interaction point (IP), which can be parameterized by two impact parameters. It might be that some of the particles originate from a particle decayed in a vertex some distance apart from the nominal IP. In a next step one tries to combine these reconstructed particles to determine the energy, momentum, charge sign and identity of the decayed particle. This process is repeated, until the event is fully reconstructed in space.
Gluons or quarks produced in the primary interaction hadronize into stable and meta-stable particles such as mesons. These are usually contained in a narrow solid angle element. Such an object is called a *jet*. In this case it is sometimes difficult to determine the identity of each single particle, if the identification procedure is based on the cluster information.

[10] An interaction creating a certain number of secondary particles is called an event.

In the particle flow concept, the energy of all charged particles is determined from their tracks. Using this information, the clusters are assigned to these particles. The remaining clusters belong to the neutral jet particles and their energy is added to the jet. By separating charged and neutral components the energy of the jet can be determined more precisely than using only the calorimeter energy.

Chapter 2

The International Linear Collider

2.1 Physics Case

To understand the physics case of the International Linear Collider (ILC) it is worthwhile to consider first the prospects of the Large Hadron Collider (LHC) [75], which will operate before the ILC.
The LHC is a proton-proton collider and is designed as discovery machine. The protons are accelerated up to about 7 TeV in a circular accelerator of about 27 km circumference. The Higgs boson is a key element of the Standard Model, and it is enormously important for the confirmation of the Standard Model to discover it. If there is a Higgs boson within the Standard Model, which is responsible for the masses of the weak gauge bosons and the fermions, and which has a mass in the range of about 114 GeV to 1 TeV, it will be detected at the LHC. If extensions of the Standard Model such as the supersymmetric one are the appropriate description of the elementary particles then it is at least probable to discover a Higgs boson.
If the Higgs mechanism is not realized then the Standard Model loses its validity above 1 TeV due to the violation of the unitary limit in certain scattering processes. Operating in the energy range of up to 14 TeV, the LHC will decide, which kind of new physics beyond the Standard Model is realized in our universe in the case that no Higgs boson is found. Except the Higgs boson, it is also a hope to find new particles predicted, for example, in the supersymmetric models. Some of them serve currently as candidates for the dark matter, needed for the explanation of observations in the cosmology.

The ILC is an electron-positron collider. It will start to operate after the era of the LHC. Discoveries about the Higgs boson and the Standard Model extensions are then probably made. The ILC is designed to study systematically and in detail the phenomena expected at the 1 TeV scale [76, 77, 78]. As a lepton collider, the ILC will provide much cleaner events than a hadron collider. There will be a chance to find new particles with signatures hidden and therefore undiscovered in the complex events of the LHC. Furthermore, the initial conditions of the scattered particles such as the initial center-of-mass energy and the

lepton spin states can be controlled in a lepton collider. Using the ILC, the dependence of the cross-sections on the polarization state of the scattered leptons can be determined, and scans for cross-sections can be perform at the production threshold of certain processes, e.g. the Higgs-strahlung process. In the rather clean events of a lepton collider, also e.g. missing energy due to particles that are invisible inside the detector such as neutrinos will be measured much more precisely.
One benchmark of the ILC is the Higgs physics. If there is a Higgs boson found at the LHC then it must be checked whether it is really a Higgs boson, i.e. whether it has the correct quantum numbers. In addition, it is to be clarified whether the found particle is the Standard Model Higgs boson or one from some of the extensions. If there is no Higgs boson found at the LHC then it must be investigated which new physics scenarios can give an alternative to the Higgs mechanism and stabilize the electroweak scale.
Due to the polarized electrons (and positrons), also spin correlated cross-sections can be measured to determine precisely the couplings of the gauge bosons to fermions as well as the couplings between the gauge bosons in the Standard Model. Operating at a higher energy than former accelerators, the renormalization running of the couplings can be traced to higher energies rendering the extrapolations to the GUT scale more precisely. Using these extrapolations, a possible unification of the coupling constants at a certain energy can be specified in the scope of certain physics model such as for instance in the Standard Model or in its supersymmetric extension.
An important issue is the detection and identification of particle candidates for the cold dark matter, which amounts to about one fourth of the energy content in the universe. Related to this is the detection of new particles such as e.g. the supersymmetric partners of the Standard Model particles. Also surprising other particles could be found not belonging to any particle content of proposed models alternative to the Standard Model. If these new particles were found at the LHC, the task for the ILC is to determine its properties and to understand the underlying structure of the new model. If supersymmetry is realized, it is for sure broken and the mechanism of its breaking must be investigated.
If new gauge bosons are found at the LHC, the properties of the corresponding force have to be determined at the ILC and the meaning of them for the cosmology and the unification of the forces at the GUT scale has to be investigated.

2.2 General Properties of the ILC

2.2.1 Machine Setup and Parameters

The International Linear Collider (ILC) will be a linear accelerator, which collides electrons and positrons with a center-of-mass energy of up to 500 GeV, and up to 1 TeV after an upgrade, respectively. A circular machine operating with electrons and positrons at these energies would need a huge radius not to be dominated and limited by synchrotron radiation. At the time of writing of this thesis, the ILC is still an ambitious plan in the design phase. It will consist of two main linacs accelerating electrons and positrons to the

designated energy. There is one interaction region foreseen with a beam crossing angle of 14 mrad. Two detectors are planned, which work alternately in the so-called push-pull regime.

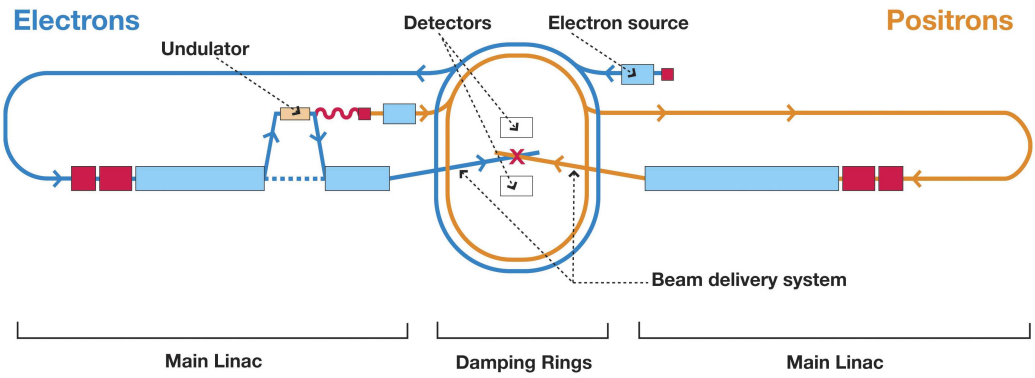

Figure 2.1: Baseline design of the International Linear Collider.

Figure 2.1 shows the baseline design of the ILC as specified in the reference design report [79].

Electrons with polarizations up to 85 % are created with a special electron gun. The photo cathode is fabricated as strained GaAs/GaAsP superlattice structure, and a pulsed intense laser beam releases bunches of photo-electrons from it. This gun must meet specifically the requirements for the bunch generation timing, the beam intensity and the bunch extensions as are listed in Table 2.1. There is an option for a polarized positron beam with a polarization of up to 60 %. Such polarized positrons can be created by passing electrons through an undulator, where high-energetic photons are created, which are converted into electron-positron pairs. The positrons are separated and further accelerated.

Bunches of electrons and positrons are shaped in the bunch compressors, their emittances are damped down in the damping rings to meet the luminosity requirements, and they are finally accelerated in the main linear accelerators. The main linacs consist of superconducting niobium cavities, each creating accelerating fields of 31.5 MV/m. A special challenge for the cavities is the necessity for an extremely smooth surface to avoid heating spots due to the extremely high fields. This is achieved by chemical etching and electropolishing. The technology was developed at the TESLA collaboration to launch the TESLA-project – the precursor project of the ILC.

The beam delivery system focuses the beams eventually into the nominal interaction point, which is surrounded by the detector.

The accelerator provides a high luminosity due to small transversal bunch dimensions. It is intended to provide an integrated luminosity of 500 fb^{-1} in the first four years. The luminosity, as introduced in Equations (1.28) and (1.29), depends on the beam parameters.

The geometric luminosity is given by

$$\mathcal{L}_{\text{geom}} = f_{\text{rep}} n_b \frac{N^2}{4\pi\sigma_x\sigma_y} \ , \tag{2.1}$$

where f_{rep} is the train[1] repetition rate, n_b is the number of bunches per train, N is the number of particles per bunch, which is assumed to be equal for both the electron and the positron beam. σ_x and σ_y are the widths of the Gaussian transversal charge distributions of the bunches. The peak luminosity is given by

$$\mathcal{L} = H_D \mathcal{L}_{\text{geom}} \ , \tag{2.2}$$

where the enhancement factor due to the pinch effect, H_D, can be expressed in terms of the beam extensions from a model for beam optics [80, 81, 82]. The nominal beam parameters, i.e. their design values, are summarized in the Table 2.1.

parameter	value
center-of-mass energy $\sqrt{s}$	500 GeV
Train repetition rate f_{rep}	5 Hz
Number of Bunches per Train n_b	2820
Number of Particles per Bunch N	2×10^{10}
Bunch spacing	307.7 ns
Beam width σ_x	655 nm
Beam height σ_y	5.7 nm
Beam length σ_z	300 μm
Geometric luminosity $\mathcal{L}_{\text{geom}}$	1.2×10^{34} cm^{-2}s^{-1}
Enhancement factor H_D	1.7
Peak luminosity $\mathcal{L}$	2.03×10^{34} cm^{-2}s^{-1}

Table 2.1: The nominal beam parameter set for the ILC.

The crossing angle of 14 mrad at the interaction point is compensated by a crab cavity [83, 84] to keep the luminosity as high as possible. That is, the bunches are rotated short before the interaction to ensure a head-on collision with a full penetration length of the single particles through the oncoming bunch. Figure 2.2 shows the coordinate system of the ILC and the definition of the crossing angle.

2.2.2 Beam-Beam Interaction: Pinch Effect and Beamstrahlung

At the ILC there will be a strong beam-beam interaction near the IP due to the comparably high charge density of the bunches [85, 86, 87, 88]. The moving bunches represent current densities, which are of equal sign (for oppositely charged positrons moving in opposite direction) in the laboratory frame, i.e. the nominal ILC rest frame. As soon as the

[1] A train contains a certain number of consecutive bunches.

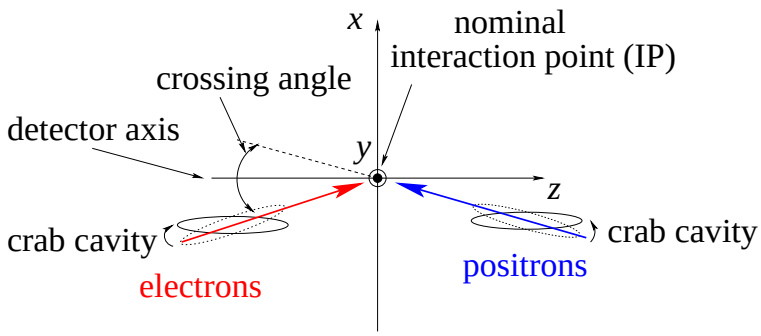

Figure 2.2: Coordinate system of the International Linear Collider and definition of the crossing angle.

bunches approach each other and start to overlap, the particles of a bunch will experience the strong Lorentz force due to the magnetic field caused by the current densities. The charges are roughly compensated so that the electric fields of the both oncoming and overlapping bunches are compensated while the magnetic fields add up. In the first order one can consider the magnetic field as given by the current densities, and the particles which actually cause this field are moving inside this field.

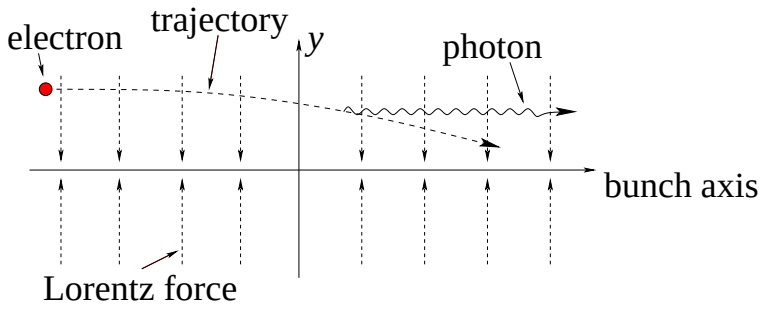

Figure 2.3: Schematic of beamstrahlung process.

The Lorentz force for each bunch particle is directed to the bunch axis, as is illustrated in Figure 2.3. For uniformly distributed charge densities this force is proportional to the distance of the particle from this axis. Hence, all particles with a non-zero distance to the bunch axis are deflected towards this axis. This is called *pinch effect* [89, 90]. The effective beam size in x- and y-direction is reduced, i.e. the effective charge density is increased. This increases the luminosity as indicated in Equation (2.2).
Since accelerated charges emit electromagnetic radiation, the bunch particles accelerated by the Lorentz force radiate photons, which are mostly collinear with the direction of the bunch motion. These photons are called *beamstrahlung*. The beamstrahlung photons are directed into a polar angle range of a few 100 μrad. For the nominal ILC parameters as given in Table 2.1, the total number of photons for one beam direction is about 2.5 per bunch particle, i.e. 5×10^{10} photons per bunch crossing in each direction. The total energy of all beamstrahlung photons per beam direction is 1.14×10^{11} GeV, leading to an average photon energy of 2.28 GeV per photon.

As the beamstrahlung photons are going into the forward direction, they must penetrate the oncoming bunch. Thereby, interactions of the photons with the primary bunch particles are induced, by which few percent of the photons are converted into electron-positron pairs – the so-called *beamstrahlung pairs*. The dominant beamstrahlung pair creation processes at the ILC are the incoherent ones, i.e. individual particle interactions: Bethe-Heitler, Breit-Wheeler, and Landau-Lifshitz processes [91, 82, 80]. While the Bethe-Heitler and the Breit-Wheeler process involve real beamstrahlung photons, the Landau-Lifshitz process contains only virtual photons i.e. e^+e^- interactions by which an additional electron-positron pair is created. The dominant incoherent pair production process is the Bethe-Heitler process. Figure 2.4 shows schematically the lowest order Feynman diagram for a pair creation process.

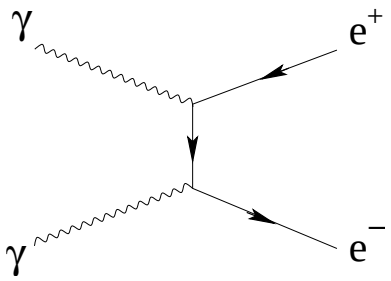

Figure 2.4: Schematic beamstrahlung pair creation process. The photons can be real or virtual depending on how they are created.

There is also the coherent pair production possible, i.e. the electromagnetic interaction of a photon with the collective electromagnetic field of the oncoming bunch. However, this process is highly suppressed at the nominal beam parameters at the ILC [92].
With nominal ILC parameters, about 2.6×10^5 beamstrahlung pairs per bunch crossing will be created in each direction. Their energy distribution depends on the the beamstrahlung photon spectrum. The average energy of the electrons and positrons can be roughly estimated to be the half of the average photon energy, i.e. about 1.14 GeV per pair particle. This corresponds to a total energy of the pairs of about 1.2×10^6 GeV per bunch crossing. Electrons and positrons with high energies possess momentum directions with small polar angles with respect to the direction of the bunch motion, while for those with smaller energies also larger polar angles are possible. A magnetic field of about 4 T inside the ILC detector confines the beamstrahlung pairs to a cylinder of about 10 cm in diameter. Nevertheless, the beamstrahlung pairs represent the main machine-induced background for the ILC detectors [93, 94].

2.3 The ILC Detector

The motivation for the current detector design is given by the requirements from the physics case for the precision of the momentum measurement of single particles and for the energy measurement of jets: $\frac{\Delta p_\perp}{p_\perp} \simeq 5 \times 10^{-5}\,\mathrm{GeV}^{-1}\,p_\perp$ for tracks and $\frac{\Delta E}{E} \simeq 0.3\,\mathrm{GeV}^{1/2}/\sqrt{E}$

for jets. Each charged particle momentum is reconstructed from its track, which is more precise than the energy reconstruction from calorimeter clusters. The clusters matched to the tracks are then ignored, and the remaining calorimeter clusters belong to neutral particles, the energy of which is reconstructed from the cluster energy.
For the ILC detector there are four general concepts – LDC, GLD, SID and 'The Fourth Concept'[2], which differ in the technology of the sub-detectors intended. In the following only the Large Detector Concept (LDC) is described, since the analyses in this thesis are performed using this concept. This and the other concepts are described in detail in Reference [79]. Figure 2.5 shows the LDC detector.

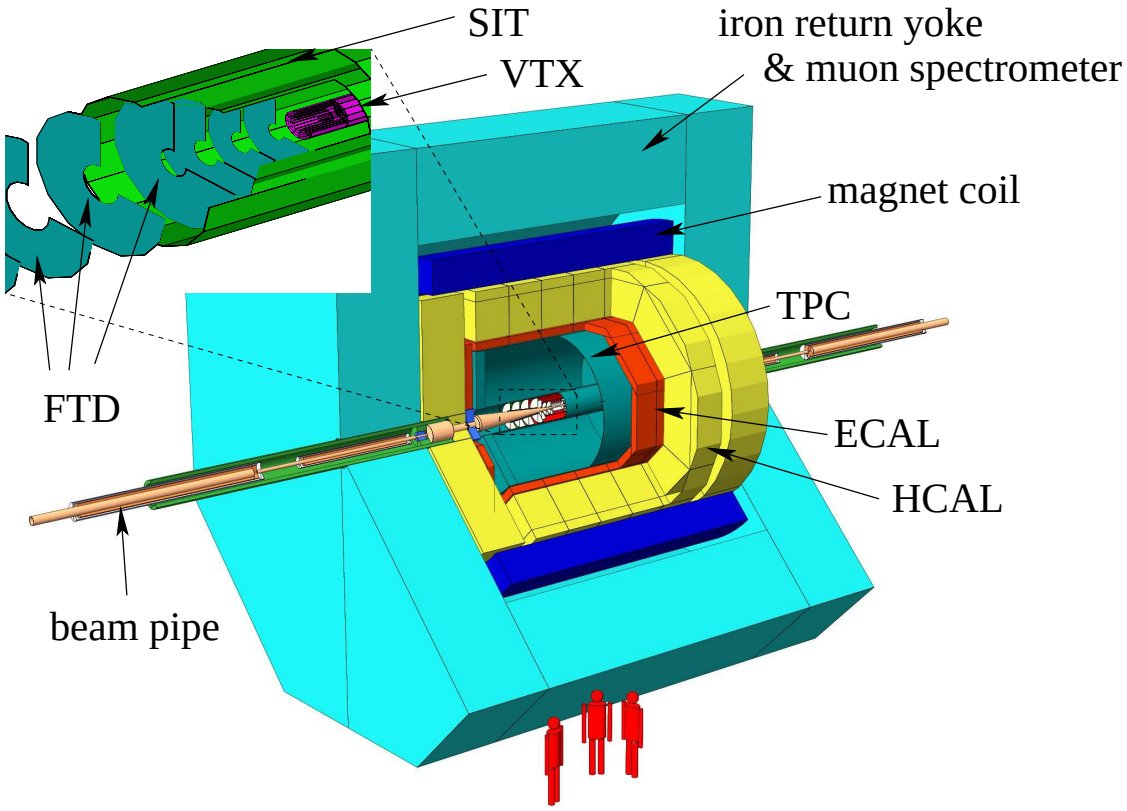

Figure 2.5: Structure of the ILC detector of the LDC. The enlarged detail depicts the silicon vertex tracking detectors surrounding the IP.

Starting from the IP and the beam pipe (beige) the LDC detector consists of a vertex tracker system (white), a large volume tracker (turquoise), an electromagnetic (red) and a hadron calorimeter (yellow), and a magnet coil (dark blue) which provides a solenoidal magnetic field of four Tesla inside the tracker volume. The whole detector is surrounded by an iron yoke (cyan) which is also used as muon spectrometer. In both directions from the IP along the beam pipe, there are the forward tracker planes near the IP, and the electromagnetic and hadron calorimeter endcaps and the iron yoke endcaps are adjacent

[2]LDC and GLD are merged now to ILD.

to the TPC end planes to provide a maximum hermeticity.

The vertex tracking system consists of the vertex tracker (VTX), a silicon intermediate tracker (SIT), and the forward tracking disks (FTD). They are made with silicon pixel and strip technology and have an excellent point resolution - a pixel area smaller than about 20 μm^2 is destined for a position resolution of 5 to 10 μm - and low material budget. The coverage is almost the full solid angle.

The central tracker is a gaseous large volume time projection chamber (TPC), which provides up to 200 three-dimensional space points per track with very good resolution. Also here the material budget was kept as small as possible to keep material effects small for the track reconstruction. A point location uncertainty of 100 μm in the radial-azimuthal plane is achieved. The third coordinate is obtained with an uncertainty of about 500 μm by the measurement of the drift time, which depends on the electric field and the working gas. Additionally, the mean energy loss per unit path length, dE/dx, is determined with an uncertainty of 5 %, which can be used for the particle identification of low momentum tracks [95].

The electromagnetic calorimeter (ECAL) is made of silicon sensor layers and tungsten absorbers. To meet the particle flow requirements, the ECAL has a very high granularity. Up to 30 layers in radial direction and cell sizes of 0.55×0.55 cm^2 provide a very good shower cluster resolution. The hadron calorimeter (HCAL) is made of an iron absorber structure instrumented with scintillator tiles of the size 3×3 cm^2. There are 40 radial layers. The calorimeters are split into a barrel part and an endcap part for an almost Hermitian coverage.

The tracker and calorimeter systems are embedded in a solenoidal magnetic field of up to 4 T, provided by a large superconducting coil, which bends the trajectories of the charged particles inside the tracker for a precision determination of the particle momenta. The iron return yoke is instrumented with tracker layers between the iron layers and serves also as muon spectrometer.

2.4 The Sub-detectors in the Forward Region

The region very close to the beam pipe inside the ILC detector is called *very forward region*. The design and development of the electromagnetic calorimeters in this region are the tasks of the FCAL collaboration and reached an advanced status [96, 97, 98, 99, 100]. A sketch of this region is shown in Figure 2.6. Two important sub-detector systems are located in this region – the LumiCal and the BeamCal. About 100 m apart from the interaction point, another detector is foreseen close to the beam pipe – the GamCal.

The task of LumiCal is to measure very precisely the integrated luminosity, L, by detecting high-energetic, back-to-back electron-positron pairs from Bhabha scattering events, $e^+e^- \rightarrow e^+e^-$ [101, 10, 102]. The theoretical cross-section for Bhabha scattering, σ_{Bhabha}, for the solid angle range of the LumiCal can be calculated precisely in quantum electrodynamics. The integrated luminosity can be determined by counting the Bhabha events,

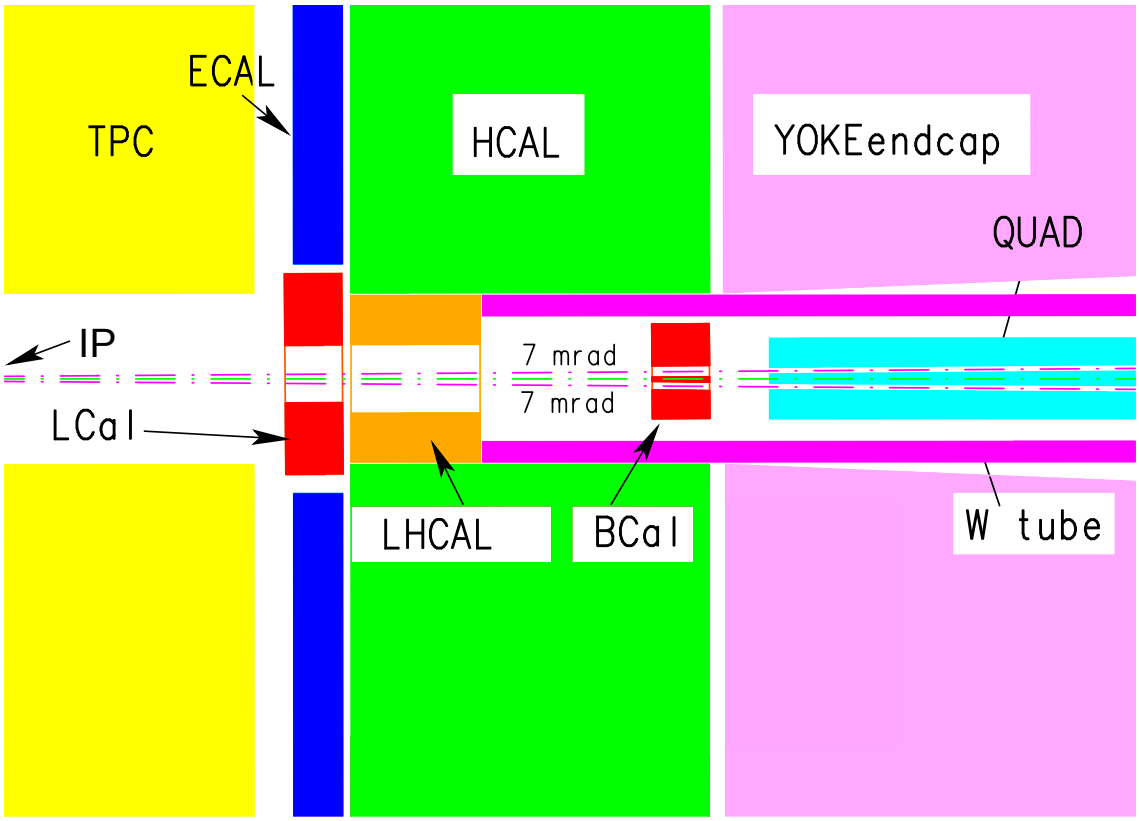

Figure 2.6: The Very Forward Region of the LDC detector. (BCal=BeamCal, LCal=LumiCal) ECAL and HCAL denote the electromagnetic and hadronic calorimeter endcaps adjacent to the TPC end plane. The tungsten tube (W tube) is the support tube for the final quadrupole magnet, BeamCal and other devices and equipment. LHCAL=hadronic luminosity calorimeter, which extends the hadron calorimeter to small polar angles.

N_{Bhabha}, as

$$L = \frac{N_{\mathrm{Bhabha}}}{\sigma_{\mathrm{Bhabha}}} \, .$$

A relative precision of $\Delta L/L = 10^{-3}$ shall be attained. LumiCal is designed as cylindrical sampling calorimeter surrounding the beam pipe. It is made of alternating tungsten absorber layers and silicon sensor layers, which are finely segmented in the radial and azimuthal directions. There are 30 such layers planned. LumiCal is located at about 2.3 m apart from the nominal IP. Its inner radius is 60 mm and the outer radius 350 mm. The total thickness is 200 mm.

The BeamCal has two tasks. First, it monitors the electron-positron pairs induced by the beamstrahlung, and serves for the beam diagnostics and post collision analysis [103, 104, 105, 106]. The bunch parameters can be reconstructed bunch-by-bunch using BeamCal, and will be delivered to the fast feedback control system (FONT) of the

ILC beam control [107, 108]. BeamCal can provide 3D information about the energy deposition of the beamstrahlung pair background, since it is both transversally and longitudinally segmented. This information is used to reconstruct the beam parameters as small deviations from the nominal ones [109, 110].
The second task is a physics case. For example, in some extensions of the Standard Model such as in supersymmetry, there are final states possible with a large missing momentum and energy. One supersymmetric particle – the neutralino – could be stable and can escape the detector without being detected. These final states can be confused with so-called two-photon fusion processes[3] in the Standard Model, as depicted in Figure 2.7, if the high-energetic electron and positron are not detected. The latter are going mainly into the very forward region and may hit the BeamCal. They have to be detected on top of the very intense, but widely spread background from the beamstrahlung pairs. The task of BeamCal is, thus, to discriminate between these Standard Model events and those of new physics [111].

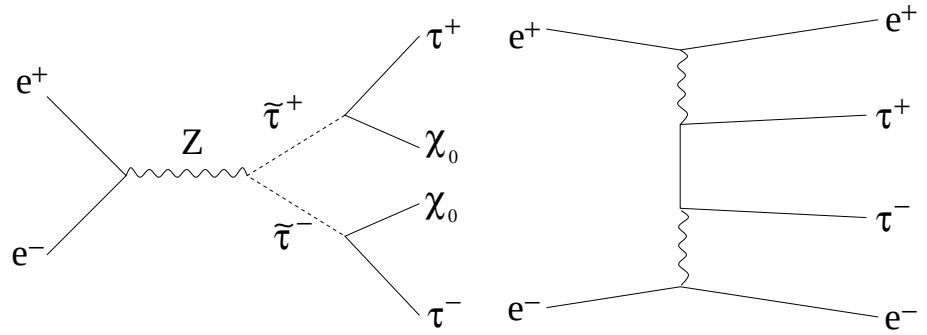

Figure 2.7: A supersymmetric process (left), in which tauons and neutralinos are created. A two-photon fusion process in the Standard Model (right).

The GamCal will investigate the beamstrahlung photons far downstream from the IP. These have already a significant intensity when beams are just missing each other due to an offset and no beamstrahlung pairs are created. In this regime the beam parameters are quite far apart from the nominal ones, and the above mentioned reconstruction using only BeamCal will not work. Thus, GamCal provides additional valuable information in the phase when the beams are tuned and their alignment is not correct. The left-hand plot of Figure 2.8 shows as an example the beamstrahlung photon energy, E_γ and the energy of all beamstrahlung pair particles hitting the BeamCal front face[4], $E_{\text{pair}}^{\text{BCal}}$, as functions of the vertical beam offset, δ_y, i.e. the distance between the bunch axes of the approaching bunches.
BeamCal and GamCal together can also provide a fast relative luminosity measurement by measuring the energy and/or the number of beamstrahlung photons and pairs, and can therefore perform a fast luminosity optimization [112]. The right-hand plot of Figure

[3] If the pair created in this process is an electron-positron pair, then this is the aforementioned Landau-Lifshitz process.

[4] A simplified scenario with a zero crossing angle and a uniform magnetic field of 4 T is assumed.

2.8 shows the ratio of $E_{\text{pair}}^{\text{BCal}}/E_\gamma$ and the luminosity as functions of the vertical offset, δ_y. This ratio traces obviously the luminosity quite well and can be used for the luminosity optimization. For beam parameters other than the bunch offsets, a more complicated combination of the BeamCal and GamCal energies or particle numbers registered per bunch crossing might be necessary.

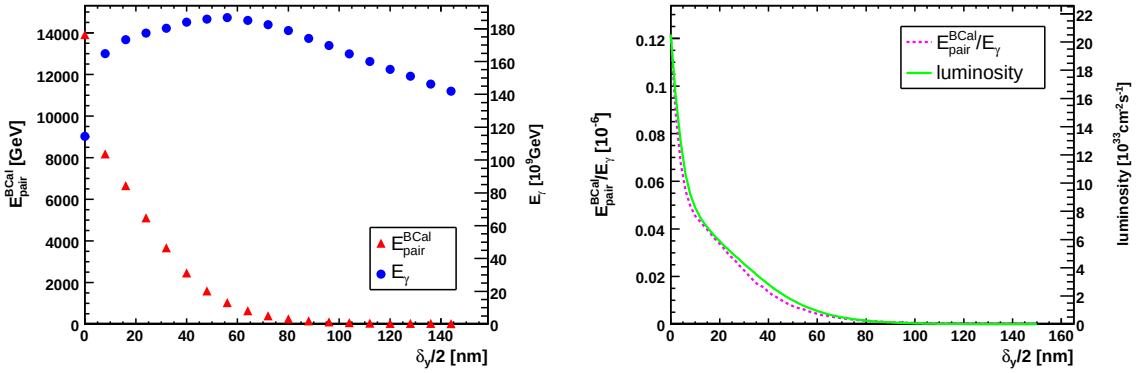

Figure 2.8: Energy of beamstrahlung photons, E_γ, and Energy of beamstrahlung pairs hitting BeamCal, $E_{\text{pair}}^{\text{BCal}}$, as function of the vertical bunch offset, δ_y, (left). Luminosity and ratio of the aforementioned energies as function of the vertical bunch offset, δ_y, (right). The plots were obtained using GuineaPig [113].

The design of the GamCal is still in the planning phase, but advanced proposals already exist [114, 115] and several application studies for the beam diagnostics including also GamCal as well as for a fast relative luminosity optimization have been performed [116].

2.5 BeamCal Requirements and Design

BeamCal will be a compact cylindrical sandwich calorimeter made of absorber and sensor layers and surrounding the beam pipe. The absorber material is already decided to be tungsten, because it is a high Z material with a short radiation length. The outer radius is 15 cm, the inner radius is 2 cm, and the thickness of 12 cm corresponds to thirty radiation lengths of the absorber plus 0.05 cm spacing for sensor material and readout circuitry. The radiation length of tungsten is 0.35 cm, according to Equation (1.45). In Table 2.2 the relevant BeamCal parameters and absorber properties are summarized.
The current design of BeamCal is a result of a lot of optimization studies using Monte-Carlo simulations. For example, the sensor segmentation of 0.8 R_M is a result of the maximization of the reconstruction efficiency of showers of high-energetic electrons on top of the widely spread beamstrahlung pair background at a simultaneous minimization of the number of pads [117], which determines the number of channels to be readout.
The sensor material is not chosen, yet. However, is must meet some unprecedented requirements. At ILC beam parameters, about 6500 beamstrahlung electrons and positrons

Properties of Tungsten		
Density ρ		19.25 $\mathrm{g\,cm^{-3}}$
Atomic Number Z		74
Atomic Mass A		183.84 u
Radiation Length X_0	Eq. (1.45)	0.35 cm
Critical Energy $\varepsilon_{\mathrm{cr}}$	Eq. (1.48)	8.11 MeV
Shower Maximum for 250 GeV e^-, $t_{\max}$	Eq. (1.47)	10 X_0
Shower Length for 250 GeV e^-, $t_{95\%}$	Eq. (1.49)	25.5 X_0
Moliére Radius R_M	Eq. (1.50)	0.91 cm
BeamCal specification		
Inner Radius		2 cm
Outer Radius		15 cm
Length		12 cm
Absorber Material		tungsten
Absorber Layer Thickness		3.5 mm
Sensor Layer Thickness		0.3 mm
Air/Electronics Spacing		0.2 mm
Sensor Segmentation		0.8 R_M

Table 2.2: Properties of tungsten and BeamCal specifications. Considerations and optimizations are done for electromagnetic showers.

will hit the BeamCal per bunch crossing with a total energy of about 1.4×10^4 GeV. This energy is dissipated mainly in the absorber layers, but a considerable fraction will also be dissipated in the sensor layers. Including a safety factor, the maximum dose rate the sensor material must withstand is estimated to be 10 MGy per year, i.e. the sensor material must be radiation hard to remain operational. It is desireable that the sensors are capable to detect MIP signals, because these may be used for the calibration of the electronics.
Figure 2.9 shows on the left-hand side a mechanical design proposal of the BeamCal. It contains the rack carrying the weight of about 200 kg tungsten and the sensor segments including the support structure for the readout electronics.
A typical energy spectrum of the shower electrons and positrons is shown for one bunch crossing inside the sixth sensor layer in the right-hand plot of Figure 2.9. A typical energy of the shower particles is about 10 MeV, though, the spectrum extends from few keV up to about 5 GeV.

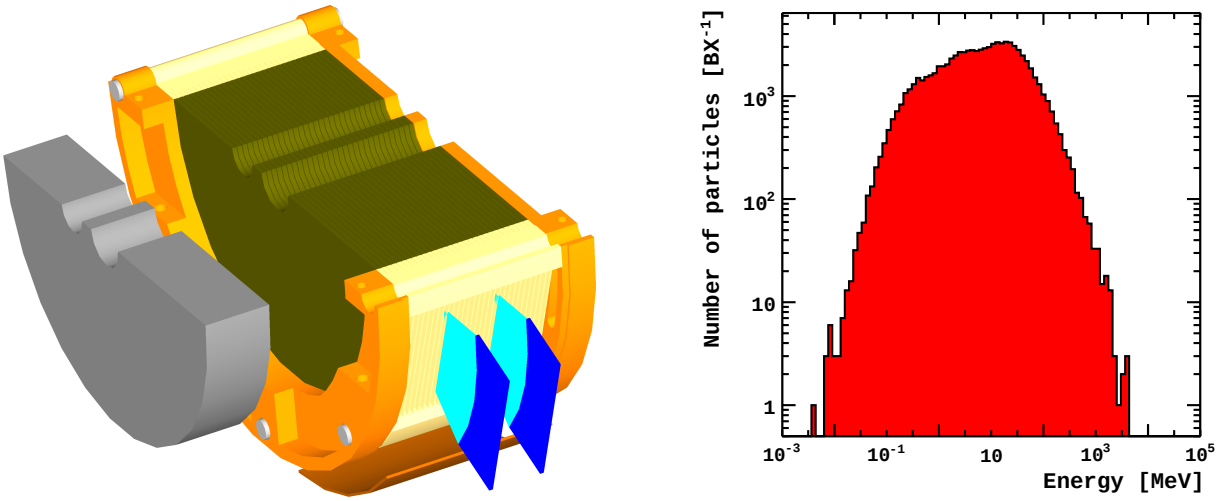

Figure 2.9: One half of the BeamCal (left). The absorber layers (green) are interspersed with the sensor plane segments (cyan). The absorber and sensor planes are carried by a support structure (yellow, orange). The block (gray) in front of BeamCal is a graphite absorber for particles backscattered from BeamCal. – Energy spectrum of the shower electrons and positrons at $6X_0$ (6^{th} sensor layer) for one bunch crossing (BX) (right).

Chapter 3

Reconstruction Performance Studies

3.1 Simulation and Reconstruction Software Tools

To estimate the performance of detectors, simulation tools have been developed. Here we use simulators of electron and positron bunch crossings, event generators for physics processes derived from theoretical calculations, and programs simulating the transport of particles through material.
A major issue for any advanced analysis of events in high-energy collision experiments is the precise momentum reconstruction and the correct particle identification for each particle flow object inside an event as explained in Section 1.2.5. Furthermore, the treatment of the huge amount of data collected in the experiments has to be automatized – most conveniently via software. Therefore, reconstruction software must be tested and optimized for these tasks.
For the ILC, the following simulation and analysis tools are commonly used.

Event Generators

Event generators are based on Monte-Carlo techniques and provide four momenta of final state particles following the differential cross-sections obtained from the theory. The differential cross-sections describing the probabilities for certain scattering processes and depending on the momenta of the incoming and outgoing particles refer to the basic interactions of the elementary particles as described in Chapter 1. This approach is sufficient for leptons. However, for scattering processes involving quarks and gluons, which do not exist as free particles, the initial quarks and gluons originate from compound state hadrons, and the final state quarks and gluons hadronize immediately after the basic scattering process. Therefore, the hadronic form factors have to be convoluted with the cross-sections of these processes.
Monte-Carlo generators provide samples of scattering events of a certain process, containing the four-momenta of all particles contained in an event, and are also used to calculate the corresponding total cross-section numerically.

GuineaPig [113] is a beam-beam interaction simulator, which solves numerically partial differential equations that describe the interaction of electron and positron bunches. The shape of the bunches can be defined, and the main beam parameters, lateral offsets, bunch tilt angles, focal points and other parameters can be changed. As output it provides the number and momenta of beamstrahlung pairs, of beamstrahlung photons and of beam particles.

Sherpa [118] is a multi-process general-purpose event generator. It provides cross-sections and weighted and unweighted event samples of scattering processes on tree-level, i.e. no loops are accounted for.[1] The beam particle energy spectrum can be used as input to account for the energy loss by beamstrahlung. Furthermore, initial and final state radiation can be accounted for. The full event generation includes the final state parton showering and the subsequent hadronization of the partons of QCD into detectable hadrons. A new scheme ensures color and flavor consistency in this hadronization process. Sherpa checks for gauge invariance of the cross-sections of the considered processes. Processes from several models additional to the Standard Model can be simulated, such as supersymmetry or extra dimensions.

Pythia [119] is similar to Sherpa. Phenomenological approaches are used that are developed and validated amongst others by the LEP experiment. Specifically, the hadronization is parametrized instead of using an underlying theory, and might therefore not consistently account for flavor conservation. Nevertheless, it is currently one of the most efficient and often used event generators.

BHWide [120] is an event generator for the Bhabha scattering process, $e^+e^- \rightarrow e^+e^-(\gamma)$, including the Z boson exchange and higher order corrections such as initial and final state radiation.

Detector Simulation, Reconstruction and Analysis Tools

All the ILC simulation and reconstruction software is prepared and maintained by special software groups and is available on the ILC software portal [121].

Mokka is the ILC detector simulation tool based on Geant4 [59, 60], which in turn is a C++ based class hierarchy for detector description and particle transport simulation. In Mokka several detector concepts are available, as well as several interfaces for Monte-Carlo event generators to feed sample events into the detector simulator. We used the LDC Sc01 detector model corresponding to the detector shown in Figure 2.5. The output data are tracker hits and energy depositions in calorimeter pads and tiles, and the Monte-Carlo

[1] Loops are only accounted for in effective couplings, renormalization running of couplings and masses, initial state radiation, hadron decays and QED and QCD shower evolution, but not in the matrix element generation.

particle records, which are written to files in the slcio-format, event-by-event.

MARLIN is an analysis framework which provides tools to parse through the events stored in slcio-files. Furthermore, it provides an interface for so-called processors, which perform the analysis work on the content of the collection, event-by-event.

MARLINRECO is a modular part of MARLIN, which provides already processors for the reconstruction of full events. There are processors to digitize the simulated tracker and calorimeter hits from MOKKA. To approach a more realistic simulation these hits are superimposed by background depositions and electronic noise. Further processors perform the pattern recognition that is the track finding in the tracker hits and the cluster finding in the calorimeter hits. The particle flow concept determines the order of the application of these processors. Another processor assigns these clusters to reconstructed tracks resulting in particle flow objects. The remaining "neutral" clusters, i.e. clusters without any matching track are considered as neutral particle flow objects. A final processor performs the particle identification of the particle flow objects, so that these objects become reconstructed particles. The full event reconstruction follows and can be also accomplished by a MARLINRECO processor.

While writing this thesis, the development for the reconstruction software was still ongoing. There are at present available a Kalman filter based track reconstruction processor (FULLLDCTRACKING) [122, 123] and clustering algorithms (TRACKWISECLUSTERING/WOLF, TRACKBASEDCLUSTERING, PANDORAPFA), which perform clustering and cluster-track matching. A particle identification was developed by the author of this thesis (PFOID) as described in Appendix B) in collaboration with others.

ROOT [124] is a flexible, C/C++ based class hierarchy and command-line interface for data analysis containing classes for histograms, functions, graphs, trees, tuples, visualizations, etc. and routines for treating large amounts of data, for fitting, for image processing, etc.

Figure 3.1 shows a scheme of the simulation and reconstruction chain as is usually used in simulation studies and analyses. The generation, simulation and reconstruction of events of a certain process pass through this chain event by event.

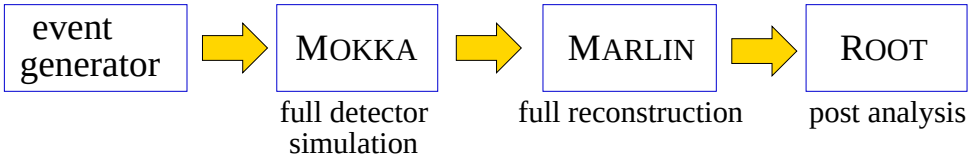

Figure 3.1: Simulation and reconstruction chain. MARLINRECO is included in MARLIN.

3.2 Track Reconstruction Performance Studies

We investigated the performance of the FullLDCTracking processor, i.e. the uncertainties of the measurement of track parameters for the reconstructed electrons and muons from a Monte-Carlo sample of Higgs-strahlung events for center-of-mass energies $\sqrt{s} = 250$, 350 and 500 GeV and $e^+e^- \to \mu^+\mu^-$ events for $\sqrt{s} = 250$ GeV, as described in Chapter 4. In an ideal homogeneous magnetic field, charged particles move on a helix, which can be parameterized by five parameters. The helix parameters are referred to one reference point, which is chosen to be that point on the helix with smallest distance to the IP.
The radius of curvature, R, and the transverse momentum, $p_\perp$, are related to each other via Equation (1.52). The projection of the distance between the reference point and the IP onto the (r, ϕ)-plane is d_0, the projection if this distance onto the z-axis is z_0. d_0 and z_0 are called *impact parameters*. To completely define a helix one needs the direction of the tangent of the helix in the reference point. This can be parametrized by two slopes or angles such as one in the (r, ϕ)-plane, ϕ_0, with respect to the x-axis, and the polar angle with respect to the z-axis, ϑ. Figure 3.2 shows a scheme to illustrate the definition of these track parameters.
The precision of the measurement of the impact parameters is important for resolving secondary vertices near the IP. The precision of the measurement of the angles and the transverse momentum gives the precision of the momentum measurement for a particle.
The uncertainties of the track parameter measurements are shown in the Figure 3.4 as functions of the particle momentum and for different polar angle ranges. We define these uncertainties as the standard deviations of the Gaussian distributions, $G(x; \mu, \sigma_G)$, as defined in Equation (D.2) in the following manner,

$$\delta d_0 := d_0^{\mathrm{MC}} - d_0^{\mathrm{reco}} \sim G(d_0^{\mathrm{MC}} - d_0^{\mathrm{reco}}; 0, \Delta d_0) \ , \tag{3.1}$$

$$\delta z_0 := z_0^{\mathrm{MC}} - z_0^{\mathrm{reco}} \sim G(z_0^{\mathrm{MC}} - z_0^{\mathrm{reco}}; 0, \Delta z_0) \ , \tag{3.2}$$

$$\delta\phi_0 := \sin\vartheta^{\mathrm{MC}}(\phi_0^{\mathrm{MC}} - \phi_0^{\mathrm{reco}}) \sim G\big(\sin\vartheta^{\mathrm{MC}}(\phi_0^{\mathrm{MC}} - \phi_0^{\mathrm{reco}}); 0, \Delta\phi_0\big) \ , \tag{3.3}$$

$$\delta\vartheta := \vartheta^{\mathrm{MC}} - \vartheta^{\mathrm{reco}} \sim G(\vartheta^{\mathrm{MC}} - \vartheta^{\mathrm{reco}}; 0, \Delta\vartheta) \ , \tag{3.4}$$

$$\delta(p_\perp^{-1}) := \frac{p_\perp^{\mathrm{MC}} - p_\perp^{\mathrm{reco}}}{(p_\perp^{\mathrm{MC}})^2} \sim G\big((p_\perp^{\mathrm{MC}} - p_\perp^{\mathrm{reco}})/(p_\perp^{\mathrm{MC}})^2; 0, \Delta(p_\perp^{-1})\big) \ . \tag{3.5}$$

The index "MC" denotes the original value of a track parameter known from the event generator, while "reco" indicates the reconstructed value for this track parameter.
The reason for the choice of $\delta(p_\perp^{-1})$ as a Gaussian distribution is the measurement principle for the transverse momentum. We call ζ the sagitta, i.e. the measured maximum perpendicular distance between a straight line from the entrance to the exit point of the particle trajectory inside the tracker and the trajectory in the (r, ϕ) projection. Then the radius of the trajectory is

$$R = \frac{\zeta}{2} + \frac{1}{\zeta}\frac{d_{\mathrm{tracker}}^2}{8} \ ,$$

where d_{tracker} is the tracker radius, i.e. approximately the straight distance between the entrance and the exit point in the tracker system. If the transverse momentum is large,

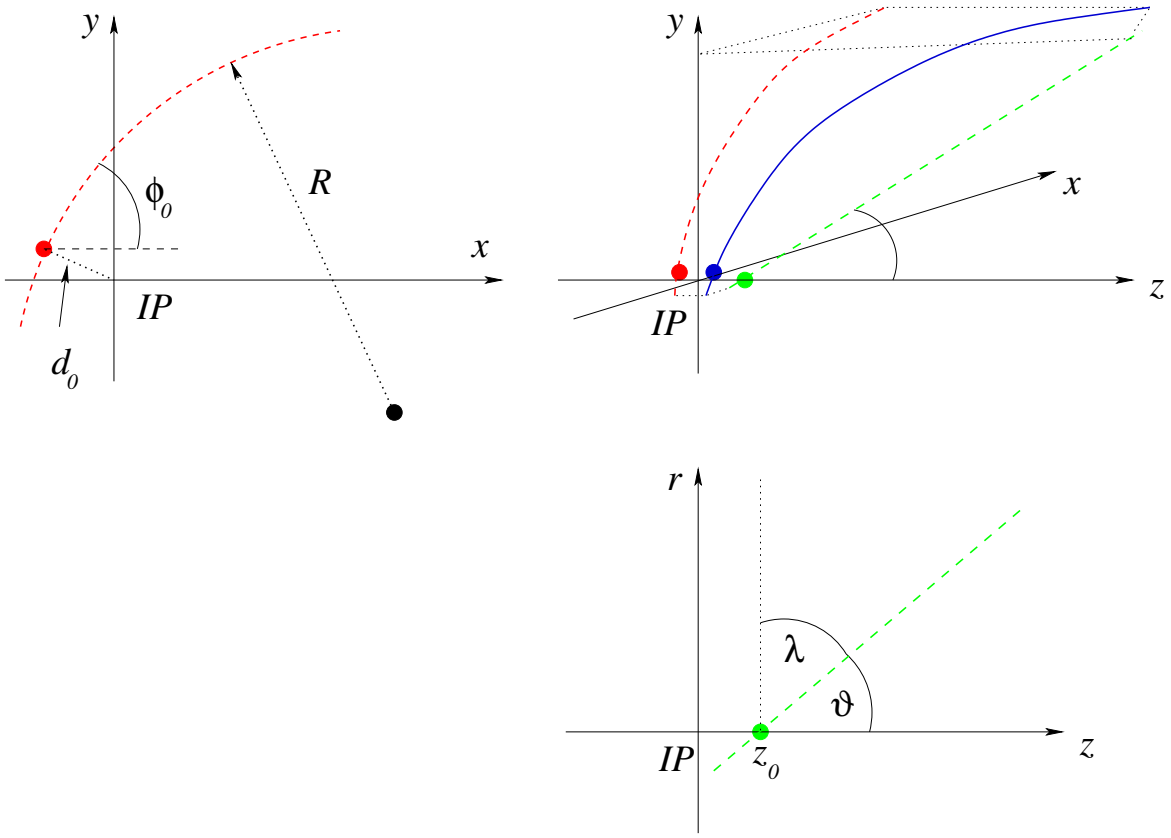

Figure 3.2: Track parameters as described in the LC note [125]. The blue line represents the 3D particle trajectory. Red and green dashed lines are the projections to the (r, ϕ)- and the (r, z)-plane, respectively.

the radius R is large and the sagitta small. For $\zeta \ll d_{\text{Tracker}}/2$ one can neglect the term $\zeta/2$. Using Equation (1.52), we get in first order for the transverse momentum

$$p_\perp \propto R \propto \frac{1}{\zeta}\frac{d^2_{\text{tracker}}}{8} \text{ , i.e. } \quad \delta(p_\perp^{-1}) \propto \delta\zeta.$$

Since the sagitta is measured in the experiment we expect it to be Gaussian distributed, i.e. $\delta\zeta = \zeta^{\text{MC}} - \zeta^{\text{reco}} \sim G(\zeta^{\text{MC}} - \zeta^{\text{reco}}; 0, \Delta\zeta)$ with the standard deviation $\Delta\zeta$. Therefore, $\delta(p_\perp^{-1})$ is also Gaussian distributed according to Equation (3.5).
For δz_0, δd_0, $\delta\vartheta$ and $\phi_0^{\text{MC}} - \phi_0^{\text{reco}}$, we assume that they are almost Gaussian distributed, since they are directly measured. However, the standard deviation of the distribution of $\phi_0^{\text{MC}} - \phi_0^{\text{reco}}$ depends on $\sin\vartheta$ since the smaller $\sin\vartheta$ is, the smaller is the lever arm in the (r, ϕ) projection of the track and the less precise ϕ_0 can be determined. Therefore, we assume that the standard deviation of the distribution of $\delta\phi_0$, as defined in Equation (3.3), is independent of ϑ. The middle row plots in Figure 3.4 confirm this assumption.

We investigated electrons and muons. Since the muon has a relatively large mass and does

not interact hadronically, there should be only a small impact of the detector material on the momentum measurement. Electrons, in contrast, have a quite small mass and may radiate bremsstrahlung photons when passing though the tracker material. Since this loss of energy leads to a smaller radius of curvature, the measurement of the momentum and the impact parameters are affected [122, 126]. As well, electrons might be affected stronger by multiple scattering than muons. We could, therefore, expect larger uncertainties of the track parameters for electrons than for muons. On the other hand, the track reconstruction based on Kalman filtering includes also multiple scattering into the track model.
In this analysis, we observe only slight deviations between the uncertainties of the track parameters of electrons and muons in the energy and angle range studied. However, cases occur where multiple scattering cannot be compensated and enhanced tails occur in the distributions of the track parameter uncertainties. Figure 3.3 shows as example the $\delta p_\perp^{-1}$ distribution for electrons and muons. Generally, larger tails are observed than expected for a Gaussian distribution. There is a larger right-hand side tail in the $\delta p_\perp^{-1}$ distribution for electrons originating from bremsstrahlung losses, demonstrating the underestimation of $p_\perp$. These tails were not considered and omitted in this analysis.

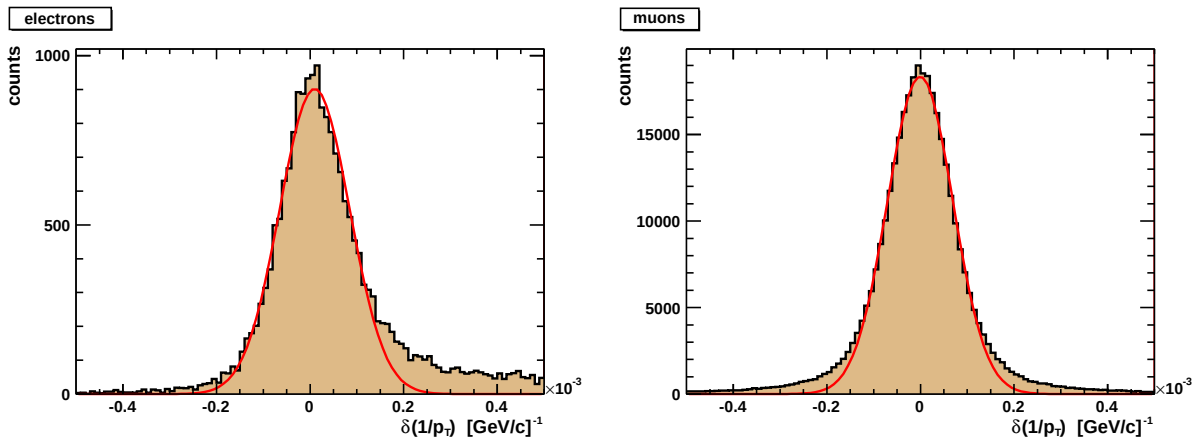

Figure 3.3: Distributions of $\delta(p_\perp^{-1})$ for electrons (left) and muons (right). The peak was fitted with a Gaussian.

Generally, larger uncertainties of all track parameters are found for small particle momenta in Figure 3.4. The reason is that for small momenta the influence of multiple scattering in the detector material becomes important. The average of the squared scattering angle for a thin layer is proportional to $\langle\Theta^2\rangle \propto (p^2 + m^2)/(p^4\beta^2)$ [127, 63, 128], where p, m and β are the momentum, the mass and the speed, respectively, of the particle traversing the detector material.
The uncertainties of d_0 and z_0 are around 4 μm as can be observed in the both top rows of plots in Figure 3.4. The smallest uncertainties of the impact parameters are between about 30 GeV to 100 GeV. The uncertainty for z_0 is almost doubled in the small polar angle range. This effect is not so significant for the radial impact parameter, d_0.
The polar and azimuth angle uncertainties are around 0.05 mrad as shown in third and

fourth row of plot in Figure 3.4. They decrease monotonically with increasing particle momentum up to about 180 GeV, and deviate only slightly from each other for different polar angle ranges. Furthermore, the uncertainties are smaller for small polar angles. The reason is the improved tracking with the forward tracker disks (FTD), which are depicted in Figure 2.5 and which provide additional track points in this region.
The transverse momentum uncertainty, given as $\Delta(p_\perp^{-1})$, also decreases with increasing particle momentum up to about 180 GeV and is mostly at about 10^{-4} $(\mathrm{GeV}/c)^{-1}$, as shown in the bottom row of plots in Figure 3.4. However, even for muons the baseline design[2] transverse momentum uncertainty of 5×10^{-5} $(\mathrm{GeV}/c)^{-1}$ [79] is not achieved in this momentum range.
It should be noted that the relative transverse momentum uncertainty grows with increasing transverse momentum

$$\delta p_\perp / p_\perp \propto p_\perp \ .$$

Therefore, for very large momenta the measured calorimeter energy can be used for the momentum reconstruction instead of the track reconstruction, because it can be more precise due the decrease of the relative energy measurement uncertainty Equation (1.53).
We use as baseline values for the uncertainty of the impact parameters about 5 μm for a particle momentum of 100 GeV/c, which is well achieved[3]. There are no baseline values specified for the uncertainties of the polar and azimuthal angle.

[2]The 'baseline design' covers the currently accepted design goals to meet the requirements for the physics cases.

[3]Required for some benchmark processes is $(\Delta\sqrt{z_0^2 + d_0^2})^2 = 5\ \mu\mathrm{m} \oplus 10\ \mu\mathrm{m}/(p[\mathrm{GeV/c}]\ \sin^{3/2}\vartheta)$ [79]

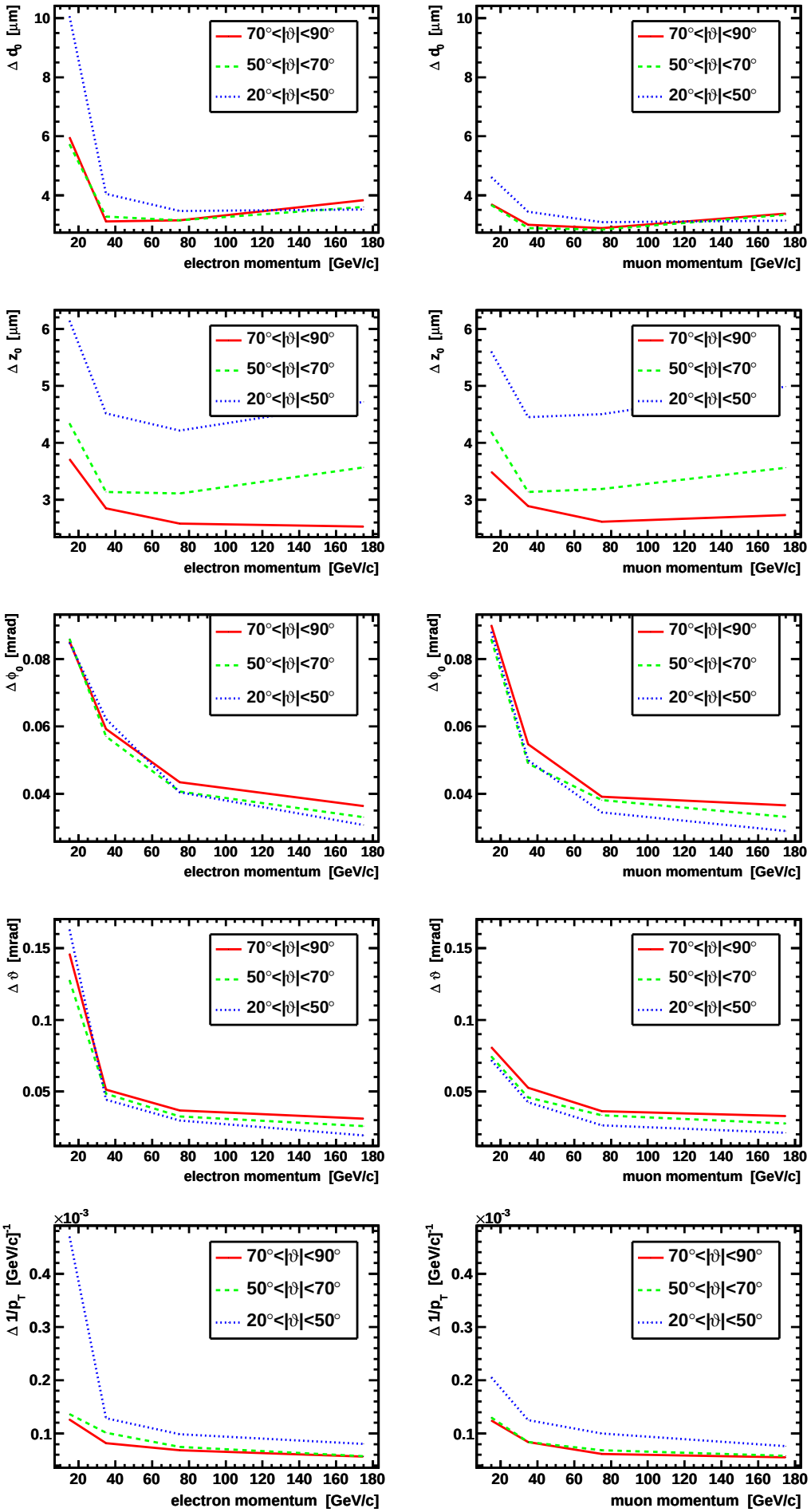

Figure 3.4: From top to bottom the uncertainties of the track parameters d_0, z_0, ϕ_0, ϑ, $p_\perp$ as function of the particle momentum for electrons (left) and muons (right).

3.3 Particle Identification Studies

Particle identification is based on the diversities of specific properties of the particles. These properties lead to different signatures inside the sub-detectors. The first rough classification is whether a particle is stable or not, i.e. whether it decays inside the detector or not. Decayed particles must be reconstructed in a second step after the decay products have been reconstructed.

For the geometry of the ILC detector all primary particles created in an event start in a vertex close to the interaction point around which the detector is concentrically designed, as described in Section 2.3. There are stable and long-living particles, which can be detected inside the detectors. Stable particles are photons (γ), protons (p), electrons and positrons ($e^{\pm}$). Long-living particles are muons ($\mu^{\pm}$), pions ($\pi^{\pm}$), kaons (K_L^0) and neutrons (n), and their decay time might be dilated relativistically.

For the particle identification we distinguish neutral and charged particles. Neutral particles are either photons, which deposit their energy almost completely inside the electromagnetic calorimeter (ECAL), or neutral hadrons. The latter can be neutrons or neutral kaons, which deposit most of their energy inside the hadronic calorimeter (HCAL). The charged particles are classified as electrons, muons and charged pions. Charged particles and antiparticles are distinguished by the sign of the curvature of the reconstructed tracks. Electrons deposit most of their energy in the ECAL, whereas pions deposit the larger part of their energy in the HCAL. Muons create deposits inside the calorimeter, which look like tracks. This pattern is called a MIP signature.

The choice of the particle types to be distinguished was geared to the requirements of the Higgs recoil mass analysis in Chapter 4, in which electrons and muons and charged hadrons (mainly pions) have to be distinguished. Therefore, there is no finer separation.

Neutrons are assigned to the group of neutral kaons. Similarly, protons are counted as charged pions.

Particle Identification Method

We use a probabilistic case distinction method for the particle identification as described in Chapter A.

We distinguish charged particles having a reconstructed track and neutral particles, which do not have a reconstructed track, in different branches of the decision tree.

We assume $N = 3$ charged particle types – electrons, muons and charged pions – and $N = 2$ neutral particle types – photons and kaons. For each of the both decision branches, variables, x_i $(i = 1, \ldots, M)$, are chosen, which characterize the detector response for the different particle types. For convenience, we write these variables as a vector, $\vec{x} = (x_1, x_2, \ldots, x_M)^T$. There are M one-dimensional probability density functions (PDF) of the variables $f_{j,i}(x_i)$ $(i = 1, \ldots, M)$, according to which the x_i are distributed, for each particle type j.

The probability to have a particle of type j for a given value of the variable x_i is given by

Equation (A.3)

$$P_i(j|x_i) = \frac{f_{j,i}(x_i)}{\sum_l f_{l,i}(x_i)} \,. \tag{3.6}$$

Assuming that all variables are independent, the combined probability to have a particle of type j under the condition of having a set of values of the variables in $\vec{x}$ is then

$$P(j|\vec{x}) = \frac{\prod_i P_i(j|x_i)}{\sum_l \prod_i P_i(l|x_i)} \,. \tag{3.7}$$

The denominator is just the normalization such that $\sum_j P(j|\vec{x}) = 1$. That is we assume for each arbitrary particle flow object to be one of the above assumed particle types according to the maximum probability.

Variables for Particle Identification

The variables for the particle identification, x_i, must be characteristic for the particles to be identified, i.e. their distributions, $f_{j,i}(x_i)$, should be as different as possible for the different particle types. Then we can expect a good separation of the particles types for a given set of variables.
We consider reconstructed clusters in the electromagnetic and hadronic calorimeters. Figure 3.5 shows schematically such a cluster. Available information from a cluster are the

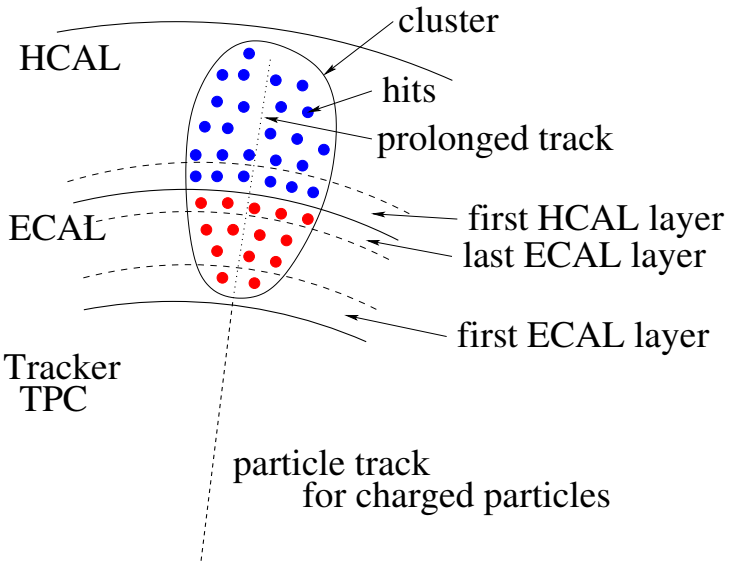

Figure 3.5: Schematic 2D representation of a calorimeter cluster. Blue dots are hits in the hadronic calorimeter (HCAL), red dots are hits in the electromagnetic calorimeter (ECAL).

total energy contained in the cluster, E_{total}, the total number of hits in this cluster, N_{total}, the energy of the HCAL part of the cluster, E_{HCAL}, the number of hits in the HCAL part of the cluster, N_{HCAL}, the energy of the ECAL part of the cluster, E_{ECAL}, and the number of hits in the ECAL part of the cluster, N_{ECAL}.

We chose the ratio of the ECAL cluster energy, E_{ECAL}, and the total cluster energy, E_{total}, i.e. $E_{\mathrm{ECAL}}/E_{\mathrm{total}}$. This ratio should be one for electrons and smaller than one for muon and pions. Other quantities used are $E_{\mathrm{ECAL}}/N_{\mathrm{ECAL}}$ and $E_{\mathrm{HCAL}}/N_{\mathrm{HCAL}}$.
Additional information about the particle type can be the radially last HCAL layer containing a hit. For example, a muon will probably have a hit in the outer most HCAL layer, while a pion and an electron will not, because they are stopped inside the calorimeter volume and their showers may not reach the last HCAL layer. Hence, the number of the radially last HCAL layer containing hits was also used for the particle identification.
Valuable information is obtained from the cluster shape. The cluster can be roughly described by an ellipsoid having principle axes. The ellipsoid dimensions along these axes are a, b and c, where we assume $a \geq b \geq c$. We use a variable that parametrizes the excentricity of a cluster, i.e. the deviation from a sphere, defined as

$$\epsilon_{\mathrm{cluster}} = \frac{(b+c)/2}{a} \ .$$

$\epsilon_{\mathrm{cluster}}$ is one for a sphere, and else smaller than one for an ellipsoid.
For charged particles there is a track from the tracker, which can be extrapolated into the calorimeters. The distances of the hits of a cluster to this extrapolated track are calculated and their arithmetic mean determined. The obtained quantity is called the *average hit-track distance*, $\langle d_{\mathrm{hit-track}} \rangle$. For neutral particles a straight line from the interaction point to the center of gravity of the cluster, i.e.

$$\vec{R}_{\mathrm{center-of-gravity}} = \frac{\sum_i E_i \vec{R}_i}{E_{\mathrm{total}}},$$

is used to determine $\langle d_{\mathrm{hit-track}} \rangle$. Herein, the sum goes over all hits of the considered cluster, E_i is the registered energy and $\vec{R}_i$ the position of the i-th hit.
The distributions of $E_{\mathrm{ECAL}}/E_{\mathrm{total}}$ and $\langle d_{\mathrm{hit-track}} \rangle$ are shown in Figure 3.6 for electrons, muons and pions. They show significant differences for the different particle types.
The specified variables for the particle identification were chosen in an earlier analysis stage due to their discrimination power. However, further optimization is possible by using more or different variables, such as for instance the energy deposition per unit path length, $d\varepsilon_{\mathrm{dep}}/dx$ [56, 129, 130], from the reconstructed track or the muon chamber energy deposition. The variables necessary for exploiting these effects were not available at the current stage of the reconstruction software.
Figure 3.7 illustrates the general particle identification procedure.

Usage of the Particle Identification Method

In general, the PDFs in Equation (3.6), $f_{j,i}(\vec{x})$, are not known analytically. They are different for different detector technologies and geometries, and must therefore be determined for each new detector design numerically. Here, Monte-Carlo simulations are used to obtain the functions $f_{j,i}$ as normalized histograms.

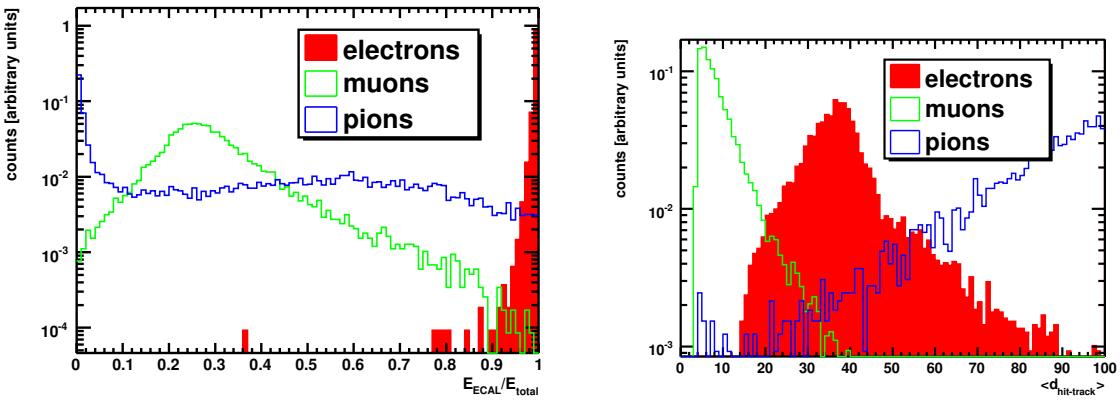

Figure 3.6: The distributions of the ratio $E_{\mathrm{ECAL}}/E_{\mathrm{total}}$ (left) and of the mean hit-track distance, $\langle d_{\mathrm{hit-track}} \rangle$, (right) for electrons (red), muons (green) and pions (blue).

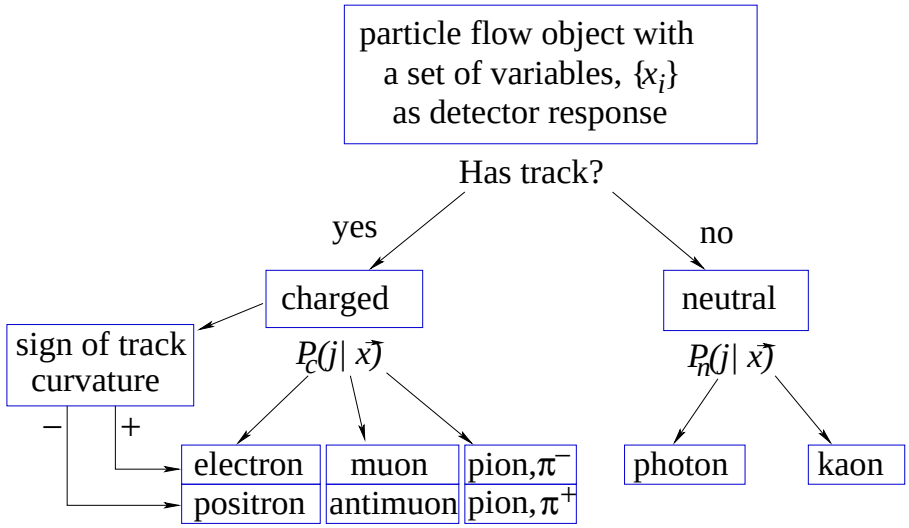

Figure 3.7: Scheme of the particle identification procedure. P_c and P_n are the different likelihoods used in different branches of the decision tree.

The first step is to determine the distributions, i.e. to fill the corresponding histograms. This is accomplished by creating a sample of single particle events for each particle type, which we call the *calibration sample*. The particle momenta are uniformly distributed in direction and in the energy range between zero and 250 GeV. These events are passed through the detector simulation, and the subsequent track and cluster reconstruction, and the cluster-track matching. The information from the clusters of the particle flow objects are converted into the relevant variables, which are filled into the histograms. Finally, the content of these histograms is normalized to one.
The particle identification is then done in a second step in the following general way. A sample of events is used, either from another Monte-Carlo sample, which is passed through the detector simulation as was done for the Higgs-Recoil analysis in this thesis, or,

later, from experimental data samples. Track and cluster reconstruction, and the cluster-track matching are performed for these event samples. The variables introduced above are calculated for each reconstructed particle flow object in each event. Using Equations (3.6) and (3.7) the likelihoods are calculated for each particle flow object to be a particle of a certain type. The most probable particle type is assign to this particle flow object.

Performance of the Particle Identification

We define the ratio 'number of particles of type b reconstructed as particle of type a divided by the number of particles being of type b', where a and b can be, for example, electron, muon or pion. For $a = b$, this ratio is the *efficiency* to identify a particle correctly. It ranges between zero and one, as it must be for an efficiency. For $a \neq b$ this ratio is the *impurity*, i.e. the fraction of particles that are identified incorrectly as one of the alternative particle types.
Table 3.1 shows the result of an analysis using single charged particle Monte-Carlo events. The initial particle momenta are between zero and 250 GeV as for the calibration sample. Secondaries created inside the detector are accounted for in the table, as well. The information about the original particle type for charged particles is taken from the track information. Since a particle might convert into or release other particles on its path through the tracker, one reconstructed track could contain hits of particles of several types. That particle type with the largest hit amount contribution is assumed as the true type.

MC PID ↓ \Reco PID →	electron	muon	pion
electron	98.84 %	0.01 %	1.15 %
muon	0.13 %	97.32 %	2.55 %
pion	2.41 %	0.51 %	97.08 %

Table 3.1: Particle identification efficiencies and impurities for charged particle types. Lines add to 100 %. MC PID is the original particle type, Reco PID is the reconstructed particle type.

The separation between electrons and muons is very good. The separation between pions and leptons is worse, but in total well above 95 %. The numbers in Table 3.1 are almost the pure particle identification efficiencies and impurities. No momentum or polar angle cut is applied, which would exclude low-energetic particles and particles flying into the forward region. However, effects of the detector geometry in certain polar angle ranges on the cluster reconstruction cannot be avoided. This is discussed in the following.

We investigated particle identification efficiencies and impurities for electrons, muons, pions, and also for photons as functions of the momentum and the polar angle. For a more precise understanding, only those events were considered where exactly one particle was reconstructed that is assumed to be the initial one originating from the IP. Therefore, secondaries are excluded. Figure 3.8 shows the ability of the LDC detector and the reconstruction software to reproduce exactly one particle if a single particle started initially

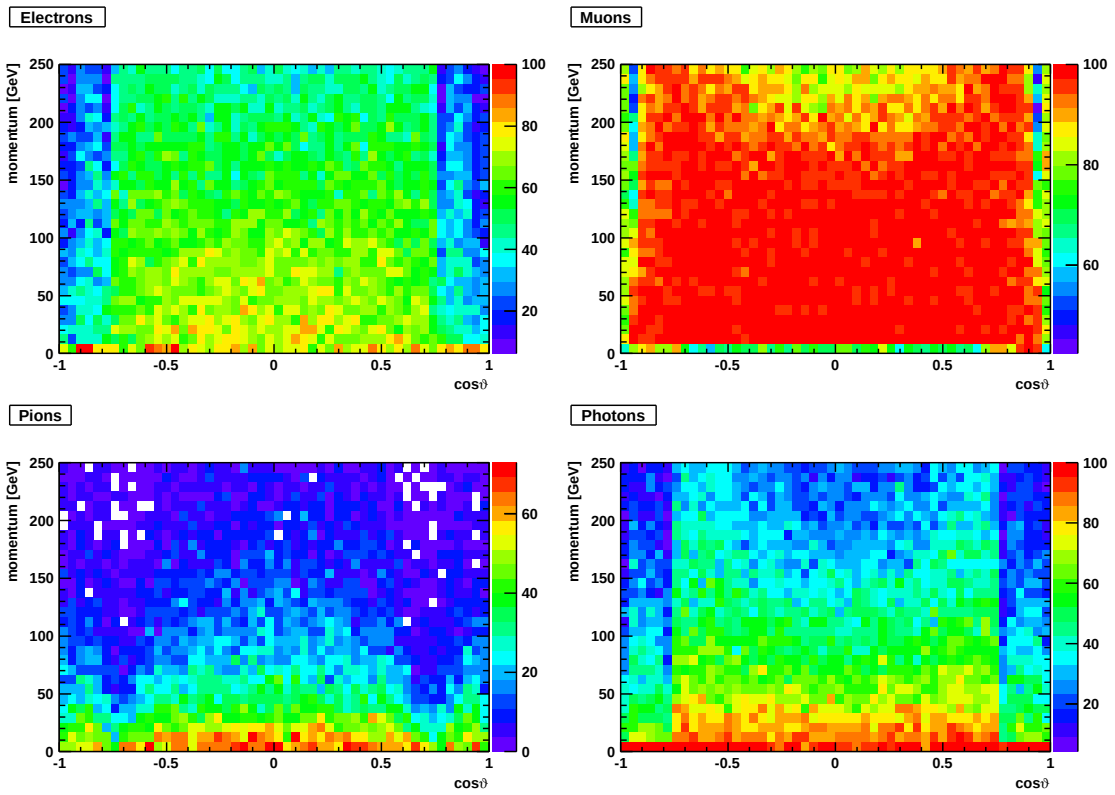

Figure 3.8: Fraction of events with one single particle reconstructed in the final state as function of their MC particle momentum and cosine of the polar angle, $\cos\vartheta$, for electrons (top left), muons (top right), pions (bottom left) and photons (bottom right).The color axis is in % with respect to number of single particle events generated in the corresponding momentum and polar angle interval.

at the IP. Only single muons are reconstructed in nearly the whole angle and momentum range one single particle flow object per event. At very low momenta, in the forward regions and at rather high energies, either no muon is reconstructed or secondaries are produced. Electrons and photons undergo at larger momenta processes in which secondaries might be created. Specifically, in the forward region, the direction of the calorimeter endcaps for the range $|cos\vartheta| > 0.7$, there is a strong drop in the detector ability to reproduce a single particle. The reconstruction of a pion as a single particle does hardly reach 70 % for small momenta. Otherwise it drops fast below 20 %.

Generally, there is almost no charged particle identified as a neutral one and vice versa, which can only occur if the track reconstruction or the cluster-track matching do not work properly. The efficiencies are generally close to 100 % and the impurities on a few percent level for nearly the total momentum and polar angle range, except for small momenta and small and large polar angles.

The probabilistic case distinction method for the particle identification is expected to be

rather independent of the momentum of the particle, which is to be identified, because the method deals with probability distributions, which are composed of particles of all possible energies. An energy dependence can occur if one or more variables used for this method are correlated with the particle momentum or are only insignificantly different for several particle types in a certain momentum range. Also, if the detector geometry pretends a certain signature for a particle type in some detector regions due to e.g. a bad cluster reconstruction, then the discrimination power might be rather small diminishing the identification efficiency.
For very small momenta, below some tenth of MeV, a lot of particles from the IP do not reach the calorimeters and are not reconstructed at all. The same is true for the very forward region, i.e. for small and large polar angles, because in this region the particles leave only few detector hits if at all. These objects are not considered in the particle identification. However, if clusters are reconstructed (with or without an assigned track) a particle identification is performed. In these limiting angle ranges of the very forward region, it is still possible that clusters reconstructed even if badly. Here, the cluster reconstruction inefficiency is convoluted with the particle identification efficiency. This cannot be avoided except by an explicit polar angle cut excluding these ranges from the reconstruction.

About 52.5 % of all events with an initial electron are reconstructed with a single particle in the final state being an electron, because electrons often undergo bremsstrahlung inside the tracker causing secondary photons, which in turn leave clusters in the ECAL. Such events with two and more reconstructed particles are omitted in the consideration. In the remaining events, single electrons are correctly identified as electrons with an almost 100 % efficiency in nearly the full momentum[4] and angle range, as shown in Figure 3.9. Only for the very forward polar angle ranges at all energies and at about $|\cos\vartheta| \approx 0.8$ (37° and 143°) for larger energies, electrons are more frequently identified incorrectly as pions. Both angle ranges are detector regions, where leakage of the ECAL shower into the HCAL can occur causing a pion signature. This can happen also randomly in the whole momentum and angle range, but with very small probability.

About 94 % of all events with an initial muon are reconstructed with a single particle in the final state being a muon. Out of these, more than 90 % are correctly identified as muons in nearly the whole momentum and angle range, as shown in Figure 3.10. Only muons with a small energy or a momentum directed into the forward regions are quite often identified incorrectly as pions. For larger muon momenta, larger than about 90 GeV, there seems to be a gradual degradation of the muon identification efficiency. About 5 % of the muons in this momentum range are incorrectly identified as pions. The reason might be an increased stopping power of muons due to radiative losses. The bremsstrahlung photons cause clusters inside HCAL pretending a signature of a pion stopped inside HCAL. The number of cases with an incorrect reconstruction due to bremsstrahlung might be reduced

[4]The binning is to rough to see the drop in the electron identification efficiency at small momentum, where it is probable that no particle is reconstructed because the electron does not reach the ECAL.

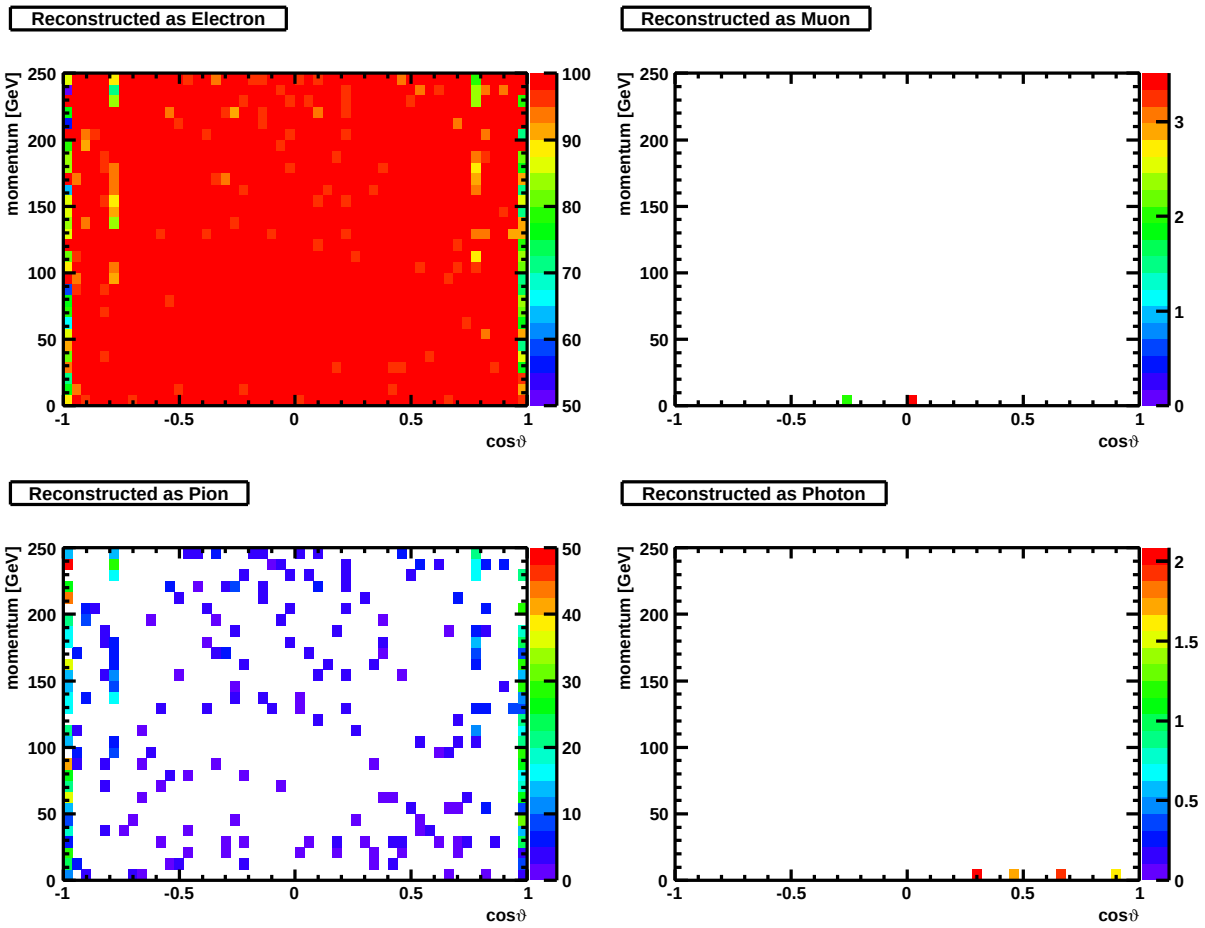

Figure 3.9: Particle identification efficiency for electrons as function of their MC particle momentum and cosine of the polar angle, $\cos\vartheta$ (top left). Fraction of electrons incorrectly identified as muons (top right), as pions (bottom left) and as photons (bottom right) as functions of the electron momentum and $\cos\vartheta$.

if the information from the muon spectrometer is included as variable into the particle identification procedure, since pions are mostly stopped inside the HCAL and then do not cause signals in the muon spectrometer.

Only about 17 % of all events with an initial pion are reconstructed with a single particle in the final state being a pion. In the other cases, pions interact with the tracker and calorimeter material or convert into several other particles creating secondaries. Such events are omitted in the considerations.

Single pions are identified as pions generally with more than 80 % efficiency in the most momentum and angle range, as shown in Figure 3.11. At smaller momenta, smaller than about 30 GeV, about 10 % of the pions are identified as electrons. Low-energetic pions might be stopped in the ECAL leaving no significant energy inside HCAL. As well, pions

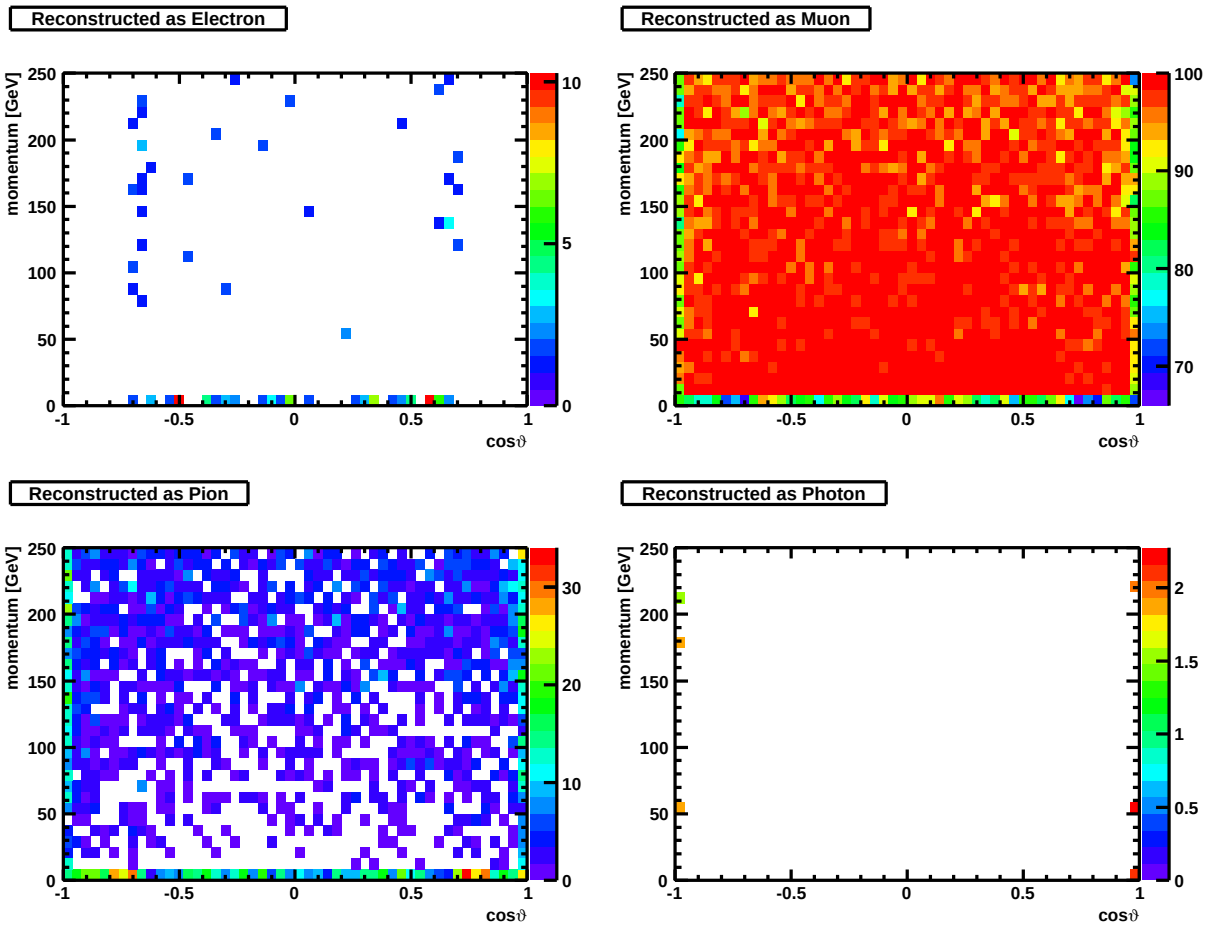

Figure 3.10: Particle identification efficiency for muons as function of their MC particle momentum and cosine of the polar angle, $\cos\vartheta$ (top right). Fraction of muons incorrectly identified as electrons (top left), as pions (bottom left) and as photons (bottom right) as functions of the muon momentum and $\cos\vartheta$.

might enter deeply into the HCAL before interacting in a hard scattering process with the HCAL material and leave a MIP signature.

For larger momenta and specifically in the polar angle ranges around $|\cos\vartheta| \approx 0.7$, there are drops of the pion identification efficiency even down to few percent. In this region of the detector, pions are frequently identified as muons.

Also decay of the pions into electrons or muons or processes like $\pi^- p \to \pi^0 n$ can occur inside the calorimeters or short before reaching these, where π^0 immediately decay to photons. These secondary electrons, muons or photons cause then either an electron or a muon signature and are counted here if no other reconstructed particle appears. In this case we would indeed have an electron or a muon, which is correctly identified but incorrectly assigned to the group of original pions, since the corresponding track consists mainly of pion hits. This cannot be avoided. Another conversion process occurs if a negatively

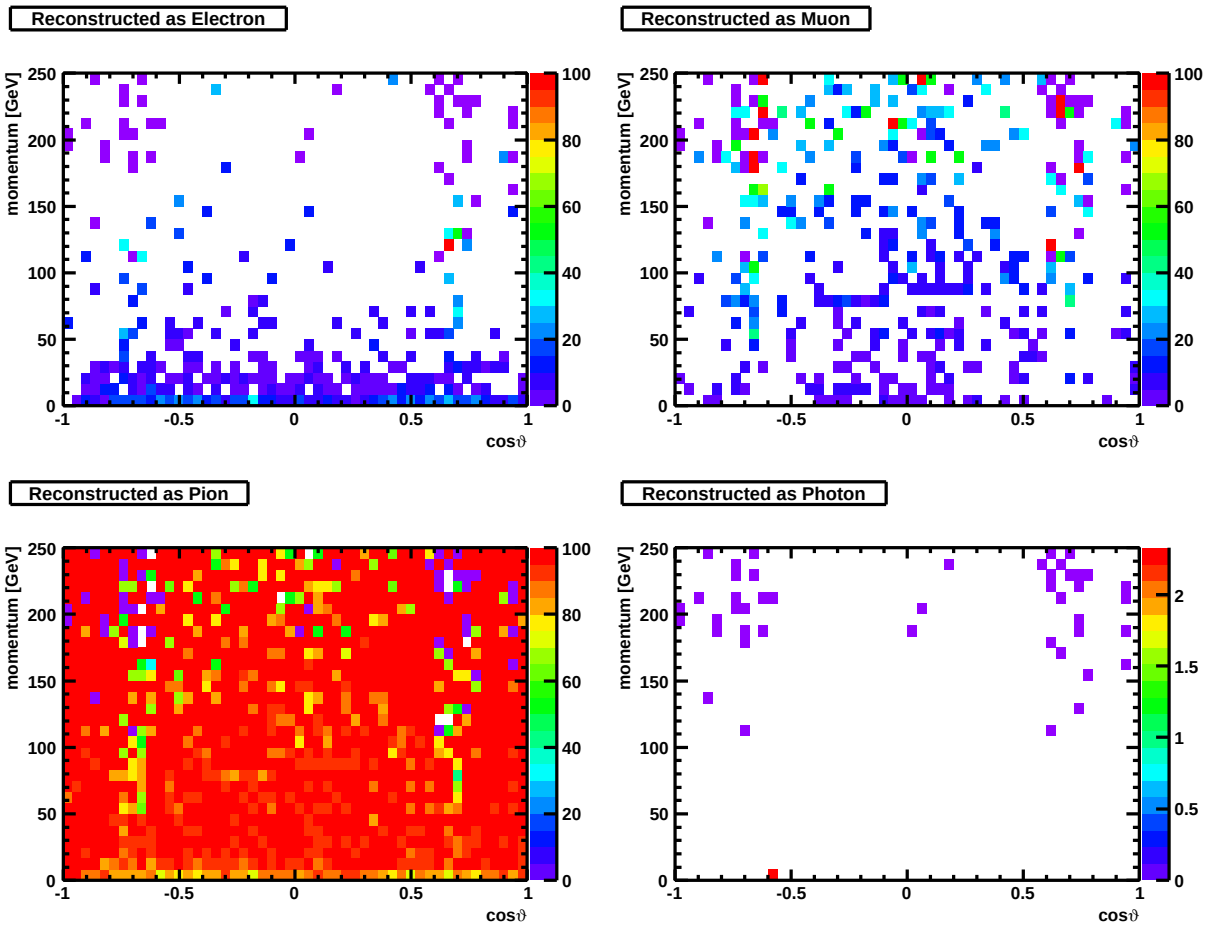

Figure 3.11: Particle identification efficiency for pions as function of their MC particle momentum and cosine of the polar angle, $\cos\vartheta$ (bottom left). Fraction of pions incorrectly identified as electrons (top left), as muons (top right) and as photons (bottom right) as functions of the pion momentum and $\cos\vartheta$.

charged pion interacts with a proton of the detector material. The result is a neutron and neutral pion, which decays immediately into two photons causing ECAL clusters. If the most energy was transferred to the neutral pion, then there will be almost no impact of the remaining neutron to the cluster energy. In this way, the pion might be incorrectly identified as an electron due to the immediate decay $\pi^0 \rightarrow \gamma\gamma$.

To some extend, these cases of an incorrect identification due to physical processes are accounted for and damped by the probabilistic particle identification method, since the calibration sample also contains such cases, and the corresponding values of the variables are filled into the histograms.

In rare cases and mainly in the forward region at higher pion momenta, pions are identified incorrectly as photons. This only happens, if no reconstructed track is associated to the cluster, because either there is none or the cluster-track matching does not work properly

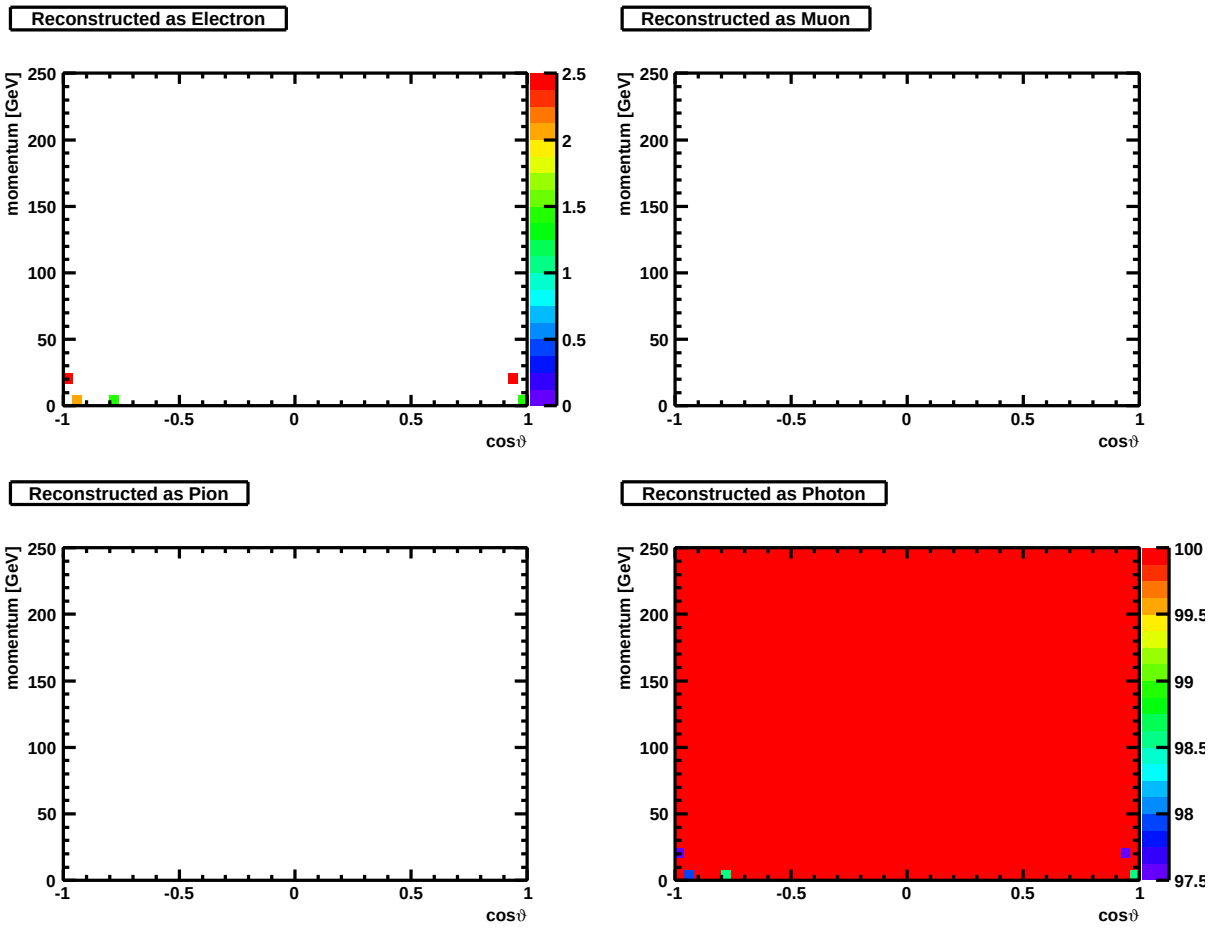

Figure 3.12: Particle identification efficiency for photons as function of their MC particle momentum and cosine of the polar angle, $\cos\vartheta$ (bottom right). Fraction of photons incorrectly identified as electrons (top left), as muons (top right) and as pions (bottom left) as functions of the photon momentum and $\cos\vartheta$.

in these cases.

About 46 % of all events with an initial photon are reconstructed with a single particle in the final state. Photons can undergo Compton-scattering releasing secondary electrons from the material or direct pair production, therefore causing final states with more than one reconstructed particle. However, there is another important reason for events with e.g. two photons in the final state – the ECAL cluster stemming from one photon is split into two parts due to the improper working clustering algorithm. This was also true for the electron cluster, where, however, the track momentum could be used to correct for it. This is generally not possible for photons. Photons are correctly identified as photons with nearly 100 % efficiency in the whole momentum and polar angle range, as shown in Figure 3.12. A photon should have no track and can therefore not be identified as a charged par-

ticle. If a photon causes the release of matter electrons inside the tracker due to ionization or Compton-scattering, or converts into an electron-positron pair in the tracker, then there might be a track from the charged particles. These, in turn, cause clusters if they reach the ECAL. If the cluster-track matching works properly, these particles should be identified correctly as electrons. Specifically, since the information about the true particle type is taken from the track, a particle flow object containing a track cannot have a neutral particle type as original type. The very rare cases of the identification of a photon as an electron must be therefore considered as ill cases, maybe being a bug in the reconstruction software[5].

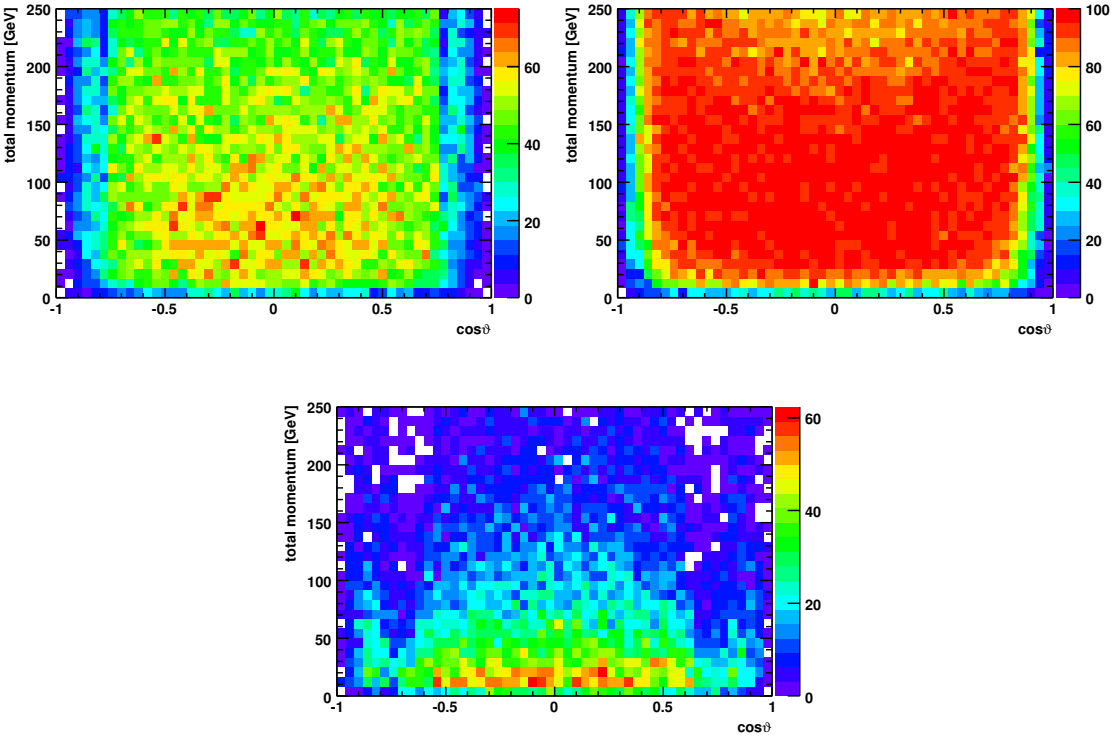

Figure 3.13: Single particle reconstruction efficiencies as functions of the initial particle momentum and the polar angle of the momentum, $\cos\vartheta$, for electrons (top left), muons (top right) and pions (bottom). The color axis is in % with respect to number of events with initial momentum in this interval. Only particles passing a cut on $\delta(p_\perp^{-1})$ of $2\times\Delta(p_\perp^{-1})$ and with a correct reconstructed particle type assigned are accepted.

Generally, the rates for wrong identifications of particles with a small momentum or a momentum polar angle in the forward regions, $|\cos\vartheta| > 0.95$, are not very significant because in these momentum and polar angle ranges the track parameter reconstruction is not very good as can be extrapolated from the results in the previous section. Therefore, one

[5]Possible candidates are the cluster-track matching, but also the assignment of the Monte-Carlo information about the particle type to the track or the cluster.

cannot speak about reconstructed particles in this range if the reconstructed momentum deviates significantly from the initial momentum. Figure 3.13 shows the single particle identification efficiencies for electrons, muons and pions if the reconstructed momentum does not deviate from the initial momentum by more than two times the standard deviation of $\delta(p_\perp^{-1})$. The standard deviations are $\Delta(p_\perp^{-1}) = 6.76 \times 10^{-5}$ GeV^{-1} for electrons, $\Delta(p_\perp^{-1}) = 6.31 \times 10^{-5}$ GeV^{-1} for muons and $\Delta(p_\perp^{-1}) = 7.51 \times 10^{-5}$ GeV^{-1} for pions, respectively. Diminished single particle reconstruction efficiencies are found particularly for small momenta.

Chapter 4

The Profile of the Higgs Particle – A Major Physics Case of the ILC

In Section 1.1.4 we pointed out, how important it is to find the Higgs boson and to determine its properties to complete the Standard Model. In e^+e^- annihilations, one can use the so-called Higgs-strahlung process to measure the Higgs boson mass and the Higgs-strahlung cross-section, and to determine the coupling of the Higgs boson to the Z boson (hZZ-coupling). Assuming the Standard Model and taking from other measurements the vacuum amplitude, v, (via G_F) one can determine the parameters μ and λ in the Higgs potential (1.25).
The Higgs boson is not found, yet, at the writing of this thesis. Therefore, all results presented here refer to simulation studies. Similar studies have been performed, also in conjunction with the search for the Higgs boson at LEP, but also as prospects for the next linear lepton collider, either on generator level or using fast detector simulations, i.e. with a parametric transport through the detector [131, 132, 133, 134, 135, 136, 137, 138].
There are also studies on the determination of the spin, the parity and the CP quantum numbers of the Higgs boson in the Higgs-strahlung process [139, 140, 141, 142, 143].
The current analysis concentrates on the capabilities of the ILC for measuring the Higgs boson mass and the Higgs-strahlung cross-section using a full detector simulation and event reconstruction with GEANT4 and MARLINRECO. The goal is to evaluate the effects of a realistic detector, beamstrahlung and initial and final state radiation, and partly also the beam energy spread on the precision of these quantities as well as to estimate the reconstruction efficiency for the Higgs-strahlung under realistic conditions including also the background due to other Standard Model processes, which were partly neglected in previous studies.
For this task, we apply the so-called *recoil technique*, in which the Higgs boson has not to be reconstructed. Instead, the knowledge about the initial state electron and positron energies and the reconstructed Z boson is used to reconstruct the recoiled Higgs boson. We want to show that the analysis result of the Higgs recoil mass analysis is independent of the decay modes of the Higgs boson, providing a tool that is independent of the model of Higgs boson decays. Therefore, this analysis can be applied to a Standard Model Higgs boson

as well as to the lightest Higgs boson in the supersymmetric model or even for models in which the Higgs boson decays into non-detected particles. For the reconstruction of the Z boson we use its decays into electron-positron and muon-antimuon pairs, respectively, because it is expected that these rather high-energetic leptons are quite easy to identify. Throughout the whole analysis, a Higgs boson mass of $M_h = 120$ GeV is assumed, unless specified differently. This value for the mass is about a probable value for a Standard Model Higgs boson as outlined in Section 1.1.5.

4.1 The Higgs-Strahlung Process and the Recoil Technique

4.1.1 The Kinematics of the Higgs-Strahlung Process

Figure 4.1 shows schematically the Higgs-strahlung process. The initial leptons from the incoming beams annihilate to a virtual Z boson, Z^{*1}.

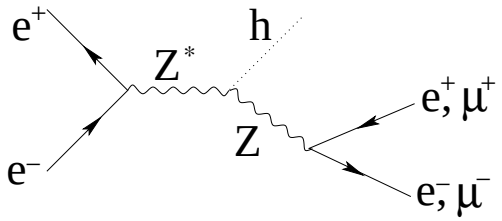

Figure 4.1: Higgs-strahlung process including the leptonic decay of the Z boson. The Higgs boson decays in any of the possible decay modes.

The Z^* becomes almost on-shell while emitting the Higgs boson, which is also almost on-shell. We consider the Higgs-Strahlung processes in which the Z boson decays into an electron-positron or a muon-antimuon pair.
We denote the center-of-mass (cms) energy of the two initial leptons by $\sqrt{s}$. The energy-momentum conservation at the first vertex enforces the virtual Z boson to have an energy of $\sqrt{s}$ and a zero momentum in the e^+e^- cms frame. The energy-momentum conservation at the hZZ-vertex in the same reference frame reads

$$\begin{pmatrix} \sqrt{s} \\ \vec{0} \end{pmatrix} = \begin{pmatrix} E_Z \\ \vec{p}_Z \end{pmatrix} + \begin{pmatrix} E_h \\ \vec{p}_h \end{pmatrix} , \tag{4.1}$$

where E_Z and $\vec{p}_Z$ are energy and momentum of the recoiled on-shell Z boson, E_h and $\vec{p}_h$ those of the Higgs boson. Exploiting the energy-momentum relations for both bosons, i.e.

$$E_Z^2 = \vec{p}_Z^{\,2} + m_Z^2 \qquad \text{and} \qquad E_h^2 = \vec{p}_h^{\,2} + m_h^2 ,$$

[1] That is, its invariant mass m_{Z^*} is not equal to the pole mass M_Z (if p_{Z^*} is the four momentum of the Z^* then $p_{Z^*}^2 = m_{Z^*}^2$)

where m_h and m_Z are the invariant masses of the Z and the Higgs boson, respectively. The energy of the Z boson is determined by m_h, m_Z and $\sqrt{s}$. It is given by

$$E_Z = \frac{s + m_Z^2 - m_h^2}{2\sqrt{s}} \ . \tag{4.2}$$

Equation (4.1) represents four equations for the six momentum components of the Z and the Higgs boson (energy-momentum relation fixes the energies of both bosons). Two parameters, e.g. the polar and azimuthal angles of the Z boson momentum are not prescribed kinematically.
The energy-momentum conservation at the vertex of the decaying Z boson is given by

$$\begin{pmatrix} E_Z \\ \vec{p}_Z \end{pmatrix} = \begin{pmatrix} E_+ \\ \vec{p}_+ \end{pmatrix} + \begin{pmatrix} E_- \\ \vec{p}_- \end{pmatrix} , \tag{4.3}$$

where $E_\pm$ and $\vec{p}_\pm$ are the energies and momenta of the leptons obeying the energy-momentum relations $E_\pm^2 = \vec{p}_\pm^{\,2} + m_\ell^2$, where m_ℓ denotes the lepton mass. If the Z boson decays into e^+e^- we call this the *e-channel*, otherwise, if the Z boson decays into $\mu^+\mu^-$, the *μ-channel*. Equation (4.3) represents four equations for the six lepton momentum components so that again two variables are free, for instance the polar and the azimuthal angle of one lepton. Still, one can express the energy and the invariant mass of the Z boson in terms of the lepton momenta,

$$E_Z = E_+ + E_- \ , \qquad m_Z^2 = 2(m_\ell^2 + E_+E_- - \vec{p}_+ \cdot \vec{p}_-) \ . \tag{4.4}$$

4.1.2 Cross-Section of the Higgs-Strahlung Process

We assume for a moment that the invariant masses are equal to the pole masses, i.e. the bosons are exactly on-shell, $m_h = M_h$ and $m_Z = M_Z$. The diagram in Figure 4.2 represents

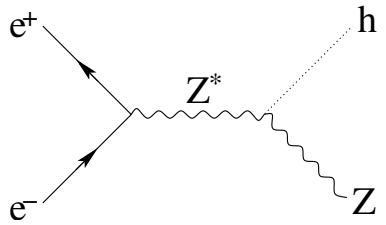

Figure 4.2: Higgs-strahlung process in the Standard Model. Z* is a off-mass shell Z boson. h denotes the Higgs boson.

the first term in the perturbation expansion and the corresponding total cross-section of the Higgs-strahlung process can be calculated using the formalism sketched in Section 1.1. The coupling of the Higgs boson to the Z boson is in the Standard Model given by

$$i\frac{g}{\cos\theta_W} M_Z \eta_{\mu\nu} \equiv i\frac{\sqrt{2}M_Z^2}{v}\eta_{\mu\nu} \ ,$$

where g is the gauge coupling of the $SU_L(2)$, θ_W the weak mixing angle and v the Higgs field vacuum amplitude, as introduced in Section 1.1.4. In the Standard Model, the cross-section, $\sigma_{hZ}^{\text{theo}}$, as function of $\sqrt{s}$ is then given in lowest order by [144, 140]

$$\sigma_{hZ}^{\text{theo}} = \frac{G_F^2 M_Z^4}{96\pi s}\left(1 + (-1 + 4\sin^2\theta_W)^2\right)\beta\frac{\beta^2 + 12M_Z^2/s}{(1 - M_Z^2/s)^2} \,, \tag{4.5}$$

where β is given by

$$\beta^2 = \left[1 - (M_h + M_Z)^2/s\right]\left[1 - (M_h - M_Z)^2/s\right] \,.$$

The simplifying assumption of a zero-lepton mass is used, which is rather good, since the lepton momenta are much larger than their masses.[2]
The kinematic threshold for this process is $\sqrt{s_{\text{th}}} = M_h + M_Z = 211.2$ GeV. For an increasing $\sqrt{s}$ above this threshold, $\sigma_{hZ}^{\text{theo}}$ increases fast to its maximum of 267.4 fb at $\sqrt{s} = 238.3$ GeV. For large $\sqrt{s}$ it decreases as $1/s$. Figure 4.3 shows $\sigma_{hZ}^{\text{theo}}$ as a function of $\sqrt{s}$ in the range [200 GeV,300 GeV].
Working at the maximum of $\sigma_{hZ}^{\text{theo}}$, we would expect about $L\sigma_{hZ}^{\text{theo}} = 133700$ Higgs-strahlung events for $L = 500$ fb^{-1}. Out of these about $L\sigma_{hZ}^{\text{theo}} \times B(Z \to \text{e}^+\text{e}^-) = 4496$ events occur in the e-channel [3].

4.1.3 The Reconstruction of the Higgs-Strahlung Process

In an experiment, we reconstruct first the momenta of the leptons, $\vec{p}_{\ell^\pm}$, from the signals inside the detector. By identifying the leptons as electrons and muons, we also know their mass m_ℓ, and consequently their energies, $E_{\ell^\pm}$, from the energy-momentum relation. Tracing back Equations (4.4) and (4.2), we first calculate the di-lepton energy, $E_{\text{di-lepton}}$, and the invariant di-lepton mass, $m_{\text{di-lepton}}$,

$$E_{\text{di-lepton}} = E_{\ell^+} + E_{\ell^-} \,, \qquad m_{\text{di-lepton}}^2 = 2(m_\ell^2 + E_{\ell^+}E_{\ell^-} - \vec{p}_{\ell^+} \cdot \vec{p}_{\ell^-}) \,, \tag{4.6}$$

which are equal to E_Z and m_Z, respectively, if the reconstructed momenta are equal to those of the leptons after the Z boson decay. In a second step the recoil mass is determined by

$$m_{\text{recoil}}^2 = s + m_{\text{di-lepton}}^2 - 2E_{\text{di-lepton}}\sqrt{s} \,, \tag{4.7}$$

[2] Relativistic factor and speed of the Z boson are $\gamma_Z = \frac{E_Z}{M_Z}$ and $\beta_Z^2 = 1 - \gamma_Z^{-2}$, respectively. A lepton from the Z decay obtains an energy of $E_\pm^r = M_Z/2 \gg m_\ell$ in the rest frame of the Z boson (index r denotes this frame). One can therefore neglect m_ℓ and equate energy and momentum of the lepton in this frame, $|\vec{p}_\pm| = E_\pm$. In the e^+e^- cms frame, a lepton can at most be ejected into negative Z boson momentum direction. Then the lepton energy in this frame, obtained by a Lorentz transformation with β_Z into Z boson momentum direction, is $E_\pm = \gamma_Z(1 - \beta_Z)E_\pm^r = \frac{E_Z}{2}(1 - \beta_Z)$. For electrons and positron is $E_\pm > 5$ GeV even for $\sqrt{s} = 500$ GeV and, thus, $E_\pm \gg m_{\text{e}}$. The muon mass, however, constitutes already about 10 % of the total muon energy in this case. Nevertheless, for lepton momentum directions other than the negative Z boson momentum direction the lepton energies are usually larger so that our approach is generally good.

[3] $B(Z \to \text{e}^+\text{e}^-) = 0.03363$ is the branching fraction for Z boson decay into e^+e^- pairs [5].

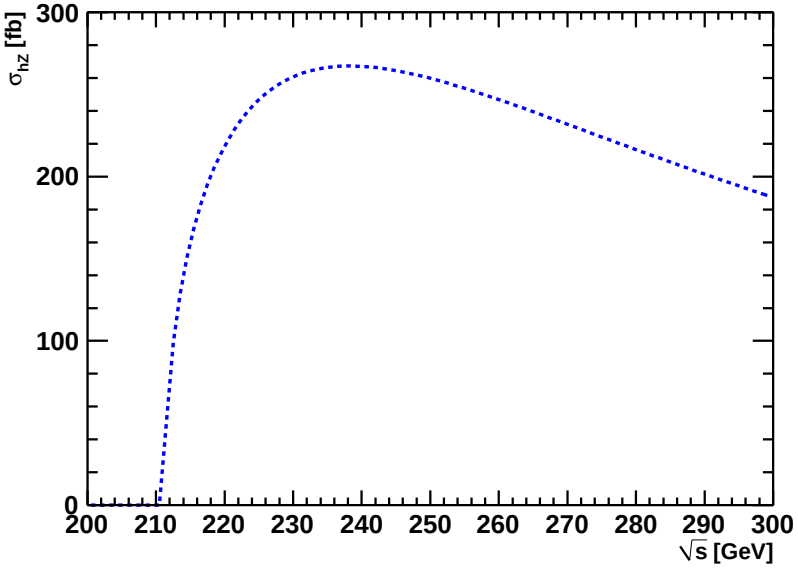

Figure 4.3: Cross-section of the Higgs-strahlung process from a theoretical calculation, Equation (4.5)

which is equal to m_h^2 in the ideal case. The nominal value of the cms energy is assumed for $\sqrt{s}$.[4] For each occurred Higgs-strahlung event in the ideal case, a value of $m_h = m_{\text{recoil}}$ can be calculated and, assuming e.g. a Gaussian distribution of m_h with mean M_h, an estimate of M_h could be made by fitting. This is, however, not appropriate by reasons given below. First, the invariant masses of the Higgs and Z boson, m_h and m_Z, are different from the pole masses, M_h and M_Z, for a certain event. The pole mass is a parameter, i.e. a constant in the model such as the Standard Model. In the diagram of Figure 4.1 the recoiled on-shell Z boson is described by a propagator of an unstable boson, which is proportional to

$$\frac{1}{p_Z^2 - M_Z^2 + i\Gamma_Z M_Z} \,,$$

where $\Gamma_Z = 2.4952$ GeV is the decay width of the Z boson. If we use $p_Z^2 = m_Z^2$, then the squared modulus of this propagator is

$$\frac{1}{(m_Z^2 - M_Z^2)^2 + M_Z^2\Gamma_Z^2} \,, \tag{4.8}$$

which occurs finally as factor in the Higgs-strahlung cross-section. That is, m_Z obeys a Breit-Wigner distribution. A similar statement is true for the Higgs boson, the invariant mass of which is also Breit-Wigner distributed but with the mean value M_h and width

[4] At the ILC, the mean beam energy and, consequently, $\sqrt{s}$ will be measured with a precision of $\Delta E_{\text{beam}}/E_{\text{beam}} = 10^{-4}$, possibly bunch-by-bunch. In the experiment the measured value of $\sqrt{s}$ should be used in Equation (4.7).

Γ_h. The cross-section is therefore enhanced if both the recoiled Z boson and the Higgs boson are on-shell. Otherwise, if this not possible kinematically e.g. due to $\sqrt{s} < \sqrt{s_{\text{th}}}$ the cross-section is small and the process suppressed.

4.1.4 Physical and Experimental Impacts on the Recoil Mass

Several physical and measurement effects influence the reconstruction of the invariant di-lepton and the recoil mass, leading to a general difference of the Higgs boson pole mass and the recoil mass for each event. Figure 4.4 shows the different stages of the analysis and the impacts of the effects on the measurement of M_h.

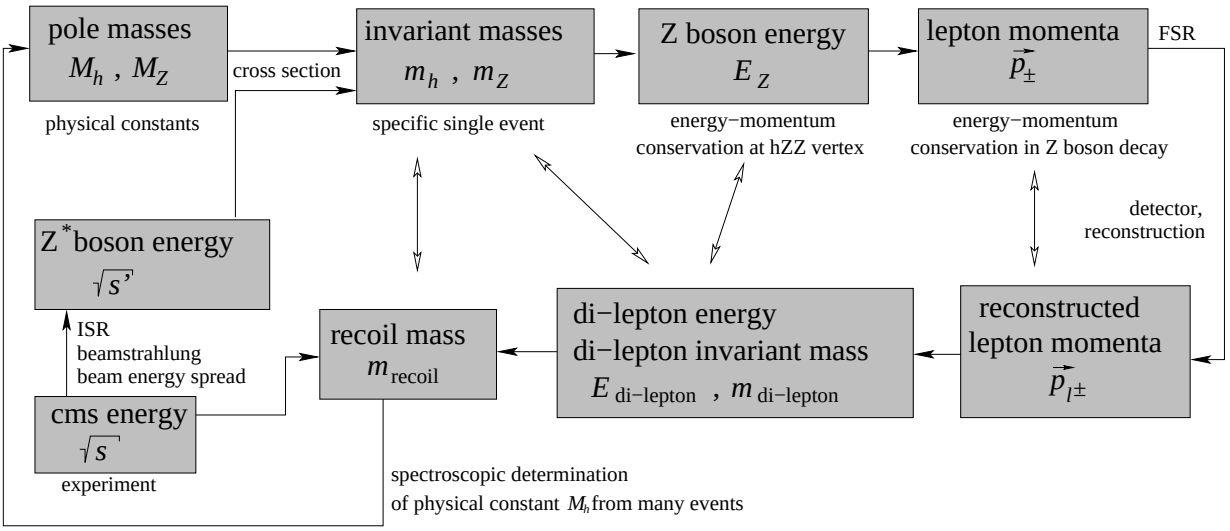

Figure 4.4: Kinematics and reconstruction chain including all deteriorating effects.

First, we assume $\sqrt{s} = E^{\text{e}}_{\text{beam}} + E^{\text{p}}_{\text{beam}}$ to be the nominal value in the reconstruction. However, the energies of the electrons and positrons in a bunch are Gaussian distributed around the nominal beam energy $E^{\text{e}}_{\text{beam}} = E^{\text{p}}_{\text{beam}} = E_{\text{beam}}$, leading to a cms energy $\sqrt{s'}$ distributed around $\sqrt{s}$ and different from $\sqrt{s}$ for each event. The standard deviations of these distributions are 0.28 % for electrons and 0.18 % positrons, respectively, of the nominal cms energy $\sqrt{s} = 250$ GeV.
Also affecting the actual cms energy in a single Higgs-strahlung event are beamstrahlung and initial state radiation (ISR).
The second kind of influences on the measurement of M_h concerns the fact, that the pole and invariant masses of the Higgs boson differ. Although the decay width of the Higgs boson, Γ_h, is rather small, 3.5 MeV for $M_h = 120$ GeV, and one can approximate $m_h = M_h$, this does not hold anymore for Higgs boson masses larger than about 140 GeV in the Standard Model, as is demonstrated in Figure 1.1.
Finally, there are effects that deteriorate the measurement of M_h and which concern the reconstruction of the momenta of the final state leptons. First of all, the leptons can undergo final state radiation (FSR) decreasing their momenta. The final state leptons in

the detector are then reconstructed, which introduces an uncertainty amongst others due to the detector resolution as described in Section 3.2.
In the following, we estimate the different effects on the measurement of M_h.

Initial State Radiation and Beamstrahlung

ISR denotes the emission of one or more photons by one or both initial leptons prior to the annihilation into the virtual Z boson as illustrated in Figure 4.5. ISR photons are mostly collinear with the beam particles, i.e. they are emitted in the direction of initial leptons. The ISR energy spectrum behaves roughly like $1/E_{\mathrm{ISR}}$, where E_{ISR} is the photon energy. They can therefore hardly be detected inside the LDC detector, because they leave it through the beam pipe.

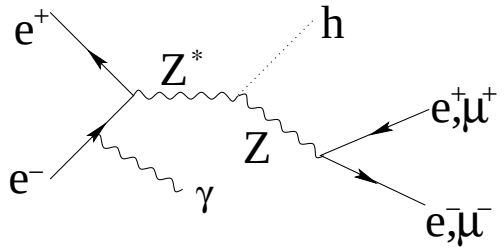

Figure 4.5: Example of a diagram of the Higgs-strahlung process including initial state radiation.

The effect of ISR is a decrease of the fraction of $\sqrt{s}$ transferred by the virtual Z boson, i.e. $\sqrt{s} = \sqrt{s'} + E_{\mathrm{ISR}}$, where $\sqrt{s'}$ is the remaining energy for the virtual Z boson.[5] The cross-section for the diagram in Figure 4.5 including ISR can be obtained as a convolution of the cross-section without ISR, Equation (4.5), and the QED structure functions for each initial lepton [145]. The result is a reduction of the Higgs-strahlung cross-section near the threshold and a shift of the maximum of the cross-section to higher values of $\sqrt{s}$.

Beamstrahlung was introduced in Section 2.2.2. Its origin can be described by the deflection of the bunch leptons in the coherent electromagnetic field of the oncoming bunch and can be influenced by the bunch design. Beamstrahlung and ISR are very similar and have therefore the same effect on the cross-section and Higgs boson mass measurement. Their fractional contributions might change, depending on the accelerator parameters.
The amount of energy losses due to beamstrahlung photon emissions increases with $\sqrt{s}$ when the beam parameters are kept constant, since the average energy loss due to beamstrahlung is proportional to the relativistic factor of one bunch particle with respect to the rest frame of the oncoming bunch [80].

[5] A boost of the virtual Z boson along the beam pipe due to an asymmetry of the energy of the initial leptons is neglected.

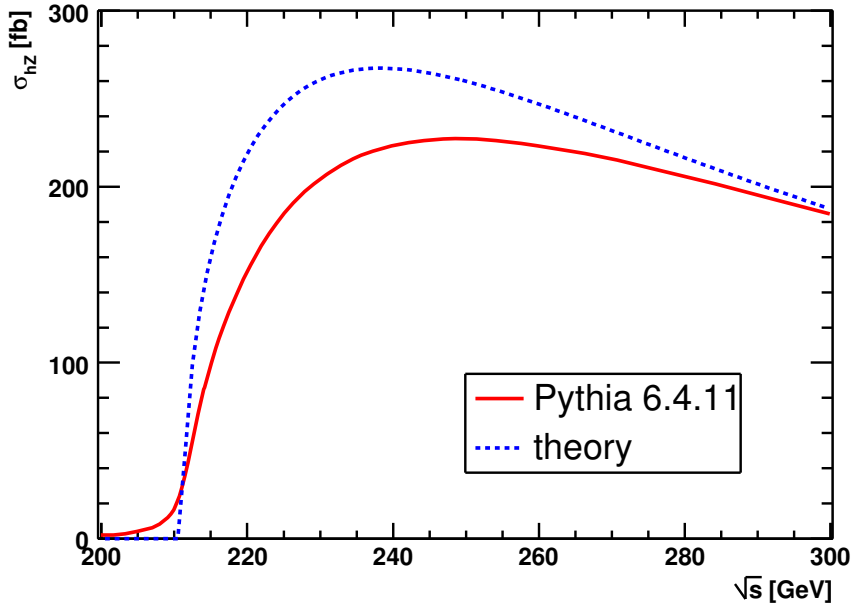

Figure 4.6: Cross-section of the Higgs-strahlung process from a theoretical calculation, Equation (4.5), (blue dashed line), and from the Monte-Carlo Generator PYTHIA, (red solid line). In the latter case, the finite Z decay width, higher order diagrams and beamstrahlung are accounted for.

Figure 4.6 shows the cross-section of the Higgs-strahlung process (red solid line), if higher order processes are accounted for. Specifically, ISR and beamstrahlung are included. Also the Z decay width was taken into account causing a fuzzy threshold behavior of the Higgs-strahlung cross-section. For comparison, the theoretical cross-section, Equation (4.5), is also displayed (blue dashed line).
ISR and beamstrahlung cause a reduction of $\sqrt{s}$ down to $\sqrt{s'}$ corresponding to the photon energy spectra. The Higgs-strahlung process is just still possible to occur above the energy threshold $\sqrt{s_{\mathrm{th}}}$. Since ISR and beamstrahlung photons are dominantly low-energetic, $\sqrt{s'}$ is in most of the cases only a bit smaller than $\sqrt{s}$. With smaller probability also larger amounts of energy are emitted.
To estimate the effect of ISR and beamstrahlung on the recoil mass we consider Equation (4.7). For the estimation, we assume the exact on-shell situation, $m_h = M_h$ and $m_Z = M_Z$, and replace $\sqrt{s}$ by $\sqrt{s'}$. The value of E_Z is given by Equation (4.2),

$$E_Z = \frac{s' + M_Z^2 - M_h^2}{2\sqrt{s'}} \ ,$$

where $\sqrt{s'} = \sqrt{s} - E_{\mathrm{ISR}}$ is the actual energy of the virtual Z boson. Then, Equation (4.7) results in

$$m^2_{\mathrm{recoil}} = s + M_Z^2 - \sqrt{s}\frac{(\sqrt{s} - E_{\mathrm{ISR}})^2 + M_Z^2 - M_h^2}{\sqrt{s} - E_{\mathrm{ISR}}} \ .$$

Omitting E_{ISR} in the reconstruction, one gets a larger value for E_Z and therefore also for m_{recoil}. The quantity m_{recoil} will be shifted to values, which are slightly larger than M_h. However, if $\sqrt{s'} = \sqrt{s_{\mathrm{th}}} = M_h + M_Z$, i.e. the maximum energy is emitted by ISR or beamstrahlung, $E_{\mathrm{ISR}}^{\mathrm{max}} = \sqrt{s} - \sqrt{s_{\mathrm{th}}}$, and where the Higgs-strahlung process is still allowed kinematically, then $E_Z = M_Z$, and we obtain for m_{recoil}

$$m_{\mathrm{recoil}}^2 = s + M_Z^2 - 2M_Z\sqrt{s} = (\sqrt{s} - M_Z)^2 = (\sqrt{s_{\mathrm{th}}} + E_{\mathrm{ISR}}^{\mathrm{max}} - M_Z)^2 = (M_h + E_{\mathrm{ISR}}^{\mathrm{max}})^2 \ ,$$

i.e. $m_{\mathrm{recoil}} = M_h + E_{\mathrm{ISR}}^{\mathrm{max}} > M_h$. The values of m_{recoil} are therefore distributed between about M_h and $M_h + \sqrt{s} - \sqrt{s_{\mathrm{th}}} \equiv \sqrt{s} - M_Z$. Figure 4.7 illustrates this. The recoil mass distribution including beamstrahlung and ISR (pink filled) are generated using PYTHIA [119] for $M_h = 120$ GeV for different values of $\sqrt{s} = 250$ GeV, 350 GeV and 500 GeV. The m_{recoil} values for e.g. $\sqrt{s} = 250$ GeV should be between 120 GeV and about 250 GeV $-$ 91.2 GeV $\approx$ 160 GeV as it is obviously the case.

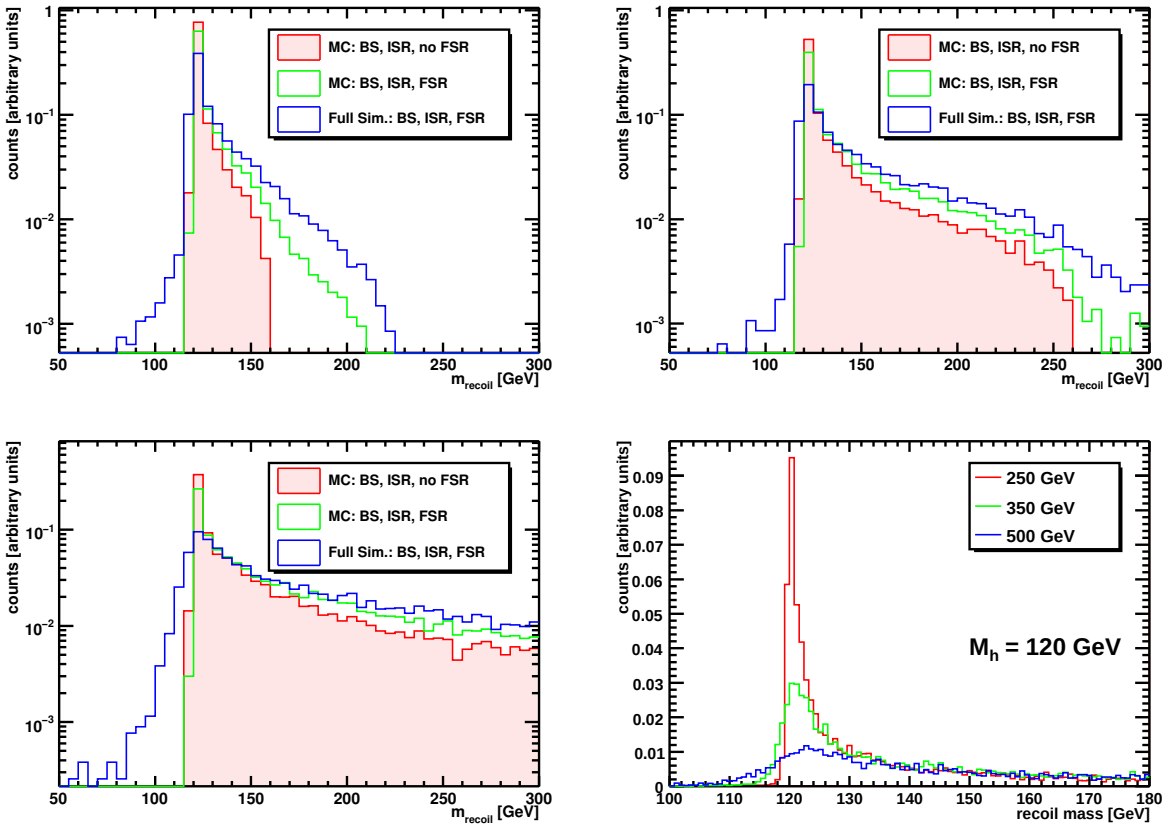

Figure 4.7: The effect of beamstrahlung and ISR, FSR and the detector resolution on the recoil mass distribution for $\sqrt{s} = 250$ GeV (top left), $\sqrt{s} = 350$ GeV (top right) and $\sqrt{s} = 500$ GeV (bottom left). Comparison of the Higgs recoil mass distribution for cms energies of 250, 350 and 500 GeV including all deteriorating effects (bottom right).

For a certain fixed Higgs boson pole mass, M_h, ISR and beamstrahlung cause pronounced

tails in the recoil mass distribution, which are the larger, the farther the used nominal cms energy, $\sqrt{s}$, is above the threshold, $M_h + M_Z$. This migration of recoil mass values into the tail and a broadening of the recoil mass peak reduces significantly the capabilities of measuring precisely the Higgs boson mass and the Higgs-strahlung cross-section as will be shown below. Already now one can state that a Higgs recoil mass analysis at $\sqrt{s} = 500$ GeV – the baseline cms energy of the ILC – is prohibitive, if the $M_h = 120$ GeV, as becomes obvious in the bottom right-hand plot of Figure 4.7.

Final State Radiation

FSR denotes the emission of photons by the final state leptons directly after the Z boson decay, as depicted in Figure 4.8. Similar to ISR, FSR photons are mostly low-energetic and collinear with the momentum of the emitting lepton.

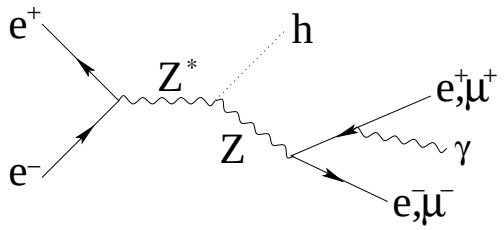

Figure 4.8: Example of a diagram of the Higgs-strahlung process including final state radiation.

Unlike ISR photons, FSR photons are mostly registered in the detector and can, in principle, be accounted for in the event reconstruction. Up to now, such an algorithm is not developed for MarlinReco. We estimate therefore the effects of FSR onto the recoil mass distribution.
First, we exploit that the lepton masses are negligible with respect to their momenta. The Equation (4.6) for $m^2_{\mathrm{di-lepton}}$ can then be simplified by

$$m^2_{\mathrm{di-lepton}} \approx 2(m^2_\ell + E_{\ell^+}E_{\ell^-}(1 - \cos\alpha_{\mathrm{acoll}})) \ , \tag{4.9}$$

where α_{acoll} is the angle between the momenta of the two final state leptons in the ILC reference frame, also referred to as *acollinearity*. We assume that FSR does hardly change the momentum directions of the leptons and that α_{acoll} is therefore unchanged. We denote the FSR photon energies by $K_\pm$, where + and − correspond to the charge of the lepton that emitted the photon, i.e.

$$E_\pm = E_{\ell^\pm} + K_\pm \ .$$

$E_{\ell^\pm}$ are the reconstructed lepton energies. The momentum uncertainties and detector effects are neglected for the moment. The values of $K_\pm$ are assumed to be small appropriate for low-energetic FSR photons. According to Equation (4.4), E_Z and m^2_Z are then given

by

$$
\begin{aligned}
E_Z &= E_{\ell^+} + E_{\ell^-} + K_+ + K_- = E_{\text{di-lepton}} + K_+ + K_- \ , \\
m_Z^2 &= 2\big(m_\ell^2 + E_{\ell^+}E_{\ell^-}(1-\cos\alpha_{\text{acoll}})\big) + 2(E_{\ell^+}K_- + E_{\ell^-}K_+ + K_+K_-)(1-\cos\alpha_{\text{acoll}}) \\
&= m_{\text{di-lepton}}^2 + 2(E_{\ell^+}K_- + E_{\ell^-}K_+ + K_+K_-)(1-\cos\alpha_{\text{acoll}}) \ .
\end{aligned}
$$

where $E_{\text{di-lepton}}$ and $m_{\text{di-lepton}}$ are defined in Equation (4.6). Solving Equation (4.2) for m_h^2 and inserting the above expressions for E_Z and m_Z results in

$$
m_h^2 = m_{\text{recoil}}^2 + 2\big((E_{\ell^+}K_- + E_{\ell^-}K_+ + K_-K_+)(1-\cos\alpha_{\text{acoll}}) - \sqrt{s}(K_+ + K_-)\big) \ ,
$$

where m_{recoil} was defined in Equation (4.7). This expression is not very conclusive, but it holds $E_{\ell^\pm} < E_\pm < \sqrt{s}/2$.[6] We set therefore arbitrarily $K_+ = 0$ and obtain

$$
m_h^2 = m_{\text{recoil}}^2 + \underbrace{2\big((E_{\ell^+}(1-\cos\alpha_{\text{acoll}}) - \sqrt{s})K_-\big)}_{<0} \ .
$$

In this case, we get $m_h^2 \leq m_{\text{recoil}}^2$, since $1-\cos\alpha_{\text{acoll}} \leq 2$. Therefore, we assume that FSR generally causes a migration of the recoiled mass to larger values and enhances therefore the right-hand side tail of the recoil mass distribution. The plots in Figure 4.7 confirm this estimate.

Momentum Reconstruction Uncertainties

When the final state leptons move through the detector they interact with the detector medium as explained in Section 1.2. The energy losses diminish gradually the momentum of the particle traversing the detector. However, depending on the trajectory model used in the reconstruction, the energy loss can be accounted for as is done in the Kalman filter based track reconstruction algorithm of MarlinReco. Otherwise, a systematic underestimation of the particle momentum occurs, as is still the case for electrons when bremsstrahlung losses are not accounted for in the track reconstruction. Such a bias has a similar effect on the recoil mass distribution as FSR.
Since the energy deposition is a stochastic process there is a random component in the momentum reconstruction as pointed out in Section 3.2. The influences of these stochastic momentum reconstruction uncertainties on the recoil mass distribution are difficult to quantify analytically since the polar angle of the Z boson as well as the polar and azimuthal angles of one final state lepton are still free parameters. Using Mokka for the transport of particles through the detector, and using the reconstruction tools Marlin and MarlinReco, one obtains the histogram drawn with a blue line in the two top and the left-hand bottom plots in Figure 4.7. Qualitatively, a Gaussian-like broadening and

[6] Note that in the on-shell situation $E_+ + E_- = E_Z = \frac{s+M_Z^2-M_h^2}{2\sqrt{s}} < \frac{\sqrt{s}}{2}$ for $M_h > M_Z$.

a reduction of the peak are observed. This is the reason why the parametrization of the recoil mass distribution as will be introduced below contains a Gaussian contribution.
A lengthy and rather complicated calculation for one special case as worked out in Appendix C, in which the Z boson and lepton polar angles are equal to $\pi/2$, yields an analytical formula for the recoil mass uncertainty, which is the standard deviation of the recoil mass peak and also called *recoil mass resolution*,

$$(\Delta m_{\text{recoil}})^2 = \frac{E_Z^4}{8M_h^2}\left(\left(\frac{E_Z}{2}(1-\cos\alpha_{\text{acoll}})-\sqrt{s}\right)^2(\Delta p_\perp^{-1})^2+\sin^2\alpha_{\text{acoll}}\,(\Delta\phi_0)^2\right) . \quad (4.10)$$

For $\sqrt{s} = 250$ GeV and $M_h = 120$ GeV, and for $\Delta p_\perp^{-1} = 10^{-4}$ GeV^{-1} and $\Delta\phi_0 = 0.05$ mrad as results from Section 3.2, we obtain therefore

$$\Delta m_{\text{recoil}} = 0.661 \text{ GeV} . \quad (4.11)$$

Here was assumed that $m_{\text{di-lepton}} \approx M_Z$ and $m_{\text{recoil}} \approx M_h$ in the on-shell situation. There is no dependency on the uncertainty of the polar angle measurement of the leptons in this specific case. The acollinearity is equal to about 108° as was found in Equation (C.1) in Appendix C.1. The recoil mass uncertainty, Equation (4.10), is fast growing with E_Z, i.e. also with $\sqrt{s}$, causing the large width of the recoil mass peak at 500 GeV, demonstrated by the right-hand bottom plot of Figure 4.7.

Beam Energy Spread

The beam energy spread, $\Delta E^{\text{e}}_{\text{beam}}$ and $\Delta E^{\text{p}}_{\text{beam}}$, causes a distribution of the cms energy as outlined above. We neglect ISR and beamstrahlung, and assume a Gaussian distribution of the cms energy

$$\sqrt{s'} \sim G(\sqrt{s'}, \sqrt{s}, \Delta\sqrt{s}) ,$$

where the nominal energy, $\sqrt{s}$, is the mean value. The standard deviation is given by $\Delta\sqrt{s} = \sqrt{(\Delta E^{\text{e}}_{\text{beam}})^2 + (\Delta E^{\text{p}}_{\text{beam}})^2}$, using Gaussian error propagation.
Inserting E_Z from Equation (4.2) as $E_{\text{di-lepton}}$ with $\sqrt{s} \to \sqrt{s'}$ replaced into Equation (4.7), and assuming again the on-shell situation, we obtain

$$m^2_{\text{recoil}} = s + M_Z^2 - \sqrt{s}\frac{s' + M_Z^2 - M_h^2}{\sqrt{s'}} .$$

The recoil mass resolution is therefore

$$\Delta m_{\text{recoil}} = \frac{s}{2M_h}\left(1+\frac{M_h^2 - M_Z^2}{s}\right)\frac{\Delta\sqrt{s}}{\sqrt{s}} , \quad (4.12)$$

where we inserted the mean values $m_{\text{recoil}} \approx M_h$ and $\sqrt{s'} \approx \sqrt{s}$. If one ignores beamstrahlung, ISR, FSR and the momentum reconstruction uncertainties, the beam energy spread leads to distribution of the recoil mass around M_h, the standard deviation of which

grows with $\sqrt{s}$, provided that $\Delta\sqrt{s}/\sqrt{s} = const.$ For $\sqrt{s} = 250$ GeV, $M_h = 120$ GeV and a beam energy spread of about $\Delta\sqrt{s}/\sqrt{s} = 10^{-3}$ [146] results in

$$\Delta m_{\text{recoil}} = 0.286 \text{ GeV} .$$

The beam energy spread was not included in the following analysis although it represents already a non-negligible contribution to the uncertainty of Higgs recoil mass measurement at $\sqrt{s} = 250$ GeV.[7] Figure 4.9 shows the estimated uncertainty of the Higgs recoil mass according to Equations (4.10) and (4.12) in the cms energy range between 210 GeV and 500 GeV, and the sum of both contributions.

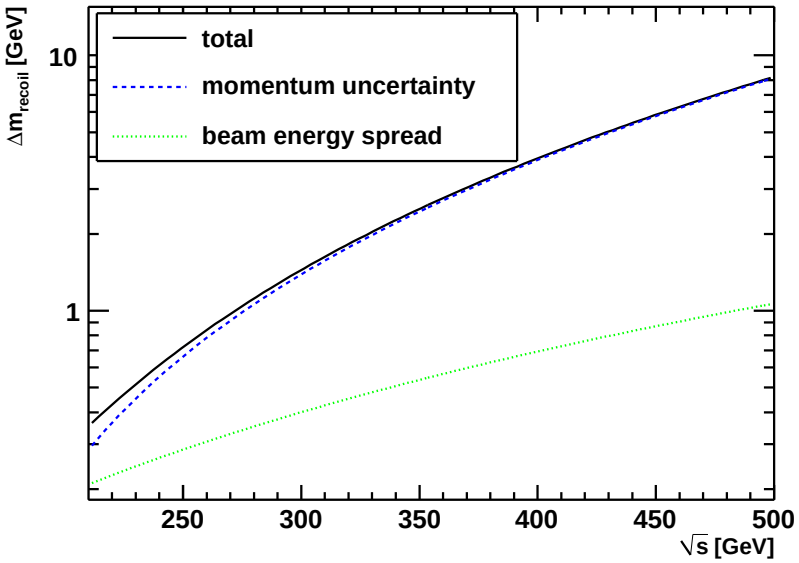

Figure 4.9: Recoil mass uncertainty due to momentum uncertainty (dashed blue), beam energy spread (dotted green) and total uncertainty (black solid).

4.1.5 Determination of the Higgs Boson Pole Mass from the Recoil Mass Distribution

Once a recoil mass distribution for the Higgs-strahlung process is obtained from the experiment, it is desired to determine the Higgs boson pole mass, M_h. If an analytical formula can be derived in terms of M_h describing the recoil mass distribution, which includes all physical and accelerator and detector related effects, a parameter fit of this formula to the distribution can be performed to obtain M_h. However, it is usually not possible to find such a function analytically, since the various impacts of the effects on the recoil mass

[7] For values of $\sqrt{s}$ less than 250 GeV one has to account for it, because the actual relative beam energy spread grows for decreasing $\sqrt{s}$ [146].

distribution are rather complicated. The describing function can therefore be obtained in an approximate way by Monte-Carlo simulations only.
Another possibility is a reasonable, but heuristic parametrization. The Higgs recoil mass distribution is parametrized by

$$s(m_{\text{recoil}}) = F_{\text{Norm}} \begin{cases} \exp\left\{-\frac{(m_{\text{recoil}}-m_0)^2}{2(\Delta m_{\text{recoil}})^2}\right\} & : m_{\text{recoil}} < m_0 \ , \\ \beta \exp\left\{-\frac{(m_{\text{recoil}}-m_0)^2}{2(\Delta m_{\text{recoil}})^2}\right\} + (1-\beta)\exp\left\{-\frac{m_{\text{recoil}}-m_0}{\lambda}\right\} & : m_{\text{recoil}} > m_0 \ . \end{cases} \tag{4.13}$$

Herein, m_0 is the central recoil mass peak position. In the ideal case, it is equal to M_h. The recoil mass resolution Δm_{recoil} characterizes the width of the recoil mass peak caused by the Gaussian-like broadening due to amongst others the momentum measurement. The exponential contribution on the right-hand side, and therein the parameter λ, describe the tail of the distribution introduced by ISR, FSR and beamstrahlung. β is the fraction of the Gaussian contribution. F_{Norm} was introduced as normalization constant, to consider $s(m_{\text{recoil}})$ as a probability density function, which is normalized according to

$$\int_0^\infty s(m_{\text{recoil}})\, dm_{\text{recoil}} = 1 \ .$$

Figure 4.10 shows an example of a Higgs recoil mass distribution obtained for $M_h = 120$ GeV. Events are generate using PYTHIA. A full detector simulation and reconstruction is done using MOKKA and MARLIN/MARLINRECO. Beamstrahlung (GUINEAPIG), ISR and FSR are included. A sample of events corresponding to an integrated luminosity of about $L = 500$ fb^{-1} was used. Also shown in the figure is the fitted function given in Equation (4.13). The value for m_0 is obtained to be 120.24 ± 0.03 GeV. For the recoil mass uncertainty Δm_{recoil}, we obtained $\Delta m_{\text{recoil}} = 0.665 \pm 0.025$ GeV, which is in remarkable agreement with our estimate for Δm_{recoil} due to the momentum measurement uncertainty Equation (4.11).
The question arises whether m_0 can be identified with M_h. Beamstrahlung, ISR and FSR introduce a bias such that m_0 is systematically larger than M_h. This ratio, m_0/M_h, should be one if there is no bias. However, for a cms energy of 250 GeV, we find for the ratio $m_0/M_h \approx 1.002$ for the μ- and 1.004 for the e-channel. For cms energies of 350 and 500 GeV the ratio increases to 1.013 (1.026) and 1.026 (1.058) for the μ- (e-) channel, respectively. This deviation of m_0 from M_h exceeds already the statistical uncertainty, $\Delta_N m_0$, of m_0 for an integrated luminosity of $L = 500$ fb^{-1}. The bias depends on $\sqrt{s}$ and is the larger, the farther away $\sqrt{s}$ is from the production threshold. The larger bias in the e-channel may be explained by the tails in the electron momentum measurement due to bremsstrahlung inside the detector.

To avoid the bias the maximum likelihood method can be used. Assume the recoil mass is distributed according to a probability density function $f(m_{\text{recoil}}; M_h)$, which parametrically depends on the Higgs boson pole mass M_h. Then we can construct a likelihood function

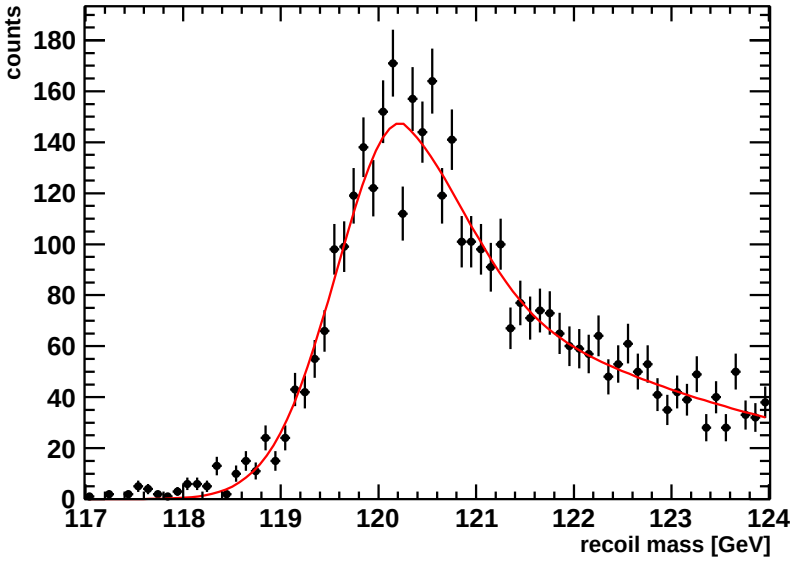

Figure 4.10: Recoil mass distribution as obtained from the Monte-Carlo generator PYTHIA after the full detector simulation and reconstruction using MOKKA and MARLIN (black dots), and the fitted parametrization Equation (4.13) (red line).

for a sample $\{m^i_{\text{recoil}}\}$ of recoil mass values,

$$L_h(M_h) = \prod_i f(m^i_{\text{recoil}}; M_h) \ ,$$

which is a function of M_h. For the given recoil mass sample, $L_h(M_h)$ can be maximized with respect to M_h to obtain the most probable value of M_h.[8]
However, the distribution function f is unknown and difficult to obtain from theoretical considerations. Therefore, following the idea of Reference [147], we determine f as function of M_h by Monte-Carlo simulations. For different values of M_h around the expected value[9], $\{M^j_h\}$, high-statistic samples are generated, passed through the full detector simulation and the reconstruction. Finally, for each j a recoil mass distribution is obtained. These are fitted with the parametrization, Equation (4.13), to obtain the parameters m^j_0, $\Delta m^j_{\text{recoil}}$, λ^j and β^j.
We calculate for each Higgs boson mass value M^j_h the likelihood functions using the normalized parametrizations, $s(m_{\text{recoil}}; m^j_0, \Delta m^j_{\text{recoil}}, \lambda^j, \beta^j)$,

$$L_h(M^j_h) = \prod_i s(m^i_{\text{recoil}}; m^j_0, \Delta m^j_{\text{recoil}}, \lambda^j, \beta^j) \ . \tag{4.14}$$

[8] Usually, it is more convenient to minimize $-\ln L_h(M_h)$.

[9] At the LHC, the Higgs boson mass will be measured with sufficient precision to apply this method. Also from the recoil mass peak, one can estimate the relevant mass range.

If the values M_h^j are close enough to $\widetilde{M_h}$, then the graph $(M_j, -\ln L_h(M_h^j))$ should exhibit a parabolic minimum and can be fitted by

$$-\ln L_h(M_h) = \frac{(M_h - \widehat{M_h})^2}{2(\Delta_N M_h)^2} + a \ . \tag{4.15}$$

Herein, $\widehat{M_h}$ denotes the estimate for $\widetilde{M_h}$, and $\Delta_N M_h$ its standard deviation according to

$$\left.\frac{d \ln L_h(M_h)}{dM_h}\right|_{M_h=\widehat{M_h}} = 0 \ , \quad \left. -\frac{d^2 \ln L_h(M_h)}{dM_h^2}\right|_{M_h=\widehat{M_h}} = \frac{1}{(\Delta_N M_h)^2} \tag{4.16}$$

The statistical uncertainty for m_0, which is also related to the statistical uncertainty of the estimate for the Higgs boson mass, $\widehat{M_h}$, depends on the number of events, N_S, used for the analysis and can be estimated by the standard deviation of the recoil mass distribution Δm_{recoil} [148],

$$\Delta_N M_h = \Delta_N m_0 = \frac{\Delta m_{\text{recoil}}}{\sqrt{N_S}} \ . \tag{4.17}$$

$\Delta_N M_h$ characterizes therefore the precision of Higgs boson pole mass determination at a given number of events and a certain recoil mass resolution.

4.1.6 Determination of the Higgs-Strahlung Cross-Section

The cross-section of the Higgs-strahlung process, σ_{hZ}, is obtained in an experiment by Equation (1.30). By counting the events of this process, N_S, we obtain the cross-section by

$$\sigma_{hZ} = \frac{N_S}{L} \ ,$$

with the integrated luminosity L, which characterizes the accelerator properties and the run time of the experiment and is independent of the considered process. In a realistic experiment, it is however unlikely to register all events. Already the gaps in the detector due to the beam pipe lead to a limited *acceptance* of the detector. This and other effects are accounted for by the so-called *selection efficiency*, ε^S,

$$N_S^a = \varepsilon^S N_S \ , \tag{4.18}$$

where N_S^a is the number of accepted events. ε^S is different for each process under consideration and will be therefore different for the e- and the μ-channel of the Higgs-strahlung process. We denote them, hence, by ε_{e}^S and ε_μ^S, respectively. Furthermore, it might depend on the cms energy used in the experiment. ε^S will also depend on any cut used in the event reconstruction. This applies specifically if one only accepts events with recoil masses inside a certain recoil mass range. Such a cut will be necessary as we show in the next section.

The Higgs-strahlung cross-section measured in an experiment is therefore given by

$$\sigma_{hZ} = \frac{N_S^a}{\varepsilon^S L} \,. \tag{4.19}$$

In principle, the selection efficiency can be determined arbitrarily precise by simulation studies. The uncertainty of the measurement of the Higgs-strahlung cross-section is, hence, due to the uncertainties of N_S^a and L,

$$\left(\frac{\Delta\sigma_{hZ}}{\sigma_{hZ}}\right)^2 = \left(\frac{\Delta N_S^a}{N_S^a}\right)^2 + \left(\frac{\Delta L}{L}\right)^2 = \frac{1}{N_S^a} + \left(\frac{\Delta L}{L}\right)^2 \,. \tag{4.20}$$

Herein, it was again assumed that $\Delta N_S^a = \sqrt{N_S^a}$. The ILC baseline value for the luminosity measurement uncertainty is $\Delta L/L = 10^{-3}$. To reach a similar uncertainty for N_S^a, one would need more than 10^6 registered events, which in turn would require an experimental run time of about 10 years at the ILC peak luminosity assuming $\varepsilon^S = 100$ %. We therefore neglect the luminosity uncertainty, and obtain

$$\frac{\Delta\sigma_{hZ}}{\sigma_{hZ}} = \frac{1}{\sqrt{N_S^a}} \,. \tag{4.21}$$

4.1.7 Optimization Study for Precision Measurements

We want to discuss now the question, which cms energy $\sqrt{s}$ is most appropriate for the precise measurement of the Higgs boson mass and the Higgs-strahlung cross-section. An integrated luminosity of $L = 500$ fb^{-1} is assumed in these considerations. The momentum and angle measurement uncertainties are $\Delta(p_\perp^{-1}) = 10^{-4}$ GeV^{-1}, $\Delta\vartheta = 10^{-4}$ rad, $\Delta\phi_0 = 5 \times 10^{-5}$ rad, respectively, as results from Section 3.2. If used, we assume the beam energy spread $\Delta\sqrt{s}/\sqrt{s} = 10^{-3}$. The Higgs boson pole mass is taken to be $M_h = 120$ GeV.
The relative precision of the cross-section measurement depends solely on the number of registered event, Equation (4.21), i.e. on the cross-section itself,

$$\frac{\Delta\sigma_{hZ}}{\sigma_{hZ}} = \frac{1}{\sqrt{\varepsilon^S L \sigma_{hZ}}} \,.$$

The left-hand plot of Figure 4.11 shows $\Delta\sigma_{hZ}/\sigma_{hZ}$ as function of $\sqrt{s}$ using a selection efficiency $\varepsilon^S = 100$ % and the cross-section that was obtained using PYTHIA and is shown in Figure 4.6 (red solid line). That is, ISR and FSR are included. As expected, the relative uncertainty of the cross-section measurement is minimal at the peak value of the cross-section at about $\sqrt{s} \approx 250$ GeV.

The statistical uncertainty of the Higgs boson mass measurement depends on the cross-section as well, but also on the recoil mass resolution, as demonstrated in Equation (4.17),

$$\Delta_N M_h = \frac{\Delta m_{\text{recoil}}}{\sqrt{\varepsilon^S L \sigma_{hZ}}} \,,$$

where Δm_{recoil} includes at least the momentum uncertainty, $\Delta m_{\text{recoil}}^{\text{mom}}$ in Equation (4.10), and the beam energy spread, $\Delta m_{\text{recoil}}^{\text{BES}}$ in Equation (4.12),

$$\Delta m_{\text{recoil}} = \sqrt{(\Delta m_{\text{recoil}}^{\text{mom}})^2 + (\Delta m_{\text{recoil}}^{\text{BES}})^2} \,,$$

The cross-section rises fast at the threshold, therefore reducing the Higgs mass uncertainty. Then, after the cross-section reaches its maximum, it decreases again which increases $\Delta_N M_h$. On the other hand, the recoil mass resolution grows monotonously as can be seen in Figure 4.9. The consequence is a steep minimum in the uncertainty, $\Delta_N M_h$, at $\sqrt{s} \approx 222.5$ GeV, as shown in the right-hand plot of Figure 4.11.

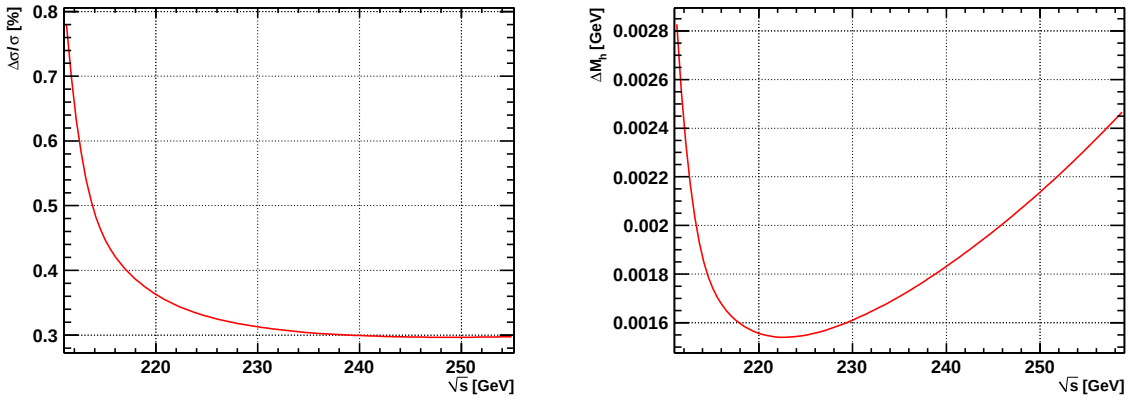

Figure 4.11: The relative cross-section uncertainty for the Higgs-strahlung process (left), and the estimated uncertainty of the Higgs boson mass measurement (right) as function of the cms energy, $\sqrt{s}$, from an analytical calculation. The cross-section of the Higgs-strahlung process was calculated using PYTHIA.

To estimate the effect of the selection efficiency, ε^S, a toy Monte-Carlo was used. First, events were generated using PYTHIA for several values of $\sqrt{s}$. ISR, FSR and the momentum uncertainty were included, and Beamstrahlung and beam energy spread were neglected. In each event the leptons from the Z boson decay were identified using the Monte-Carlo information. The di-lepton energy, the invariant di-lepton mass and the recoil mass were determined according to Equations (4.6) and (4.7). To simulate the selection efficiency, only events with a recoil mass in the range [119 GeV, 122 GeV] were accepted. The cross-section uncertainty obtained by using Equation (4.21) is shown in the left-hand plot of Figure 4.12. It exhibits qualitatively a similar behavior as a function of $\sqrt{s}$ as that in our semi-analytical consideration above. However, looking on the details, the minimum is now shifted down to about $\sqrt{s} = 230$ GeV. The reason is that although the cross-section further grows, more and more event are rejected because the recoil mass is not inside the dedicated mass range due to ISR and FSR. Of course, the absolute value of $\Delta\sigma_{hZ}/\sigma_{hZ}$ is larger than before because only the e- and μ-channel events are used and because of $\varepsilon^S < 100$ %.

The Higgs boson mass uncertainty was estimated. However, only the momentum uncertainty was accounted for so that the recoil mass peak appeared to be a Gaussian distribution here. The standard deviation was determined and multiplied by the relative cross-section uncertainty determined in the previous step. The result is shown in the right-hand plot of Figure 4.12.

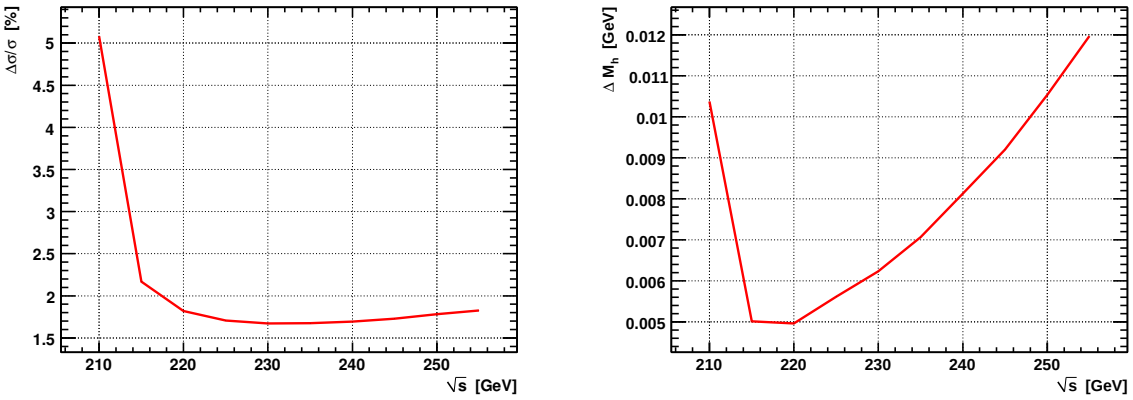

Figure 4.12: The relative cross-section uncertainty for the Higgs-strahlung process (left), and the estimated uncertainty of Higgs boson mass measurement (right) as function of the cms energy, $\sqrt{s}$, from a toy Monte-Carlo study .

Again, the qualitative behavior of ΔM_h as a function of $\sqrt{s}$ is similar that of the above consideration, and in detail, the minimum moved again to the left for the same reasons as for the shift of the cross-section uncertainty curve when accounting for a selection efficiency. The result of this study is that the cross-section can be measured most precisely using $\sqrt{s} \approx 230$ GeV. The impact of $\sqrt{s}$ on the relative precision of the cross-section is not very significant in this range. The Higgs boson mass is most precisely determined at $\sqrt{s} \approx 220$ GeV. The uncertainty grows fast with deviations of $\sqrt{s}$ from 220 GeV. However, the precise minimum position depends on many parameters such as, for instance, selection cuts used in a more realistic simulation.

4.2 Higgs-Recoil Mass Analysis under realistic Conditions

In an experiment, Higgs-strahlung events constitute only a small fraction of the e^+e^- annihilation events recorded by the detector. Hence, we have to define criteria to select Higgs-strahlung events exploiting the decay of the Z boson in an lepton pair of opposite charge. Eventually, there are events of processes other than the Higgs-strahlung process with lepton pairs among the reconstructed final state particles, which look like Higgs-strahlung events. We call these processes *background processes* in contrast to the Higgs-strahlung process, which is hereafter referred to as *signal process*.

We simulated a complete Higgs-recoil mass analysis for an integrated luminosity of $L = 50$ fb^{-1} and for $M_h = 120$ GeV and $\sqrt{s} = 250$ GeV.[10] Signal and Standard Model background events are generated with Monte-Carlo generators including beamstrahlung, ISR and FSR, and are passed through the full detector simulation of MOKKA providing the realistic detector simulation including all interactions of charged and neutral particles detector.
The reconstruction procedure follows after the detector simulation and is performed for all simulation samples as it would be done in a future experiment. The single particle reconstruction is accomplished using the tool MARLIN/MARLINRECO, which operates on the detector hit collections from the sub-detectors and creates a set of reconstructed particles in each event as was described in Section 3.1.
In each event, leptons are searched for and matched to pairs of opposite charge, out of which the invariant di-lepton mass, the di-lepton energy and the recoil mass are determined. The invariant di-lepton mass should be close to the Z boson pole mass, M_Z, if the selected lepton pair originates from a decay of an on-shell Z boson. In cases where more than one lepton pair is found, the pair with the invariant di-lepton mass closest to M_Z is selected.
All events passing pre-selection cuts are used in the following analysis. These cuts are introduced to reduce the number of accepted background events. The upper part of Figure 4.13 summarizes the simulation and reconstruction steps.
After applying the pre-selection cuts, there are still a lot of accepted background events. To further reduce the number of these events, we exploit the difference of the distributions of the variables describing the kinematics of the different processes. These are summarized in Appendix C.3. The same probabilistic case distinction method as was used for the particle identification is utilized for the process distinction. However, here we are not interested in the identification of a specific process, but in the probability of a single event to be a signal event. For this purpose, a cut on the signal likelihood is introduced that acts as a filter, and each event passing it is accepted as signal event. This signal likelihood cut is optimized in a multivariate analysis (MVA) such that as much as possible signal events are accepted and background events rejected.
Both, for the calibration of the case distinction method, i.e. the filling of the histograms representing the PDFs, and for the MVA indicated by the black dashed line in Figure 4.13, the full statistics samples are used. The variable distributions, from which the PDFs are constructed, are smoothed e.g. with a Laplacian smoother or by fitting polynoms of low order. This was done firstly to smooth statistical fluctuations in kinematic regions with low statistics and secondly since a small fraction of the high statistic sample is used as mockup data sample. The reason to follow this procedure was simply a lack of computing time and storage amount for the large event samples. Later, when this analysis is repeated in an actual experiment, the Monte-Carlo samples must have much larger statistics, and, specifically, they should be different for the PDF filling and for the MVA.

[10] We decided to exploit the maximum statistics instead the minimum uncertainty estimate given in the previous chapter. At the ILC, the cross-section of the Higgs-strahlung process will be measured anyway at different $\sqrt{s}$ in the threshold region due to other Higgs physics related topics such as the Higgs boson spin.

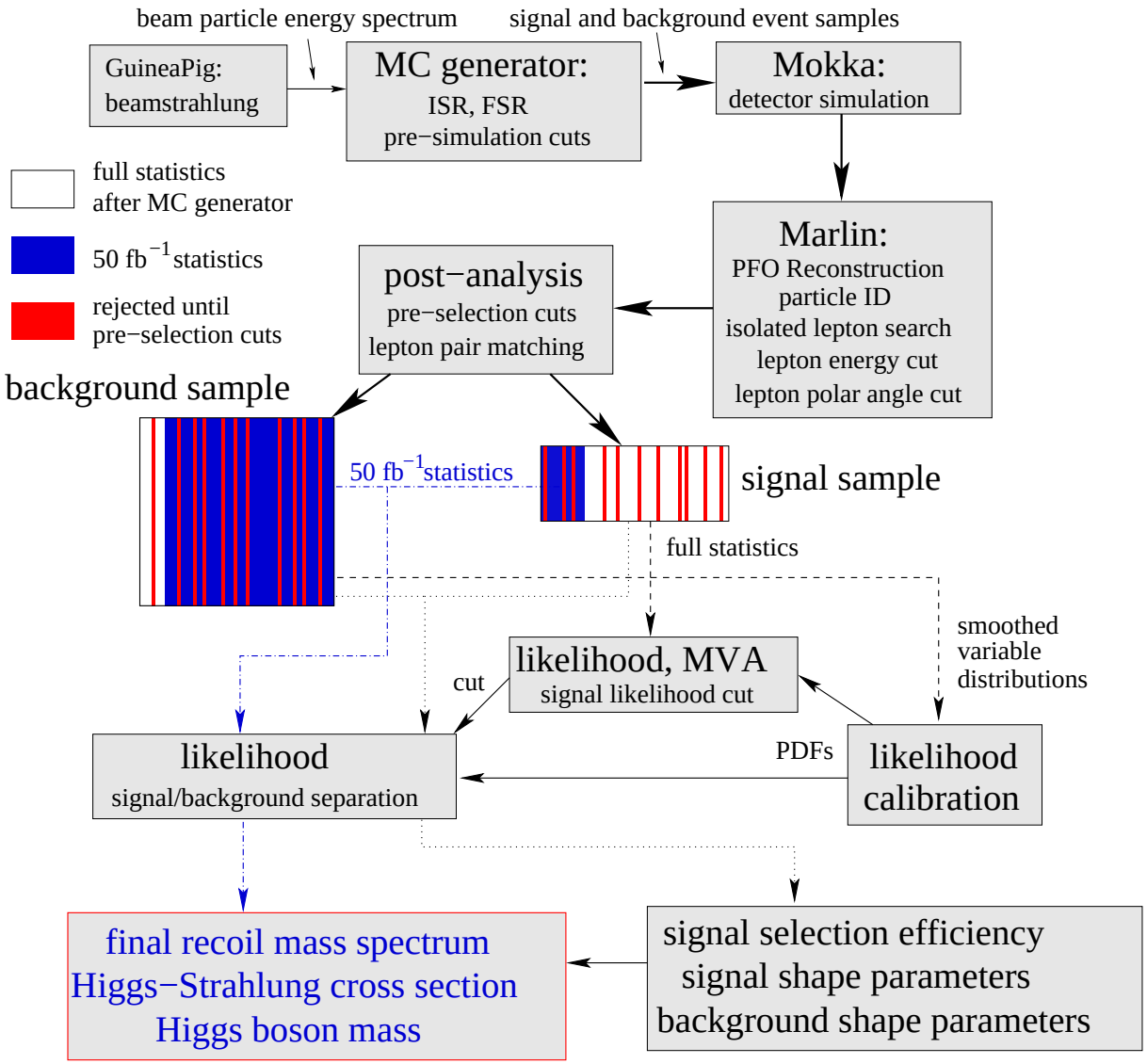

Figure 4.13: Simulation and analysis scheme as described in this section. PFO denotes Particle Flow Object and MVA Multi-Variate Analysis.

The full statistics sample of the signal process is passed through the signal-background separation and the optimized signal likelihood cut to obtain the signal selection efficiency needed for cross-section determination. Likewise, the signal shape parameters such as the recoil mass resolution and tail parameter are determined in this step. Also the full-statistics of the background event sample passes through this analysis chain to obtain the recoil mass background shape parameters. This is indicated by the black dotted line in Figure 4.13. These shape parameters are independent of the Higgs boson mass. They result from known Standard Model processes.
In a final step, a part of the high-statistics Monte-Carlo sample of the signal and background events corresponding to $L = 50$ fb^{-1}, the blue sample boxes in Figure 4.13, is used as 'data

sample', which is passed through the signal-background separation and the likelihood cut. The recoil mass distribution finally obtained is analyzed, and the Higgs boson pole mass, M_h, and the cross-section for the Higgs-strahlung process are determined. This is depicted by the blue chain line in Figure 4.13. In the following subsections, the details of the procedure are described and the results of the analysis are presented.

4.2.1 Search for the Leptons from the Z Boson Decay

From the considerations about the kinematics of the Higgs-strahlung process in the previous section, it is obvious that leptons from the Z boson decay will fly into solid angle regions, which are usually well separated from those into which the Higgs boson decay products fly for $\sqrt{s}$ well above the threshold. We therefore have to look for isolated leptons in an event, where no momentum of another charged particle is inside a solid angle element around the lepton momentum. This solid angle element is most conveniently a cone parametrized by an opening angle. Figure 4.14 illustrates the definition of this cone.

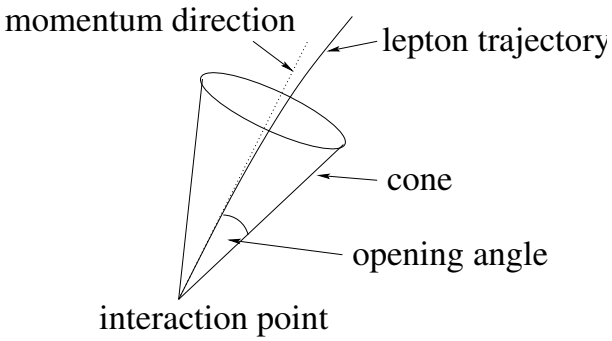

Figure 4.14: Schematics of the definition of a cone for an isolation criterion.

An opening angle of the cone of 10° was found to be the optimum. For larger opening angles, less leptons are accepted reducing the selection efficiency. A smaller opening angle increases the efficiency, but also more isolated leptons are accepted from events of processes other than the Higgs-strahlung process enhancing the background.
The isolation criterion introduced in this manner has the disadvantage that also leptons are rejected if low-energetic charged particles are inside the cone. Particles with energies up to about 5 GeV may appear in the cone from the hadronic decays of the Higgs boson. A modification of the isolation criterion can therefore be the introduction of a limit on the energy, which must not be exceeded by any charged particle inside the lepton cone to accept this lepton as isolated. We investigated an energy cut of 10 GeV and a dynamic cut equal to the energy of the considered lepton. Thereby, the selection efficiency of the signal process was generally increased, but a significant enhancement of the signal above the background was not observed. We summarize the selection efficiencies for the different isolation criteria later in this section.

4.2.2 Background Processes

From the procedure of finding lepton pairs, as described above, we accept events that contain either a reconstructed electron-positron pair or a muon-antimuon pair.

Cross-Sections and Pre-Simulation Cuts

Table 4.1 summarizes the cross-sections and the number of events for all processes, considered as background, and for the Higgs-strahlung process for an integrated luminosity of 50 fb^{-1}. The cross-sections listed below depend on the cuts applied on Monte-Carlo generator level, which we call *pre-simulation cuts*. These are in several cases necessary to reduce the amount of events, which had to be processed, and saving computing time.

No	process	cross-section [fb]	# events (for $L = 50$ fb^{-1})
1	$e^+e^- \to hZ \to X\ell^+\ell^-$	15.02	751
2	$e^+e^- \to e^+e^-$	4144.5	207223
3	$e^+e^- \to \mu^+\mu^-$	4281.0	214050
4	$e^+e^- \to \tau^+\tau^-$	4182.0	209100
5	$e^+e^- \to W^+W^- \to [e,\mu]X$ *)	5650.0	282277
6	$e^+e^- \to e^+e^- f\bar{f}$	475.7	23784
7	$e^+e^- \to \mu^+\mu^- f\bar{f}$	359.4	17970
8	$e^+e^- \to e^+e^-e^+e^-$	24.6	1231
9	$e^+e^- \to \mu^+\mu^-\mu^+\mu^-$	7.2	360
10	$e^+e^- \to e^+e^-\mu^+\mu^-$	177.0	8850

Table 4.1: Cross-sections and number of events for 50 fb^{-1} for signal and background processes in the Higgs recoil mass analysis used. A Higgs boson mass of $M_h = 120$ GeV and a cms energy $\sqrt{s} = 250$ GeV is assumed. ($\ell = e, \mu$; f denotes quarks, neutrinos and tauons; *) specifications for process no. 5 are given in the text)

The cross-sections and the event samples of the processes 1, 3, 4 and 5 were generated using PYTHIA. No extra cuts[11] were applied to the lepton momenta and invariant masses. In process 5 only events were processed with either one lepton, e^-, e^+, μ^+ or μ^-, in the final state, or pairs such as $e^-\mu^-$, $e^-\mu^+$, $e^+\mu^-$ or $e^+\mu^+$. Events with e^+e^- and $\mu^+\mu^-$ pairs were rejected because such events are already accounted for in the processes 6 to 10. An example of such processes is given in Figure 4.15.
The cross-section and the event samples of the Bhabha process, process 2, were produced using BHWIDE. Because of the strong t-channel contribution, the cross-section of this process diverges for small scattering angles. We applied therefore the following pre-simulation cuts to the final state lepton momenta: lepton energy $E_{e^\pm} > 10$ GeV and polar angle of the momentum direction $|\cos\vartheta_{e^\pm}| < 0.985$. To reduce further the large amount of events, we applied additional cuts to the invariant di-electron mass, $|m_{\mathrm{di-lepton}} - M_Z| < 40$ GeV, and to the recoil mass, 90 GeV $< m_{\mathrm{recoil}} <$ 190 GeV.

[11] Default cuts set by PYTHIA are not changed.

The cross-sections and the event samples of the processes 6 to 10 were produced using SHERPA. The reason for using SHERPA was to retain gauge invariance, which might be violated when separating certain processes. Figure 4.15 shows an example for two processes, the amplitudes of which might interfere. However, SHERPA thereby also offers a convenient way to include all relevant background processes with four fermions in the final state. This is the first time that such a complete background was accounted for in such an analysis. The following cuts were applied: the energy of the final state fermions $E_f > 5$ GeV, the polar angle $|\cos\vartheta_f| < 0.985$ and the invariant di-fermion mass $m_{ff} > 5$ GeV.

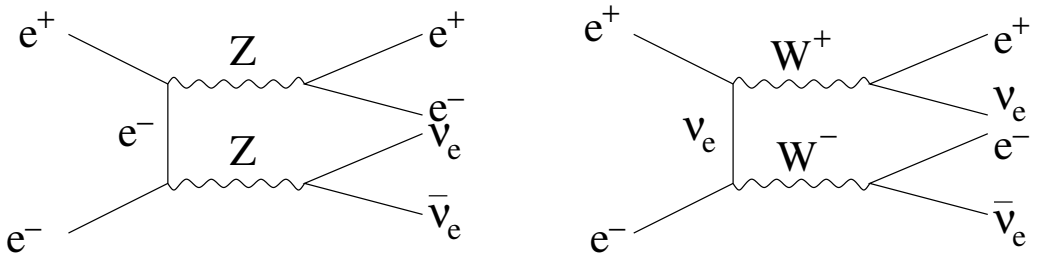

Figure 4.15: Example of processes with four fermion final state, the amplitudes of which might interfere.

The dominant background is the process $e^+e^- \to ZZ$, where one or both Z bosons decay in lepton-antilepton pairs, because both Z bosons are almost on-shell. The invariant di-lepton mass of the accepted lepton-antilepton pair might therefore be close to M_Z. This process is included into the processes 6 to 10.
The Processes 2 and 3 represent also a strong background. The intermediate boson in the s-channel of these processes can be either a photon or a Z boson. In the latter case, the propagator of the Z boson becomes dominant at the momentum $p^2_{Z^*} = M^2_Z$. Therefore, the cross-section becomes enhanced if by ISR emission the effective energy carried by the Z boson is close to M_Z. This mechanism is called *radiative return*. The invariant di-lepton mass is then found to be close to M_Z.
The process 4 and the process $e^+e^- \to W^+W^-$, which is contained in the processes 5, 6 and 7, contribute a background, since there are also leptons in the final state. This background becomes enhanced if pions from hadronic decays fulfill the lepton identification and isolation criteria are combined with another lepton to a lepton-antilepton pair. Fortunately, the invariant di-lepton mass is only by chance close to M_Z. Proper pre-selection cuts can suppress a large fraction of such events.

Pre-Selection Cuts

After the single particle reconstruction the following cuts, for the energy of leptons is required $E_{\ell^\pm} > 15$ GeV for the event reconstruction, and the polar angle of the lepton momentum $|\cos\vartheta_{\ell^\pm}| < 0.95$. When the leptons are matched to pairs, their invariant mass should be close to M_Z. We therefore accept only pairs that pass $|m_{\mathrm{di-lepton}} - M_Z| < 30$ GeV.

We also require the recoil mass to be in the range 100 GeV $< m_{\text{recoil}} <$ 150 GeV, which is the relevant recoil mass range for the signal process with $M_h = 120$ GeV.
We investigated also a cut on the di-lepton polar angle after the lepton-pair matching, $|\cos\vartheta_{\text{di-lepton}}| < 0.9$, which could specifically suppress the background of processes 2 and 3. The cross-sections of these processes rise strongly near $|\cos\vartheta_{\text{di-lepton}}| = \pm 1$ as is shown in the right plot of Figure 4.16.
These pre-selection cuts are tighter than the pre-simulation cuts and are necessary in order that the final analysis result does not depend on the pre-simulation cuts. This corresponds to the application of the pre-selection cuts in an experiment regardless of which process happened.

4.2.3 Signal-Background Separation

Since only the final state particles are detected, there is in principle no chance to conclude, which process exactly caused this final state when considering a single event in an experiment. Specifically, one cannot say whether it was a Higgs-strahlung process event or any of the background events. One can only make a probabilistic statement about the hypothesis that an event registered in the detector was a signal event based on the reconstructed quantities. These are usually not discrete but different from event to event even for the same process. We therefore have to consider and use the distributions of these variables, which might be different for the signal and the background processes.
The seven variables used here for the probabilistic process distinction are the lepton polar angles, the acollinearity and acoplanarity of a lepton pair, the invariant di-lepton mass, the di-lepton angle and the missing transverse momentum. They are defined in Appendix C.3. Figures 4.16 and 4.17 show examples of the distributions of some of these variables for the signal process, the process $\mathrm{e^+e^-} \to \ell^+\ell^-$ and the process $\mathrm{e^+e^-} \to \ell^+\ell^- f\bar{f}$, where f might be any fermion and $\ell = e, \mu$ according to which lepton pair was pre-selected.
We investigated the impact of two-dimensional distributions on the distinction performance as described in Appendix A, and found that we obtained the best results, that is the smallest cross-section uncertainties, with one-dimensional distributions for the e-channel, and with two-dimensional distributions for the μ-channel, although the differences are not significant. One can clearly observe correlations between the variables in the two-dimensional distributions.
Using these distributions, one can construct the PDFs and the likelihood according Equations (A.5) and (A.6) similar to the case of the particle identification. The likelihood distributions for the signal and the two background cases are shown for the signal process sample in Figure 4.18, and for the background sample $e^+e^- \to \ell^+\ell^- f\bar{f}$ in Figure 4.19, separately for the cases with accepted electron-positron pairs and muon-antimuon pairs, respectively. The usage of two-dimensional distributions leads to a stronger binary behavior of the likelihood. That is, the probability in a single event to be a signal becomes almost either one or zero. This is in contrast to using one-dimensional distributions, where the likelihood is smoothly distributed over the range $[0, 1]$.

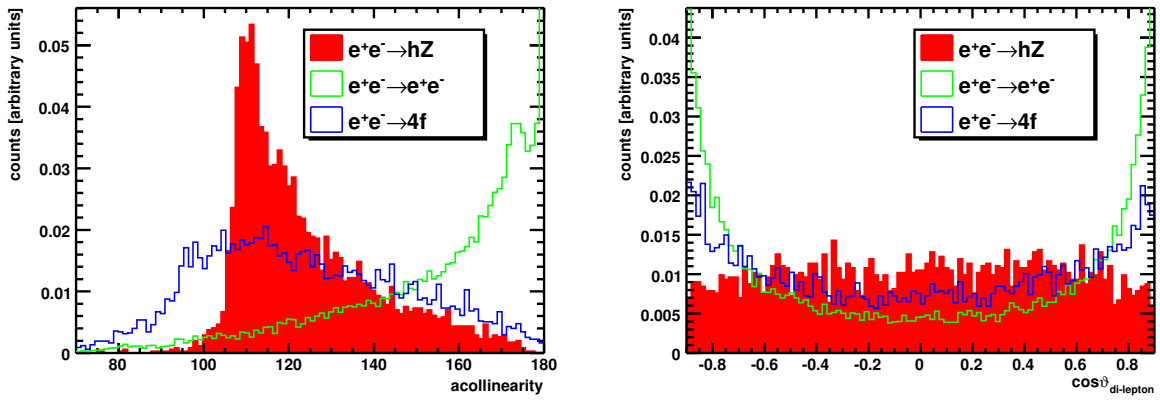

Figure 4.16: One-dimensional distributions of the acollinearity (left) and the di-lepton polar angle, $\cos\vartheta_{\mathrm{di-lepton}}$, (right) for the e-channel of the signal process (red), $\mathrm{e^+e^-} \to \mathrm{e^+e^-}$ (green) and for $e^+e^- \to \mathrm{e^+e^-}f\bar{f}$ (blue).

In contrast to the particle identification, we are not interested in the most probable process for a given event. Instead, we use the case distinction method to maximize the statistical significance of the Higgs recoil mass peak above the rather unstructured background by introducing a cut on the signal likelihood.
Most of the recoil mass values of the Higgs-strahlung events are concentrated inside the recoil mass range [119 GeV, 125 GeV]. The number of accepted signal process events is N_S^a, that of accepted background events we denote by N_B^a. If N_S^a is considered as the expected number of accepted signal events, the standard deviation of the total number of accepted events is given by $\sqrt{N_S^a + N_B^a}$, assuming that a Gaussian distribution is appropriate for $N_S^a + N_B^a$. We define the *significance* as the ratio [148, 126]

$$S = \frac{N_S^a}{\sqrt{N_S^a + N_B^a}} \,. \tag{4.22}$$

S depends on the cut that is applied to the signal likelihood. Maximizing S with respect to this cut, we optimize the cut to accept more signal events while reducing the number of accepted background events. The inverse of the significance is the uncertainty of the Higgs-strahlung cross-section measurement. Therefore, a maximization of the significance corresponds to a minimization of the cross-section measurement uncertainty.
Figure 4.20 shows the inverse significance as function of the signal likelihood cut for the e-channel and the μ-channel. The largest value for S was obtained in the e-channel, for a likelihood cut of about 0.65. It was also required for the di-lepton angle $|\cos\vartheta_{\mathrm{di-lepton}}| < 0.9$ and using the isolation criterion, where particles are allowed to be inside the cone with an energy $E < 10$ GeV. For the μ-channel, the largest significance was obtained for a likelihood cut of 0.93. Here, we allowed particles inside the isolation cone with an energy smaller than the muon energy. All results shown here refer to these both cases.
In the described process distinction method, no Higgs-strahlung μ-channel event was reconstructed with an $\mathrm{e^+e^-}$ pair and accepted after all the cuts and the case distinction, and

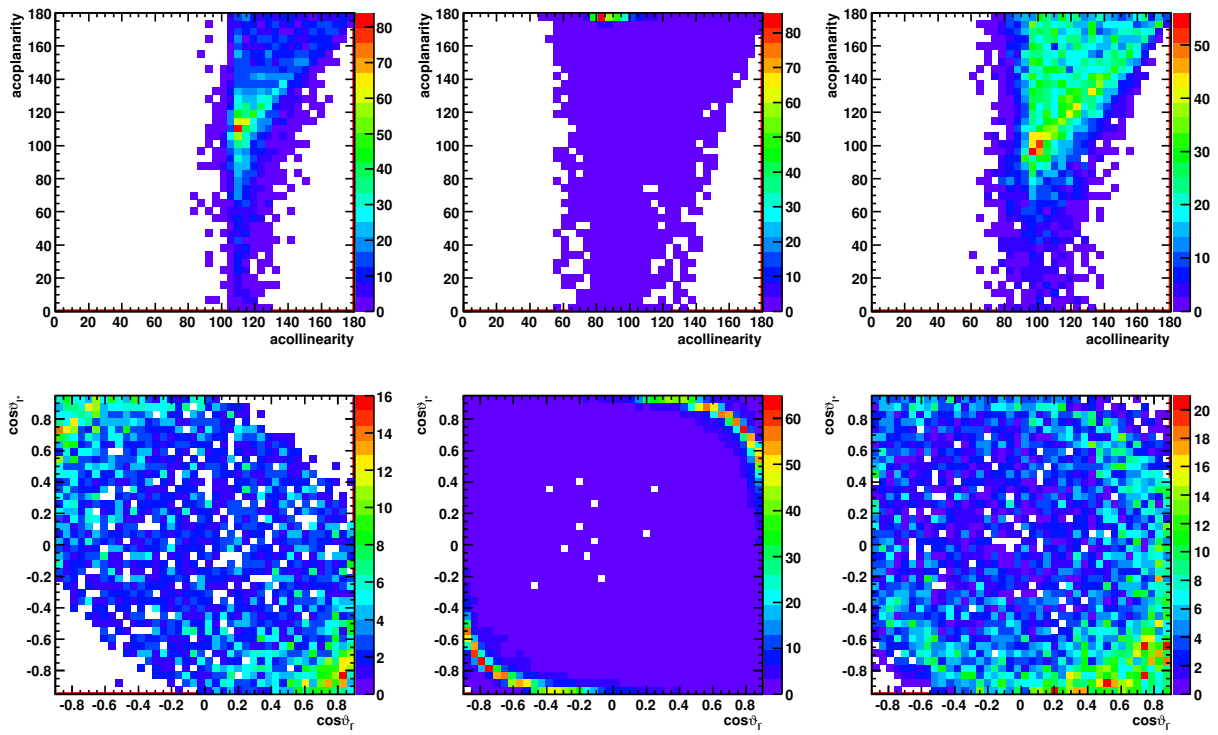

Figure 4.17: Two-dimensional distributions for acoplanarity vs acollinearity (top) and for $\cos\vartheta_{\ell^+}$ vs $\cos\vartheta_{\ell^-}$ (bottom) each for the signal process (left), $e^+e^- \to \mu^+\mu^-$ (center) and for $e^+e^- \to \mu^+\mu^- f\bar{f}$ (right).

vice versa. How many of the lepton pairs from the Z boson decay are indeed correctly selected and assigned to the Z boson, was not separately investigated.

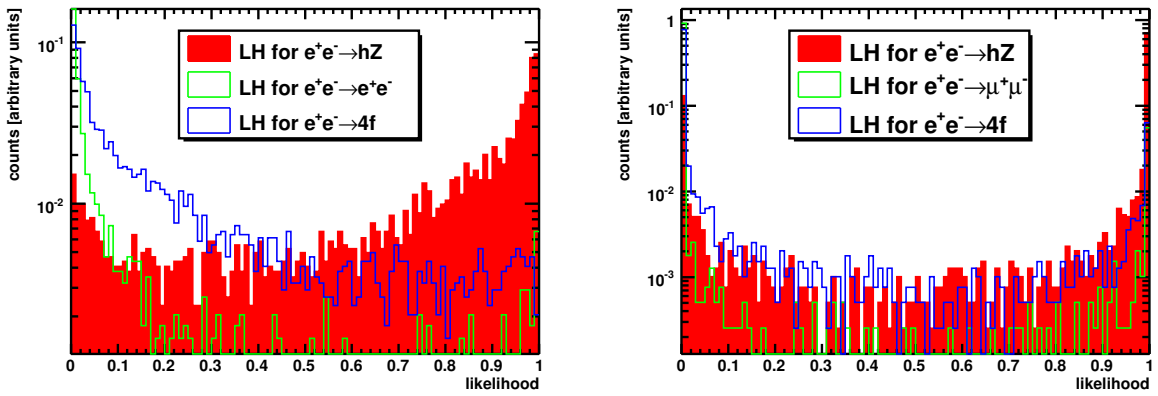

Figure 4.18: Likelihood distributions for the signal process for e^+e^- pairs (left) and $\mu^+\mu^-$ pairs (right). The latter one used 2D distributions. The blue and green lines indicate the likelihood for being a background process, either $e^+e^- \to \ell^+\ell^-$ (blue), or $e^+e^- \to \ell^+\ell^- f\bar{f}$ (green). The histogram (red, filled) represents the signal likelihood.

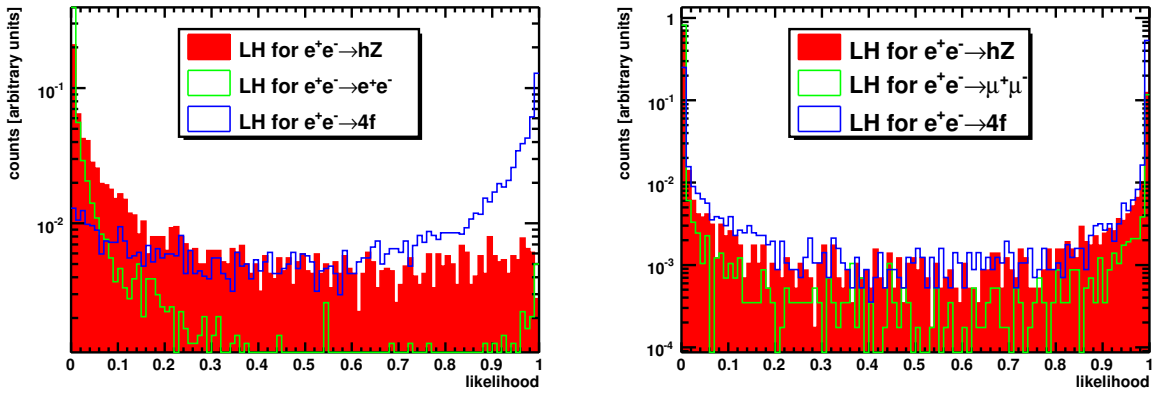

Figure 4.19: Likelihood distributions for the processes $e^+e^- \to \ell^+\ell^- f\bar{f}$ for the e-channel (left) and the μ-channel (right). The red filled histogram is the likelihood for $e^+e \to hZ \to X\ell^+\ell^-$. The green and blue histograms are the likelihoods for $e^+e^- \to \ell^+\ell^-$ and $e^+e^- \to \ell^+\ell^- f\bar{f}$, respectively.

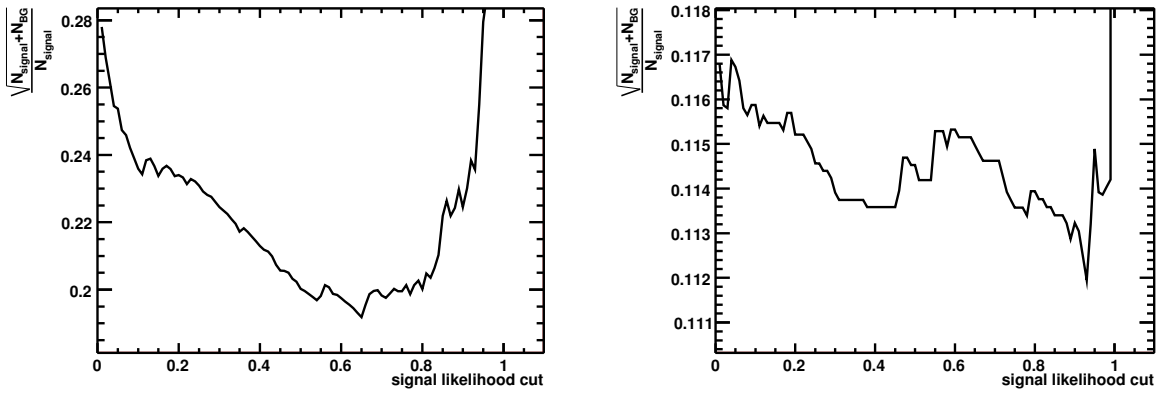

Figure 4.20: The inverse of the significance, S^{-1}, as a function of the signal likelihood cut for the e-channel (left) and for the μ-channel (right).

4.2.4 Signal Selection Efficiency

Selection Efficiency and Background Fractions

Table 4.2 summarizes the selection efficiencies for the signal and background processes, separately, at the different analysis stages for the different isolation criteria. After the reconstruction using MARLIN, the isolated lepton search and the lepton pair matching only the cuts on the lepton polar angle were applied. After the application of the probabilistic case distinction including the likelihood cut, the pre-selection cuts have been applied.[12] At the end of the analysis, denoted by the term 'final' in the table, the cut on the recoil mass was made stricter, 119 GeV $< m_{\text{recoil}} <$125 GeV, for performing the significance maximization.

analysis stage	empty cone		cone $E < 10$ GeV		cone $E < E_{\text{lepton}}$	
	e-channel	μ-channel	e-channel	μ-channel	e-channel	μ-channel
signal process (5018 events in the in e-channel and 4982 events in the μ-channel)						
after MARLIN	62.11 %	68.55 %	74.17 %	78.34 %	76.82 %	79.23 %
after likelihood	-	-	44.50 %	-	-	59.51 %
final	-	-	22.18 %	-	-	42.57 %
background processes (1019800 processed background events)						
after MARLIN	4.54 %	1.52 %	4.94 %	1.58 %	5.73 %	1.60 %
after likelihood	-	-	0.13 %	-	-	0.09 %
final	-	-	0.02 %	-	-	0.01 %

Table 4.2: Selection efficiencies for the signal process and the background processes for different isolation criteria and at different analysis stages. $E < 10$ GeV corresponds to 'no further particle inside the lepton cone with energy larger than 10 GeV' and $E < E_{\text{lepton}}$ to 'no further particle inside the lepton cone with energy larger than the lepton energy'.

The signal selection efficiencies for the μ-channel are after each step larger than that for the e-channel. The different isolation criteria result in a difference in the selection efficiencies of about 10 % for the signal process. About 5 % of all background events remain in the e-channel, about 1.5 % in μ-channel. For different lepton isolation criteria, the differences are less than 1 %. In spite of the significant increase the in the signal selection efficiency for the $E < E_{\text{lepton}}$ criterion with simultaneously a not so large increase of the background selection efficiency, the differences in the significance are rather small. The reason is that a lot of events are rejected by the process distinction and the stricter recoil mass range cut such that the final selection efficiencies are similar.

Signal Selection Efficiency versus Higgs boson Decay Mode

We have to check whether the signal selection efficiency is indeed independent of the Higgs decay modes. We generated therefore for each relevant decay mode of the Standard Model

[12] For electrons also the cut $|\cos\vartheta_{\text{di-lepton}}| < 0.9$ was applied.

Higgs boson samples with $N_S = 10000$ events separately for both the e-channel and the μ-channel of the Z boson decay. These samples are passed through the full simulation, reconstruction and analysis chain including the probablistic case distinction procedure, and the same pre-selection cuts where applied as for the significance study. Solely, for the e-channel we used here the $E < E_{\text{lepton}}$ isolation criterion as for the μ-channel and no cut on the di-lepton angle. The selection efficiency should be therefore larger than for the case considered above. This is however not relevant here.
The selection efficiencies are calculated by Equation (4.18). The Gaussian error propagation is used to estimate the statistical uncertainties of the obtained efficiencies, where N_S has no uncertainty and the number of accepted events, N_S^a, is binomially distributed with N_S trials in total and a single success probability of ε^S. We assume that the expectation value is given by the value of N_S^a found in each channel. The variance of N_S^a is then given by $(\Delta N_S^a)^2 = N_S \varepsilon^S (1 - \varepsilon^S)$, and we obtain the selection efficiency uncertainty by

$$\Delta\varepsilon^S = \frac{\Delta N_S^a}{N_S} = \frac{\sqrt{N_S \varepsilon^S (1-\varepsilon^S)}}{N_S} = \sqrt{\frac{\varepsilon^S (1-\varepsilon^S)}{N_S}} \,.$$

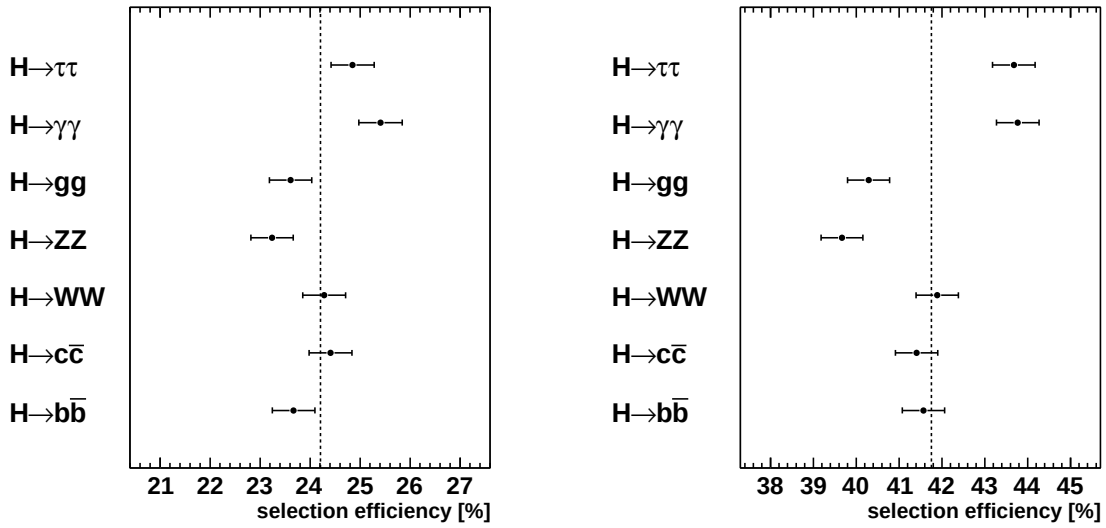

Figure 4.21: Selection efficiencies for different decay modes of the Standard Model Higgs boson for the e-channel (left) and the μ-channel (right).

Figure 4.21 shows the signal selection efficiency for the considered Higgs decay channels, separately for both the e- and the μ-channel of the Higgs-strahlung process. Within the precision of this study, there are slight differences of ε^S for the different Higgs decay channels. It is the isolation criterion, which might introduce a slight dependency on the Higgs decay mode. If the Higgs boson decays into two photons the Higgs-strahlung reconstruction efficiency is higher since photons are ignored in the Z boson reconstruction. By contrast, the Z bosons from the Higgs decay mode $h \to ZZ$ decay also into leptons, which are

incorporated in the lepton search and lepton pair matching. Such lepton pairs have an invariant close to M_Z and might be selected, but the recoil mass does not necessarily coincide with the Higgs boson mass. Such events are therefore rejected and the selection efficiency diminished.

The result is that the selection efficiency depends on the Higgs decay mode with differences of a few percent. The mean signal selection efficiency as obtained in Table 4.2 is a weighted average over the single selection efficiencies with the branching fractions as weight. In the subsequent determination of the cross-section and the Higgs-boson mass we assumed a certain Higgs model, here the Standard Model Higgs boson, and the correct branching fractions to obtain the correct signal selection efficiency, which can be in principle arbitrarily precise.

The impact of the systematic uncertainty of the signal selection efficiency on the measurements of Higgs-strahlung cross-section and the Higgs boson mass might be small, if it is much smaller than the relative uncertainty of the number of accepted events. If we, however, assume that the signal selection efficiencies move on a 2 % level, i.e. between the efficiency of the $h \to \gamma\gamma$ decay mode and that of the $h \to ZZ$, then we find the relative uncertainty of the selection efficiency to be already of the order 10 %, which is a systematic uncertainty. We need to add $(\Delta\varepsilon^S/\varepsilon^S)^2$ to Equation (4.20), which causes an uncertainty of Higgs-strahlung cross-section of at least 10 %. That is, assuming no specific Higgs model limits the cross-section measurement precision. The precision of the Higgs boson pole mass measurement is therefore also changed, as discussed in Section 4.1.7.

Summary of Signal Selection Efficiencies

The signal selection efficiencies necessary for the calculation of the Higgs-strahlung cross-section with the 50 fb^{-1} sample, are given for the recoil mass interval 119 GeV $< m_{\text{recoil}} <$ 125 GeV by

$$\begin{aligned} \varepsilon_{\text{e}}^S &= (22.18 \pm 0.59)\ \% \text{ for the e-channel, and} \\ \varepsilon_{\mu}^S &= (42.57 \pm 0.70)\ \% \text{ for the } \mu\text{-channel .} \end{aligned} \tag{4.23}$$

For the recoil mass range, 100 GeV $< m_{\text{recoil}} <$ 150 GeV, i.e. after the pre-selection cuts, we find

$$\begin{aligned} \varepsilon_{\text{e}} &= (44.50 \pm 0.70)\ \% \text{ for the e-channel, and} \\ \varepsilon_{\mu} &= (59.51 \pm 0.70)\ \% \text{ for the } \mu\text{-channel .} \end{aligned} \tag{4.24}$$

The uncertainties are here only formally mentioned. In principle, one can determine the selection efficiencies with smaller uncertainties by using higher statistics. We assume therefore in the following a negligible uncertainty for the selection efficiencies.

4.2.5 Higgs-strahlung Cross-Section and the Higgs Boson Pole Mass

Final recoil mass distributions as obtained after the full reconstruction and the probabilistic process distinction including all pre-selection cuts are shown in Figure 4.22 for 50 fb^{-1} for the e-channel and the μ-channel. The Higgs recoil mass peak is clearly visible above the rather unstructured background for both channels. As expected from the previous discussion, the Higgs recoil peak in the μ-channel is more pronounced than in the e-channel. In a first step we fitted the distributions. The parametrization, Equation (4.13), was used for the description of Higgs recoil mass peak. The normalization was chosen such that $s(m_{\text{recoil}})$ is normalized on the interval [100 GeV, 150 GeV]. The background was parametrized by a polynomial of second order, $b(m_{\text{recoil}})$, which is also normalized on this interval

$$\int_{100\ \text{GeV}}^{150\ \text{GeV}} b(m_{\text{recoil}})\, dm_{\text{recoil}} = 1\ .$$

Both, the shape parameters β, Δm_{recoil} and λ of the signal function and the remaining free coefficients of the background parametrization were determined with a higher statistic sample, and then kept fix.
The function that describes the total recoil mass distribution including the background is then given by

$$f(m_{\text{recoil}}) = N_S^a \cdot s(m_{\text{recoil}}) + N_B^a \cdot b(m_{\text{recoil}})\ , \tag{4.25}$$

where N_S^a and N_B^a are the accepted events with a recoil mass in the range [100 GeV, 150 GeV]. The free parameters to be fitted are N_S^a, N_B^a and m_0. The results of the fits are shown as well in Figure 4.22.

Determination of the Higgs-Strahlung Cross-Section

The cross-section of the Higgs-strahlung process is determined using Equation (4.19) for e- and μ-channel separately. For the 50 fb^{-1} sample, there were 751 Higgs-strahlung events, 396 of them in the e-channel and 355 in the μ-channel. As outlined above, the signal and background events with a recoil mass in the range [119 GeV, 125 GeV] were counted. In the e-channel, $N_S^a = 88$ signal events and $N_B^a = 197$ background events are finally accepted. In the μ-channel, there are $N_S^a = 156$ signal events and $N_B^a = 149$ background events accepted. Using the signal selection efficiencies from Equation (4.23), we obtain, thus, the cross-sections of the Higgs-strahlung process with the leptonic Z boson decays, σ_{hZ}^{e} and σ_{hZ}^{μ},

$$\sigma_{hZ}^{\text{e}} = 7.94\ \text{fb} \qquad \text{and} \qquad \sigma_{hZ}^{\mu} = 7.33\ \text{fb}\ . \tag{4.26}$$

The relative uncertainty is the inverse significance, as mentioned earlier,

$$\frac{\Delta\sigma_{hZ}}{\sigma_{hZ}} = \frac{\sqrt{N_S^a + N_B^a}}{N_S^a}\ ,$$

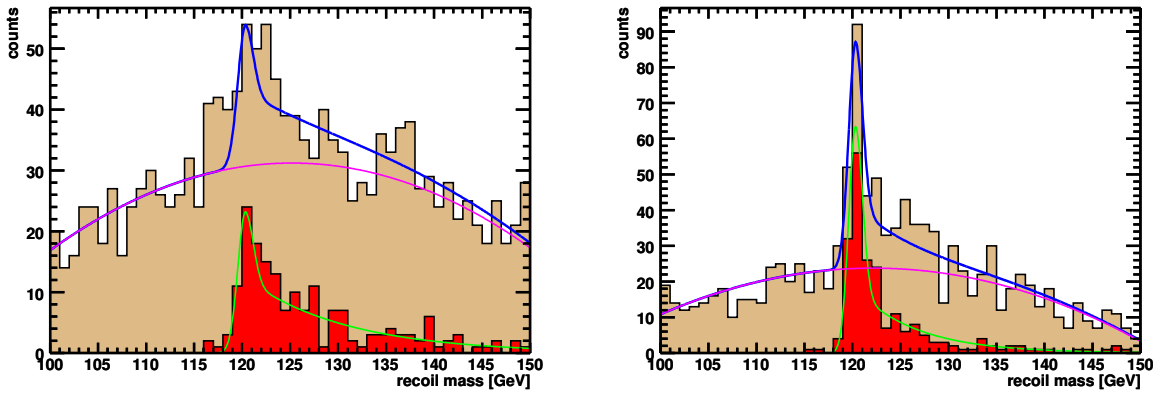

Figure 4.22: Final recoil mass distributions for the e-channel (left) and the μ-channel (right) including signal and background events. The red filled histogram in the foreground is the recoil mass distribution from the Higgs-strahlung events only. The blue curve is the fitted $f(m_{\text{recoil}})$, Equation (4.25). The green curve is the fitted signal parametrization, Equation (4.13), and the violet curve is the fitted second order polynomial, which parametrizes the background shape.

since $\sigma_{hZ} \propto N_S^a$, but $(\Delta\sigma_{hZ})^2 \propto N_S^a + N_B^a$. This yields a relative uncertainty for the cross-section measurement of 19.18 % for the e-channel and 11.20 % for the μ-channel.

Adding both cross-sections in Equation (4.26) yields 15.27 fb with a relative uncertainty of 11.33 % in good agreement with the value of Table 4.1.

Since we know the branching fractions $B(Z \to \mathrm{e^+e^-}) = 0.03363$ and $B(Z \to \mu^+\mu^-) = 0.03366$ [5], we can determine the total Higgs-strahlung cross-section in each channel separately,

$$\sigma_{hZ,\mathrm{e}} = \frac{\sigma_{hZ}^{\mathrm{e}}}{B(Z \to \mathrm{e^+e^-})} = 235.95 \text{ fb} \qquad \text{and} \qquad \sigma_{hZ,\mu} = \frac{\sigma_{hZ}^{\mu}}{B(Z \to \mu^+\mu^-)} = 217.74 \text{ fb} .$$

Both, $\sigma_{hZ,\mathrm{e}}$ and $\sigma_{hZ,\mu}$, are two independent measurements of the same cross-section, σ_{hZ}. The relative uncertainties of $\sigma_{hZ,\mathrm{e}}$ and $\sigma_{hZ,\mu}$ are the same as those of σ_{hZ}^{e} and σ_{hZ}^{μ}, respectively, if we assume no uncertainty of the branching fractions.
One can combine both measurements to obtain the best estimate for σ_{hZ} by minimizing

$$\chi^2(\sigma_{hZ}) = -\frac{(\sigma_{hZ,\mathrm{e}} - \sigma_{hZ})^2}{2(\Delta\sigma_{hZ,\mathrm{e}})^2} - \frac{(\sigma_{hZ,\mu} - \sigma_{hZ})^2}{2(\Delta\sigma_{hZ,\mu})^2} \tag{4.27}$$

with respect to σ_{hZ} [148]. The result, $\sigma_{hZ} = 221.84$ fb with an relative uncertainty of 9.68 %, is consistent with the cross-section value of 226.8 fb, obtained by the Monte-Carlo generator PYTHIA in Section 4.1.3.
With the numbers N_S^a and N_B^a from the result of fitting Equation (4.25) to the recoil mass distribution in the mass range [100 GeV, 150 GeV], and using the signal selection efficiency

for the recoil mass range used for the fit, Equation (4.24), we obtain a similar result and relative uncertainty for the total Higgs-strahlung cross-section.

Determination of the Higgs Boson Pole Mass

The Higgs boson pole mass is determined as outlined in the Section 4.1.5. Here, however, we have to account for the background and, instead of $s(m_{\text{recoil}})$, Equation (4.13), we use a modification of $f(m_{\text{recoil}})$, Equation (4.25), for the likelihood method,

$$\tilde{f}(m_{\text{recoil}}) = p \cdot s(m_{\text{recoil}}) + (1-p) \cdot b(m_{\text{recoil}}) \ ,$$

which is normalized as $s(m_{\text{recoil}})$ and $b(m_{\text{recoil}})$ are, i.e. $\tilde{f}$ is a PDF. Herein, $p = N_S^a/(N_S^a + N_B^a)$.
High-statistics Higgs-strahlung event samples passed the detector simulation, the reconstruction, the pre-selection cuts and the probabilistic process distinction for different Higgs-boson mass values M_h^j between 119.5 GeV and 120.5 GeV. Finally, the parametrization of the Higgs recoil mass peak, Equation (4.13), was fitted to the obtained recoil mass distributions to determine the values of m_0^j. The mapping $M_h^j \leftrightarrow m_0^j$ was maintained.
The shape parameters were determined as well in this step, but they did not differ significantly with different values M_h^j. The value of p is determined using the number of accepted signal and background events from the fit in the preceding cross-section calculation within the recoil mass range $[100\ \text{GeV}, 150\ \text{GeV}]$.
For the calculation of the likelihood values for the different values of m_0^j according to (4.14), the same 50 fb^{-1} sample was used as for the cross-section determination above, where s is now replaced by $\tilde{f}$. The averaged shape parameters and p were kept constant. Due to the mapping $M_h^j \leftrightarrow m_0^j$, each likelihood value could be assigned to a M_h^j value as well. The resulting likelihood values represented as $-2 \times \ln L_h(M_h)$ are shown in Figure 4.23 for the e- and μ-channel.

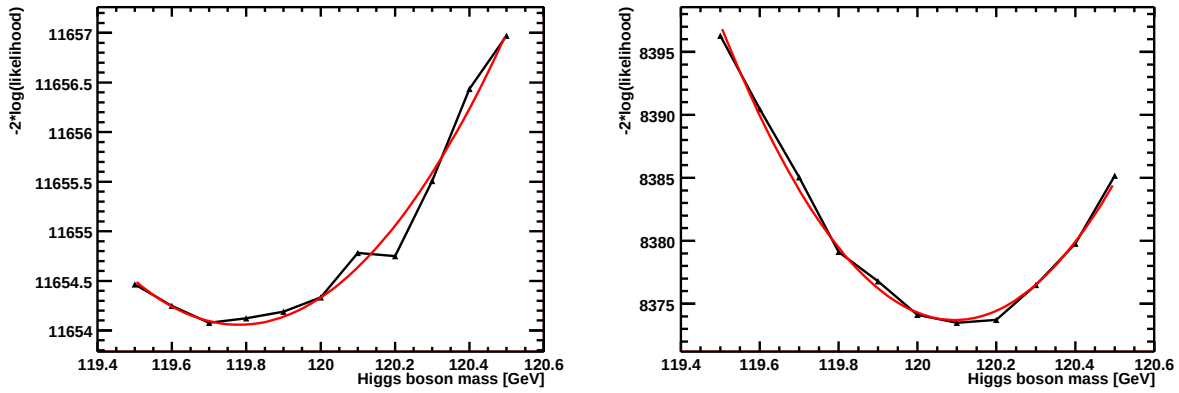

Figure 4.23: Log likelihood functions versus Higgs boson mass, M_h, for the e-channel (left) and the μ-channel (right).

To find the maximum likelihood, or equivalently the minimum of $-\ln L_h$, the parabola Equation (4.15) is fitted to $-\ln L_h(M_h)$. The best estimate of M_h and its uncertainty are determined using Equations (4.16). The results of the fits are also shown in Figure 4.23. We obtain $\widehat{M_h} = 119.780 \pm 0.420$ GeV for the e-channel and $\widehat{M_h} = 120.094 \pm 0.123$ GeV for the μ-channel. These results represent two separate measurements of the Higgs boson pole mass and can be again combined similar as for the cross-section, Equation (4.27). We obtain $\widehat{M_h} = 120.070 \pm 0.118$ GeV, without any bias.

4.2.6 A heavier Higgs Boson

We performed the recoil mass analysis also for a Higgs boson mass of 180 GeV assuming 50 fb^{-1} of integrated luminosity. A cms energy of 350 GeV was chosen, where the Higgs-strahlung cross-section is maximal. The pre-selection cuts were the same as for the previous study at $M_h = 120$ GeV. Only the accepted recoil mass window was changed to 120 GeV $< m_{\text{recoil}} <$ 240 GeV. Also the probabilistic process distinction together with the significance maximization with respect to the likelihood cut were repeated.
The resulting recoil mass distributions for the e- and the μ-channel are shown in Figure 4.24. The Higgs recoil mass peaks are hardly visible on top of the background for both the e- and the μ-channel.

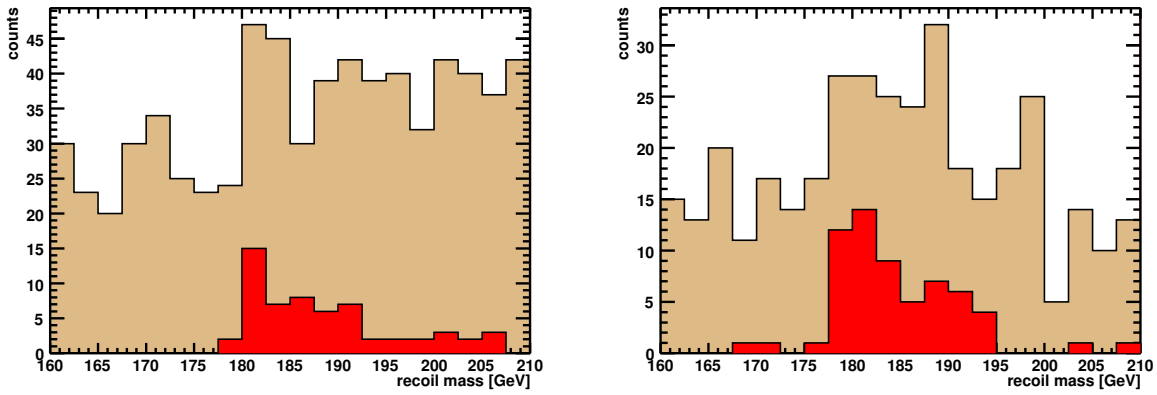

Figure 4.24: Recoil mass distributions for a Higgs mass of $M_h = 180$ GeV and a cms energy of $\sqrt{s} = 350$ GeV for the e-channel (left) and the μ-channel (right).

There are several reasons for this. Firstly, the Higgs-strahlung cross-section is reduced to about 5.3 fb, just 35 % of the statistics as used in the previous case of $M_h = 120$ GeV and $\sqrt{s} = 250$ GeV. The cross-section for the $e^+e^- \to \ell^+\ell^- f\bar{f}$ does not decrease by the same fraction, as can be seen in Table 4.3.
Secondly, according to the conclusions of Section 4.1.4 the recoil masses are distributed between 180 GeV and about 260 GeV due to ISR, i.e. over a range of 80 GeV, which is twice as much as for the previous study with $M_h = 120$ GeV and $\sqrt{s} = 250$ GeV. An additional broadering of the spectrum occurs due to the uncertainty of the lepton

momentum measurement, $\Delta m_{\text{recoil}}^{\text{mom}} = 1.129$ GeV, Equation (4.10), and due to the Higgs boson decay width, $\Delta m_{\text{recoil}}^{\text{m}_\text{h}} = 0.628$ GeV as obtained from Figure 1.1 in Section 1.1.5.[13] In addition, the beam energy spread leads to $\Delta m_{\text{recoil}}^{\text{BES}} = 0.407$ GeV, using Equation (4.12). The total Higgs recoil mass resolution reads then

$$\Delta m_{\text{recoil}} = \sqrt{(\Delta m_{\text{recoil}}^{\text{mom}})^2 + (\Delta m_{\text{recoil}}^{\text{BES}})^2 + (\Delta m_{\text{recoil}}^{\text{m}_\text{h}})^2} = 1.355 \text{ GeV} .$$

Although the selection efficiency is about 40 % in both the e- and the μ-channel, the significance is therefore dramatically declined. A fit and the Higgs mass determination are therefore hardly possible.
However, we can count the number of accepted signal and background events in a mass range of [179 GeV, 185 GeV]. Since the background originates from Standard Model processes, we can compare the total number of accepted events with the expected one. In this way, we can measure the cross-section despite the small statistics. The relative uncertainty of the cross-section measurement can be obtained from the significance, which was maximized using this mass range, to give $\Delta\sigma_{hZ}/\sigma_{hZ} = 27$ % in the μ-channel and $\Delta\sigma_{hZ}/\sigma_{hZ} = 43$ % in the e-channel. Finally, the total relative uncertainty for the Higgs-strahlung cross-section is about 23 %.

No	process	cross-section [fb]	# events (for $L = 50$ fb^{-1})
1	$e^+e^- \to hZ \to X\ell^+\ell^-$	5.3	264
2	$e^+e^- \to e^+e^-$	973.1	48657
3	$e^+e^- \to \mu^+\mu^-$	2181.0	109050
4	$e^+e^- \to \tau^+\tau^-$	2128.0	106400
5	$e^+e^- \to W^+W^- \to [e,\mu]X$	4187.0	209335
6	$e^+e^- \to e^+e^- f\bar{f}$	437.5	21873
7	$e^+e^- \to \mu^+\mu^- f\bar{f}$	244.2	12209
8	$e^+e^- \to e^+e^-e^+e^-$	170.2	8510
9	$e^+e^- \to \mu^+\mu^-\mu^+\mu^-$	1.7	88
10	$e^+e^- \to e^+e^-\mu^+\mu^-$	19.8	989

Table 4.3: Cross-sections and number of events for 50 fb^{-1} for signal and background processes for the Higgs recoil mass analysis. A Higgs boson mass of $m_h = 180$ GeV and a cms energy of $\sqrt{s} = 350$ GeV are assumed ($\ell = e, \mu$). For $e^+e^- \to e^+e^-$ the loose recoil mass cut, 120 GeV $< m_{\text{recoil}} <$ 240 GeV, is used.

For a Higgs boson mass of $m_h = 180$ GeV, a higher statistics is necessary to obtain a similarly significant recoil mass peak at $\sqrt{s} = 350$ GeV as for a Higgs boson mass of $m_h = 120$ GeV at $\sqrt{s} = 250$ GeV. To estimate the necessary integrated luminosity, we use Equation (4.22),

$$S = \frac{L\varepsilon^S\sigma_{hZ}}{\sqrt{L\varepsilon^S\sigma_{hZ} + L\varepsilon^B\sigma_B}} = \sqrt{\frac{L}{L_0}}S_0 ,$$

[13] We assume a Gaussian distribution for simplicity instead of the Breit-Wigner distribution

where $N_S^a = L\varepsilon^S\sigma_{hZ}$ and $N_B^a = L\varepsilon^B\sigma_B$ was used, with ε^B being the background selection efficiency and σ_B the total cross-section of all background processes. S_0 is the significance at some reference integrated luminosity L_0. We use for $L_0 = 50$ fb^{-1} the result found above, $S_0^{-1} = \Delta\sigma_{hZ}/\sigma_{hZ} = 23$ %. To obtain a significance corresponding to $S^{-1} = 10$ %, we therefore need an integrated luminosity of about $L = 264.5$ fb^{-1}.

A similar optimization study as was performed in Section 4.1.7 for $M_h = 120$ GeV, results in no improvement for the significance, i.e. also for the uncertainty of the Higgs-strahlung cross-section measurement for $M_h = 180$ GeV over a wide range of $\sqrt{s}$. The left-hand plot in Figure 4.25 shows the relative cross-section uncertainty as function of $\sqrt{s}$ for $L = 500$ fb^{-1}. The corresponding cross-sections were determined using PYTHIA, including ISR, FSR and the momentum uncertainties as used in Section 4.1.7.

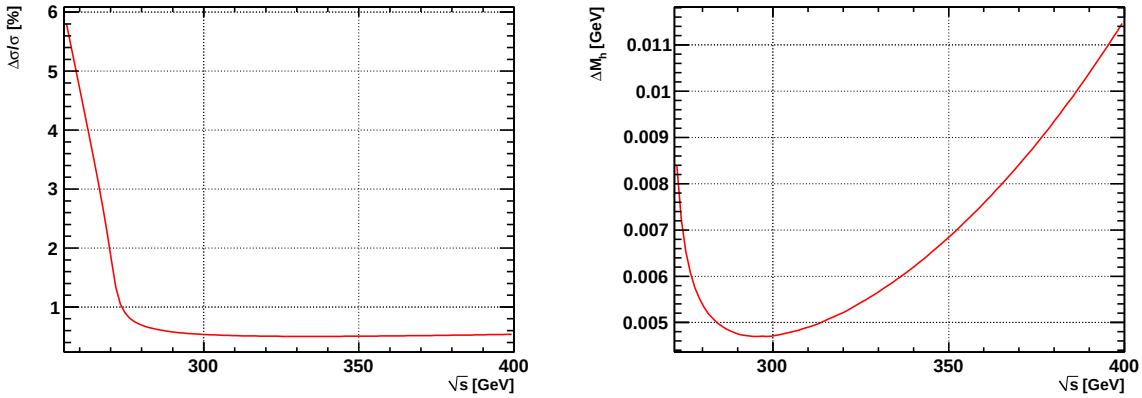

Figure 4.25: The relative cross-section uncertainty for the Higgs-strahlung process (left), and the estimated uncertainty of the Higgs boson mass measurement (right) as function of the cms energy, $\sqrt{s}$, from an analytical calculation for $M_h = 180$ GeV. The cross-sections obtained from PYTHIA were used.

The right-hand plot in Figure 4.25 shows the uncertainty of the Higgs boson mass measurement as a function of $\sqrt{s}$ using the recoil mass resolution due to the lepton momentum measurement uncertainty and the beam energy spread, which were analytically derived in Section 4.1.4, and due to the Higgs decay width, which represents just a constant contribution. The optimum is found at about $\sqrt{s} = 300$ GeV.

Chapter 5

Radiation-Hard Sensors for the BeamCal

The sensor layers of the BeamCal will be made from semiconductor or isolator material, and will work as solid state ionization chambers. The advantages of such devices were outlined in Section 1.2.4. BeamCal should not acquire much space, and between the absorber layers is not much space for bulky sensors. The slits between the absorber layers should be small to keep the Moliëre radius small for a good detection efficiency of high-energetic electrons. Solid state ionization chambers offer the possibility for a very compact design of BeamCal. Despite their smallness, solid state ionization chambers generate signals sufficiently large to ensure a save operation and a good performance.
The other issue is that the BeamCal must stay operational in spite of the huge energy deposit due to the beamstrahlung pairs. Results from investigations of sensor candidates for their radiation hardness, i.e. functionality with increasing dose accumulation, are shown and discussed in this chapter.

5.1 Solid State Ionization Chambers

5.1.1 Working Principle

The simplest principle of a solid state ionization chamber (in contrast to a diode), hereafter called *sensor*, is a semiconducting or isolating material with metalized pads on both opposite sides. The metalized pads serve as electrodes to which a voltage is applied. The situation is comparable to a plate capacitor as shown in Figure 5.1. A current flows when the voltage is applied. To avoid large heat generation by power dissipation, the sensor material should be high-ohmic. Hence, only high-resistive semiconductors or isolators can be used. The current flowing through the biased sensor is caused by the intrinsic conductivity of the material and is called *dark current*.
Charged particles passing through the sensor lose a fraction of their kinetic energy by ionizing the material, i.e. by exciting electrons in an atom to higher energetic levels as

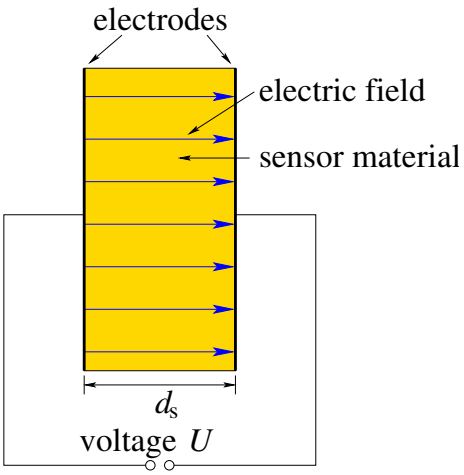

Figure 5.1: The basic sensor setup for a solid state ionization chamber without a signal load.

described in Section 1.2.2. In semiconductors and isolators, a part of the deposited energy leads to the creation of electron-hole pairs, which drift in the respective directions towards the electrodes. These drifting charges represent a current – the *signal current*. The total current measured in the outer circuitry is the sum of both dark and signal current as illustrated in Figure 5.2. We call this total current the *sensor current*.

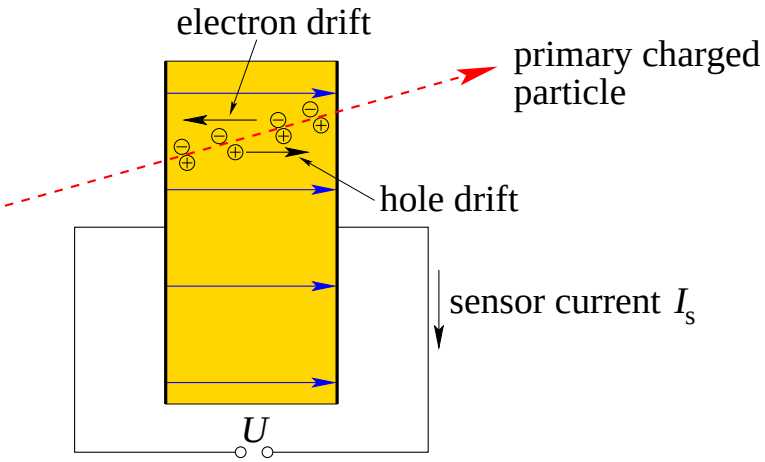

Figure 5.2: Working principle of a solid state ionization chamber with ionizing particle incidence.

The signal current is proportional to the energy deposited by the primary particle. Thus, the deposited energy can be measured by integrating the signal current scaled by a calibration factor of the used setup. The integrated signal current is called signal or *collected charge*, Q_{coll}.

Signal Generation

We consider impinging charged particles of a fixed energy, E_0. In Section 1.2.2, it was shown that the energy loss in a thin material layer, δE, obeys a certain distribution, e.g. a Landau distribution. Only a part of it is deposited inside the material. Some of the energy lost by the primary particle is transferred to secondary electrons. These δ-electrons deposit also a part of their energy and might then leave the detector. Energy can be deposited inside the material by e.g. ionization, excitation of atomic levels, lattice vibrations or lattice atom displacements. Likewise, photons can be created either by bremsstrahlung or by relaxation of excited material electrons, which can leave the detector carrying away a certain amount of energy. Since these processes are of stochastical nature, their contributions to the energy deposition cause fluctuations for the distributions of energy loss and deposition, which where not accounted for in the Landau distribution [56, 57, 58].
The energy deposited by ionization inside semi-conductors or isolators is translated into a number of electrons and holes, which are created as pairs and which can drift inside an electric field, which is externally applied, causing the signal current, I_s. The electrons and holes can be stopped, however, before reaching the electrode e.g. by recombination. Therefore, not all charges induced in the ionization process, Q_ind, are visible as signal charge, Q_coll, and only a fraction of the total energy lost by the primary particle is transformed into a detectable signal. Figure 5.3 illustrates the situation.

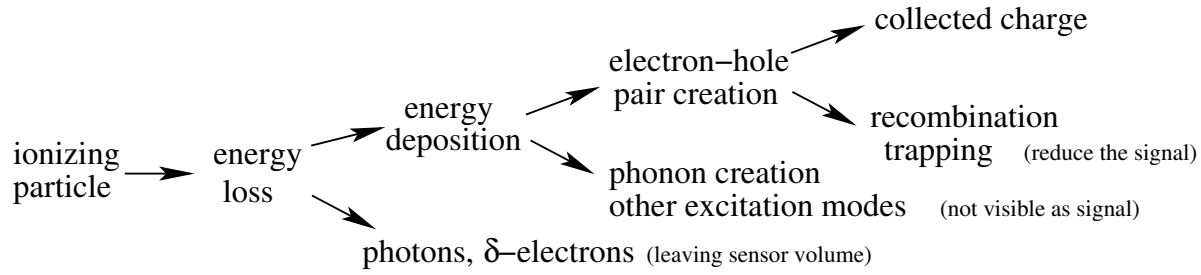

Figure 5.3: Scheme of the creation of the measured signal charge in the ionization process.

The number of created electron-hole pairs per path length of the traversing particle fluctuates even for a fixed amount of energy deposited by ionization. The reason is the stochastic nature of the ionization process, where a continuous quantity, namely the deposited energy, is translated into a discrete number, influenced by the Fano factor introduced in Section 1.2.2. The fraction of energy lost by the impinging particle, which is observable as signal, is therefore difficult to estimate precisely.
Instead, one parametrizes the ignorance about the detailed signal creation mechanism by introducing an averaged electron-hole pair creation energy, ε_eh, which describes effectively the translation of the energy injected into the sensor into the signal charge amount, Q_ind. This quantity is also difficult to determine theoretically, but it can at least be measured. This is accomplished by injecting a known amount of energy, e.g. by irradiating the sensor with photons of known energy. The energy of these photons must be large enough to

release an electron via photo-effect, which moves through the sensor and ionizes the atoms creating electron-hole pairs on its path. On the other hand, the photon energy must also be sufficiently small in order that no particle leaves the sensor due to its own kinetic energy. Therefore, the whole photon energy, E_γ, is deposited inside the sensor volume. Another important condition is that the sensor material should not diminish the number of electron-hole pairs by e.g. recombination or trapping, i.e. $Q_{\text{coll}} \equiv Q_{\text{ind}}$. By measuring the collected charge and dividing the photon energy by Q_{coll} one obtains

$$\varepsilon_{\text{eh}} = \frac{E_\gamma}{Q_{\text{coll}}/e} \ . \tag{5.1}$$

Instead of photons, ionizing particles of a known energy can be also used. The energy deposited by these particles must be known. For diamond sensors such experiments were performed with the result $\varepsilon_{\text{eh}}^{\text{diamond}} = 13.19$ eV for α- and β-particles [149]. For silicon the value $\varepsilon_{\text{eh}}^{\text{silicon}} = 3.6$ eV is also known [150]. Values of ε_{eh} are published in [151] for further materials. It is experimentally verified, that ε_{eh} is rather independent of the type of the ionizing particle [70, 151]. A dependency on the temperature and the electric field applied to the sensor is reported in [152], which, however, was proven to be small.
A phenomenological approach [153, 154, 151] gives a relation between ε_{eh} and a characteristic quantity of a solid – the *band gap energy*, E_{gap},

$$\varepsilon_{\text{eh}} = \alpha_1 E_{\text{gap}} + \alpha_2 \ . \tag{5.2}$$

$\alpha_1 > 1$ describes that more energy than just the band gap energy is needed to create an electron-hole pair. α_2 describes the dissipation of energy by phonon excitations. Numerical values were experimentally found as $\alpha_1 = 2.73$ and $\alpha_2 = 0.55$ eV [151]. A connection to a theoretical description of a solid is not found, yet. Deviations of ε_{eh} in Equation (5.2) from measured values of up to 20 % were found for larger band gaps, such as the one for diamond.
While Q_{coll} is determined by the measurement, Q_{ind}, is not known for each single particle passing the sensor. However, one can estimate the most probable value of Q_{ind} by

$$Q_{\text{ind}} = e\frac{\delta E_{\text{MPV}}}{\varepsilon_{\text{eh}}} \ , \tag{5.3}$$

where the most probable energy loss, δE_{MPV}, is used. δE_{MPV} can be determined using Equation (1.44) or Monte-Carlo simulations.
Dividing Q_{ind} by d_{s} yields a quantity that can be considered as constant in a certain range of the sensor thickness. One defines the most probable number of electron-hole pairs created per path length of a traversing MIP,[1]

$$\eta_{\text{eh}} = \frac{Q_{\text{ind}}}{e d_{\text{s}}} = \frac{\delta E_{\text{MPV}}}{d_{\text{s}} \varepsilon_{\text{eh}}} \ . \tag{5.4}$$

[1] MIPs are usually used to characterize sensors.

Values of η_{eh} were determined using Monte-Carlo simulations and are published for diamond [155, 156, 157].
We have to distinguish between η_{eh} and the average number of electron-hole pairs created per path length of the traversing MIP,

$$N_{\mathrm{eh}} = \frac{\left\langle \frac{d\varepsilon_{\mathrm{dep}}}{dx} \right\rangle}{\varepsilon_{\mathrm{eh}}} = \frac{\langle \varepsilon_{\mathrm{dep}} \rangle}{d_{\mathrm{s}} \varepsilon_{\mathrm{eh}}} \,, \tag{5.5}$$

where the average deposited energy, $\langle \varepsilon_{\mathrm{dep}} \rangle$ is used in Equation (5.3) instead of δE_{MPV}. For a given sensor thickness, $\langle \varepsilon_{\mathrm{dep}} \rangle$ is determined by GEANT4 simulations. The most probable value is more characteristic for cases where single particles pass through the sensor. The average deposited energy is relevant for investigations involving signals from many particles penetrating the sensor or when the sensor is thick.

5.1.2 Requirements for Sensors in Major Applications

Application as Current Monitor

The passage of incident particles adds a signal current to the permanent dark current. This signal current is related to the totally deposited energy. This operation mode can be used for a beam monitoring system, such as in the CMS detector at the LHC [158]. Since these sensors are positioned close to the beam pipe they have to withstand large fluxes of particles from the the beam halo, which are mainly hadrons and photons. Previous studies [159] have shown that diamond sensors are most promising for this purpose.

Application as Flux Counter

If the incident particle flux is small enough that single particles passing through the sensor can be separated in time, the number of particles can be counted. The flux is just this number divided by the sensor area per unit time.
To obtain also the spatial distribution of the particle flux a tracker composed of pixeled sensors may be used. The metalization on the sensor is then finely segmented.
A flux detector based on diamond pixel sensors is just under development for the CMS experiment [158, 160, 161].
Spectra of the energy deposited by high-energetic particles can be acquired in this mode, as well. An energy calibration and a long-term operational stability monitoring can be performed using these spectra.

Application as Calorimeter Sensors (BEAMCAL)

In an electromagnetic sampling calorimeter – such as BEAMCAL – the primary particle dissipates all its energy in an electromagnetic shower. This primarily happens inside the absorber layers. A lot of shower electrons and positrons then pass through the interspersed

sensor layers depositing a small fraction of their energy. This deposited energy gives information about the shower shape and the total energy of the primary particle. At the ILC, there will be a lot of beamstrahlung electrons and positrons along the beam pipe causing showers in the BeamCal. This energy deposition has to be determined bunch-by-bunch. A calibration needs to be done for determining the shower energy out of the deposited energy inside the sensors. The calibration factor depends on the sampling ratio, i.e. the ratio of the thicknesses of sensor and absorber layers. Each sensitive segment – also called *pad* – of the sensor layers has to be calibrated such that the electronic signals are related to the energy deposited inside this pad.

General Sensor Material Requirements

A large signal-to-noise ratio (SNR) is important to observe signals above the background noise due to e.g. thermal fluctuations. A large signal yield is helpful, but not necessary if the noise stays small. This is specifically important for thin sensors, where the energy deposit from a single particle is not large.
A large resistance is necessary to avoid large power dissipation by the dark current. A good heat conductivity prevents an active cooling, which in turn reduces the costs and the maintenance efforts for a detector system. Since the sensors are exposed to radiation, their performance might be diminished with the time of operation. Therefore, sensor materials are needed that are *radiation hard* in the sense that the sensor stays operational with increasing radiation load. Of course, it would be desirable that the sensor properties are not changed at all during the run time of operation.
Mechanical and thermal stability are desirable properties for sensor materials, to avoid accidental destruction during the assembly or the operation. Specifically under high radiation load, the sensors might heat up during a short time. Temperature independent material properties are then very adjuvant.
Sensors that shall provide fast response to a traversing particle need sensor materials with a high drift speed. A high drift speed can be achieved either by a large electric field or by large charge carrier mobility. The latter might be affected during the irradiation if the material properties are changed with the radiation load. A large electric field, on the other hand, might not be tolerated by some materials which suffer from a breakthrough if the electric field exceeds some value. This breakthrough field might be sensitive to the irradiation as well.

5.1.3 Characterization of Sensors and Charge Collection Distance

One can introduce the *charge collection efficiency* (CCE) by the definition

$$\mathrm{CCE} = \frac{Q_{\mathrm{coll}}}{Q_{\mathrm{ind}}} \,. \tag{5.6}$$

Since we can compare the collected charge, Q_{coll}, only with the mean or most probable value of the induced charge, Q_{ind}, the CCE as defined in Equation (5.6) is distributed

according to Q_{coll} and scaled with the mean or most probable value of Q_{ind}. The such defined CCE is a number between zero and one, where the value of one corresponds to the maximum charge collection efficiency.
The comparison of the most probable values is used for measurements with single relativistic particles[2], because this value is the characteristic parameter for the description of straggling functions similar to the Landau distribution, Equation (1.43). The measured values of Q_{coll} follow roughly such a distribution. On the other hand, in experiments with a lot of particles passing simultaneously through the sensor, the mean energy deposition is the crucial quantity. In such cases, the mean values should be compared.
A quantity, also frequently used for the characterization of sensors, is the *charge collection distance* (CCD) , defined by

$$\mathrm{CCD} = \frac{Q_{\mathrm{coll}}}{Q_{\mathrm{ind}}} d_{\mathrm{s}} = \mathrm{CCE}\ d_{\mathrm{s}}\ , \tag{5.7}$$

It is completely equivalent to the CCE, and its maximum is the sensor thickness. On a first glance, it seems to be more complicated quantity, because one has to determine Q_{ind} and the value of the sensor thickness, d_{s}. However, it is a convenient quantity in experiments with single particles, because one can exploit Equation (5.4). We obtain

$$\mathrm{CCD} = \frac{Q_{\mathrm{coll}}/e}{\eta_{\mathrm{eh}}}\ . \tag{5.8}$$

The reason for the introduction of the CCD is that it is approximately the mean drift distance of the charges in the electric field inside the sensor for small values of the CCE. Hence, one can relate the CCD to material properties such as characteristic time constants and mobilities.

The Setup for CCD Measurements

Figure 5.4 shows a schematic setup for the CCD measurements of sensors. A ^{90}Sr β-emitter is used to generate an electron flux through the sensor. Electrons of a sufficient energy cross the sensor and deposit energy inside the sensor volume and inside the scintillators of the trigger as well. The signal current is amplified and shaped [69, 162], and then fed into a charge-integrating analog-to-digital converter (ADC). The signal is digitized, if both scintillators below the electron source registered the particle simultaneously (coincidence of scintillator signals). The coincidence unit generates a *gate*, i.e. the time interval, in which the sensor signal is integrated and then digitized.
Figure 5.5 shows a typical spectrum of Q_{coll}. The right peak corresponds to the Landau-like energy deposition, the *signal*, while the left peak has a Gaussian shape and reflects the noise distribution of the baseline of the electronics, the *pedestal*. The ADC digitizes the input charge into arbitrary numbers, the so-called ADC channels. To convert these numbers into electric charges, a calibration needs to be done. For this purpose, a known amount of

[2]Experiments with high-energetic single particles of almost the same energy.

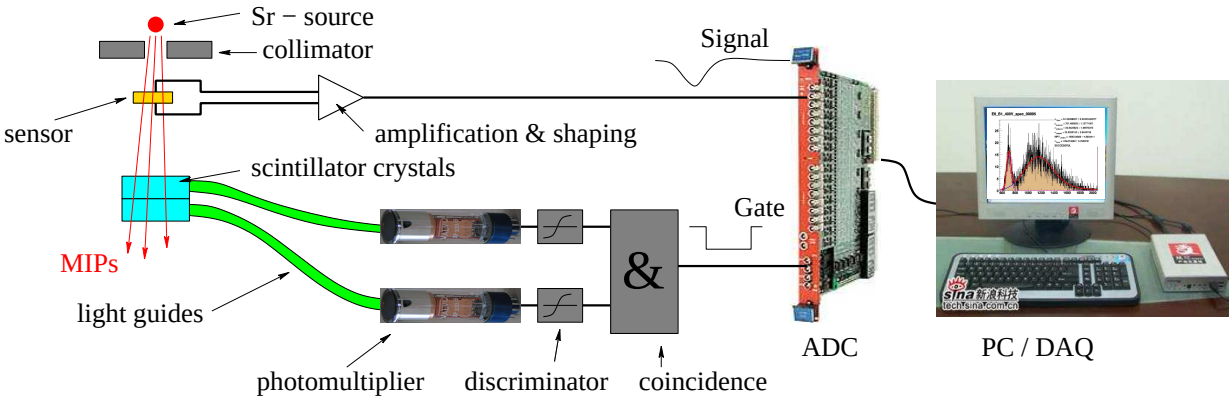

Figure 5.4: Scheme of the CCD measurement setup.

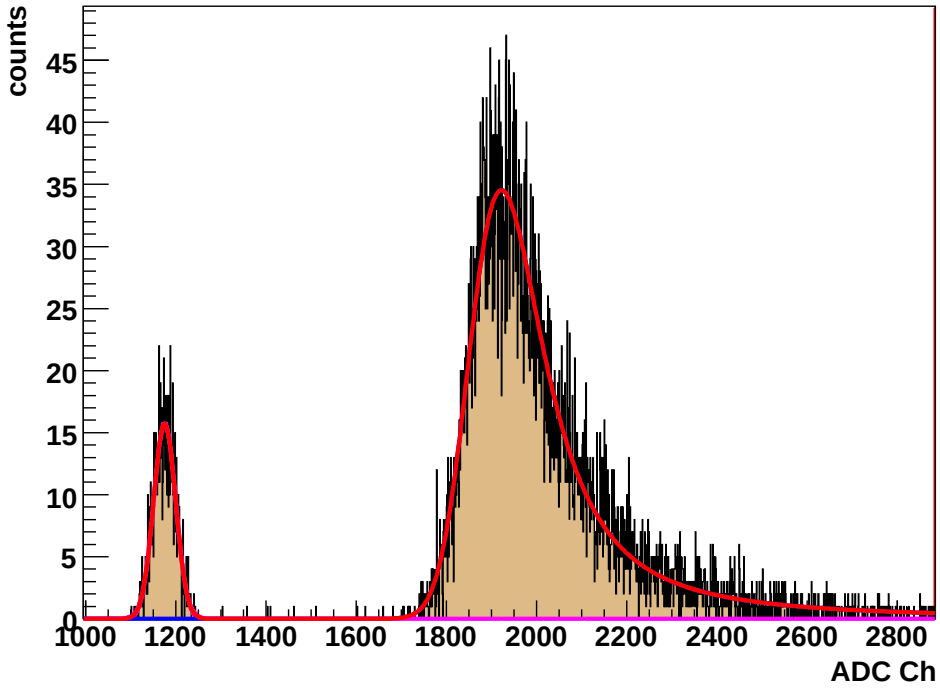

Figure 5.5: An example CCD spectrum.

charge is injected into the input of the preamplifier and is then digitized. From the relation between the injected charge and the ADC output value one obtains the *calibration factor*, k_Q:

$$Q = k_Q \times \text{ADC channel} .$$

The pedestal is well described by a Gaussian distribution, the mean value of which, μ_p, is the pedestal position. The standard deviation of the pedestal, σ_p, is a measure of the electronic noise. The signal peak is assumed to be a convolution of a Gaussian, describing

the noise, and a Landau distribution, describing the signal, $GL(q; \mathrm{MPV}, \sigma_\mathrm{L}, \sigma_\mathrm{G})$ as define in Equation (D.3), where q is in units of ADC channels. MPV is the most probable value of the Landau distribution in units of ADC channels, σ_L is the scaling factor and σ_G is the standard deviation of the Gaussian, both in units of ADC channels.[3]
The usage of this signal distribution is motivated by the distribution of the energy loss, Equation (1.43). The convolution with a Gaussian parametrizes the fluctuations from thermal and electronics noise, which are equal to σ_p, as well as intrinsic fluctuations of the number of electron-hole pairs. The latter is the reason why in general the condition holds $\sigma_\mathrm{G} > \sigma_\mathrm{p}$.
The most probable collected charge, Q_coll, is given by

$$Q_\mathrm{coll} = k_Q(\mathrm{MPV} - \mu_\mathrm{p}) \; . \tag{5.9}$$

The CCD is then given by Equation (5.8). It should be noted that the most probable value of the Gauss-Landau convolution, GL, differs from that of the Landau distribution L, as shown in Appendix D. Thus, a parameter fit of GL to the spectrum is necessary to get the parameter values, instead of taking the maximum of the measured spectrum.
A calibration-independent quantity is the SNR defined as

$$\mathrm{SNR} = \frac{\mathrm{MPV} - \mu_\mathrm{p}}{\sigma_\mathrm{p}} \; . \tag{5.10}$$

It characterizes the whole system – sensor and readout electronics. If, however, the electronic noise in the readout electronics is negligible in comparison with the noise due to the dark current through the sensor, then the SNR describes an intrinsic property of the sensor.

Further Characterization Measurements

The applied voltage is a parameter of the system. Both the dark current and the CCD depend on it.
The dark current is measured with a picoamperemeter. To avoid surface currents due to humidity, especially in the case of isolators such as diamond, a nitrogen atmosphere is used for this measurement.
Thermally stimulated currents [163, 164] can be used to investigate the trap densities and levels in crystals. Thereby, trapped charge carriers are released by thermal excitation and measured as current.

[3] In should be noted that MPV and σ_L correspond only formally to δE_MPV and ξ, respectively, in Equation (1.43), which describes the energy loss of mono-energetic particles. In contrast, Equation (D.3) parametrizes the shape of the spectrum of Q_coll, the origin of which are electrons from a ^{90}Sr source, which follow a broader energy distribution. MPV and σ_L are treated here as free parameters.

5.1.4 Investigated Materials

In the following, three materials as candidates mainly for BeamCal sensors are described: CVD diamond, GaAs and specially processed silicon. Table 5.1 summarizes their intrinsic properties.

Material Property	Diamond	Silicon	GaAs
Density, ρ, [g/cm^3]	3.52	2.32	5.32
Dielectric Constant	5.7	11.9	12.9
Resistivity [Ω cm]	$10^{13} - 10^{16}$	$2.5 \cdot 10^5$	$4 \cdot 10^8$
Thermal Conductivity [W cm^{-1} K^1]	20	1.5	0.45
Thermal Expansion Coefficient [K^{-1}]	$0.8 \cdot 10^{-6}$	$2.6 \cdot 10^{-6}$	$5.73 \cdot 10^{-6}$
Breakdown Field [V cm^{-1}]	10^7	$3 \cdot 10^5$	$4 \cdot 10^5$
Lattice Structure	diamond	diamond	sphalerite
Band Gap, E_{gap}, [eV]	5.45	1.12	1.42
Electron-Hole Pair Creation Energy, ε_{eh}, [eV]	13.2 [149]	3.62 [150]	4.3 [165]
Electron Mobility, μ_{e}, [cm^2 V^{-1} s^{-1}]	1800-4500 [166]	1350	8500-8800
Hole Mobility, μ_{h}, [cm^2 V^{-1} s^{-1}]	1200-3800 [166]	480	320-400
Radiation Length, X_0, [cm]	18.8	9.4	2.3

Table 5.1: Intrinsic properties of the undoped materials, which are sensor material candidates [167, 168]. The mobilities and the resistivity of diamond depend strongly on its purity.

Diamond

Chemical Vapor Deposition (CVD) [169] diamond is a relatively new sensor material, both as single crystal (sc) and polycrystalline (pc). scCVD diamond is of special interest, because it has very small impurity and defect densities.[4] Diamond is formed out of carbon atoms arranged in a tetragonal lattice. There are no internal dipole moments as in ion lattices, and the possibilities for point defects are limited to those of single element lattices (vacancies and interstitials). Therefore, diamond is potentially more tolerant to radiation damages than e.g. mixtures and is a promising candidate for radiation hard sensors.
The scCVD and pcCVD sensor samples of diamond, which were investigated, were bought from Element Six [170].
The grain boundaries of the pcCVD diamond sensors are along with the growth direction, i.e. they are perpendicular to the sensor plane. They cause considerable inherent defects limiting the CCD. Several authors published about the radiation hardness, applications in high-energy physics experiments, and modeling of CVD diamond [155, 156, 157, 164, 171, 162, 172, 173]. We concentrate on radiation hardness against electromagnetic radiation

[4] Information about densities of the reaction gas remnants and admixtures are not available from the producer.

and on the reproducibility of the sensor properties, which is necessary to built a uniformly working detector.
The investigated pcCVD diamond samples were metalized with titanium (≈30 nm), platinum (≈20 nm) and gold (≈100 nm). The sensor size is of about 12 mm × 12 mm × 500 μm, the metalization covers an area on the front and back faces, which is about 10 mm × 10 mm to avoid surface currents.
The scCVD diamond samples have a size of about 4 mm × 4 mm × 326 μm. The metalizations are round pads of 3 mm diameter. The resistivity is in the order of $10^{13} - 10^{16}\ \Omega\,\mathrm{cm}$ [167][5].
For these sensor samples we used a most probable number of electron-hole pairs created per micrometer of $\eta_{\mathrm{eh}} = 36\ \mu\mathrm{m}^{-1}$ per MIP electron.[6] The averaged number of electron-hole pairs is $N_{\mathrm{eh}} = 46\ \mu\mathrm{m}^{-1}$, estimated using GEANT4.

Gallium Arsenide

We investigated gallium arsenide (GaAs) samples, which were produced by the Siberian Institute of Technology in Tomsk using the Liquid Encapsulated Czochralski method [174]. GaAs was already considered for particle detectors [175, 176, 177, 178, 179]. The GaAs bulk is doped with tellurium (shallow donor) and compensated with chromium (deep acceptor). The doping is necessary to obtain a high-resistive material with passivated energy levels inside the band gap that then do not act as traps or recombination centers. The chromium and tellurium densities are of the order of $10^{16}-10^{17}\ \mathrm{cm}^{-3}$.[7] The sensor thickness is 500 μm, and the sensor is segmented into pads of about $5\times5\ \mathrm{mm}^2$ in size. The metalization is made of 30 nm vanadium and 1 μm gold. The resistivity was measured to be about 25 M$\Omega\,$cm. For these sensor samples investigated by us, the most probable number of electron-hole pairs created per micrometer a MIP of $\eta_{\mathrm{eh}} = 150\ \mu\mathrm{m}^{-1}$ and the averaged number of electron-hole pairs of about $N_{\mathrm{eh}} = 315\ \mu\mathrm{m}^{-1}$ were estimated using GEANT4.

Radiation Hard Silicon

The investigated silicon sensor sample was provided by the Brookhaven National Laboratory [112, 181]. It is a p+/n/n+ diode structure, where the silicon substrate was produced in [1 1 1] lattice orientation using the Magnet-Czochralski method. The n bulk material is doped with phosphorus ($4 \cdot 10^{12}\ \mathrm{cm}^{-3}$). The p+ region is ion implanted with boron ($10^{19}\ \mathrm{cm}^{-3}$, 100 nm). The n+ layer is ion implanted with phosphorus ($10^{19}\ \mathrm{cm}^{-3}$, 100 nm). The active area of the diode is $0.5 \times 0.5\ \mathrm{cm}^2$. The total thickness is 380 μm. The resistivity of about 1 k$\Omega\,$cm was specified by the provider.

[5] And references therein.

[6] A most probable number of 36 electron-hole pairs created per μm and per electron (MIP) is a generally accepted value. However, in the literature deviations by ±1 are found due to different procedures for determining η_{eh} [155, 156].

[7] We have no information about a possible space-dependent doping density. Therefore, and also in consistency with the results of our measurements, we assume almost uniform doping densities, although GaAs particle detectors can be made as semiconductor devices with inhomogeneous doping densities [180].

5.2 Testbeam Irradiation and Measurements

5.2.1 Description of the Testbeam Experiment

Investigations of the radiation hardness of sensor materials were performed at the Darmstadt Linear Accelerator (DALINAC) [182, 183]. The sensor material candidates, introduced above, were irradiated using a 10 MeV electron beam with currents of several 10 to 100 nA to accumulate doses of up to 5 MGy. The beam currents correspond to dose rates of few 100 kGy/h to 1 MGy/h. It should be noted that one expects at maximum about 1 kGy/h for the BeamCal operation at the ILC. The decision to use 10 MeV electrons was motivated by Monte-Carlo simulations for BeamCal, mentioned in Section 2.5. The energy spectrum of shower particles passing through the sixth BeamCal sensor layer, shown in Figure 2.9, corresponds to the shower maximum ($6X_0$). 10 MeV is a typical energy, well in the energy range of the shower particles.

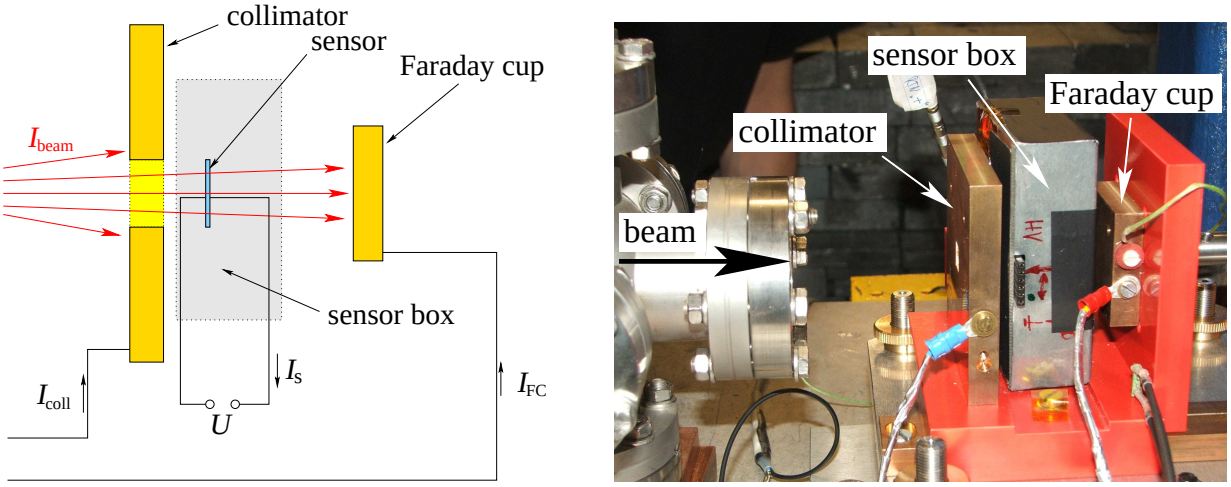

Figure 5.6: Scheme of the testbeam setup (left) and a picture of the experimental area (right).

Figure 5.6 shows the experimental setup. The electron beam leaves the beam pipe through the exit window. The transverse beam profile is then shaped by the collimator, after which the beam particles traverse the sensor under investigation. Behind the sensor a Faraday cup is located. It is made from copper and collects the beam electrons passed through the sensor, which is measurable as current, the Faraday cup current, I_{FC}. The collimator, also made from copper, blends off tails of the beam. In this way almost each beam particle reaching the Faraday cup also passed the collimator window and penetrated the sensor. The geometry of the setup was optimized for efficient and homogeneous exposure of the sensor using Geant4 [93].
The collimator current, I_{coll}, was monitored as well. The setup was aligned with respect to the beam and the currents of the collimator and the Faraday cup were used to optimize the transversal beam position by maximizing I_{FC}/I_{coll}.

The currents through the Faraday cup, the collimator, and the sensor were recorded throughout the irradiation of the sensor. From the Faraday cup current, I_{FC}, the dose accumulated by the sensor is calculated. The irradiation was interrupted in regular intervals to perform an external CCD measurement. Constant high voltage was permanently applied to the sensors, also during the CCD measurement periods.

5.2.2 Dose Calculation

The dose rate, dD/dt, is the energy deposited per time unit, dE_{dep}/dt, divided by the mass of the exposed sensor volume, $\rho A_{\mathrm{beam}} d_{\mathrm{s}}$. A_{beam} is the beam spot area on the sensor given by the collimator window, $A_{\mathrm{beam}} = 1\ \mathrm{cm}^2$. ρ is the mass density and d_{s} the thickness of the sensor. The rate of energy deposition, dE_{dep}/dt, can be rewritten as number of particles penetrating the sensor, $R_c I_{\mathrm{FC}}/e$, multiplied by the averaged deposited energy per primary electron, $\langle \varepsilon_{\mathrm{dep}} \rangle$, which traverses a sensor of thickness d_{s}. R_c is a correction factor that accounts for electrons not registered in the Faraday cup due to backscattering as well as for registered beam particles that did not pass through the sensor e.g. because of a smaller sensor size. Additionally, the non-uniformity of the beam (i.e. beam divergence) is accounted for by R_c. R_c and $\langle \varepsilon_{\mathrm{dep}} \rangle$ are determined using GEANT4 simulations since they depend on the sensor geometry [93]. The dose rate is then given by

$$\frac{dD}{dt} = \frac{\langle \varepsilon_{\mathrm{dep}} \rangle}{d_{\mathrm{s}}} \frac{R_c I_{\mathrm{FC}}/e}{\rho A_{\mathrm{beam}}} \,. \tag{5.11}$$

As the Faraday cup current is a function of time, $I_{\mathrm{FC}}(t)$, the dose can be obtained by integration

$$D(t) = \left\langle \frac{d\varepsilon_{\mathrm{dep}}}{dx} \right\rangle \frac{R_c}{e\rho A_{\mathrm{beam}}} \int_{t_0}^{t} I_{\mathrm{FC}}(t')\, dt' \,, \tag{5.12}$$

where we used $\frac{\langle \varepsilon_{\mathrm{dep}} \rangle}{d_{\mathrm{s}}} = \left\langle \frac{d\varepsilon_{\mathrm{dep}}}{dx} \right\rangle$. The flux through the sensor, i.e. the number of particles per unit area and unit time, is given by

$$\phi = \frac{R_c I_{\mathrm{FC}}}{e A_{\mathrm{beam}}} \,. \tag{5.13}$$

The dose rate can then be written as

$$\frac{dD(t)}{dt} = \left\langle \frac{d\varepsilon_{\mathrm{dep}}}{dx} \right\rangle \frac{\phi}{\rho} \,. \tag{5.14}$$

5.2.3 Results of the Testbeam Experiment

Single Crystal Diamond

We irradiated one scCVD diamond sample up to about 5 MGy. Figure 5.7 shows the CCD as a function of the accumulated dose. The voltage applied was 100 V, which is well above

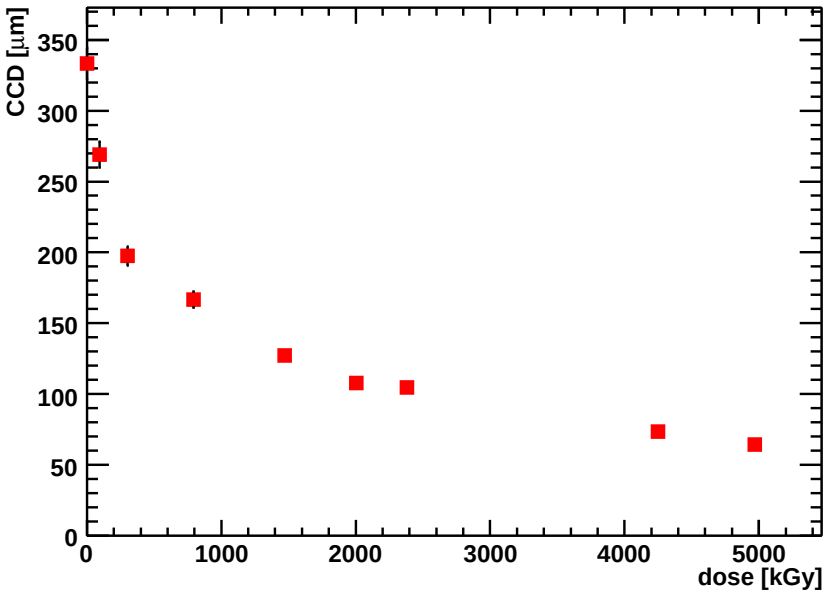

Figure 5.7: CCD as a function of the dose for scCVD diamond.

30 V (about 1 kV/cm) where the CCD saturates as a function of the applied voltage, as will be reported in Section 5.3.3. The CCD is equal to the sensor thickness of 326 μm for zero dose. The CCD decreases to about 65 μm, i.e. down to about 20 %, with an exponential-like curve, as seen in Figure 5.7.
In Figure 5.8 the sensor current, I_s, the Faraday cup current, I_{FC}, and the ratio of both, I_s/I_{FC}, are shown as functions of the accumulated dose. I_s depends obviously on the dose rate, which is proportional to the Faraday cup current, Equation (5.11). For a constant dose rate, the sensor current decreases with the dose, similarly to the decrease in the CCD. The ratio of the sensor and Faraday cup currents is a smooth function of the dose. A dose rate dependence of this ratio was not observed. The ratio is normalized at the beginning of the irradiation, so it is a measure of the efficiency of the sensor to create a signal current after being irradiated. This efficiency was reduced to about 5 % after 5 MGy.
The dark current of the scCVD diamond was measured before and after irradiation. It was in both cases smaller than the sensitivity of the picoamperemeter, i.e. smaller than about 1 pA.

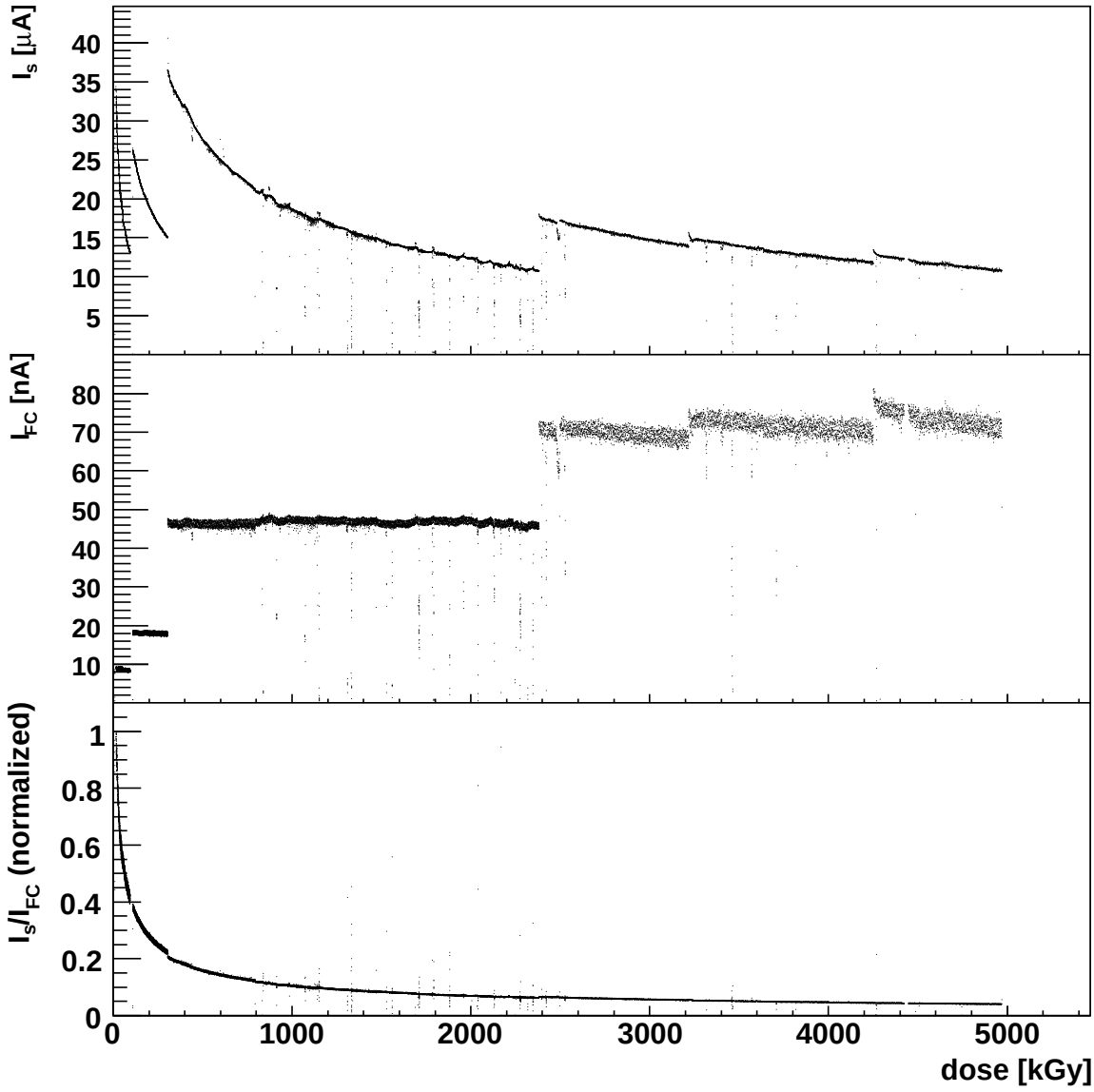

Figure 5.8: Currents of the sensor, I_s, the Faraday cup, I_FC, and the ratio of both, $I_\mathrm{s}/I_\mathrm{FC}$ as functions of the accumulated dose for scCVD diamond.

Polycrystalline Diamond

We irradiated two samples of pcCVD diamonds, which initially had the same properties, up to 4.5 MGy and 5.6 MGy, respectively. The CCDs as functions of the accumulated

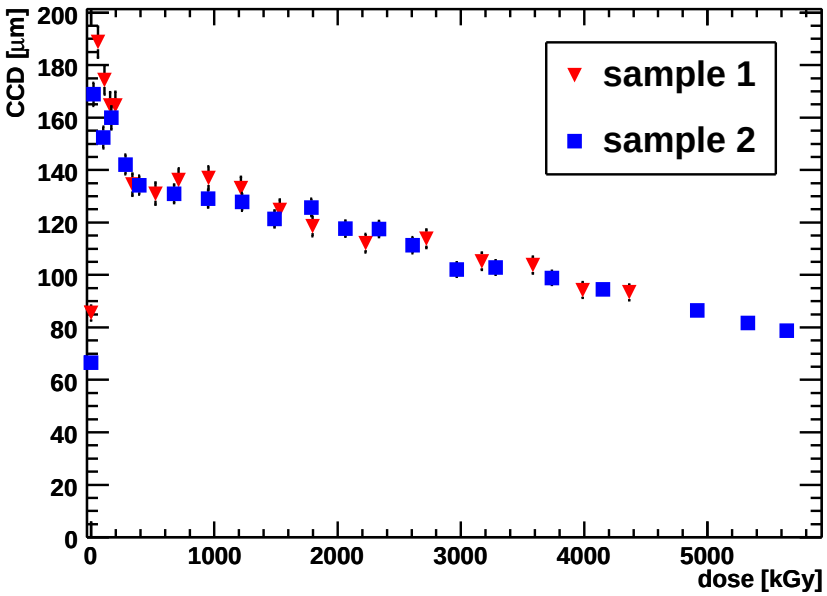

Figure 5.9: CCD as a function of the dose for pcCVD diamond samples 1 and 2.

dose are shown for both samples in Figure 5.9. They are very similar. For both samples a voltage of 400 V was applied, corresponding to an electric field of 8 kV/cm. At the very beginning, i.e. at zero dose, the values of the CCD are about the half of the maximum values. The latter are reached after a few minutes of irradiation. This increase of the CCD at small doses is called *pumping* [184], described in more detail in the next section. The maximum CCD goes up to 190 μm, about 38 % of the sensor thickness. Then a sharp drop follows. Above about 500 kGy, the CCD decreases almost linearly, clearly different to the behavior of the scCVD diamond.
The sensor current, Faraday cup current and the ratio of both for sample 1 are shown in Figure 5.10. The corresponding currents of sample 2 are very similar. The ratio, I_s/I_{FC}, decreases smoothly with the dose down to about 20 % of the initial value starting from 200 kGy. Similar to the scCVD diamond there is no dose rate dependence visible in the sensor efficiency above 200 kGy. There are deviations from the smooth course of the curve in the range up to 200 kGy which originate from problems with the current measurement device.
The dark current as a function of the applied voltage is shown in Figure 5.11. The current-voltage characteristics directly after the irradiation exhibits a three times larger current. After applying an UV light illumination for about half an hour (15 min from each side) the current-voltage characteristics is similar to the one before the irradiation. The UV lamp

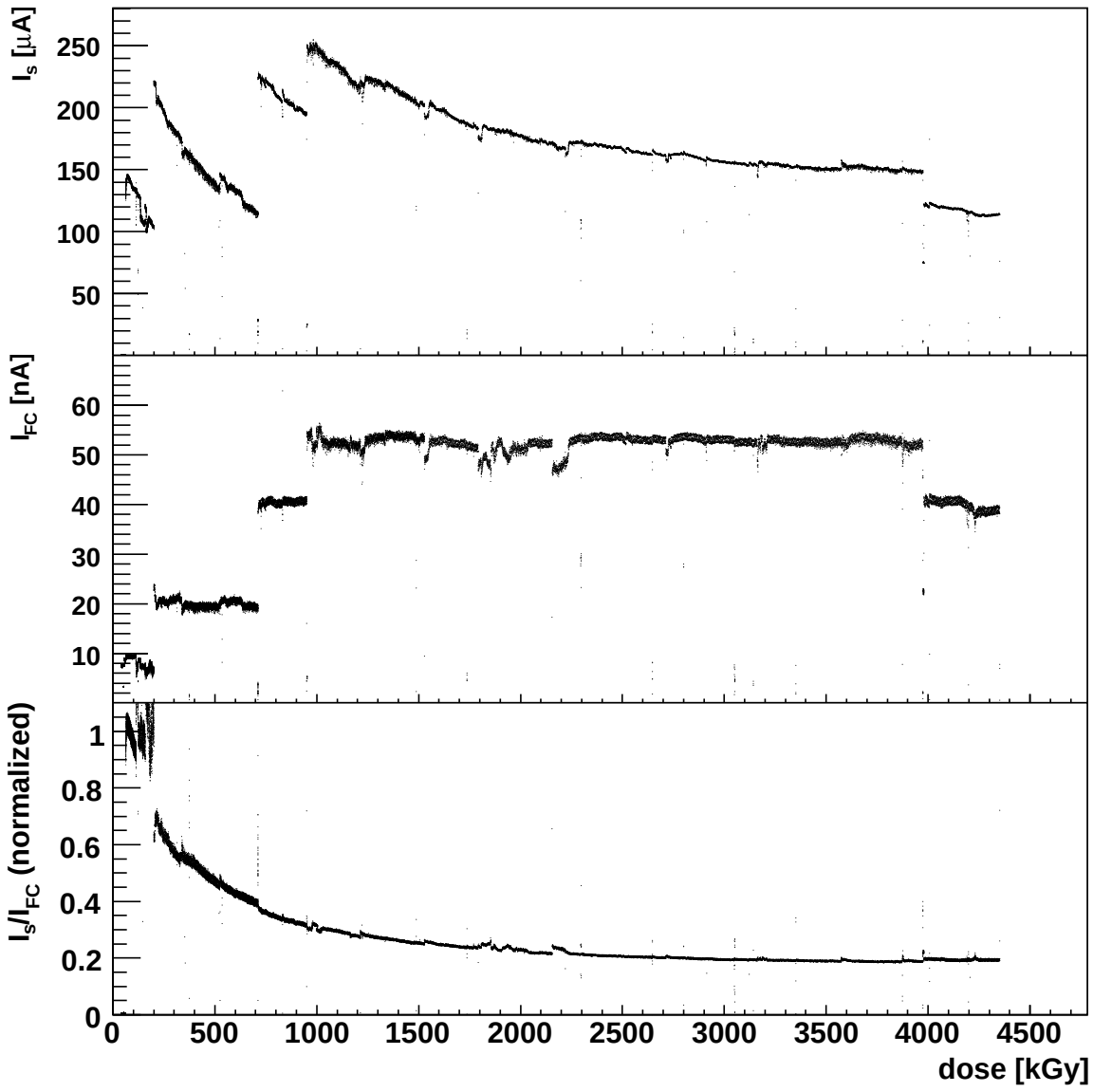

Figure 5.10: Currents of the sensor, I_s, the Faraday cup, I_FC, and the ratio of both, $I_\mathrm{s}/I_\mathrm{FC}$ as functions of the accumulated dose for pcCVD diamond sample 1.

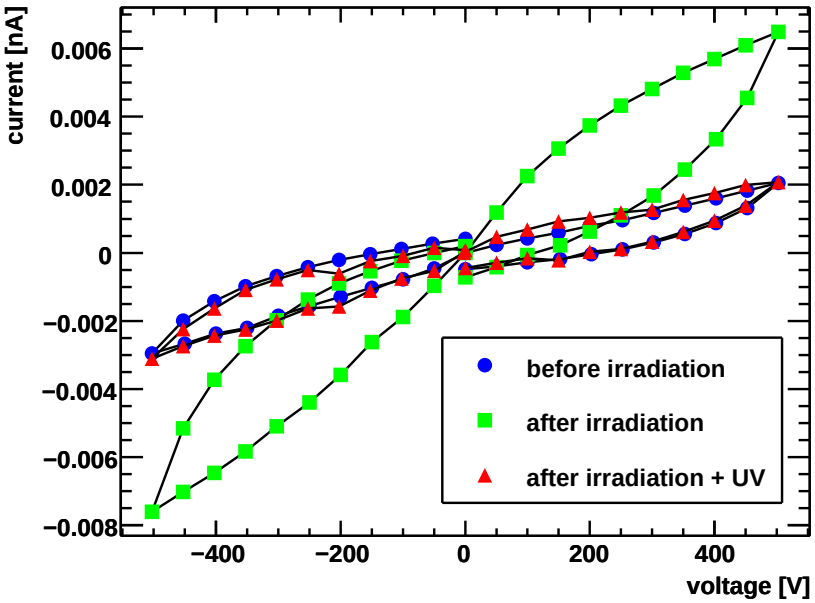

Figure 5.11: Dark current as a function of the applied voltage for pcCVD diamond sample 1, before and after the irradiation, and after UV illumination.

supplies photons with energies between 6 and 12 eV (UV-C range). Probably, the UV light depleted the defects, which act as traps for electrons (or holes). If they are mostly filled, they may serve as reservoir for the conduction band charge density by thermally releasing electrons (or holes). Therefore, the conduction (or valence) band charge carrier density is higher directly after irradiation, what explains the higher conductivity. Nevertheless, the dark current is still in the range of a few pico-Ampere, uncritical for the application as sensor.
The current-voltage characteristics exhibits a hysteresis. Polarization effects may occur, and after switching the voltage one has to wait for the stabilization of the polarization currents, which might take minutes. Thus, if the voltage is increased, a measurement of the sensor current before the stabilization will result in a slightly higher sensor current due to the inertia of the stabilization.

Gallium Arsenide

Two samples of GaAs produced with the same technological parameters and similar electrical features were irradiated up to 0.85 MGy and 1.5 MGy, respectively. The CCDs as functions of the accumulated dose are shown for both samples in Figure 5.12. They are almost identical. For both samples a voltage of 200 V was used corresponding to an electric field of 4 kV/cm. Similar to the scCVD diamond, the CCD decreases almost exponentially with increasing dose from about 250 μm (half of sensor thickness) to about 20 μm (4 % of the sensor thickness). However, after about 1 MGy the signal and the pedestal cannot be

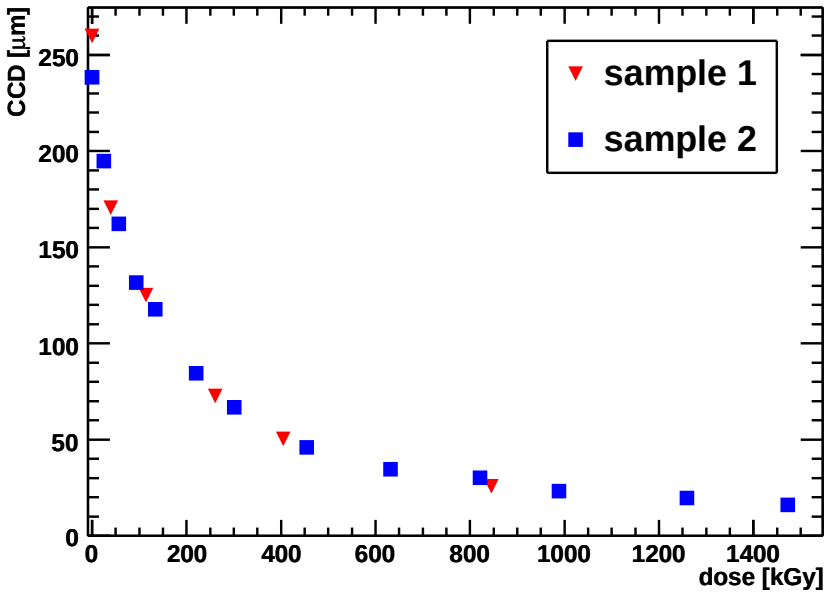

Figure 5.12: CCD as a function of the dose for GaAs samples 1 and 2.

well separated anymore on an event-by-event basis.
The sensor current, the Faraday cup current and the ratio of both for sample 1 are shown in Figure 5.13. The values for sample 2 are similar. The sensor current depends slightly on the dose, but strongly on the dose rate. The ratio of sensor and Faraday cup currents decreases in steps when the dose rate is increased in a step. The sensor current does not grow proportionally with the dose rate. The reason for the nonlinear relation between the sensor and the Faraday cup current is explained later in this chapter.
The current-voltage characteristics for sample 1 is shown in Figure 5.14. After about 1 MGy of accumulated dose the dark current is doubled, but it does not exceed 2 μA at 500 V. The current-voltage characteristics are almost linear.
Figure 5.15 shows the CCD as function of the electric field for sample 1. The result for sample 2 is similar. Before the irradiation, the CCD is saturated at about 200 V (4 kV/cm) at a value of half the sensor thickness. After the irradiation the CCD is not saturated anymore until 500 V (10 kV/cm).

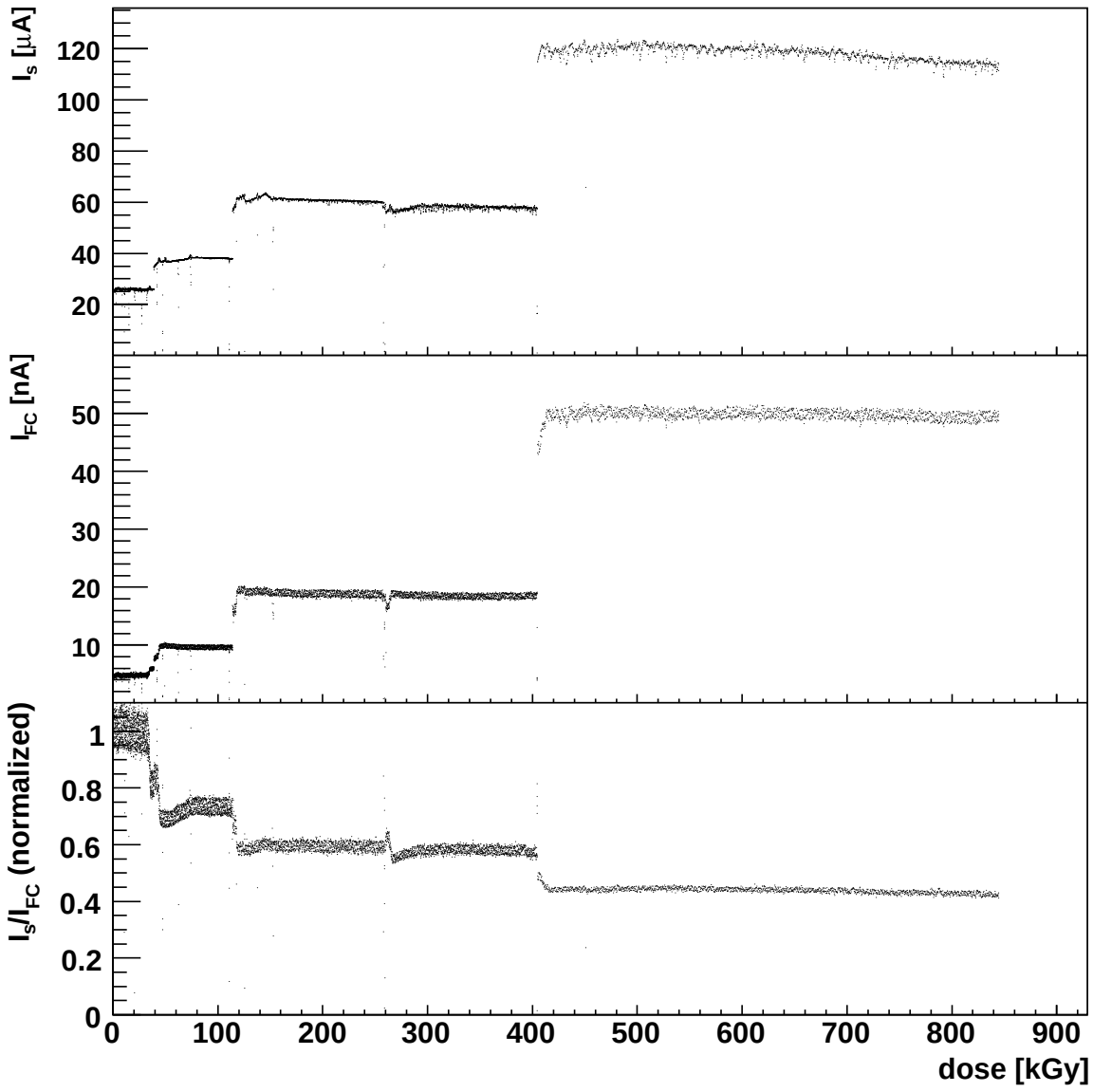

Figure 5.13: Currents of the sensor, I_s, the Faraday cup, I_FC, and the ratio of both, $I_\mathrm{s}/I_\mathrm{FC}$ as functions of the accumulated dose for GaAs sample 1.

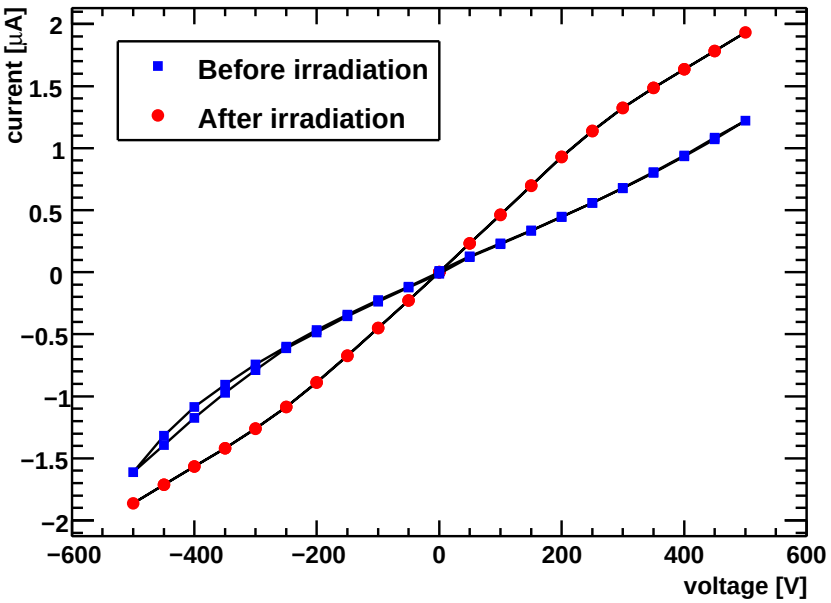

Figure 5.14: Dark current as a function voltage for GaAs sample 1, before and after the irradiation.

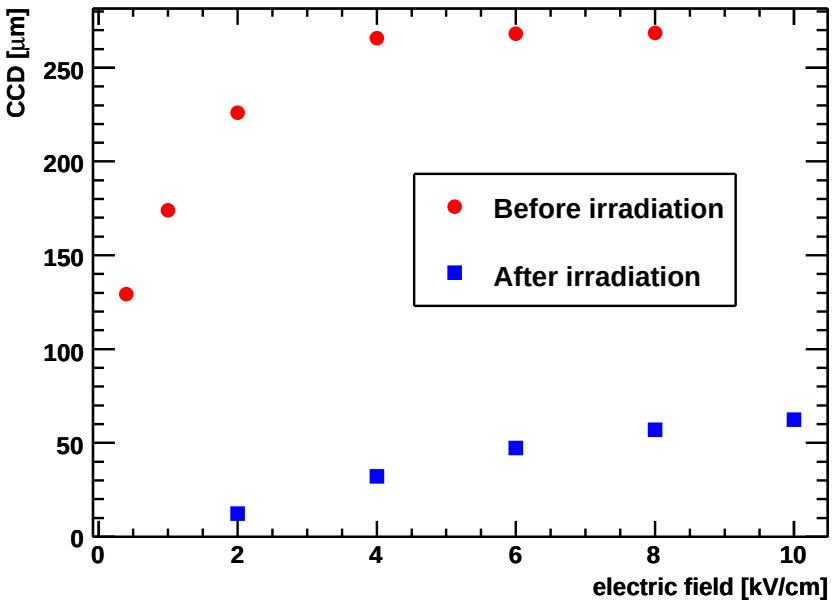

Figure 5.15: CCD as a function of the applied electric field for GaAs sample 1, before and after the irradiation.

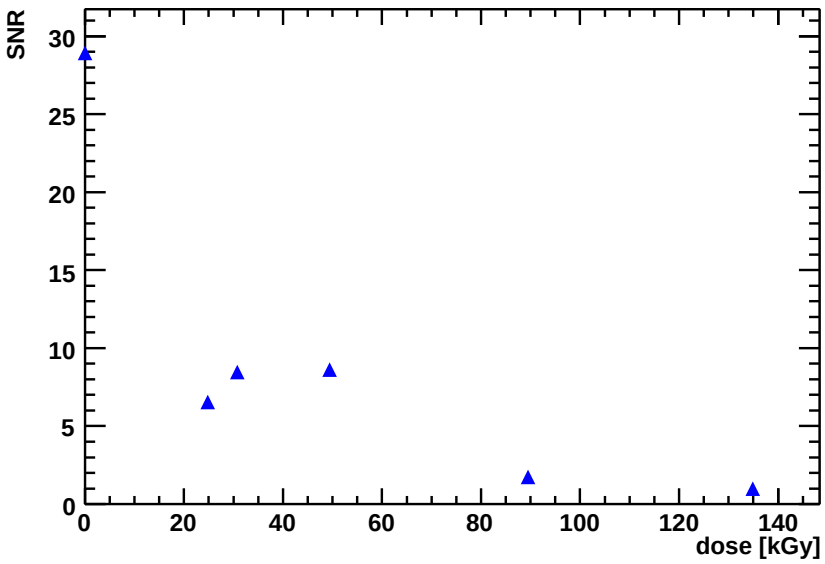

Figure 5.16: Signal-to-noise ratio as a function of the dose for the radiation hard silicon sensor sample.

The depletion voltage was determined by measuring the capacitance-voltage characteristic to be about 380 V. The silicon sample was irradiated up to 135 kGy. A voltage of 400 V (10.8 kV/cm) was applied, which is sufficient to keep the sensor permanently depleted during the irradiation.

The CCD remained constant and equal to the sensor thickness with increasing dose. The decrease in the signal-to-noise ratio with the dose, as shown in Figure 5.16, originates from an increase of the dark current to up to 3.5 μA and a huge increase of the noise correlated with this current. This silicon sample was not operational above 90 kGy, i.e. signal and pedestal could not be separated anymore. Therefore, it was ruled out as sensor, to be applied in a harsh radiation environment at room temperature such as BeamCal.

5.3 Model for the Description of the Sensor Behavior

We apply the concepts of semiconductor physics [185, 186, 187] to understand the results of the testbeam experiments, and the related laboratory measurements such as the current as a function of the voltage or the CCD as function of the electric field.

5.3.1 Basics of Semiconductor Physics

The sensor candidates under investigation are crystals. We restrict ourselves to single crystals. For polycrystalline diamonds, models were made specifically for the growth process [157, 155]. The specific crystalline structure plays however just a minor role for the current considerations.

In solid crystals, the constituting atoms are arranged in a regular pattern – a *lattice*. The symmetry of the lattice, the lattice constant and the composition of the solid determine its properties. For all crystals is in common that the atom spacing is dense such that the wave functions of highest occupied electron energy levels overlap. Due to the Pauli exclusion principle, which states that two fermions are not allowed to be in the same quantum state, the electron states delocalize. Furthermore the energetic degeneration is lost and the discrete atomic levels split into bands of allowed levels.

Except energy bands of allowed electron states, there are also bands of forbidden electron states. The solids are classified according to the occupation of these states at zero temperature. The relevant quantity is the *Fermi level*, E_F, which is defined as the chemical potential for the electrons at zero temperature, $E_\mathrm{F} = \mu(T = 0)$. E_F is the energy up to which all allowed levels are filled for $T = 0$.

In metals, the *Fermi level*, E_F, lays inside an allowed band. Minimal energies suffice to excite an electron to a higher level inside this band. The conduction process in solids corresponds to an electron jumping from lattice atom to lattice atom. The excited electron can easily jump to another lattice atom, if this state is not already occupied. The electrons in lower energy levels below E_F will most likely not participate in the conduction process.

For semiconductors and isolators the Fermi level is inside a forbidden gap – the *band gap*. Hence, for $T = 0$ the highest occupied level, E_V, is the upper edge of the so-called *valence band*, and it holds $E_\mathrm{V} < E_\mathrm{F}$. The lowest allowed not occupied level is the lower edge of the so-called *conduction band*, and it holds $E_\mathrm{F} < E_\mathrm{C}$. The spacing between E_C and E_V is called *band gap*, $E_\mathrm{gap} = E_\mathrm{C} - E_\mathrm{V}$, and the minimum energy necessary to excite an electron from the valence band to the conduction band is E_gap. There is no conduction at $T = 0$.

The classification in semiconductors and isolators is done a bit arbitrary by the size of the band gap energy. For $E_\mathrm{gap} < 3$ eV the solid is considered to be a semiconductor, whereas in the other case it is an isolator.

In general, the chemical potential, $\mu(T)$, depends on the temperature[8]. At non-zero temperatures the probability of occupation is described by the Fermi distribution, $f(E)$, which is a function of the energy E of an electron,

$$f(E) = \frac{1}{e^{\frac{E-\mu(T)}{k_\mathrm{B}T}} + 1} \,. \tag{5.15}$$

k_B is the Boltzmann constant and T the temperature.

The number of electron states in the allowed energy bands is not uniform, rather it follows a certain distribution as a function of the level energy – the *density of states*, $\mathcal{D}(E)$. For

[8]The chemical potential depends also on the impurity density, what we will completely neglect here.

three-dimensional lattices at the band edges, the density of states is proportional to $\sqrt{E}$. For the conduction band holds

$$\mathcal{D}_{\mathrm{e}}(E) \propto \sqrt{E - E_{\mathrm{C}}}\,, \qquad \text{for } E > E_{\mathrm{C}}\,,$$

where E_{C} is the energy level of the lowest allowed electron state, which is not occupied at $T = 0$, also called the conduction band edge.
In semiconductors and isolators there is also the possibility of the conduction by the drift of electrons inside the valence band, additionally to the electrical conduction by the drift of electrons in the conduction band. Since this process can be considered as jumping of electrons from one atom to the next one, the electrons have to wait until there is a free place in a neighboring atom. This process can also be considered as a free place moving in the opposite direction to the electrons and having a positive charge sign. A quasi-particle is introduced, called a *hole*, which has a positive elementary charge. One can also introduce a density of states also for the holes, $\mathcal{D}_{\mathrm{h}}(E) \propto \sqrt{E_{\mathrm{V}} - E}$, accounting for the fact that higher excited holes correspond to smaller energies of not occupied electron levels. Herein, E_{V} is the highest allowed electron level, which is still occupied at $T = 0$, also called valence band edge. In terms of holes, E_{V} is the lowest allowed hole level, which is not occupied at $T = 0$.
The motion of the electrons and holes is not completely free, but quasi-free. The lattice exerts a certain resistance to the electrons when they are jumping from one to the next atom. For the electrons and holes close to the respective band edges (i.e. the conduction band edge for the electrons and the valence band edge for the holes) this resistance can be parametrized in an effective mass. This effective mass is in general different for electrons and holes, and also depends usually on the direction of motion in the lattice.
The density of electrons, i.e. the number of electrons per unit volume, in the conduction band with an energy between E and $E + dE$ is $\mathcal{D}(E)\, f(E)\, dE$ in thermal equilibrium. Hence, the total density of electrons in the conduction band, n, is

$$n = \int_{-\infty}^{\infty} \mathcal{D}_{\mathrm{e}}(E)\, f(E)\, dE \approx N_{\mathrm{C}} e^{-\frac{E_{\mathrm{C}} - \mu(T)}{k_{\mathrm{B}} T}}\,. \tag{5.16}$$

The approximation in the last step refers to the fact that the Fermi distribution (5.15) can be approached by the Boltzmann distribution, $e^{-(E-\mu(T))/k_{\mathrm{B}}T}$, for non-degenerated semiconductors, i.e. $E_{\mathrm{C}} - \mu(T) \gg k_{\mathrm{B}}T$. This approach holds even better for isolators. N_{C} is called the *effective density of states*,

$$N_{\mathrm{C}} = 2\left(\frac{m^{\mathrm{e}}_{\mathrm{eff}} k_{\mathrm{B}} T}{2\pi\hbar^2}\right)^{3/2} = 2.5 \times 10^{19}\ \mathrm{cm}^{-3} \left(\frac{m^{\mathrm{e}}_{\mathrm{eff}}}{m_{\mathrm{e}}} \frac{T}{300\ \mathrm{K}}\right)^{3/2}\,. \tag{5.17}$$

The quantity $m^{\mathrm{e}}_{\mathrm{eff}}$ is the effective mass of the electrons. Similarly, for the density of holes in the valence band, p, we obtain

$$p \approx N_{\mathrm{V}} e^{-\frac{\mu(T) - E_{\mathrm{V}}}{k_{\mathrm{B}} T}}\,, \qquad \text{where} \quad N_{\mathrm{V}} = 2\left(\frac{m^{\mathrm{h}}_{\mathrm{eff}} k_{\mathrm{B}} T}{2\pi\hbar^2}\right)^{3/2}\,, \tag{5.18}$$

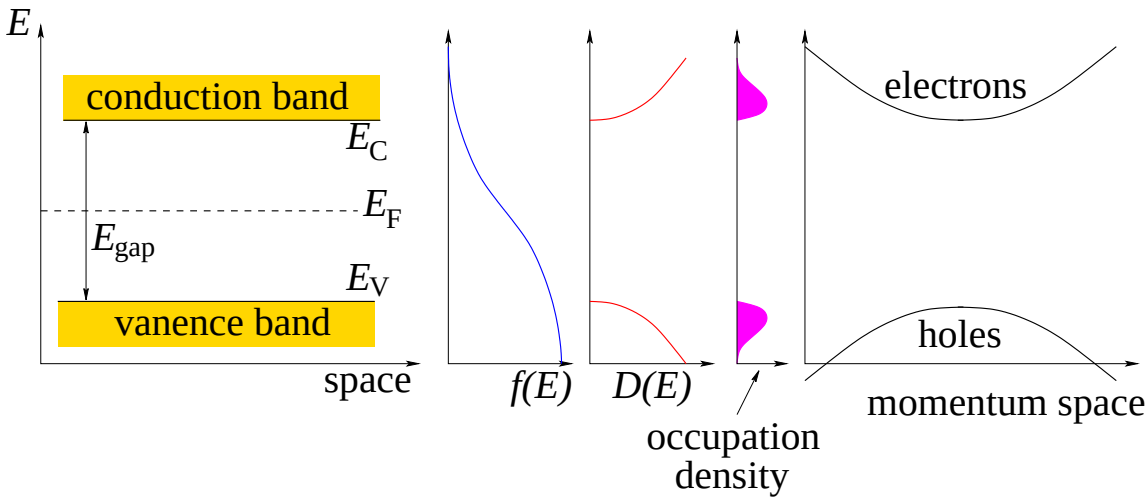

Figure 5.17: Scheme of the band gap in position space and momentum space, Fermi distribution, $f(E)$, density of states, $\mathcal{D}(E) = \mathcal{D}_\mathrm{e}(E) + \mathcal{D}_\mathrm{h}(E)$, and occupation density ($f(E)\,\mathcal{D}_\mathrm{e}(E)$ for electrons, $\big(1 - f(E)\big)\mathcal{D}_\mathrm{h}(E)$ for holes). The curvatures of the bands in the momentum space are related to the effective masses. Furthermore, the band structure determines the density of states, $\mathcal{D}(E)$.

where $m^\mathrm{h}_\mathrm{eff}$ is the effective mass of the holes. Figure 5.17 sketches the explained situation. n and p follow a kind of a law of mass action,

$$np = N_\mathrm{C} \cdot N_\mathrm{V} e^{-\frac{E_\mathrm{C}-E_\mathrm{V}}{k_\mathrm{B}T}} = N_\mathrm{C} \cdot N_\mathrm{V} e^{-\frac{E_\mathrm{gap}}{k_\mathrm{B}T}} \equiv n_i^2 \,, \tag{5.19}$$

where n_i is called the *intrinsic charge carrier density*, i.e. the carriers which contribute to the electrical conduction. It is a constant for a given semiconductor and a given temperature.
For an intrinsic semiconductor holds $n = p$. Thus, dividing both, n/p, yields

$$1 = \frac{N_\mathrm{C}}{N_\mathrm{V}} \exp\left(\frac{-E_\mathrm{C} - E_\mathrm{V} + 2\mu(T)}{k_\mathrm{B}T}\right) \quad \longrightarrow \quad \mu(T) = \underbrace{\frac{1}{2}(E_\mathrm{C} + E_\mathrm{V})}_{=E_\mathrm{F}} + \frac{3}{4} k_\mathrm{B} T \ln\left(\frac{m^\mathrm{h}_\mathrm{eff}}{m^\mathrm{e}_\mathrm{eff}}\right) \,.$$

Hence, at small temperatures or for $m^\mathrm{e}_\mathrm{eff} \approx m^\mathrm{h}_\mathrm{eff}$, it holds $\mu(T) = E_\mathrm{F}$, the value of which is located in the center of the band gap for an intrinsic semiconductor. We use throughout this thesis the approximation $\mu(T) \equiv E_\mathrm{F}$.

5.3.2 Drift-Diffusion Model

We define the current densities for electrons and holes, $\vec{j}_\mathrm{e}$ and $\vec{j}_\mathrm{h}$, by

$$\vec{j}_\mathrm{e} = e\mu_\mathrm{e} n \vec{\mathcal{E}} + \mu_\mathrm{e} k_\mathrm{B} T \nabla n \,, \qquad \vec{j}_\mathrm{h} = e\mu_\mathrm{h} p \vec{\mathcal{E}} - \mu_\mathrm{h} k_\mathrm{B} T \nabla p \,. \tag{5.20}$$

The first terms in each equation represent the drift currents driven by an external electric field $\vec{\mathcal{E}}$. μ_{e} and μ_{h} are the respective mobilities of electrons and holes, i.e. the proportionality factor between drift velocity and electric field,

$$\vec{v}_{\mathrm{drift}} = \pm\mu\vec{\mathcal{E}} \qquad \text{(minus sign for electrons)} \; . \tag{5.21}$$

The drift current can be written as $\vec{j} = q\vec{v}_{\mathrm{drift}}$, where q is the particle charge. Since holes and electrons have opposite sign of the charge, they drift also in different directions. Thus, the electron and hole current densities point in the same direction.
The second terms are the diffusion current contributions driven by spatial differences in the charge carrier density. It represents the affinity of the system to equally distributed charge carrier densities in the thermal equilibrium. The proportionality factor between the diffusion current and the gradient of the charge carrier density is the diffusion constant, $D_{\mathrm{e,h}}$, which is related to the mobility by the Einstein relation [188, 189, 190]

$$D_{\mathrm{e,h}} = \mu_{\mathrm{e,h}} k_{\mathrm{B}} T/e \; .$$

To describe dynamic, non-equilibrium effects we use the continuity equation ensuring local charge conservation:

$$\frac{\partial n}{\partial t} = \frac{1}{e}\nabla \cdot \vec{j}_{\mathrm{e}} + G_{\mathrm{e}} - R_{\mathrm{e}} \; , \qquad \frac{\partial p}{\partial t} = -\frac{1}{e}\nabla \cdot \vec{j}_{\mathrm{h}} + G_{\mathrm{h}} - R_{\mathrm{h}} \; . \tag{5.22}$$

The density of charges in a volume is changed either by in or out flowing currents or by generation of charges, $G_{\mathrm{e,h}}$, and by a loss of charges, $R_{\mathrm{e,h}}$.

The Intrinsic Semiconductor

We consider first the case of uniformly distributed charge carriers, i.e. there is no space dependence of n and p. In this case, the current densities are constants and do not contribute to the change of the charge carrier densities inside the bands. For intrinsic semiconductors, the generation of electrons is due to the thermal excitation from the valence band, creating in addition also a hole. The opposite process is called *recombination*. We can write the rate equation for the density of electrons in the conduction band,

$$\frac{dn}{dt} = \frac{dp}{dt} = g(T) - rnp \; .$$

The recombination term is proportional to np, i.e. $R_{\mathrm{e}} = R_{\mathrm{h}} = rnp$. In equilibrium, that is for $\frac{dn}{dt} = \frac{dp}{dt} = 0$, we therefore obtain using (5.19) $g(T) \equiv G_{\mathrm{e}} = G_{\mathrm{h}} = rnp = rn_i^2$, where n_i depends only on the temperature. Inserting for $g(T)$ results in

$$\frac{dn}{dt} = \frac{dp}{dt} = r(n_i^2 - np) \; . \tag{5.23}$$

r represents the reaction speed with which the system returns to the equilibrium state and has the unit cm^3/s. This can be seen by considering small perturbations from the

equilibrium states n_0 and p_0, that is $n = n_0 + \delta n$ and $p = p_0 + \delta p$. Omitting higher order terms, e.g. $(\delta n)(\delta p)$, we obtain

$$\frac{d\delta n}{dt} = r(\underbrace{n_i^2 - n_0 p_0}_{=0} - n_0\,\delta p - p_0\,\delta n) = -r(n_0 + p_0)\,\delta n\ . \tag{5.24}$$

Here, we exploited $\delta p = \delta n$ to ensure neutrality. Solving this equation leads to

$$\delta n(t) = \delta n(0)\,\exp(-t/\tau_{\mathrm{R}})\ , \quad \text{with} \quad \tau_{\mathrm{R}} = \frac{1}{r(n_0 + p_0)} = \frac{1}{2rn_i}\ . \tag{5.25}$$

The quantity τ_{R} is the characteristic time constant for the return to the equilibrium by recombination or thermal excitation. r can be expressed by $r = \sigma_{\mathrm{eh}} v_{\mathrm{th}}^{\mathrm{e,h}}$, where σ_{eh} denotes the cross-section for the electron-hole creation or recombination. $v_{\mathrm{th}}^{\mathrm{e,h}}$ is the thermal speed of the electrons or holes, and is given by equating thermal and kinetic energy,

$$v_{\mathrm{th}}^{\mathrm{e,h}} = \sqrt{\frac{3k_{\mathrm{B}}T}{m_{\mathrm{eff}}^{\mathrm{e,h}}}}\ . \tag{5.26}$$

Current as a Function of the Electric Field

Still, we consider all variables to be space independent. The current has then only the drift contribution. When an electric field is applied the total current density is then according to Equation (5.20)

$$\vec{j} = \vec{j}_{\mathrm{e}} + \vec{j}_{\mathrm{h}} = e(\mu_{\mathrm{e}} n_0 + \mu_{\mathrm{h}} p_0)\vec{\mathcal{E}} = e(\mu_{\mathrm{e}} + \mu_{\mathrm{h}}) n_i \vec{\mathcal{E}}\ , \tag{5.27}$$

where in the last step $n_0 = p_0 = n_i$ is assumed. This is *Ohm's law*, and the proportionality factor between the current density and the electric field is the conductivity

$$\sigma_{\mathrm{cond}} = e(\mu_{\mathrm{e}} n_0 + \mu_{\mathrm{h}} p_0) = e(\mu_{\mathrm{e}} + \mu_{\mathrm{h}}) n_i\ . \tag{5.28}$$

The conductivity in semiconductors is determined by two factors, the number of available charge carriers and the intrinsic resistance against the drift, i.e. the mobility. Using Equation (5.19) one can specify

$$\sigma_{\mathrm{cond}} = e(\mu_{\mathrm{e}} + \mu_{\mathrm{h}})\sqrt{N_{\mathrm{V}} N_{\mathrm{C}}}\, e^{-E_{\mathrm{gap}}/(2k_{\mathrm{B}}T)}\ . \tag{5.29}$$

Thus, for semiconductors with a given band gap the conductivity increases with the temperature. This effect becomes more pronounced, the smaller the band gap is. For instance, we expect for GaAs a stronger temperature dependence of the dark current than for diamond at smaller voltages.

The Role of Impurities

In real semiconductors the lattice structure is usually not perfect. There are lattice atom displacements or vacancies due to the entropy at finite temperatures. Also by irradiation with ionizing particles lattice defects will be introduced. Such *point defects*, i.e. spatially localized lattice defects, can create localized electronic states inside the forbidden band gap. Depending on the kind of the defect several interaction processes of electrons in the conduction or valence band with these intra-gap states are possible. The electrons from the conduction band might be captured in such an defect state, or released from it to the conduction band. A captured electron can also recombine with a hole from the valence band (hole capture) or, finally, an electron can be excited to the defect state from the valence band whereby a hole is created in the valence band (hole emission). Figure 5.18 shows the basic interaction processes. We call defect levels with an energy close to the band

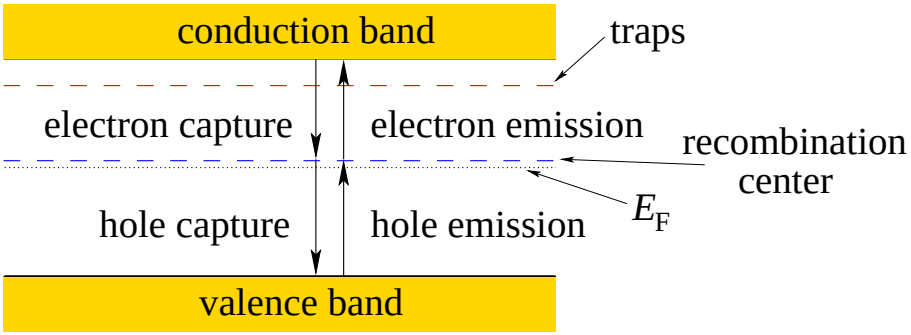

Figure 5.18: Schematic overview about the energetic location of the levels of traps and recombination centers, and the basic interaction processes. The arrows indicate the electron movement.

edges *traps*. On the other hand, levels close to the Fermi level are called *recombination centers*. For the latter, all the above mentioned processes are of similar probability, whereas for traps only the capture or release of the charge carriers to the closest band occur, i.e. electron traps dominantly capture and release electrons from and to the conduction band. Eventually, electrons and holes can simply scatter on defects, which contributes to the resistance.

There is a variety of possible point defects. A *substitial* is an impurity atom, which replaces a lattice atom. Impurity or lattice atoms can be positioned at *interstitials*. A *vacancy* is a missing atom at a lattice atom position. Even more complex defects are possible. If a defect level can provide an additional electron to the conduction band, i.e. the energy is close to the conduction band, it is called a *donor*. These are elements possessing one outer electron more than the lattice atoms. A defect level close to the valence band, which is able to accept an electron from the valence band, is called an *acceptor*. Donors and acceptors are neutral in their ground states, i.e. if the donor level is filled and the acceptor level is empty, respectively. However, traps and recombination centers can have an effective non-integer charge and , specifically, different charge states depending of whether they are

occupied or not. Color centers are vacancies in ion crystals, which might represent a locally negative or positive *partial charge*. Positive partial charges can attract electrons from the conduction band and act, thus, as traps. Then the filled trap has a negative partial charge repulsing other electrons in conduction band. It is difficult, however, to determine the effective charge of a trap.
It is also difficult to calculate precisely the defect energy levels. One way is to consider a point defect as a hydrogen atom-like charge, screened by the surrounding electrons of the solid. One starts from the electronic energy spectrum of the hydrogen atom [187],

$$E_n^H = \frac{m_\mathrm{e} e^4}{2(4\pi\varepsilon_0\hbar)^2}\frac{1}{k^2} \quad (k = 1, 2, \ldots) \; . \tag{5.30}$$

The electron mass, m_e, has to be replaced by the effective mass, $m_\mathrm{eff}^\mathrm{e}$, ε_0 by $\varepsilon\varepsilon_0$, where ε is the relative permittivity of the considered semiconductor, and e by ϱe where ϱ is the effective charge of the trap in terms of e. This yields for the defect level, E_n^defect,

$$E_n^\mathrm{defect} = \frac{m_\mathrm{eff}^\mathrm{e}}{m_\mathrm{e}}\frac{1}{\varepsilon^2}\varrho^4 E_n^H \; . \tag{5.31}$$

The ground state level ($k = 1$) of a simple donor is equal to $E_1^\mathrm{defect} \approx 0.6$ eV below the conduction band for diamond, using $m_\mathrm{eff}^\mathrm{e} = 1.4 m_\mathrm{e}$, $\varepsilon = 5.7$ [168] and $\varrho = 1$. This is at least not far from the measured value of about 1 eV [157]. Similar to the hydrogen atom, there should be a lot of discrete defect levels, which become closer to each other with higher energy, until they pass into the quasi-free continuum of the conduction band.
Equation (5.31) is, however, independent on the specific type of the defect or the impurity atom. In principle, the Coulomb potential must be replaced by a more general potential, which reflects the charge distribution causing the bound states. Finally, the Coulomb potential can be replaced by a Yukawa potential to account for the screening, which was formerly respected by the introduction of the relative dielectricity, ε.

For simplicity, we restrict ourselves to the consideration of electron traps. About the charge state of the traps we cannot decide. Let the density of traps be N_T. A trap can be filled or empty. The trap fill density is denoted by n_T. Then the rate equation for n_T can be written as [185]

$$\frac{dn_\mathrm{T}}{dt} = c_\mathrm{e}\left(n(N_\mathrm{T} - n_\mathrm{T}) - N_\mathrm{C} e^{-\frac{E_\mathrm{C}-E_\mathrm{T}}{k_\mathrm{B}T}} n_\mathrm{T}\right) \; , \tag{5.32}$$

where the first term represents the electron capture and the second term the electron emission. N_C is given in Equation (5.17). Similar to the thermal electron-hole pair creation also the electron emission to the conduction band just depends on the temperature and the distance between the conduction band edge, E_C, and the trap level, E_T. Of course, if $n_\mathrm{T} = 0$, no electron can be emitted anymore. c_e parametrizes the reaction speed with which the equilibrium is reached. It can also be written as $c_\mathrm{e} = v_\mathrm{th}^\mathrm{e}\sigma_\mathrm{e}$, where σ_e is the cross-section for electron capture and release.

Since the electrons, which are trapped, are removed from, and those, which are released, are added to the conduction band electron density, we have to subtract $\frac{dn_\mathrm{T}}{dt}$ from the right-hand-side of $\frac{dn}{dt}$ in (5.23). The equation for the holes stays unchanged.

In the equilibrium we again demand $\frac{dn_0}{dt} = \frac{dp_0}{dt} = \frac{dn_\mathrm{T}^0}{dt} = 0$. From Equation (5.32) it immediately follows that

$$n_\mathrm{T}^0 = \frac{n_0 N_\mathrm{T}}{n_0 + N_\mathrm{C} \exp\left(-\frac{E_\mathrm{C}-E_\mathrm{T}}{k_\mathrm{B}T}\right)} = N_\mathrm{T}\, f(E_\mathrm{T}) \;, \tag{5.33}$$

as it must be in thermal equilibrium and using Equations (5.15) and (5.16). No trap is filled if $n_0 = 0$, and almost every trap is filled for $n_0 \to \infty$.

If the effective charge of an empty trap in units of the elementary charge is $\varrho \in [0, 1]$, the charge of a filled trap is $\varrho - 1$. The neutrality requires

$$0 = p_0 - n_0 + \varrho(N_\mathrm{T} - n_\mathrm{T}^0) + (\varrho - 1)n_\mathrm{T}^0 = p_0 - n_0 + \varrho N_\mathrm{T} - n_\mathrm{T}^0 \;.$$

Using $n_0 p_0 = n_i^2$ and the Equations (5.16) and (5.33), we obtain

$$0 = \frac{n_i^2}{n_0(E_\mathrm{F})} - n_0(E_\mathrm{F}) + N_\mathrm{T}\big(\varrho - f(E_\mathrm{T})\big) \;,$$

which is an implicit equation for $\mu(T)$ ($= E_\mathrm{F}$ for $T = 0$) as a function of ϱ, E_gap, E_T, N_T, the temperature, and the effective masses of electrons and holes.

Applying small perturbations to the equilibrium charge carrier densities, $n = n_0 + \delta n$ and $n_\mathrm{T} = n_\mathrm{T}^0 + \delta n_\mathrm{T}$, one can again investigate how fast the system returns to the equilibrium, similar as was done for the recombination. We obtain the changing rates for δn and δn_T, respectively,

$$\frac{d\,\delta n_\mathrm{T}}{dt} = -\frac{d\,\delta n}{dt} = c_\mathrm{e}\left((N_\mathrm{T} - n_\mathrm{T}^0)\,\delta n - \left(n_0 + N_\mathrm{C} e^{-\frac{E_\mathrm{C}-E_\mathrm{T}}{k_\mathrm{B}T}}\right)\,\delta n_\mathrm{T}\right) \;.$$

The characteristic time constant for changes of the conduction band electron density by trapping is then given by

$$\frac{1}{\tau_\mathrm{T}} = \frac{1}{c_\mathrm{e}(N_\mathrm{T} - n_\mathrm{T}^0)} \qquad = \frac{1 + e^{-\frac{E_\mathrm{T}-E_\mathrm{F}}{k_\mathrm{B}T}}}{c_\mathrm{e} N_\mathrm{T}} \text{ for thermal equlibrium} \;, \tag{5.34}$$

and the time constant for changing the trap fill density by

$$\frac{1}{\tau_\mathrm{T}^{N_\mathrm{T}}} = \frac{1}{\tau_c} + \frac{1}{\tau_e} \;, \quad \text{with} \quad \tau_c = \frac{1}{c_\mathrm{e} n_0} \;, \quad \tau_e = \frac{1}{c_\mathrm{e} N_\mathrm{C} e^{-\frac{E_\mathrm{C}-E_\mathrm{T}}{k_\mathrm{B}T}}} \;. \tag{5.35}$$

Herein, τ_e is the characteristic time for electron emission from a trap to the conduction band. It becomes dominant at larger temperatures, and can be neglected at smaller temperatures.
τ_T and τ_c are the characteristic times for electron capture from the conduction band by a trap for two different limiting cases. τ_T describes the change of the electron density in the conduction band, if $\frac{\delta n}{n_0} \gg \frac{\delta n_\mathrm{T}}{N_\mathrm{T}-n_\mathrm{T}^0}$ holds. The change of the conduction band electron density is measurable as change of the current flowing through the sensor. This time scale will be important for the CCD measurement if it is dominant.
On the other hand, τ_c describes the change of the trap fill density, if $\frac{\delta n}{n_0} \ll \frac{\delta n_\mathrm{T}}{N_\mathrm{T}-n_\mathrm{T}^0}$ holds. This condition is fulfilled if n_0 is rather large by high injection due to eh-pair creation in the testbeam experiment, or when the sensor is pumped using a ^{90}Sr source, where eventually $N_\mathrm{T} - n_\mathrm{T}^0$ approaches zero.
In total, both recombination and trapping will occur for an electron in the conduction band. The total time constant for the relaxation to the equilibrium state, τ_relax, is also called the life time of an electron in the conduction band and is given by

$$\frac{1}{\tau_\mathrm{relax}} = \frac{1}{\tau_\mathrm{R}} + \frac{1}{\tau_\mathrm{T}} \,, \tag{5.36}$$

where τ_R is the recombination time constant as given in Equation (5.25). Hence, the shorter time constant dominates the total time constant. If there are more defect levels with an intrinsic time constant each, τ_i, then the total time constant is $\tau_\mathrm{relax}^{-1} = \sum_i \tau_i^{-1}$, and the shortest partial time scale dominates τ_relax.

The mobility may be also affected by the impurities. There are several contributions to the mobility. This can be understood in the framework of the Drude theory [191]. The electrons inside a solid, accelerated in an electric field, are scattered on defects and phonons. Thereby, the resistance or the conductivity is explained. The mobility can be related to the mean time between two scattering events, τ_scatter, by

$$\mu = \frac{e\tau_\mathrm{scatter}}{m_\mathrm{eff}} \,. \tag{5.37}$$

This characteristic time, τ_scatter, is related to the time constants of scattering on defects, $\tau_\mathrm{s,T}$, and that on phonons $\tau_\mathrm{s,ph}$, by

$$\frac{1}{\tau_\mathrm{scatter}} = \frac{1}{\tau_\mathrm{s,T}} + \frac{1}{\tau_\mathrm{s,ph}} \,.$$

Again, the shorter time constant dominates the total characteristic time behavior. One can rewrite this equation in terms of mobilities using Equation (5.37), which is known as *Matthiessen's rule* [185],

$$\mu_0^{-1} = \mu_\mathrm{s,T}^{-1} + \mu_\mathrm{s,ph}^{-1} \,. \tag{5.38}$$

The mobility caused by scattering on defects, $\mu_\mathrm{s,T}$, is proportional to N_T^{-1} [186] just as $\tau_\mathrm{s,T}$. If the defect density increases with the time e.g. by radiation damages, $\mu_\mathrm{s,T}$ can become

smaller than the mobility due to phonon scattering, if it is not already.

If the externally applied electric field, $\vec{\mathcal{E}}$, approaches values leading to a drift speed comparable to the thermal speed ($v_{\mathrm{th}} \approx 10^7 \mathrm{cm/s}$ estimated at room temperature with m_{e} as effective mass), then the mobility starts to depend on the electric field and the drift speed saturates. This can be parametrized as [156]

$$\mu(\mathcal{E}) = \frac{\mu_0}{1 + \mathcal{E}/\mathcal{E}_{\mathrm{saturate}}} \,, \tag{5.39}$$

where μ_0 is the low-field mobility, as given by Equation (5.38), $\mathcal{E}$ is the magnitude of $\vec{\mathcal{E}}$, and $\mathcal{E}_{\mathrm{saturate}} \approx v_{\mathrm{th}}/\mu_0$ the electric field, at which the drift speed saturates. Therefore, if the low-field mobility μ_0 decreases then the saturation field increases. Equation (5.39) holds for e.g. diamond. The drift speed of GaAs shows a more complicated dependency on the electric field, and another parametrization has to be used [168, 192]. The saturation field $\mathcal{E}_{\mathrm{saturate}}$ depends on the temperature and N_{T} via v_{th} and μ_0, respectively, because μ_0 is proportional to N_{T}^{-1} as outlined above. Finally, there are different mobilities for electrons and holes.

5.3.3 Refining the Understanding of the Charge Collection Distance

We defined the CCD in Equation (5.7) in terms of the ratio of charges induced by the ionizing particle and collected on the electrodes, respectively. We want to use the drift-diffusion model to understand this ratio, and therefore the CCD, as a function of the intrinsic material parameters, such as the relaxation time, Equation (5.36), the mobility, Equation (5.38), and of the electric field.
We solve the Equations (5.22) and (5.20) for the following one-dimensional time-dependent scenario, as illustrated in Figure 5.19. We choose the z-axis perpendicular to the electrode planes. Starting with the equilibrium state, a primary charged particle passes through the

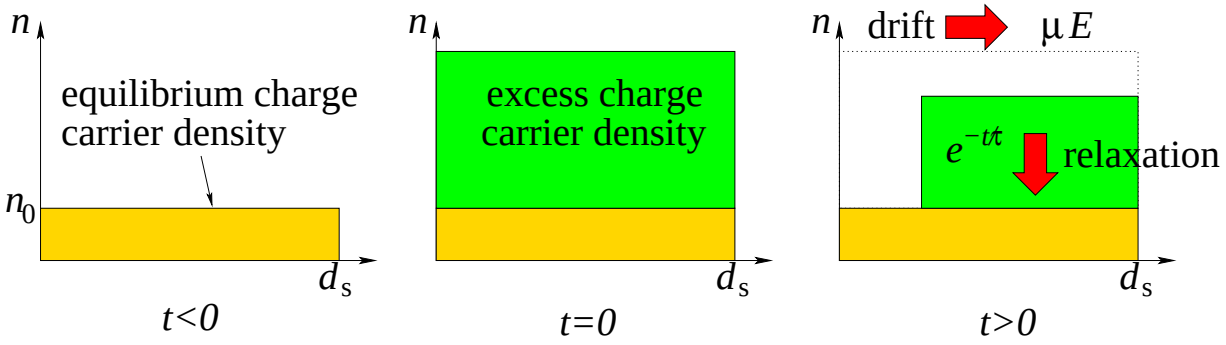

Figure 5.19: A simplified sketch of the signal current evolution by relaxation and drift processes.

sensor and excites electrons from the valence to the conduction band at time $t = 0$. If there

is no electric field applied the system would relax back to the equilibrium by recombination or trapping processes. If there is an electric field the charge carriers drift according to the electric field direction towards the electrodes, where they are collected. If no relaxation would occur then all charges would finally reach the electrodes.
Let the excess charge carrier density be n'. Then the charge carrier density in the conduction band as a function of z and t being a solution of the drift-diffusion equation can be written as

$$n(z,t) = n_i + n' e^{-t/\tau_{\text{relax}}} \theta(t) \theta\big(d_\text{s}/(\mu\mathcal{E}) - t\big) \theta(z - \mu\mathcal{E}t) \theta(d_\text{s} - z) \ , \tag{5.40}$$

where n_i is the equilibrium charge carrier density. $\theta(x)$ denotes the Heaviside function, i.e. $\theta(x) = 0$ for $x \leq 0$, else $\theta(x) = 1$. The first two θ-functions restrict the excess charge carrier density between $t = 0$, when they are injected, and

$$t_{\text{drift}} = \frac{d_\text{s}}{\mu\mathcal{E}} \ , \tag{5.41}$$

when the last charges arrive at the electrode. The last two θ-functions restrict the excess charge carrier density in space, on the right by the electrode and on the left by the drift process.
The current flowing in the sensor is

$$\begin{aligned} I_\text{s}(t) &= e\mu\mathcal{E} A_\text{s} \frac{1}{d_\text{s}} \int_0^{d_\text{s}} dz \, n(z,t) \\ &= I_{\text{dark}} + e\mu\mathcal{E} A_\text{s} n' \left(1 - \frac{\mu\mathcal{E}}{d_\text{s}} t\right) e^{-t/\tau_{\text{relax}}} \theta(t) \theta\big(d_\text{s}/(\mu\mathcal{E}) - t\big) \ , \end{aligned} \tag{5.42}$$

where $I_{\text{dark}} = e\mu\mathcal{E} A_\text{s} n_i$ is the dark current, and A_s the electrode area. The signal charge collected at the electrodes, Q_{coll} in Equation (5.7), is determined by

$$\begin{aligned} Q_{\text{coll}} &= \int dt \, \big(I_\text{s}(t) - I_{\text{dark}}\big) \\ &= Q_{\text{ind}} \frac{\tau_{\text{relax}}\mu\mathcal{E}}{d_\text{s}} \left[1 - \frac{\tau_{\text{relax}}\mu\mathcal{E}}{d_\text{s}} \left(1 - e^{-d_\text{s}/(\tau_{\text{relax}}\mu\mathcal{E})}\right)\right] \ . \end{aligned} \tag{5.43}$$

The induced charge is given by $Q_{\text{ind}} = en' A_\text{s} d_\text{s}$ and was already introduced in Equation (5.3) in terms of the energy deposition causing the perturbation from the equlibrium. The comparison with Equation (5.7) provides

$$\text{CCD} = \frac{Q_{\text{coll}}}{Q_{\text{ind}}} d_\text{s} = \tau_{\text{relax}}\mu\mathcal{E} \left[1 - \frac{\tau_{\text{relax}}\mu\mathcal{E}}{d_\text{s}} \left(1 - e^{-d_\text{s}/(\tau_{\text{relax}}\mu\mathcal{E})}\right)\right] \ . \tag{5.44}$$

This is the CCD in terms of the relevant material parameters and the electric field. We can introduce the *mean drift length* of electrons,

$$\lambda = \tau_{\text{relax}}\mu\mathcal{E} \ , \tag{5.45}$$

after which the excess charges are recombined or trapped in average. A probabilistic approach of the transport process of the charge carriers in the electric field and the effect of it on the collected charge is sketched in Appendix E.1 and leads to the same CCD as a function of λ as in Equation (5.44).
We rewrite Equation (5.44) in terms of the dimensionless charge collection efficiency, CCE, and the dimensionless drift length parameter, $y = \lambda/d_\mathrm{s}$,

$$\mathrm{CCE} = y\big(1 - y(1 - e^{-1/y})\big) \ . \tag{5.46}$$

Figure 5.20 shows $2 \cdot \mathrm{CCE}$ as function of y. The factor of two accounts for both charge carrier types, electrons and holes.

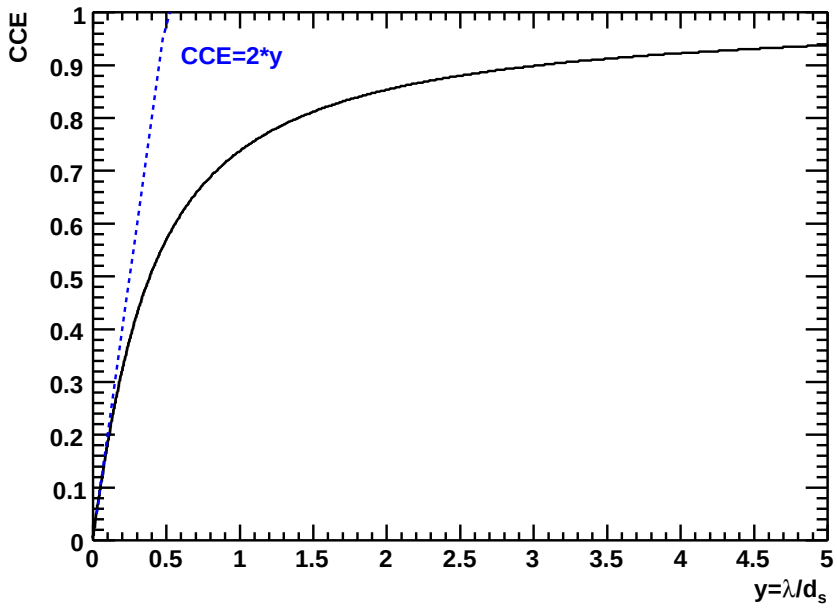

Figure 5.20: Charge collection efficiency (CCE) as function of the dimensionless drift length parameter $y = \lambda/d_\mathrm{s}$. The line $\mathrm{CCE} = 2 \cdot y$ is also shown for comparison.

If only one charge carrier type is considered then the maximum CCE is just 1/2 because the carriers cover in average at most a distance of half the sensor thickness. For both electrons and holes, however, a CCD can be derived as in Equation (5.44), where each depends on the mobility and relaxation time corresponding to the charge carrier type, respectively. The total CCD is therefore the sum of the CCDs due to the electron and the hole drift, and approaches in maximum the sensor thickness,

$$\mathrm{CCD}_\mathrm{total} = \mathrm{CCD}_\mathrm{e} + \mathrm{CCD}_\mathrm{h} \ .$$

For a very large mean drift length, e.g. for $\lambda \gtrsim 50 d_\mathrm{s}$, the CCE is almost one and the CCD equal to the sensor thickness. In this case, the CCD is said to be *sensor thickness limited*.

If λ is limited by the mobility, i.e. the drift velocity, or by the relaxation time, and smaller then about ten times d_s, then the CCD is limited by the material properties. For a CCE smaller than about 30 % the CCD and λ can be equated as a good approximation.

CCE as a Function of the Electric Field and Comparison with Measurements

In Figure 5.21, we show for a sensor thickness of $d_s = 500$ μm and a thermal speed of $v_{th} = 10^7$ cm/s the CCE, given by Equation (5.46), as a function of the electric field for several low-field mobilities and relaxation time constants, τ_{relax}. Values of the CCE smaller than one originate either from small values of τ_{relax} or from a small drift speed either due to a small low-field mobility or due to a small electric field applied to the sensor. These predictions are now compared to measurements. If the drift speed saturates also the CCE saturates, but possibly with a value smaller than one. Therefore, the CCE is limited either by the drift speed or by the sensor thickness.

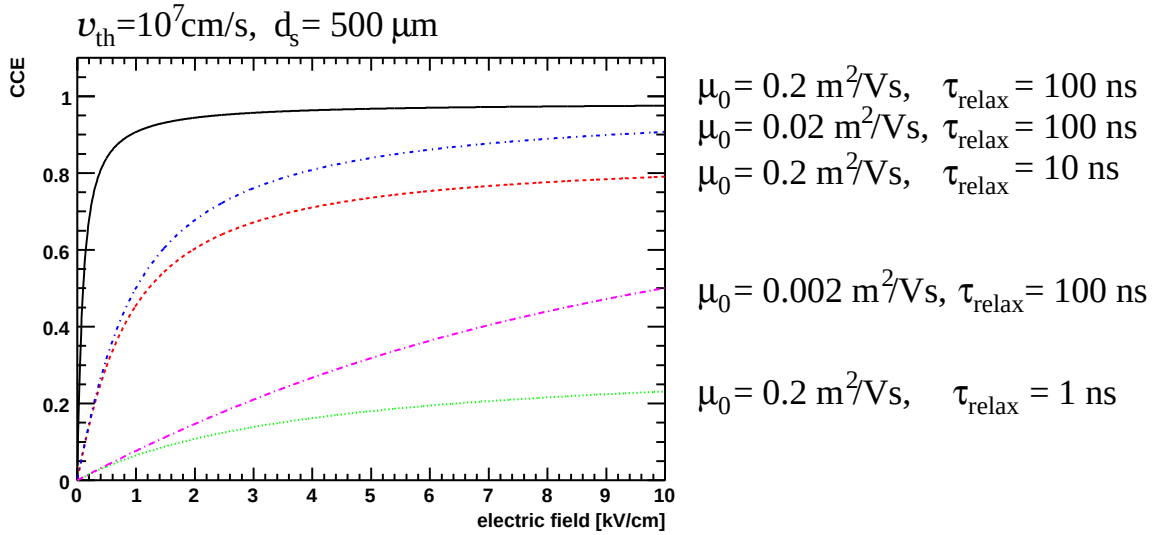

Figure 5.21: Charge collection efficiency (CCE) as function of the electric field, $\mathcal{E}$, for different combinations of the relaxation time and the mobility. The solid line represents a case, where the CCE is limited by the sensor thickness. The other lines represent cases with a drift speed limited CCE in the considered voltage range.

In Figure 5.15, the CCD of GaAs is shown as a function of the electric field, before and after irradiation. Before the irradiation, the CCD approaches at $\mathcal{E} \approx 4$ kV/cm about half of the sensor thickness, i.e. a CCE of about 50 %, and stays constant with a further increasing electric field. The reason might be that only one charge carrier type contributes to the sensor current, whereas the other type of charge carriers is suppressed by a small mobility or a high trapping probability. In the case that both charge carrier types contribute to the signal, the mobility and relaxation times of each carrier type must have accidentally values leading to a CCE of 50 %. A third possible explanation is that the doping densities are not uniformly distributed over the sensor thickness as assumed in the previous cases.

Then, local space charge regions can be formed causing low-field regions, which contribute only little to the CCE. Then, effectively only one half of the sensor thickness is used for the charge drift process.
Measurements of the CCE as a function of $\mathcal{E}$ for scCVD and pcCVD diamond are given in Figure 5.22. The scCVD diamond was not irradiated. Its CCE is limited by the sensor thickness and saturates at about 1 kV/cm. For the pcCVD diamond, CCEs as functions of the electric field are shown before and after the irradiation. Even before the irradiation, the CCE is at most slightly larger than 20 % of the sensor thickness at 10 kV/cm and does not saturate up to this electric field. After the irradiation, the CCE is reduced by 30 % of that before the irradiation. After an illumination with UV light, which should cause a release of the trapped charge carriers, the CCE diminishes further down to about 8 % at 10 kV/cm. Qualitatively, we assume that the trapping mechanism becomes again active after releasing the trapped electrons, i.e. τ_{relax} becomes essentially τ_{T}, the trapping time constant. Before the UV illumination, the traps were mostly filled and could not catch charge carriers.

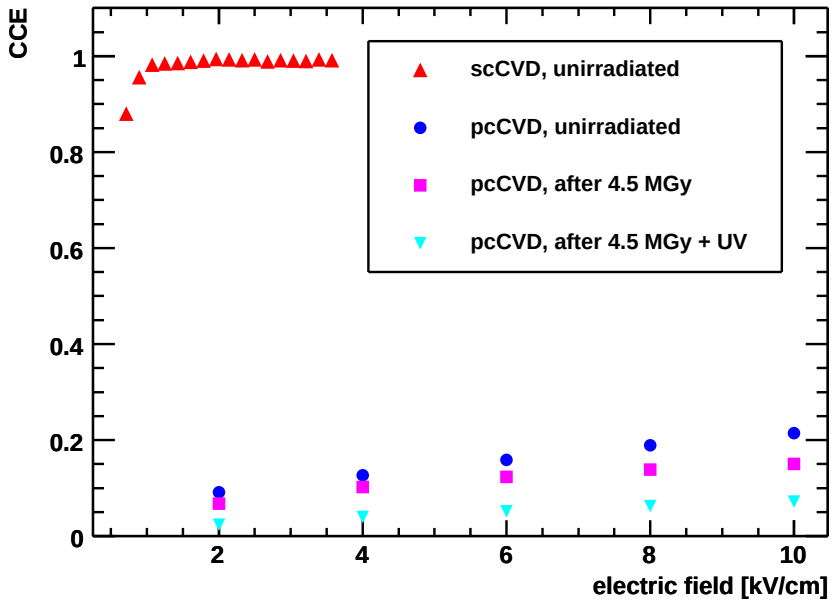

Figure 5.22: CCE as function of the electric field, $\mathcal{E}$, for the scCVD and pcCVD diamond (sample 1) samples before and after irradiation.

Using Equation (5.46), we can qualitatively understand the measurements of the CCE as a function of $\mathcal{E}$. However, since τ_{relax} and μ_0 might be different for electrons and holes, we cannot determine these quantities separately from the measurements. Only, if we assume $\mu_{\text{e}} = \mu_{\text{h}}$ and τ_{relax} also equal for electrons and holes, i.e. $\text{CCD}_{\text{e}} = \text{CCD}_{\text{h}}$, we can determine a relaxation time and a mobility.

5.3.4 Radiation Damage

To describe the CCD or the CCE as function of the accumulated dose, D, we have to relate D to the total defect density, N_T. Both, the mobility and the trapping time constant depend on N_T^{-1} and can be thereby related to the dose, as well.
The atom density of the sensor material is $n_\mathrm{A} = \rho N_A / A$. We can write a rate equation for N_T as

$$\frac{dN_\mathrm{T}}{dt} = \sigma_\mathrm{T} \phi (n_\mathrm{A} - N_\mathrm{T}) \,, \tag{5.47}$$

where σ_T is the cross-section for the creation of the defects. Since it is a priori unknown, we assume σ_T to be very small. ϕ is the flux of impinging electrons as introduced in Equation (5.13). Dose and flux are related to each other and to the Faraday cup current as shown in Section 5.2.2. If $N_\mathrm{T} \ll n_\mathrm{A}$, then Equation (5.47) simplifies to

$$\frac{dN_\mathrm{T}}{dt} = \sigma_\mathrm{T} \phi n_\mathrm{A} = \sigma_\mathrm{T} \rho \frac{n_\mathrm{A}}{\langle d\varepsilon_\mathrm{dep}/dx \rangle} \frac{dD}{dt} = \frac{\sigma_\mathrm{T} \rho^2 N_A}{\langle d\varepsilon_\mathrm{dep}/dx \rangle A} \frac{dD}{dt} \,,$$

where in the second step Equation (5.14) was used. This equation can be solved easily, because only N_T and D depend on the time,

$$N_\mathrm{T}(D) = N_\mathrm{T}^0 + \frac{\sigma_\mathrm{T} \rho^2 N_A}{\langle d\varepsilon_\mathrm{dep}/dx \rangle A} D \,, \tag{5.48}$$

with N_T^0 being the defect density before the irradiation.

CCE as a Function of the Dose

We can replace $\lambda = \tau_\mathrm{relax} \mu(\mathcal{E})\, \mathcal{E}$ in CCE(λ), Equation (5.46). τ_relax depends via Equation (5.36) on the recombination and trapping time constants, the latter of which, τ_T, is proportional to N_T^{-1} and depends therefore on the dose. With increasing dose, τ_T decreases and can become the dominant time scale, if it is not already. That is, trapping dominates the relaxation process.
The mobility, μ, depends on the low-field mobility, Equation (5.39), which in turn depends on the mobilities due to scattering on phonon and on defects via Equation (5.38). The latter mobility is proportional to N_T^{-1}, i.e. it depends also on the dose, D, and can become the dominant mobility contribution, if it is not already. Thereby, the CCE can be a complex function of the dose.
Figure 5.23 shows as example the prediction of the CCE as a function of the dose, if the mean drift length, λ, depends on N_T^{-1} only via τ_relax. The shape is comparable with the measured curves for GaAs sensors shown in Figure 5.12.

We want to parametrize λ as a function of the N_T. Since only N_T depends on the dose, we obtain immediately $\lambda(D)$, which is necessary to fit $CCE\big(\lambda(D)\big)$ to the data obtained by the measurements. To reduce the complexity, we assume that the electric field is smaller than the saturation electric field, $\mathcal{E}_\mathrm{saturate}$. Then we can neglect the saturation effect of the

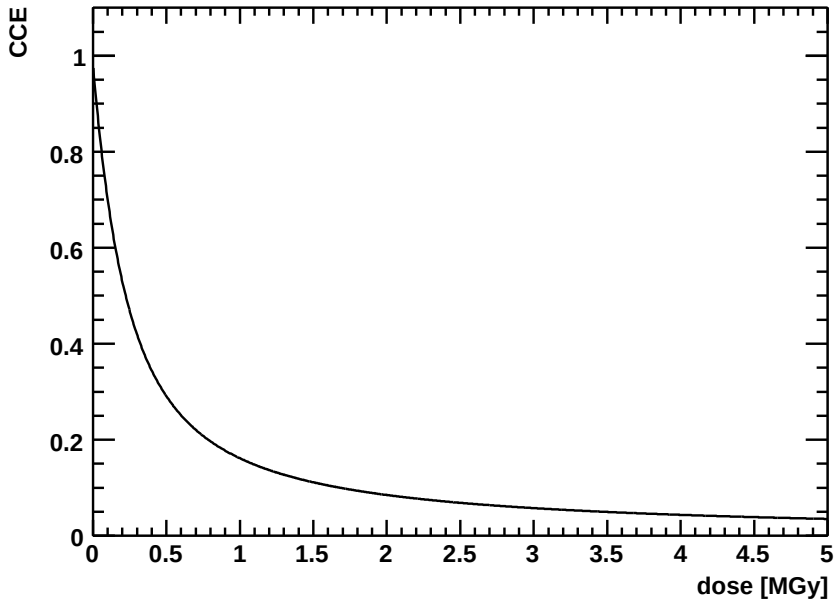

Figure 5.23: CCE as function of the dose, D, for a specific choice of the mobility and the relaxation time.

drift speed and just use, $\lambda = \tau_{\text{relax}} \mu_0 \mathcal{E}$. We insert for the low-field mobility Equation (5.38) with $\mu_{\text{s,T}} = \frac{\alpha_{\text{s,T}}}{N_{\text{T}}}$, $\alpha_{\text{s,T}}$ being a fit parameter. The relaxation time is given by Equation (5.36), and τ_{T} therein by Equation (5.34). Therefore, by inserting for μ_0 and τ_{relax} into λ, we obtain

$$\lambda = \left(r(n_0 + p_0) + c_{\text{e}}(N_{\text{T}} - n_{\text{T}}^0)\right)^{-1} \left(\frac{1}{\mu_{\text{s,ph}}} + \frac{N_{\text{T}}}{\alpha_{\text{s,T}}}\right)^{-1} \mathcal{E} \ . \tag{5.49}$$

However, the large number of free parameters, E_{T}, c_{e}, σ_{T}, $\alpha_{\text{s,T}}$, cannot be determined simultaneously from a fit to the data. Thus, we parametrize λ as a simplified function of the dose, D, motivated by the just mentioned dependency on N_{T}, by

$$\lambda(D) = \frac{1}{(\alpha + \beta D)^{\gamma}} \ , \tag{5.50}$$

to have at least a qualitative description of the measured data. Herein, α, β and γ are free fit parameters, which depend on all the basic parameters and the electric field. This parametrization is not a one-to-one correspondence and the dependencies of α, β and γ on the basic parameters are rather hidden. Only in special cases, e.g. for a constant mobility, the fit parameters can be correlated with the basic parameters.

Sensor Current as a Function of the Dose and the Dose Rate

To estimate the sensor current, I_{s}, as a function of the dose, we start with Equation (5.23) and add a generation term, G, parametrizing the creation of electron-hole pairs due to the

ionization in a particle beam,

$$\frac{dn}{dt} = r(n_i^2 - np) + G \; . \tag{5.51}$$

If a large amount of excess charge carriers are created, $G \gg rn_i$, we call this *high-injection scenario*. We neglect here the effect of trapping assuming that the traps are almost filled and do not contribute to the variation of the conduction band electron density. The generation term depends on the number of particles passing through the sensor, i.e. on the Faraday cup current, I_{FC}, by

$$G = \frac{\langle d\varepsilon_{\mathrm{dep}}/dx \rangle}{\varepsilon_{\mathrm{eh}}} \cdot \frac{R_c I_{\mathrm{FC}}}{eA_{\mathrm{beam}}} = N_{\mathrm{eh}} \frac{R_c I_{\mathrm{FC}}}{eA_{\mathrm{beam}}} \; . \tag{5.52}$$

N_{eh} is defined in Equation (5.5). The second factor is the number of primary electrons passing the sensor per unit time. Since the excess charge carriers are created in pairs we assume $n = p = n_0$ in the stationary state of Equation (5.51), where n_0 is found to be

$$n_0 = \sqrt{n_i^2 + G/r} \approx \sqrt{G/r} \; , \tag{5.53}$$

using the approximation $G \gg rn_i^2$. The Faraday cup current is proportional to the dose rate as was shown in Equation (5.11). We therefore find $n_0 \propto \sqrt{dD/dt}$. Hence, the sensor current depends also on the dose rate,

$$I_{\mathrm{s}} = e(\mu_{\mathrm{e}} + \mu_{\mathrm{h}}) \mathcal{E} A_{\mathrm{s}} \cdot n_0 \propto \sqrt{\frac{dD}{dt}} \; , \tag{5.54}$$

where A_{s} is the electrode area of the sensor, through which the sensor current I_{s} flows. In Equation (5.11) we showed $I_{\mathrm{FC}} \propto \frac{dD}{dt}$. The ratio of the sensor and the Faraday cup currents then depends on the dose rate as

$$\frac{I_{\mathrm{s}}}{I_{\mathrm{FC}}} \propto \left(\frac{dD}{dt} \right)^{-1/2} \; . \tag{5.55}$$

Hence, the response of the sensor to a primary particle beam is not proportional to the number of particles crossing the sensor, but proportional to its square root.
A part of the charge carriers contributing to the current is recombined during the motion through the sensor.[9] The recombination proceeds the faster the larger the electron density in the conduction band is. Therefore, I_{s}, grows only with the square root of I_{FC} or, equivalently of dD/dt.

The measurement of I_{s} and I_{FC} at the very beginning of irradiation offers the possibility to estimate the cross-section for electron-hole recombination, σ_{eh}, if one assumes that no traps are present and the only relaxation mechanism is recombination. If the mobilities

[9] Remember: Trapping is assumed not to play a role.

for electrons and holes are known and using $r = \sigma_{\mathrm{eh}} v_{\mathrm{th}}$, we can resolve Equation (5.54) for n_0. Using then Equations (5.53) and (5.52), we obtain

$$\sigma_{\mathrm{eh}} = \frac{G}{v_{\mathrm{th}} n_0^2} = \frac{\langle d\varepsilon_{\mathrm{dep}}/dx \rangle}{\varepsilon_{\mathrm{eh}}} \cdot \frac{e R_c I_{\mathrm{FC}}}{v_{\mathrm{th}} A_{\mathrm{beam}}} \cdot \left(\frac{(\mu_e + \mu_h) \mathcal{E} A_{\mathrm{s}}}{I_{\mathrm{s}}} \right)^2 . \tag{5.56}$$

This is, however, only a rough estimate for σ_{eh} under the assumptions that both electrons and holes contribute almost equally to the sensor current and that no defects are present.

The sensor current, I_{s}, depends also on the dose itself via the mobility. Assuming $\mu = \mu_0$ as in Equation (5.49) and inserting Equation (5.48) for N_{T}, we obtain

$$I_{\mathrm{s}}(D) = e n_0 A_{\mathrm{s}} \underbrace{\left(\frac{1}{\mu_{\mathrm{s,ph}}} + \frac{N_{\mathrm{T}}^0 + \frac{\sigma_{\mathrm{T}} \rho^2 d_{\mathrm{s}} N_A}{\varepsilon_{\mathrm{dep}} A} D}{\alpha_{\mathrm{s,T}}} \right)^{-1}}_{\mu_0} \mathcal{E} . \tag{5.57}$$

This is just the electron current and a similar current for holes has to be added. However, if there are no hole traps, the hole current just depends on the dose rate according to Equation (5.54).
As for the CCE, we want a parametrization for $I_{\mathrm{s}}(D)$. For a constant dose rate, we obtain

$$I_{\mathrm{s}}(D) = \frac{1}{\alpha + \beta D} , \tag{5.58}$$

where α and β are again fit parameters and functions of the basic parameters. Unfortunately, fitting $I_{\mathrm{s}}(D)$ to the data will give only a qualitative understanding since $\mu_{\mathrm{s,ph}}$, N_{T}^0, σ_{T} and $\alpha_{\mathrm{s,T}}$ are unknown and cannot be determined in one fit.

However, investigating I_{s}, $I_{\mathrm{s}}/I_{\mathrm{FC}}$ and the CCE gives a valuable qualitative understanding of the changes of the material properties during the irradiation. Specifically, we could in principle distinguish the impact of the characteristic relaxation time, the mobility change, or both on the observed quantities. In the reality, it is a bit more difficult for reasons to be discussed below.

Remark

In principle, it is possible to measure the CCD during the irradiation period. The electrons of the 10 MeV beam deposit energy like MIPs. The charge collected per unit time is

$$\frac{dQ_{\mathrm{coll}}}{dt} = I_{\mathrm{s}} - I_{\mathrm{dark}} .$$

As used already above, $N_{\mathrm{eh}} R_c I_{\mathrm{FC}} d_{\mathrm{s}}/e$ is the average number of electron-hole pairs created per unit time, Q_{ind}/e. The ratio is just the charge collection efficiency,

$$\mathrm{CCE} = \frac{dQ_{\mathrm{coll}}}{dQ_{\mathrm{ind}}} \equiv \frac{dQ_{\mathrm{coll}}/dt}{dQ_{\mathrm{ind}}/dt} = \frac{I_{\mathrm{s}} - I_{\mathrm{dark}}}{N_{\mathrm{eh}} R_c I_{\mathrm{FC}} d_{\mathrm{s}}} . \tag{5.59}$$

This was the original motivation for plotting the ratio $I_\mathrm{s}/I_\mathrm{FC}$, since the dark current can be neglected for diamond. The ratio of the currents is expected to behave in the same way as a function of the dose as the CCE determined from a measurement using a ^{90}Sr source. One obvious difference, however, is the dose rate used for the measurement.

Comparison with Measurements for scCVD Diamond

At the beginning of the first irradiation, we measured the currents, $I_\mathrm{s} = 34\ \mu$A and $I_\mathrm{FC} = 8.67$ nA. Using the sensor electrode area, $A_\mathrm{s} = 0.07\ \mathrm{cm}^2$, and for the other quantities in Equation (5.56) $\mathcal{E} = U/d_\mathrm{s} = 100\ \mathrm{V}/326\ \mu\mathrm{m} \approx 3\ \mathrm{kV/cm}$, and from Table 5.1 the mobilities $\mu_\mathrm{e} = \mu_\mathrm{h} = 0.2\ \mathrm{m}^2/(\mathrm{Vs})$, $R_c = 0.1312$ (from GEANT4 simulations) and $N_\mathrm{eh} = \langle \frac{d\varepsilon_\mathrm{dep}}{dx} \rangle \varepsilon_\mathrm{eh}^{-1} = 46\ \mu\mathrm{m}^{-1}$ according to Section 5.1.4,[10] we obtain for the electron-hole recombination cross-section

$$\sigma_\mathrm{eh} \approx 5.4 \cdot 10^{-9}\ \mathrm{cm}^2\ . \tag{5.60}$$

This value must be regarded, however, as an upper limit because of the following reason. The sensor current we measured is averaged over at least a few hundred milliseconds. The value used for I_s is, hence, not its maximum because the sensor current already might drop in this time interval. For the later discussion, our result will be sufficient. Equation (5.60) can be translated into the recombination time τ_R, using Equation (5.25), by

$$\tau_\mathrm{R} = \frac{1}{2rn_i} = \frac{1}{2v_\mathrm{th}\sigma_\mathrm{eh}n_i} \approx 1.34\ \mathrm{s}\ . \tag{5.61}$$

Here, we assumed $v_\mathrm{th} = 10^7$ cm/s, and determined n_i from $I_\mathrm{dark} \approx e(\mu_\mathrm{e} + \mu_\mathrm{h})n_i\mathcal{E}A_\mathrm{s}$, where we assumed a dark current of about 1 pA.[11] The result is $n_i \approx 7\ \mathrm{cm}^{-3}$. τ_R is much larger than the characteristic drift time of $t_\mathrm{drift} = \frac{d_\mathrm{s}^2}{\mu U} \approx 5$ ns. Hence, the dominant process for the reduction of excess charge carriers inside the sensor is the drift process what is consistent with the measurement of CCE ≈ 100 % before the irradiation.

The measured CCE as a function of the absorbed dose can be fitted using the parametrization for $\lambda(D)$, Equation (5.50), in Equation (5.46). The left-hand plot of Figure 5.24 shows the CCE as a functions of the dose for scCVD diamond, as measured at the testbeam experiment, and the fit result. To obtain a good fit, we assumed a sum of two CCE functions, $\mathrm{CCE_e}$ for electrons and $\mathrm{CCE_h}$ for holes, i.e. two different mean drift lengths, λ_e and λ_h, were needed. As expected, both electrons and holes contribute almost equally to the charge collection process. The power, γ in Equation (5.50), obtained in the fit is for both charge carrier types $\gamma \approx 1.15$, i.e. closer to one than to two. We might conclude that therefore either the mobility or the characteristic relaxation time decrease with the dose, but not both simultaneously.

[10] $A_\mathrm{beam} = 1\ \mathrm{cm}^2$

[11] This is the lower limit of the current measurement device. The intrinsic charge carrier density Equation (5.19) is orders of magnitude smaller and would lead to a large recombination time due to Equation (5.25). This we do not observe.

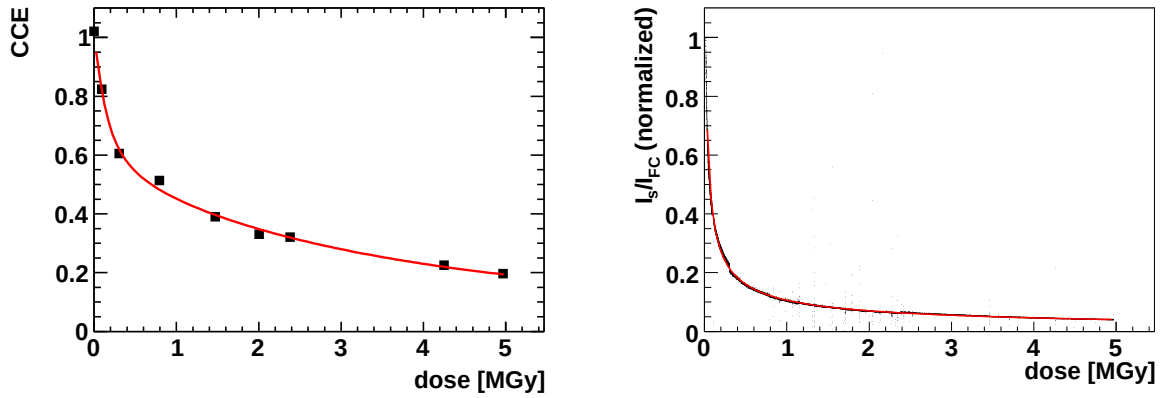

Figure 5.24: CCE as in Fig. 5.7 (left) and I_s/I_{FC} as in Fig. 5.8 (right) as functions of the dose, D, for scCVD diamond (black) in comparison with the model (red line), Eqn. (5.46), (5.50) and (5.58), respectively.

Considering I_s in Figure 5.8, we would conclude that it is the mobility, which decreases with the dose, since the only dose dependence in I_s is due to that of the mobility, as can be seen in Equation (5.57). We fitted $I_{s,e} + I_{s,h}$, each parametrized by Equation (5.58), to the data of the third beam period, where the dose rate was rather constant. Two functions, describing the contributions from electrons and holes, were needed to obtain a good fit, and both contribute equally. Just the initial mobilities of electrons and holes differ by an order of magnitude.
However, investigating I_s/I_{FC}, as shown in the right-hand plot of Figure 5.24, reveals a much more complex situation for the scCVD diamond. Unlike expected from Equation (5.55), we obtain a smooth function of the dose, without any significant step when increasing the dose rate. Furthermore, I_s/I_{FC} can be fitted with the same parametrization as for I_s as shown in the figure, this time over the full dose range. The reason proves to be polarization effects occurring due to a dynamic charge carrier separation inside the device, which diminishes the effective electric field inside the sensor.[12] This is investigated later in this chapter.

Figure 5.25 shows the CCEs determined both via Equation (5.59) from the sensor current during the irradiation periods (black) and from the measurement using a ^{90}Sr source between the periods of irradiation (violet triangles). The CCE determined in the latter way drops less steep as a function of the absorbed dose than the CCE determined from the sensor current, I_s.
The obvious difference between both methods of determining the CCE is that, using a ^{90}Sr source, the signal charge is measured with a charge integrating ADC in a gate of 1 μs. Using this gate, the release of trapped charges is not considered in the CCE. By contrast,

[12] Assuming that no recombination occurs leads to $I_s = N_{eh} R_c d_s \frac{A_s}{A_{beam}} I_{FC}$, i.e. a direct proportionality between I_s and I_{FC}, which is also not observed.

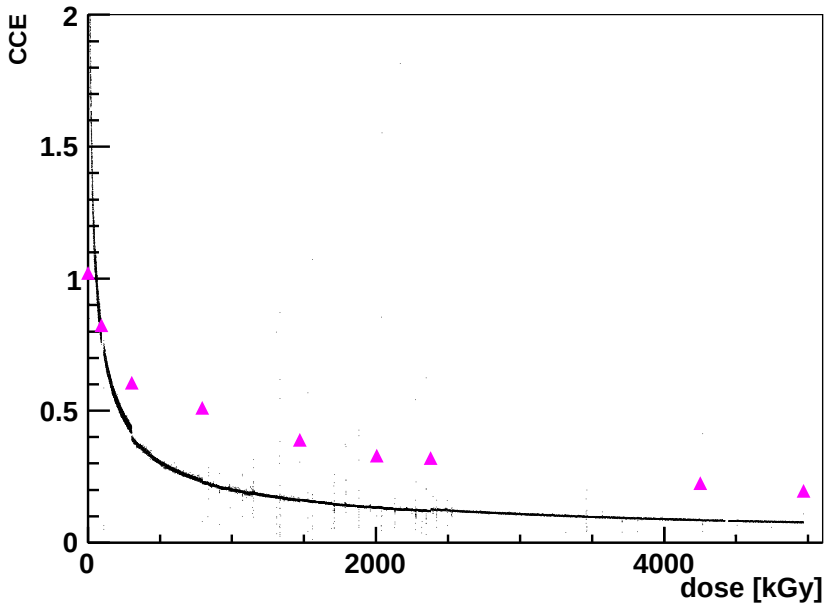

Figure 5.25: CCE as a function of the dose for scCVD diamond determined from ^{90}Sr experiment (triangles) and calculated from the currents (small black dots forming a line).

the CCE determined from I_s contains all moving charges, also those released from traps. As well, the dose rates and, therefore, the generation terms G act differently in both methods. During the testbeam, the dose rate was large and even increased with the time, whereas the dose rate of the ^{90}Sr measurement is kept small and constant. Therefore, the characteristic time scales for the relaxation are different.
Moreover, the CCE determined from I_s reaches values larger than one at the beginning of the irradiation. There flow more charges than are expected from the ionization process. This might also be connected with the polarization, but is still not understood.

For pcCVD diamond, an estimate for σ_{eh} is not possible because there are already intrinsically a lot of defects which cannot be neglected and the actual initial current is diminished by trapping processes indicated by a clear pumping behavior of the CCD.

Comparison with Measurements for Gallium Arsenide

The CCE as a function of the dose for GaAs sample 2 is shown in Figure 5.26. It starts at one-half, and, for the fitted function, only one CCE is used[13]. A similar result is obtained for GaAs sample 1.

[13]The assumption of one characterizing CCE is sufficient to obtain a good description of the measurement. The reason might be that either only one charge carrier type contributes, or the CCEs for both carrier types have by chance the such values that the total CCE is equal to 50 %.

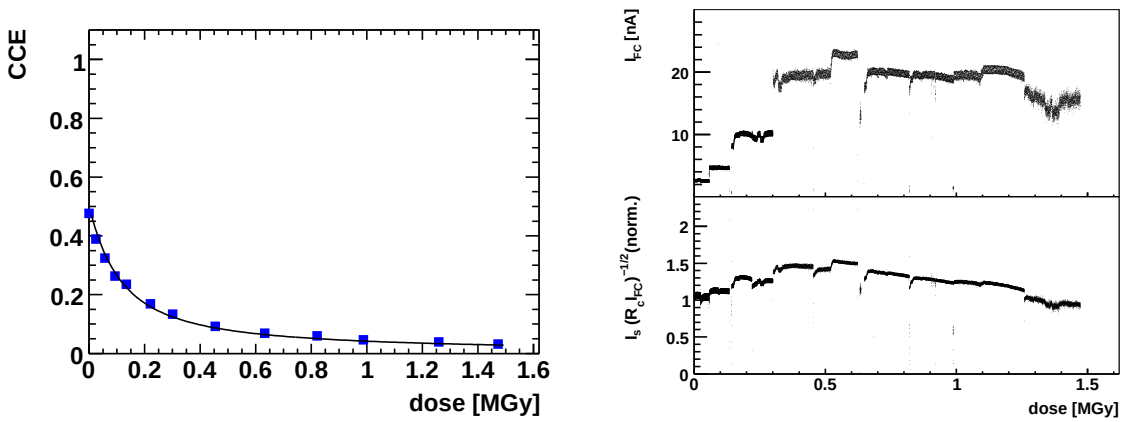

Figure 5.26: CCE (left), I_{FC} and $I_{\mathrm{s}}/\sqrt{I_{\mathrm{FC}}R_c}$ (right) as functions of the dose, D, for GaAs sample 2 in comparison with the model.

For GaAs sample 2, the ratio $I_{\mathrm{s}}/\sqrt{I_{\mathrm{FC}}R_c}$, normalized at the beginning to one, is shown in the right-hand plot of Figure 5.26. For a constant dose rate, i.e. a constant Faraday cup current, the sensor current degrades only little. We can therefore conclude that mostly the characteristic relaxation time is influenced by irradiation. Defects that are created by the traversing electron beam still do not influence the mobility. The mobility is probably dominated by the defects due to the doping itself. With respect to the doping density, we assume therefore that the density of defects due to radiation damages is smaller than 10^{16} cm^{-3}. GaAs shows qualitatively a better agreement with the model proposed above. The ratio $I_{\mathrm{s}}/\sqrt{I_{\mathrm{FC}}R_c}$ shows only a mild dependence on the accumulated dose. A small increase at the beginning of the irradiation, indicating still a slight dependence on the dose rate, is compensated at larger doses by the slight decrease of I_{s}.
It might be just accidental that one charge carrier type suffices to describe the CCD as a function of the dose. On the other hand, due to the doping, it is indeed possible that only one charge carrier type participates in the charge collection process, while the other type is immediately trapped. If we assume the electrons to be the majority charge carriers then we can use the electron mobility from Table 5.1.[14] Assuming the recombination time constant to be the dominant time scale, which is supported by not observing a pumping behavior, and with $I_{\mathrm{s}} = 26$ μA, $I_{\mathrm{FC}} = 5$ nA, $U = 200$ V and $d_{\mathrm{s}} = 500$ μm for GaAs[15] sample 1 at the beginning of the irradiation, we obtain, using Equation (5.56),

$$\sigma_{\mathrm{eh}} \approx 4.7 \cdot 10^{-5} \text{ cm}^2 \,. \tag{5.62}$$

Again before, this can be regarded as upper limit only. If holes are the majority charge carriers then the cross-section is at least one order of magnitude smaller due to the 10 times smaller mobility of the holes. To calculate the recombination time we must account for the fact that GaAs is doped and, thus, the actual charge carrier density may differ

[14] We neglect a possible change of the mobilities due to the doping with tellurium and chromium.
[15] $A_{\mathrm{beam}} = 1$ cm^2 and $R_c = 0.434$.

from the intrinsic one. With the dark current $I_{\mathrm{dark}} \approx 0.5\ \mu\mathrm{A}$ and assuming only electron transport, we obtain $n_i = 3.5 \cdot 10^5\ \mathrm{cm}^{-3}$, which is one order of magnitude smaller than for the intrinsic GaAs, where $n_i = 2.1 \cdot 10^6\ \mathrm{cm}^{-3}$, using Equation (5.19) and values from reference [168]. The recombination time constant, τ_{R}, is then obtained to be

$$\tau_{\mathrm{R}} \approx 3\ \mathrm{ns}\ , \tag{5.63}$$

which is comparable with the drift time of $t_{\mathrm{drift}} = 1.47$ ns. After t_{drift} all excess charge carriers are collected at last at the electrodes. The recombination time is an average time. Equation (5.46) predicts a CCE of about 43 % for $\tau_{\mathrm{relax}} = \tau_{\mathrm{R}}$. Hence, for the GaAs samples, which were not exposed to radiation, most of the charge carriers are still collected. Nevertheless, a small drop of τ_{relax} down to 1 ns results already in a drop of the CCE down to 32 %. This might explain the strong CCE drop for GaAs.

5.3.5 Pumping

Pumping is the process of filling defect levels inside the band gap by capturing electrons (holes) from the conduction (valence) band, i.e., the slow approach to the equilibrium state (5.33). We assume electron traps for the following considerations. Furthermore, we assume a spatiotemporal constant electron density, $n = n_0$. This can be controlled by a constant generation term G, which can be due to the electron beam in the testbeam experiment (high injection) or due to electrons from a ^{90}Sr source (low injection) crossing the sensor. Solving Equation (5.32), and assuming n_0 and T to be time-independent, we obtain

$$n_{\mathrm{T}}(t) = \frac{n_0 N_{\mathrm{T}}}{n_0 + N_{\mathrm{C}} e^{-\frac{E_{\mathrm{C}} - E_{\mathrm{T}}}{k_{\mathrm{B}} T}}} + \delta n_{\mathrm{T}}^0 \exp\left\{-c_{\mathrm{e}} \left(n_0 + N_{\mathrm{C}} e^{-(E_{\mathrm{C}} - E_{\mathrm{T}})/(k_{\mathrm{B}} T)}\right) t\right\}\ . \tag{5.64}$$

The first term is just the stationary solution of Equation (5.32). δn_{T}^0 is the initial deviation from it. The characteristic time scale to reach this stationary state is

$$\tau_{\mathrm{T}}^{N_{\mathrm{T}}} = \frac{1}{c_{\mathrm{e}} \left(n_0 + N_{\mathrm{C}} e^{-(E_{\mathrm{C}} - E_{\mathrm{T}})/(k_{\mathrm{B}} T)}\right)} = \left(1/\tau_c + 1/\tau_e\right)^{-1}\ . \tag{5.65}$$

The characteristic time constants for electron capture and release by traps, τ_c and τ_e, are defined in Equation (5.35).
Equations (5.64) and (5.65) are valid for any semicondutor possessing trap levels. We investigated scCVD diamond in more detail.

For traps with a given level, E_{T}, and a constant density, N_{T}, the stationary density of the filled traps is given by the electron density in the conduction band, n_0. For the case without a source, $n_0 = n_i \approx 7\ \mathrm{cm}^{-3}$, as estimated in the previous section for scCVD diamond from the dark current, is rather small for diamond. However, due to injecting charges by ionization due to electrons from a ^{90}Sr source or a beam crossing the sensor, n_0 can be considerably increased. Thereby, also the speed increases, with which the stationary state

is approached, i.e. $\tau_{\mathrm{T}}^{N_{\mathrm{T}}}$ is decreased. There is an intrinsic contribution of the characteristic trap fill and release time, which depends essentially only on the temperature and the distance of the trap level to the conduction band edge, $E_{\mathrm{C}} - E_{\mathrm{T}}$. For $E_{\mathrm{C}} - E_{\mathrm{T}} = 1$ eV, $T = 300$ K, and assuming the effective mass to be equal to the electron mass results in $N_{\mathrm{C}} \approx 10^{19}$ cm^{-3} and $N_{\mathrm{C}} e^{-(E_{\mathrm{C}}-E_{\mathrm{T}})/(k_{\mathrm{B}}T)} \approx 40$ cm^{-3}, which becomes largely enhanced with increasing temperature.
The remaining unknown quantity, c_{e}, can be determined in two ways, either by measuring the saturation of the CCD when the traps are continuously filled, as described below, or using thermally stimulated currents, as described in the next section.

If the traps are filled they cannot reduce further the charge carrier density of the conduction band, because the trapping mechanism does effectively not contribute anymore to the CCD. To show this, the scCVD diamond sample, irradiated in the electron beam to a dose of 5 MGy, was exposed to UV illumination for several hours to release all the trapped electrons. Then the sensor was constantly irradiated by a ^{90}Sr source with a large event rate to fill the traps again. Figure 5.27 shows the rising CCD of the scCVD diamond sensor as a function of the time. The temperature was kept constant at about 300 K. During this period, the sensor is permanently irradiated with a ^{90}Sr source. The dose rate can be estimated as follows. The MIP event rate is measured to be 640 Hz, i.e. 640 MIP electrons passing the sensor and the hitting the scintillator. This event rate just corresponds to the particles crossing the sensor. Particles that stop inside the sensor are not counted. Using Monte-Carlo simulations, we found that only about 2 % of the energy is deposited by the counted MIPs.
The CCD saturates at $\mathrm{CCD}_{\mathrm{saturate}} \approx 125$ μm and the time constant is $\tau_{\mathrm{T}}^{N_{\mathrm{T}}} \approx 65$ hours, determined by fitting the function

$$\mathrm{CCD}_{\mathrm{saturate}} \left(1 + \zeta e^{-t/\tau_{\mathrm{T}}^{N_{\mathrm{T}}}}\right) \ ,$$

where $\mathrm{CCD}_{\mathrm{saturate}}$, ζ and $\tau_{\mathrm{T}}^{N_{\mathrm{T}}}$ are the fit parameters. We assumed that the CCD saturates in the same manner as the trap fill density approaches its equilibrium state. We estimate from Equation (5.52), $G \approx 4.2 \times 10^9$ cm^{-3}s^{-1} for the scCVD diamond sample using a count rate of 640 Hz. Herein, A_{beam}/R_c can be replaced by the sensor electrode area, $A_{\mathrm{s}} = 0.07$ cm^2. Since this are just the 2 %, we find a total rate for creation of excess charge carriers of $G \approx 2.1 \times 10^{11}$ cm^{-3}s^{-1}. The recombination speed, $r = \sigma_{\mathrm{eh}} v_{\mathrm{th}}$, can be determined using Equation (5.60) and $v_{\mathrm{th}} = 10^7$ cm/s to be $r = 0.054$ cm^3/s. We obtain $n_0 \approx 2 \times 10^6$ cm^{-3}, and therefore

$$c_{\mathrm{e}} \approx 2.14 \times 10^{-12} \text{ cm}^3/\text{s} \ . \tag{5.66}$$

Using a 10 MeV electron beam of e.g. 5 nA, as done in the testbeam experiment described in Section 5.2.1, the pumping can be performed more efficiently within a few minutes for diamond. pcCVD diamond exhibits also a pronounced pumping behavior as can be seen in Figure 5.9. We assume that a lot of traps are initially present in the pcCVD diamond samples. At the beginning of the irradiation the CCD rises from about 70 μm to 170 μm after a few minutes of irradiation.

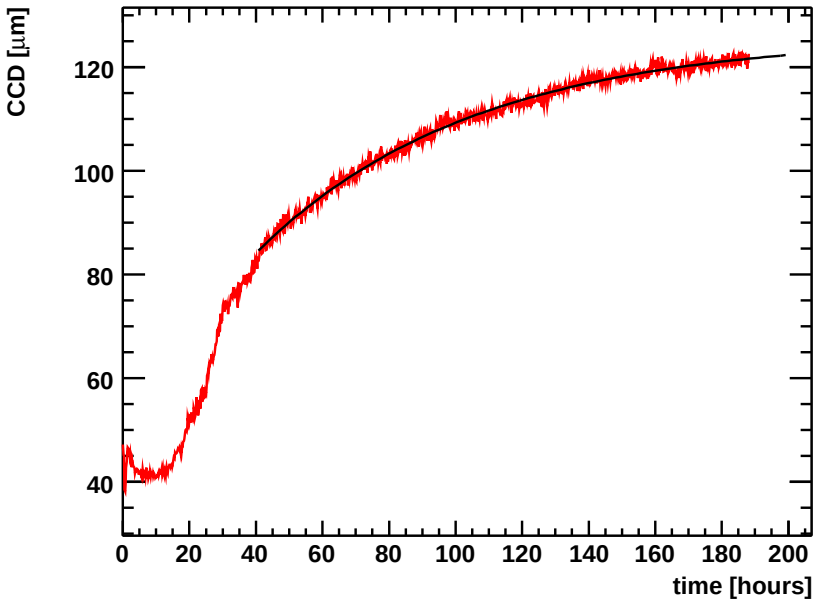

Figure 5.27: CCD as a function of the time for scCVD diamond which has accumulated already 5 MGy. During the whole time the sample was exposed to a ^{90}Sr source. The initial trap emptying was performed using UV light.

5.3.6 Thermally Stimulated Current

TSC Measurement Setup

Thermally stimulated currents (TSC) can be used to investigate trap levels in a crystal. The density of traps must be sufficiently large, and the energy level of the traps sufficiently different from the conduction and the valence band. Furthermore, the level must be rather stable, i.e. the release probability must be small enough at room temperature. We consider again electron traps, although TSC cannot distinguish between electrons and holes. We use the measurement of TSC to estimate the defect density, N_{T}. Furthermore, one can determine the distance of the trap energy level from the band edge, i.e. for electrons $E_{\mathrm{C}} - E_{\mathrm{T}}$, and the trapping speed constant, c_{e}. TSC measurements were done with a scCVD diamond sample.
The setup for the TSC measurement is depicted in Figure 5.28. The sensor is located inside an oven. A constant voltage, V, is applied to the sensor. The sensor is then heated up by the oven while the current, I_{s}, and the temperature of the sensor, T, are measured as function of the time, t.

Theoretical Background

To understand what happens inside the crystal containing the traps and the trapped charges, we start with Equation (5.32). The electron density in the conduction band

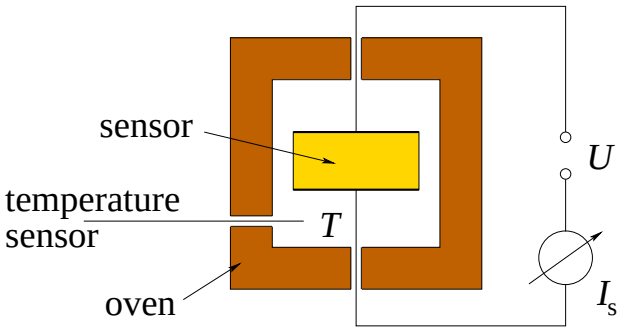

Figure 5.28: Scheme of the experimental TSC measurement setup. To the sample under investigation inside an oven a voltage, U, is applied. The oven heats up the sensor. The current through the sensor, I_s and the temperature, T, are measured.

is essentially determined by the intrinsic one causing the dark current, since no excitation by an external source is present.[16] When increasing the temperature, the probability for the release of electrons from a trap level to the conduction band rises. These electrons drift in the electric field towards the electrode causing a current additionally to the dark current, which we call the *thermally stimulated current*, I_{TSC}. Also, the TSC is time dependent, rising when arriving at a certain temperature and decreasing again when the traps get empty. In the temperature range of interest, where the trapped charges are released, the temperature should be increased as fast as possible and at constant rate for practical reasons. Although the time is the governing parameter, I_{TSC} is usually considered as a function of the temperature.
Equation (5.32) becomes with these assumptions,

$$\frac{dn_{\mathrm{T}}}{dt} = -c_{\mathrm{e}} N_{\mathrm{C}} e^{-\frac{E_{\mathrm{C}}-E_{\mathrm{T}}}{k_{\mathrm{B}}T}} n_{\mathrm{T}} \equiv -\tau_e^{-1} n_{\mathrm{T}} \ , \tag{5.67}$$

i.e. the capture term is neglected. The characteristic trap release time, τ_e, is defined in Equation (5.35). Only the temperature depends on the time. The temperature dependence of N_{C} can be neglected in comparison with the exponential term. Equation (5.67) can be solved, as

$$n_{\mathrm{T}}(t) = n_{\mathrm{T}}^0 \exp\left\{ -c_{\mathrm{e}} N_{\mathrm{C}} \int_{t_0}^{t} e^{-\frac{E_{\mathrm{C}}-E_{\mathrm{T}}}{k_{\mathrm{B}}T(t')}} \, dt' \right\} \ . \tag{5.68}$$

$n_{\mathrm{T}}^0 = n_{\mathrm{T}}(t_0)$ is the initial trap filling. We could assume $n_{\mathrm{T}}^0 \approx N_{\mathrm{T}}$, if every trap is filled.
We use Equation (5.22) for the dynamics of the conduction band electron density. Again, we consider the problem in one dimension, and we include the trap releasing rate, Equation (5.67), into the continuity equation,

$$\frac{\partial n}{\partial t} = \frac{1}{e}\frac{\partial j_{\mathrm{e}}}{\partial z} + r(n_i^2 - np) - \frac{dn_{\mathrm{T}}}{dt} \ . \tag{5.69}$$

[16] The exponential term in Equation (5.29) becomes dominant only at larger temperatures due to the large band gap of diamond.

We neglect the diffusion term in the current density, Equation (5.20), i.e. $j_\mathrm{e} = en\mu_\mathrm{e}\mathcal{E}$. To solve Equation (5.69) approximately, we perform an adimensionalization, i.e. we rewrite the variables in terms of adimensional variables and characteristic scales for these variables,

$$t = t_\mathrm{drift}\tilde{t}\ , \quad n = n_0\tilde{n}\ , \quad p = n_0\tilde{p}\ , \quad \frac{n_\mathrm{T}}{dt} = \frac{N_\mathrm{T}}{\tau_e}\widetilde{\frac{n_\mathrm{T}}{dt}}\ , \quad z = d_\mathrm{s}\tilde{z}\ , \tag{5.70}$$

with a characteristic drift time scale, t_drift, a characteristic spatial distance, d_s, a characteristic electron density, n_0, and a characteristic electron trapping rate, N_T/τ_e.
For convenience we omit the tilde for the dimensionless variables hereafter. Furthermore, we insert $j_\mathrm{e} = en\mu_\mathrm{e}\mathcal{E}$. Inserting the variables of Equation (5.70) in the Equation (5.69), we obtain

$$\frac{\partial n}{\partial t} = t_\mathrm{drift}\frac{\mu_\mathrm{e}\mathcal{E}}{d_\mathrm{s}}\frac{\partial n}{\partial z} + (rn_0t_\mathrm{drift})(n_i^2/n_0^2 - np) - \frac{N_\mathrm{T}t_\mathrm{drift}}{n_0\tau_e}\frac{dn_\mathrm{T}}{dt}\ . \tag{5.71}$$

The dimensionless variables t, z, n, p, and dn_T/dt are of the order one. Explicitly, we have again $t_\mathrm{drift} = \frac{d_\mathrm{s}}{\mu_\mathrm{e}\mathcal{E}} = \frac{d_\mathrm{s}^2}{\mu_\mathrm{e}U}$, which is the time for an electron drifting in the electric field the distance d_s. We choose, furthermore, $n_0 = n_i$, the stationary solution of the intrinsic and uniform problem[17]. We obtain

$$\frac{\partial n}{\partial t} = \frac{\partial n}{\partial z} + \frac{t_\mathrm{drift}}{2\tau_\mathrm{R}}(1 - np) - \frac{N_\mathrm{T}t_\mathrm{drift}}{n_i\tau_e}\frac{dn_\mathrm{T}}{dt}\ .$$

where we used Equation (5.25). We expand $n = 1 + \delta n$ and $p = 1 + \delta n$, again assuming neutrality. Note, this corresponds to the expansion $n = n_i + \delta n$ in Equation (5.24). We omit terms of higher order in δn and obtain

$$\frac{\partial \delta n}{\partial t} = \frac{\partial \delta n}{\partial z} - \frac{t_\mathrm{drift}}{\tau_\mathrm{R}}\delta n - \frac{N_\mathrm{T}t_\mathrm{drift}}{n_i\tau_e}\frac{dn_\mathrm{T}}{dt}\ .$$

If $t_\mathrm{drift} \ll \tau_\mathrm{R}$, τ_e we can split this equation into the drift and the relaxation part. We obtain first $\frac{\partial \delta n}{\partial t} = \frac{\partial \delta n}{\partial z}$, which is solved with the method of characteristics. The general solution is that δn depends only on $z + t$, or $\delta n = \delta n(z + \mu_e\mathcal{E}t)$ in dimensional variables (δn is scaled with n_i), i.e. a constantly moving profile. This reflects the drift of the excess charge carriers in the electric field. Equation (5.40) exhibits this property as a solution of the continuity equation.
We can assume that δn evolves much faster than n_T, such that dn_T/dt can be considered as a rather small constant. In the next order of $t_\mathrm{drift}/\tau_\mathrm{R} \approx \frac{N_\mathrm{T}t_\mathrm{drift}}{n_i\tau_e}\frac{dn_\mathrm{T}}{dt}$, we solve

$$0 = -\frac{t_\mathrm{drift}}{\tau_\mathrm{R}}\delta n - \frac{N_\mathrm{T}t_\mathrm{drift}}{n_i\tau_e}\frac{dn_\mathrm{T}}{dt}\ , \quad \text{i.e.} \quad \delta n = -\frac{N_\mathrm{T}\tau_\mathrm{R}}{n_i\tau_e}\frac{dn_\mathrm{T}}{dt}\ .$$

Expressing this in dimensional variables, we obtain

$$\delta n \equiv n - n_i = -\tau_\mathrm{R}\frac{dn_\mathrm{T}}{dt}\ .$$

[17] We neglect the time-dependence of $n_i\big(T(t)\big)$.

Inserting n in the current we obtain

$$I = j_\mathrm{e} A_\mathrm{s} = e A_\mathrm{s} \mu_\mathrm{e} \mathcal{E} \left(n_i - \tau_\mathrm{R} \frac{dn_\mathrm{T}}{dt} \right) \equiv I_\mathrm{dark} + I_\mathrm{TSC} \; . \tag{5.72}$$

Again, $I_\mathrm{dark} = e A_\mathrm{s} \mu_\mathrm{e} \mathcal{E} n_i$, is the dark current, which depends on the temperature, as can be observed in Equation (5.29). Since the probability for electron capture by traps is decreased with increasing temperature, the relaxation time constant is dominated by the characteristic recombination time. This is specifically true also at smaller temperatures when the traps are filled. The thermally stimulated current, I_TSC, can then be expressed in terms of the CCD using $\lambda \approx \tau_\mathrm{R} \mu_\mathrm{e} \mathcal{E} \approx \mathrm{CCD}$, and we can write

$$\begin{aligned} I_\mathrm{TSC}(t) &= -e A_\mathrm{s} \mathrm{CCD} \frac{dn_\mathrm{T}}{dt} \\ &= e A_\mathrm{s} \mathrm{CCD} c_\mathrm{e} N_\mathrm{C} e^{-\frac{E_\mathrm{C}-E_\mathrm{T}}{k_\mathrm{B} T}} n_\mathrm{T} \qquad \text{using Equation (5.68)} \\ &= e A_\mathrm{s} \mathrm{CCD} c_\mathrm{e} N_\mathrm{C} e^{-\frac{E_\mathrm{C}-E_\mathrm{T}}{k_\mathrm{B} T}} n_\mathrm{T}^0 \exp\left\{ -c_\mathrm{e} N_\mathrm{C} \int_{t_0}^{t} e^{-\frac{E_\mathrm{C}-E_\mathrm{T}}{k_\mathrm{B} T(t')}} \, dt' \right\} \; . \end{aligned} \tag{5.73}$$

For a linear temperature increase, $T(t) = T_0 + \beta_T t$, the integral can be solved analytically. For a measurement of $T(t)$ as an arbitrary function of the time, the integral in Equation (5.73) must be evaluated numerically.

Experimental Procedure

The TSC measurement is accomplished in two steps. First, the traps inside a sensor are filled by pumping using e.g. a ^{90}Sr source as described in the previous section. Second, the sensor is heated up the first time to a maximum temperature and then cooled down. The sensor temperature and the sensor current are measured as functions of the time.
The traps should be empty when the sensor cools down. Therefore, in an ideal case, the sensor current as a function of the temperature is the dark current during this period, which follows the Equation

$$I_\mathrm{dark}(T) = I_0 e^{-\frac{E_\mathrm{gap}}{2 k_\mathrm{B} T}} \; , \tag{5.74}$$

as already shown in Equation (5.29). The result of such a measurement for a scCVD diamond sample is shown in Figure 5.29. The red data points are measured when the temperature was raised the first time. Before the relevant parameters of the TSC can be determined by fitting Equation (5.73) to the data, the temperature dependent dark current, Equation (5.74), must be subtracted. For this task, one could use the cooling down current, because this should be the dark current if all traps are empty.
However, the measured temperature and the actual sensor temperature differ a bit due to some delay of the heat conduction. Therefore, we heated up and cooled down the sensor once more under the same conditions as for the first time, and sensor current and temperature are again measured as functions of the time. The delay of the heat conduction in the measured temperature is reflected in the missing coincidence of the heating-up and

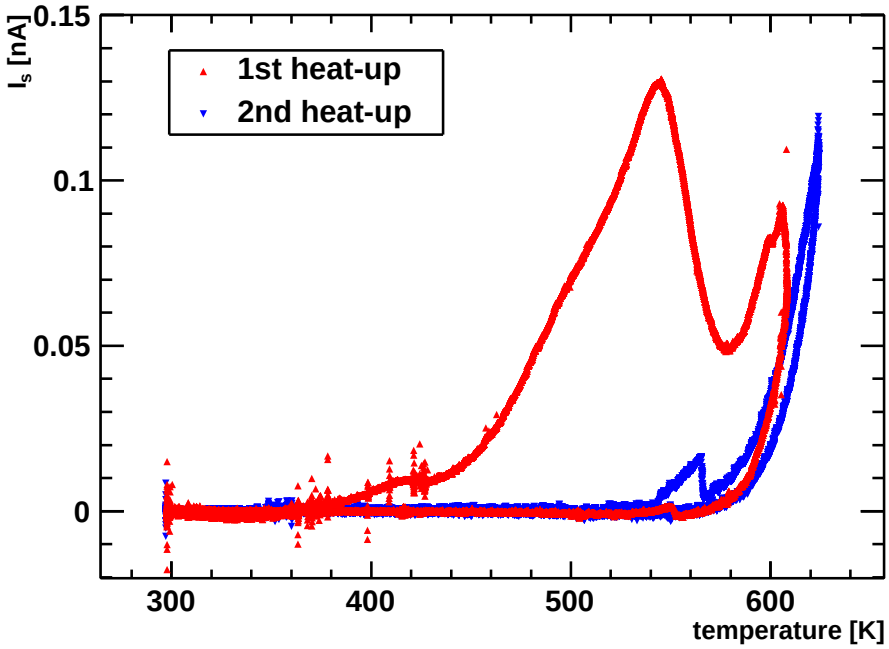

Figure 5.29: Current as a function of the temperature, measured with the TSC setup. The red curve is measured while heating the first time. The upper branch exhibits peaks corresponding to the thermally stimulated current by release of traps. The blue curve is measured while heating the second time.

cooling-down curves at higher temperatures, as can be observed in Figure 5.29 (blue data points, 2nd heat-up).
One can correct for this delay, however, by assuming that the sensor temperature, T_s, and the dark current, I_dark, are uniquely related to each other by Equation (5.74), and that the thermo couple temperature, T_TC, and the sensor temperature are related to each other by

$$\dot{T}_\mathrm{TC} \equiv \frac{dT_\mathrm{TC}}{dt} = \alpha(T_\mathrm{s} - T_\mathrm{TC}) \; .$$

Herein, α has to be determined e.g. by the following procedure. For a given dark current value, the values of time are determined, one for the heating-up period, t_+, and one for the cooling-down period, t_-. For both points of time, the sensor temperature is the same and we find

$$T_\mathrm{s} = \frac{\dot{T}_\mathrm{TC}(t_+)}{\alpha} + T_\mathrm{TC}(t_+) = \frac{\dot{T}_\mathrm{TC}(t_-)}{\alpha} + T_\mathrm{TC}(t_-) \; ,$$

that is

$$\alpha = \frac{\dot{T}_\mathrm{TC}(t_+) - \dot{T}_\mathrm{TC}(t_-)}{T_\mathrm{TC}(t_-) - T_\mathrm{TC}(t_+)} \; .$$

For different values of I_dark, an α is determined and all values obtained are averaged, $\langle\alpha\rangle$.

The sensor temperature as a function of the time is then given by

$$T_{\mathrm{s}}(t) = T_{\mathrm{TC}}(t) + \frac{1}{\langle\alpha\rangle}\dot{T}_{\mathrm{TC}} \; .$$

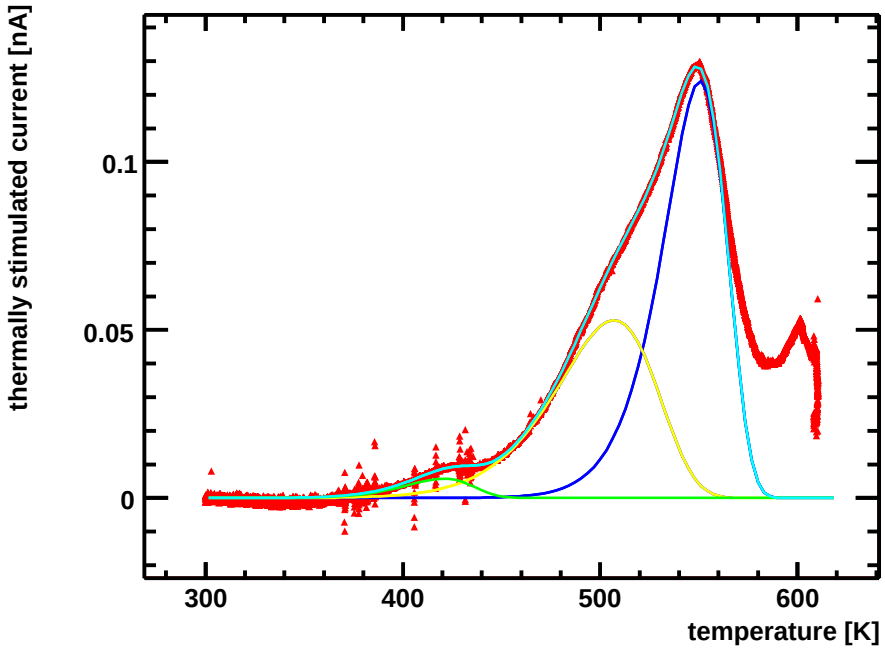

Figure 5.30: The thermally stimulated current, I_{TSC}, as a function of the temperature after dark current subtraction.

After this temperature correction for the TSC measurement, the dark current is subtracted from the total sensor current of the first heating-up. The result is shown in Figure 5.30. Also shown is the result of fitting three I_{TSC} functions according to Equation (5.73).

Results and Discussion

The CCD for the applied voltage of 200 V was measured to be 76 μm, but dropped to about 40 μm after a while due to the development of polarization as will be discussed in the next section. The sensor sample was, thus, not completely pumped, i.e. not all traps were filled. In the latter case, the CCD is about 125 μm and almost no polarization exists. Therefore, the assumption $n_{\mathrm{T}}^0 = N_{\mathrm{T}}$ is not valid.
Three obvious TSC peaks are observed in Figure 5.30, corresponding to at least three pronounced levels inside the band gap. The results of the fits are listed in Table 5.2. The value of c_{e} of the trap number 1 agrees reasonably with the value obtained in Equation (5.66) using the pumping behavior.
For CCD = 76 μm, the density of filled traps, n_{T}^0, is 5.7×10^{14} cm^{-3} for the first trap level in Table 5.2. Since the saturated CCD is about twice as large, 125 μm, we can assume

trap $\longrightarrow$		1. (dark blue)	2. (yellow)	3. (green)
$E_\mathrm{C} - E_\mathrm{T}$	[eV]	1.144 ± 0.002	0.851 ± 0.002	0.746 ± 0.006
$c_\mathrm{e} N_\mathrm{C}$	[10^6 s^{-1}]	193.4 ± 9.0	2.8 ± 0.1	7.6 ± 1.5
$n_\mathrm{T}^0 A_\mathrm{s}$CCD	[10^{10}]	30.31 ± 0.05	7.89 ± 0.04	0.98 ± 0.01
c_e	[10^{-12} cm^3/s]	4.84	0.07	0.19
n_T^0	[10^{14} cm^{-3}]	5.7	1.5	0.2
τ_e	(at 300 K)	12247 y	6.9 y	13.9 d

Table 5.2: $E_\mathrm{C} - E_\mathrm{T}$, $c_\mathrm{e} N_\mathrm{C}$, and $n_\mathrm{T}^0 A_\mathrm{s}$CCD as obtained from the fit in Figure 5.30. The uncertainties are purely from the fit. Systematic uncertainties are not included. The values for c_e were obtained using $N_\mathrm{C} = 4 \times 10^{19}$ cm^{-3} at 300 K and using $m_\mathrm{eff}^e \approx 1.4\ m_\mathrm{e}$ [168]. $\sigma_e = c_s / v_\mathrm{th}$ with $v_\mathrm{th} = 10^7$ cm/s. The initial trap fill density, n_T^0, was obtained using $A_\mathrm{s} = 0.07$ cm^2 and CCD $= 76\ \mu$m.

that about half of the traps are filled. We estimate therefore N_T to be 1.14×10^{15} cm^{-3}. This is eight orders of magnitude smaller than the atom density justifying the approach, $N_\mathrm{T} \ll n_\mathrm{A}$, in Equation (5.47).
From Equation (5.48), we can estimate the cross-section for creating defects, σ_T, assuming a dose of 5 MGy and a negligible initial defect density, $N_\mathrm{T}^0 = 0$. We obtain

$$\sigma_\mathrm{T} = 0.358 \text{ barn} = 3.58 \times 10^{-25} \text{ cm}^2 \,. \tag{5.75}$$

Since we found $E_\mathrm{C} - E_\mathrm{T} < E_\mathrm{gap}/2$, the quantity $N_\mathrm{C} e^{-\frac{E_\mathrm{C}-E_\mathrm{T}}{k_\mathrm{B} T}}$ is larger than $n_0 = N_\mathrm{C} e^{-\frac{E_\mathrm{C}-E_\mathrm{F}}{k_\mathrm{B} T}}$ and also larger than the value $n_0 = n_i \approx 7$ cm^{-3} determined via the measurement of the dark current at 300 K. Hence, the capture of electrons can be considered to be negligible. The time constant for emission of electrons from a trap, τ_e, as defined in Equation (5.35), is at least of the order few seconds even at 600 K. That is, our assumption, $t_\mathrm{drift} \ll \tau_\mathrm{R}, \tau_e$, is reasonable even at larger temperatures.

Not understood TSC Measurement Issues

Not understood is the systematic shift of the exponential of the dark current to larger values of the temperatures while heating-up the second time, which should be the same as described by Equation (5.74). Also, its effect on the fit parameters is not clear. One reason might be the large time constants for releasing electrons, τ_e, that is not all traps are empty after the first heating-up phase.
By fitting Equation (5.74) one can measure the band gap, E_gap. The fit results in $E_\mathrm{gap} \approx 4$ eV, which is smaller than the value of 5.4 eV as given in Table 5.1. Using the exponential rise in the dark current from the first heating-up period results in an even smaller band gap.
The fit of the three peaks is rather difficult and the values of the fit parameters sensitive to small perturbations of the start values for the fit due to the exponentials. Therefore, the uncertainties for the values given in the Table 5.2 are probably larger.

Eventually, because of $n_{\mathrm{T}}^0 < N_{\mathrm{T}}$, the CCD could not be determined with a good precision. This introduces a huge uncertainty for the measurements of n_{T}^0 due to polarization effects and therefore of σ_T. In future measurements, the CCD should be saturated, i.e. the sensor fully pumped according to the explanations of the previous section.

5.3.7 Polarization Effects in scCVD Diamond

Figure 5.27 shows the pumping behavior for the scCVD diamond sample, which absorbed a dose of 5 MGy. The CCD decreases at the beginning of the irradiation period within the first ten hours. We consider this to be an effect of a spatially non-uniform electric field due to *polarization*.

Candidates for Polarization

There are essentially three kinds of possible polarization mechanisms – the uniform polarization of the material by uniformly distributed microscopic dipole moments, polarization due to surface charge-up, and bulk polarization inside the volume of the material due to space charges.
The first one can be excluded, since we keep the externally applied voltage constant. Such a uniform polarization would shift the constant voltage by a certain amount, which is compensated by the voltage supply. We also assume no surface-induced polarizations, since we observe the occurrence of polarization effects with the creation of defects. The latter one is a bulk effect as can be deduced from the discussion above and in the Section 1.2.2.
There is also experimental evidence for a bulk effect. In an experiment, we pumped the scCVD diamond sample, which accumulated before a dose of 5 MGy. The pumping was, however, not complete. During the irradiation, a voltage of 500 V was permanently applied to the sensor. After removing the ^{90}Sr source, i.e. after stopping the pumping, in regular intervals the CCD was measured as function of the time changing the applied voltage in the following way. First the CCD was measured at 500 V. Then, the voltage was switched off and the CCD was measured again. Finally, the voltage was switched on again and the CCD measurement was repeated. The ^{90}Sr source was used only for the CCD measurements and was removed then to avoid a further pumping of the sensor. The sensor was maintained biased until the next measurement period such that the polarization should not resolve by diffusion.
Figure 5.31 shows the result of this experiment. The two rising CCD curves are the CCDs measured with applied voltage, one before and the other after the voltage switch-off. The decreasing curve is the CCD when the voltage was switched off. This CCD is due to the electric field created by the polarization, the direction of which is opposite to the former externally applied electric field.
At the beginning, the absolute values of the CCD with and without applied voltage are coinciding, by chance. The decrease of the CCD without voltage, and the rise of the CCD with voltage, indicate the degradation of the polarization, although the voltage is

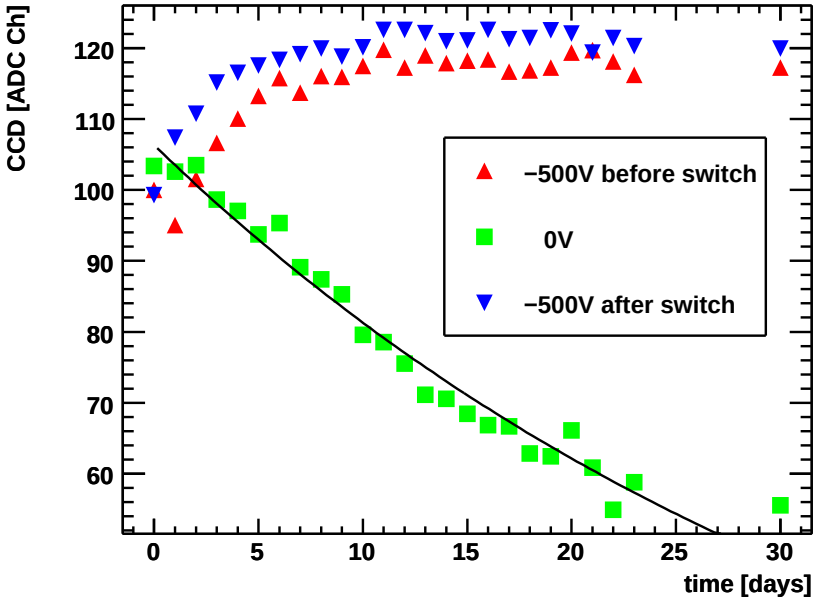

Figure 5.31: CCD as a function of the time for scCVD diamond. The CCD rises with 500 V applied (red and blue triangles). The CCD decreases when no voltage is applied (green squares).

permanently applied except the few minutes for the measurement at 0 V. We assume, that the release of trapped electrons (or holes) due to thermal excitations and the equal filling of the traps (eh-pairs are thermally generated over the whole sensor thickness) cause the reduction of the polarization field. The time constant for the decrease of the CCD at 0 V is about 35 days from a fit using a simple exponential, in rough agreement with τ_e of the third trap level in Table 5.2.[18]

This result suggests that the polarization is connected with filling and emptying of traps. We then have to conclude that the polarization is a bulk effect.

The CCD with applied voltage does not further grow, although the polarization becomes less. Apparently, the mean drift length limit is then reached. Polarization is obviously an additional effect limiting the CCD, on top of the radiation damages.

CCE and Polarization

The fact that polarization can have an effect on the CCE originates from the non-linear dependence of the CCE on $\lambda = \tau_{\text{relax}}\mu\mathcal{E}$, see Equation (5.46). Assuming a space-dependent

[18] Error propagation, and assuming an uncertainty of $\Delta T = 5$ K for the temperature measurement, leads to $\Delta\tau_e/\tau_e \approx 60$ % for this trap.

electric field, $\mathcal{E} = \mathcal{E}(z)$, we require

$$\int_0^{d_\mathrm{s}} \mathcal{E}(z)\, dz = U \ , \tag{5.76}$$

where U is the externally applied voltage. The averaged electric field is, therefore,

$$\langle \mathcal{E} \rangle = \frac{1}{d_\mathrm{s}} \int_0^{d_\mathrm{s}} \mathcal{E}(z)\, dz = \frac{U}{d_\mathrm{s}} \ . \tag{5.77}$$

According to the Equations (5.25) and (5.39), the relaxation time and the mobility might be space-dependent as well, by their dependence on the charge carrier densities, n and p, and on the electric field. For the case of a weak dependence, the averaged mean drift length is approximately given by

$$\langle \lambda \rangle = \frac{1}{d_\mathrm{s}} \int_0^{d_\mathrm{s}} \lambda\, dz \approx \frac{\tau_\mathrm{relax}\mu}{d_\mathrm{s}} \int_0^{d_\mathrm{s}} \mathcal{E}(z)\, dz = \frac{\tau_\mathrm{relax}\mu U}{d_\mathrm{s}} = \tau_\mathrm{relax}\mu \langle \mathcal{E} \rangle \ . \tag{5.78}$$

The average electric field is not changed by the polarization, and also not the mean free path length, if the mobility or the relaxation time do not depend strongly on the electric field. However, the average CCE will be changed, and it holds

$$\langle \mathrm{CCE} \rangle = \frac{1}{d_\mathrm{s}} \int_0^{d_\mathrm{s}} \mathrm{CCE}\big(\lambda(z)\big)\, dz \leq \mathrm{CCE}(\langle \lambda \rangle) \ . \tag{5.79}$$

The prove is given in Appendix E.2. To demonstrate this, we assume an electric field

$$\mathcal{E}(z) = \frac{\beta U \cosh\big(\beta(z - d_\mathrm{s}/2)\big)}{2 \sinh(\beta d_\mathrm{s}/2)} \ , \tag{5.80}$$

which fulfills Equation (5.76), and where β is proportional to the polarization and, thus, the space-dependence of $\mathcal{E}$. The left-hand plot of Figure 5.32 shows the spatial electric field distributions, Equation (5.80), for different values of β for $\tau_\mathrm{relax}\mu = 10^3\ \mu\mathrm{m}^2/\mathrm{V}$, $U = 500\ \mathrm{V}$, and for a thickness $d_\mathrm{s} = 500\ \mu\mathrm{m}$. The average CCE, Equation (5.79), as function of β is also shown in the right-hand plot.
Due to keeping the externally applied voltage constant, the electric field decreases in the sensor center and increases towards the electrodes. The averaged mean drift length is not reduced, but the averaged CCE decreases with increasing β, i.e. with increasing polarization.
The situation is usually more complicated since the mobility is a function of the electric field. Close to the electrodes the drift speed should be large due to the huge electric fields. However, the mobility may approach the saturation and, thus, also the drift speed. In contrast, the drift speed is almost zero in the sensor center. The result is that the averaged mean drift length, $\langle \lambda \rangle$, is already reduced.
The effect of the polarization on the relaxation time is more difficult to estimate since it depends on the equilibrium charge carrier densities, which we do not know a priori.

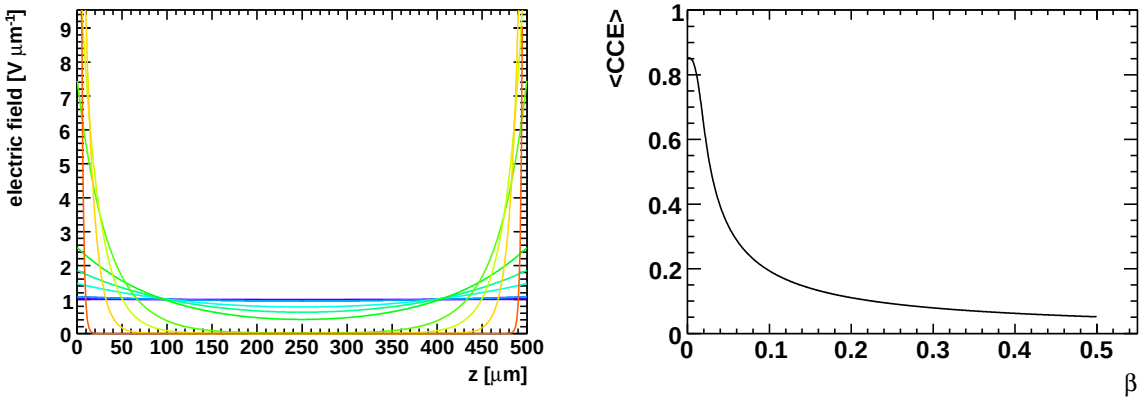

Figure 5.32: The electric field as function of the space-coordinate, z, for values of β between 10^{-4}, for a flat distribution, and 0.5, for a significantly enhanced electric field on the edges close to the electrodes, (left). β characterizes the degree of polarization. The effective CCE as a function of β in this range (right).

At places, where the electric field is almost zero, the recombination becomes dominant, because the charges do not drift. In the high-field regions close to the electrodes dominates usually only one charge carrier type – electrons or holes. Therefore, there are not enough partners for recombination. In addition, in the high-field regions there are large charge carrier density gradients, which may also cause a significant diffusion current contribution. These considerations demonstrate that polarization, i.e. more specifically charge distributions and electric fields, which are space-dependent, can cause a reduction of the effective CCE. We now have to show, how polarization arises as a dynamic effect.

Phenomenological Model for the Polarization

To account for a space-dependent electric field, we have to use the Poisson equation additional to the continuity equations (5.22) to determine the electric field in a self-consistent way. We assume that the electric field will evolve instantaneously with the charge carrier density. The full system of equations is then given by (we stay again in one dimension)

$$\frac{\partial n}{\partial t} = \frac{1}{e}\frac{\partial j_\mathrm{e}}{\partial z} + G + r(n_i^2 - np) - \frac{dn_\mathrm{T}}{dt} \,, \tag{5.81}$$

$$\frac{\partial p}{\partial t} = -\frac{1}{e}\frac{\partial j_\mathrm{h}}{\partial z} + G + r(n_i^2 - np) \,, \tag{5.82}$$

$$\frac{dn_\mathrm{T}}{dt} = c_\mathrm{e}\left((N_\mathrm{T} - n_\mathrm{T})n - N_\mathrm{C}e^{-\frac{E_\mathrm{C}-E_\mathrm{T}}{k_\mathrm{B}T}}n_\mathrm{T}\right) \,, \tag{5.83}$$

$$j_\mathrm{e} = e\mu_\mathrm{e}n\mathcal{E} + \mu_\mathrm{e}k_\mathrm{B}T\frac{\partial n}{\partial z} \,, \qquad j_\mathrm{h} = e\mu_\mathrm{h}p\mathcal{E} - \mu_\mathrm{h}k_\mathrm{B}T\frac{\partial p}{\partial z} \,, \tag{5.84}$$

$$\frac{d\mathcal{E}}{dz} = \frac{e}{\varepsilon\varepsilon_0}(p - n + \varrho N_\mathrm{T} - n_\mathrm{T}) \,, \tag{5.85}$$

where $\rho \in [0,1]$ is the relative charge of an empty trap. G is an extra source term, which parametrizes again an external source, such as ionization due to a ^{90}Sr source or an electron beam, and is defined in Equation (5.52). For the electric field we require again

$$\int_0^{d_\mathrm{s}} \mathcal{E}\, dz = U \ . \tag{5.86}$$

To demonstrate, how polarization arises, and to be able to solve approximately the Equations (5.81) to (5.85), we need some assumptions. First, we assume that we have a quasi-stationary case for the electrons and holes in the conduction and valence bands, respectively. Furthermore, we assume that the generation term, G, is the dominant one, and $r(n_i^2 - np)$ can be neglected. Finally, we assume that the trap density changing rate evolves much slower compared with G. Again we assume, that the electric potential of the charge carriers, eU, is much larger than their thermal kinetic energy, $k_\mathrm{B}T$, hence, we neglect the diffusion current contributions. We obtain

$$0 = \mu_\mathrm{e} \frac{\partial(n\mathcal{E})}{\partial z} + G \ , \tag{5.87}$$

$$0 = -\mu_\mathrm{h} \frac{\partial(p\mathcal{E})}{\partial z} + G \ . \tag{5.88}$$

Both equations are similar and integrable. With the (rather arbitrary) boundary conditions $n(z = d_\mathrm{s}) = 0$ and $p(z = 0) = 0$,[19] we obtain

$$n(z) = \frac{G}{\mu_\mathrm{e}\mathcal{E}(z)}(d_\mathrm{s} - z) \ , \qquad p(z) = \frac{G}{\mu_\mathrm{h}\mathcal{E}(z)} z \ . \tag{5.89}$$

For simplicity we assume $\mu_\mathrm{e} = \mu_h \equiv \mu$. For diamond this is reasonable.
The electron traps, which are uniformly distributed will be, therefore, faster filled at $z \approx 0$ due to Equation (5.64). We assume $n(z) \gg N_\mathrm{C} e^{-\frac{E_\mathrm{C}-E_\mathrm{T}}{k_\mathrm{B}T}}$ and $n_\mathrm{T}(t = 0) = 0$. We obtain

$$n_\mathrm{T}(z,t) = N_\mathrm{T}\left(1 - e^{-c_\mathrm{e} n(z) t}\right) \ . \tag{5.90}$$

It is obvious that for completely filled traps no space-dependent charge distribution exists due to traps.
The electric field is determined by the Poisson Equation (5.85). We distinguish two cases. In the first one the average charge densities in the conduction and valence bands, $n_0 \approx \frac{G}{\mu U/d_\mathrm{s}^2}$, are larger than N_T. We can neglect in the Poisson equation the terms $N_\mathrm{T}\varrho - n_\mathrm{T}$, and obtain

$$\frac{d\mathcal{E}}{dz} = \frac{eG}{\varepsilon\varepsilon_0\mu\mathcal{E}}(2z - d_\mathrm{s}) \ . \tag{5.91}$$

The solution of this differential equation is

$$\mathcal{E}(z) = \sqrt{\mathcal{E}_0^2 + \frac{2eG}{\varepsilon\varepsilon_0\mu}(z - d_\mathrm{s})z} \ . \tag{5.92}$$

[19] Boundary conditions are hard to pose. A more realistic condition is $n(z = d_\mathrm{s}) = n_i$, but since n_i is small, our approach is reasonable.

The integration constant, $\mathcal{E}_0$, has to be chosen to fulfill (5.86).
In the second case we assume $n_0 \ll N_\mathrm{T}$, which is true for all beam currents used by us, and obtain for the Poisson equation

$$\frac{d\mathcal{E}}{dz} = \frac{eN_\mathrm{T}}{\varepsilon\varepsilon_0}\left(\varrho - 1 + e^{-c_\mathrm{e}n(z)t}\right) \ . \tag{5.93}$$

Since $n(z)$ depends on the electric field, $\mathcal{E}$, this differential equation is difficult to solve. If we assume a not too strong space-dependence of $\mathcal{E}$, then we can replace $\mathcal{E}$ by U/d_s in $n(z)$. We get, hence, the approximate solution

$$\mathcal{E} = \frac{eN_\mathrm{T}}{\varepsilon\varepsilon_0}\left((\varrho-1)z + \frac{\mu U}{c_\mathrm{e}Gd_\mathrm{s}t}e^{-c_\mathrm{e}\frac{G}{\mu U/d_\mathrm{s}}(d_\mathrm{s}-z)t}\right) + \mathcal{E}_0 \ , \tag{5.94}$$

where $\mathcal{E}_0$ is again determined by (5.86).
Both cases could contribute to the polarization. Simple estimates show that

$$\sqrt{\frac{eGd_\mathrm{s}^2}{\varepsilon\varepsilon_0\mu}} \approx 25 \text{ V/cm} \ , \quad \text{and} \quad \frac{eN_\mathrm{T}d_\mathrm{s}}{\varepsilon\varepsilon_0} \approx 10 \text{ MV/cm} \ ,$$

for single crystal diamond under testbeam conditions ($I_\mathrm{FC} = 10$ nA). For the estimates we assumed $N_\mathrm{T} \approx 10^{15}$ cm^{-3}. Since the averaged electric field applied to the sensor is $U/d_\mathrm{s} \approx 3$ kV/cm, the first case, the polarization driven by the dose rate, can be neglected in single crystal diamond. It evolves almost instantaneously (characteristic time scale is t_drift) with switching on or off the source.
The second case is governed by the defect density, N_T, which is sufficiently large to play a role. The polarization in this case evolves according to Equation (5.90) with a time constant proportional to $\tau_c = (c_\mathrm{e}n(z))^{-1}$ and depends therefore on the dose rate as can be observed in Equation (5.89), since G does. The polarization due to traps is therefore induced by the space-dependence of the conduction band charge densities, and evolves the faster, the larger the dose rate is. Where $n(z) \approx 0$, i.e. at $z = d_\mathrm{s}$, the characteristic trap evolution time is τ_e as given in Equation (5.35), which is rather small. At $z = 0$, the trap fill time $\tau_\mathrm{T}^{N_\mathrm{T}}$ is maximal and dominated by τ_c.
Under testbeam conditions with e.g. $I_\mathrm{FC} = 10$ nA, the maximum trap fill time is about $\tau_T^{N_\mathrm{T}} = 15$ min for $\tau_c^{-1} = c_\mathrm{e}n(0) = \frac{c_\mathrm{e}Gd_\mathrm{s}^2}{\mu_e U} \approx 10^{-3}$ s^{-1} for the first trap level in Table 5.2 with the largest trap level to conduction band distance. For the shallower traps, the maximum trap fill time is more than 5 hours under the testbeam conditions.
The trap fill time at low dose rates available with a ^{90}Sr source is observed to be of the order of half a month, as is shown in Figure 5.31. The maximum trap filling time of the third trap level with the smallest trap level to conduction band distance in Table 5.2 is about $\tau_\mathrm{T}^{N_\mathrm{T}}$ =22 hours. For the other trap levels, the maximum trap filling time is of the order of years. However, the approximations leading to the Equations (5.89) are not valid at low dose rates and $n(z)$ can be a more complex function of z. Noticeable effects of polarization are already visible after few minutes under the ^{90}Sr source in the CCD setup.

Though, the deeper levels are faster filled using larger dose rates, while the shallower levels might be filled faster using smaller dose rates in our model, where also the exchange of charges between these levels is ignored. Therefore, it is a priori not obvious, which trap level plays the most essential role in the polarization.

CCD Measurement with Polarity Alternating Voltage

For scCVD diamond, the polarization due to the traps can be avoided by using a polarity alternating voltage with a frequency sufficiently large to avoid the development of polarization in the sensor material. Since the time constant for the evolution of polarization is rather large at low dose rates as provided by a ^{90}Sr source, a frequency of 1 Hz suffices to suppress polarization effects. Even with 5 Hz and 10 Hz we did not observe a significant change of the CCD. Figure 5.33 shows the CCD as function of the applied voltage for two cases: with constant voltage and with a voltage alternating with 1 Hz.
For a constant voltage (blue triangles), the bias voltage was increased in steps up to 500 V (upper branch), and then decreased in steps (lower branch). The polarization effect is clearly visible in the hysteresis. Because of the time dependence of the polarization, one has to measure carefully the time of each CCD measurement with constant voltage for the reproducibility of the measurement. This did not always succeed as is reflected in the not so smooth curve of the CCD as a function of the voltage.

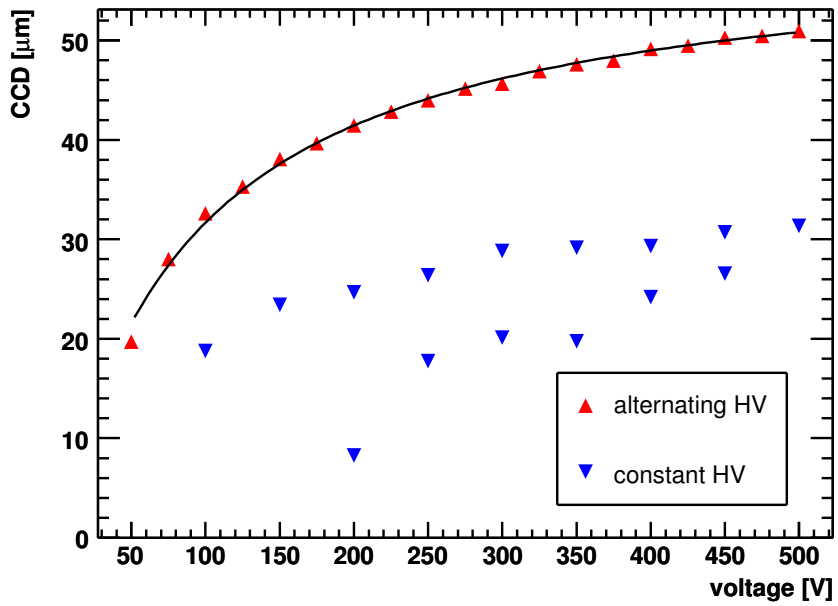

Figure 5.33: The CCD of the scCVD diamond after partly pumping, using constant and alternating high voltage (1 Hz) applied.

Using an alternating voltage results in a higher CCD for a given voltage, and a smoother and time-independent CCD as a function of the voltage (red triangles). The fit using

Equations (5.44) and (5.39) results in $\tau_{\text{relax}} \approx 10^{-4}$ s and a mobility of about 3700 cm^2/Vs. The value obtained for the mobility matches well into the range given in Table 5.1. The value of τ_{relax} indicates that only few traps were filled, i.e. $n_{\text{T}} \ll N_{\text{T}}$, and therefore $\tau_{\text{T}} \approx (c_{\text{e}} N_{\text{T}})^{-1} \approx 10^{-5} \ldots 10^{-3}$ s for $N_{\text{T}} \approx 10^{15}$ cm^{-3} and $c_{\text{e}} \approx 10^{-10} \ldots 10^{-12}$ cm^3/s as given in Table 5.2.
Hence, the mobility seems to be largely unaffected by the radiation damages, whereas the creation of traps reduces the relaxation time . The strong drop in the CCD and in the sensor current during the irradiation in the testbeam is mainly caused by the development of the polarization. This might also explain the dose rate independence of the ratio $I_{\text{s}}/I_{\text{FC}}$ in Figure 5.8. The polarization effect dominates, and jumps due to the dose rate change are hardly visible.
To avoid polarization effects, which considerably affect the measurements of the CCD of diamond sensors, a voltage with alternating polarity with a sufficiently large frequency is necessary.

Operation Modes with Polarity Alternating Voltage

One can exploit this feature of diamond also for certain operation modes as are listed in Section 5.1.2. Of course, for a current monitor, alternating voltage makes no sense, because one wishes to see the signal current above the dark current. With alternating voltage, however, also the polarization current will flow, which is much larger than the dark current. Small signal currents might not be visible on top of this background, whereas on top of the dark current they still are.
For a MIP counter, on the other hand, or for BeamCal-sensors the alternating voltage mode is applicable if the events of incident particles occur bunch-wise such as for the ILC. Due to bunch trains with breaks of 100 ms in between, there is enough time for switching the voltage polarity without creating a dead time. Whether the signals have positive or negative polarity just matters for the readout electronics, but can be accounted for technically. In this way, the deteriorating effects of polarization can be avoided and the CCE can be maintained on a higher level for a much longer time and dose than for the 5 MGy we used in the testbeam. Thus, we would have sensors with much larger radiation tolerance than sensors with constant voltage applied.
While for a MIP counter only a threshold is necessary, which needs to be exceeded by the signal to count the events, BeamCal provides information about the deposited energy via the absolute signal size, which essentially scales with the CCE. Therefore, the signal size for a fixed energy deposit must be calibrated regularly with a reference signal to monitor changes of the CCE. The characteristic trapping time constant depends on the dose rate as well as the trap fill level. Interruptions of the experiment will lead to a release of the trapped electrons reducing the CCE. This rather short term behavior is more complex than the general CCE drop due to the absorbed radiation dose, although polarization effects are suppressed, and must be monitored as well.

Chapter 6

Summary

In this thesis, we investigated the physics potential of a future linear collider to contribute to the exploration of a corner stone of the electroweak Standard Model - the Higgs mechanism. Using the *recoil mass technique*, which allows the reconstruction of the Higgs boson in the Higgs-strahlung process $e^+e^- \to Zh$ without a specific model of the Higgs boson decay, the precision reachable for the measurement of the mass and the hZZ-coupling are estimated. In this context, the development of the reconstruction software tools was advanced. The performance of the track reconstruction is investigated using a realistic detector simulation in the full momentum and polar angle range. A method to identify particles after full reconstruction of tracks and calorimeter showers is developed and tested.
For a particular sub-detector in the very forward region, the BeamCal, research and development is pursued for proper sensors. These sensors have to withstand radiation doses of up to 10 MGy.
Single and polycrystalline CVD diamond, GaAs and silicon sensor samples are exposed to doses of up to 5 MGy at the DALINAC electron accelerator and their performance is measured as function of the absorbed dose. Progress was made in the understanding of the impact of radiation damage on the performance of the sensors.

6.1 The Profile of the Higgs Particle

We performed a Higgs recoil analysis based on Monte-Carlo simulations, including a realistic detector simulation, a full reconstruction and the Standard Model background processes to estimate the precision of the measurement of the Higgs boson mass and the Higgs-strahlung cross-section.
We demonstrated, how such an analysis has to be accomplished generally when using experimental data. When experimental data are available, the Monte-Carlo sample used so far will be replaced by them in the final analysis stage. Furthermore, we found that a precision of the Higgs strahlung cross-section and Higgs boson mass measurement of about 10 % and 1 ‰, respectively, can be achieved after an integrated luminosity of 50 fb^{-1}, for $M_h = 120$ GeV. This corresponds to about one month of ILC operation at $\sqrt{s} = 250$ GeV

and with a luminosity of $\mathcal{L} = 2 \times 10^{34}$ cm^{-2}s^{-1}. A larger cms energy leads to a large drop in the precision of the Higgs boson mass measurement due to the increasing lepton momentum measurement uncertainty.

The Higgs potential parameters can be determined, using Equations (1.19) and (1.27), by

$$\mu = \frac{M_h}{\sqrt{2}} \qquad \text{and} \qquad \lambda = \frac{\mu^2}{v^2} = \sqrt{8} M_h^2 G_F \; .$$

The uncertainties of these parameters, depending on those of the Higgs boson mass measurement, are

$$\Delta\mu = \frac{\Delta M_h}{\sqrt{2}} \approx 0.085 \text{ GeV} \; ,$$

and

$$\Delta\lambda = 4 \cdot \sqrt{2} M_h G_F \, \Delta M_h \approx \frac{7.92 \times 10^{-3}}{\text{GeV}} \, \Delta M_h \approx 9.5 \times 10^{-4} \; ,$$

for an integrated luminosity of 50 fb^{-1} and $M_h = 120$ GeV.

For a Higgs boson mass of $M_h = 180$ GeV, an integrated luminosity of about 250 fb^{-1} at $\sqrt{s} = 350$ GeV is needed to obtain the same significance as for the investigations using $M_h = 120$ GeV. Using only 50 fb^{-1}, the relative uncertainty of the Higgs-strahlung cross-section is about 23 %. The determination of the Higgs boson mass is difficult to perform. Due to the larger width of the recoil mass peak and the strong fluctuations of the background the signal recoil mass peak is hardly visible on top of the background.

The statement that the recoil mass analysis in case of the Higgs-strahlung process is independent on the Higgs boson decay mode needs a revision. If the decay mode is not known then an additional relative uncertainty of the cross-section measurement of about 10 % occurs.

6.2 Radiation-Hard Sensors for BeamCal

We presented the results of current radiation hardness investigations for several sensor material candidates for the BeamCal. The most promising material matching many of the requirements is GaAs, which withstands about 1 MGy. Also single crystal (scCVD) and polycrystalline (pcCVD) chemical vapor deposition diamond, and silicon sensors were investigated at room temperature. Silicon shows a huge dark current above a dose of 90 kGy. The diamond sensors tolerate at least 5 MGy. In question is, however, whether diamond sensors are available as large-size wafers in the near future, i.e. as wafers with sizes of about 100 cm^2 or larger, and for reasonable prices.
The MIP sensitivity, which was investigated in the radiation hardness experiments, is important for the calibration and alignment of the BeamCal sensors. The investigated GaAs and diamond sensors retain their MIP sensitivity, and stay operational in this respect.

For the inner BeamCal segments much larger signals than those from MIPs are expected inside the beamstrahlung pair showers. GaAs and diamond will surely stay sensitive to these signals. Only the response will decrease with the accumulated dose, and also the sensitivity and the precision of the measurement of the energy deposited in the shower will drop.
In order to obtain a better understanding of the impact of radiation damages on the sensor performance, we investigated scCVD diamond in more detail. A model based on semiconductor physics was applied for this purpose. With the help of the drift-diffusion model we were able to estimate several phenomenological constants – time scales and cross-sections – for scCVD diamond from the experimental results. Similarly, for GaAs values for some phenomenological quantities were estimated.
The observation of strong polarization effects in diamond led to the closer investigations of this polarization under high intensity irradiation. Such strong polarization effects are expected in the model as a consequence of the increasing amount of radiation damages inducing charge trapping and therefore space charges in the bulk material. The development of polarization with increasing density of local damages may be the major reason for a signal drop also in other isolator crystals. Measurements are proposed to prove the general validity of the model.
An interesting option is to operate diamond sensors with alternating high voltage polarities. Then the drop of the signal due to polarization may be reduced. A proposal for a dedicated testbeam study is made to investigate this option also for other isolator crystals.
For the semi-insulating GaAs, we did not detect indications of polarization. The charge carrier concentrations in the valence and conduction band are usually too large such that the time scales for trapping and recombination might evolve rather fast. Hence, polarization effects in GaAs may be difficult to detect since lifetime is below our time resolution. In any case, the fast drop of the CCD with the accumulated dose is mostly an effect of the change in the trapping or recombination time since the current, and therefore also the mobility, does not change too much. Whether the persisting doping and a possible reaction to the irradiation with electrons is responsible, or whether new defects are created during the irradiation, we cannot conclude.

Acknowledgement

Ich möchte mich bei DESY und der TU Cottbus für die Ermöglichung meiner Promotion bedanken. Vielen Dank an Herrn Lohmann für die Betreuung meiner Arbeit. Ebenso danke ich den Gutachtern, W. Lohmann, J. Mnich und J. Reif für die Begutachtung der Arbeit.
Sehr herzlich möchte ich mich bei den Mitarbeitern von DESY bedanken, die mich sehr unterstützt haben. Speziell und besonders Andreas Schälicke, Sergej Schuwalow, Aleksei Raspereza und Ringo Schmidt bin ich zu Dank verplichtet für ihre Bereitschaft zur Diskussion und ihre Offenheit wenn es darum ging, Wissen und Erfahrung auszutauschen. Ich danke ihnen auch für ihre Geduld mit mir.
Bedanken möchte ich auch insbesondere beim Rechenzentrum von DESY in Zeuthen, das ich als eines der effizientesten kennenlernen durfte. Die Zusammenarbeit mit ihm hat nicht nur Spass gemacht, sondern brachte mir auch einen enormen Wissens- und Erfahrungszuwachs im Bereich der Informatik.
Nicht zuletzt möchte ich mich auch meiner Frau, Natascha, bedanken, die mich sehr unterstützt hat insbesondere in der Phase des Zusammenschreibens meiner Dissertation.
Schliesslich möchte ich auch allen danken, die mich direkt oder indirekt unterstützt und mir die Daumen gedrückt haben.

Appendix A

Probabilistic Method for Case Distinction

A.1 One Variable

Let's assume, we have a quantity x that is measured in an experiment with which we want to distinguish two cases. For example, x could be the energy deposition inside an electromagnetic calorimeter, and we want to distinguish whether an electron and or a muon is causing this deposition. The quantity x is a number, which is randomly distributed according to $f_1(x)$ for electrons and according to $f_2(x)$ for muons.
If the distributions are normalized, i.e. it holds

$$\int f_i(x)\,dx = 1\ , \qquad i = 1, 2\ , \tag{A.1}$$

then the probability to find a value $x \in [X, X + dX]$ under the condition to have a particle i is given by

$$P(X|i) \equiv P_i(X < x < X + dX) = f_i(X)\,dX\ . \tag{A.2}$$

Using the Bayesian Theorem [193], we can calculate the probability to have the particle i under the assumption that $x \in [X, X + dX]$,

$$P(i|X) = \frac{P(X|i)P(i)}{\sum_j P(X|j)P(j)} = \frac{f_i(X)\,dX \cdot P(i)}{\sum_j f_j(X)\,dX \cdot P(j)}\ . \tag{A.3}$$

The only unknown quantities are the prior probabilities, $P(i)$, to have an electron or a muon at all. If we have no information about these probabilities, we assume a uniform distribution, i.e. $P(i) = 1/2$ for $i = 1, 2$. If there are N particles to be distinguished, then $P(i) = 1/N$ for $i = 1, \ldots, N$. That is, the probability that a particle i caused the energy deposition X is given by

$$P(i|X) = \frac{f_i(X)}{\sum_j f_j(X)}\ . \tag{A.4}$$

An Example

Assume we want to distinguish electrons and muons from the energy deposited by them inside the electromagnetic calorimeter divided by the particle energy, $x = E_{\mathrm{ECAL}}/E$. It is obvious that $x \in [0,1]$. We assume the following (arbitrarily chosen) distributions normalized in $x \in [0,1]$

$$f_e(x) = 2x \ , \qquad f_\mu(x) = 2(1-x) \ .$$

If we measure a certain value $x = X$, then the probability that this deposition is caused by an electron is given by Equation (A.4),

$$P(e|X) = \frac{2X}{2X + 2(1-X)} = X \ .$$

Accordingly, the probability for a muon causing this deposition is given by

$$P(\mu|X) = \frac{2(1-X)}{2X + 2(1-X)} = 1 - X \ .$$

The discrimination power is the more significant, the farther X is away from $1/2$.

A.2 More Variables

We now want to distinguish N particles. This time we have M variables x_i for this purpose. The distributions can be now quite complex accounting for possible correlations between these variables. For example, one can use M functions for each particle type, where each single distribution is a function of one of the variables, such as in the previous section,

$$f_j(x_i) \ , \qquad i = 1, \ldots, M \ ; \ j = 1, \ldots N \ .$$

On the other hand, we could also use two-dimensional distributions being function of two of the variables, which are pairwise different

$$f_{j,k}(x_i, x_l) \ , \qquad i, l = 1, \ldots, M \ ; \ j = 1, \ldots N \ .$$

The index k runs from 1 to the number of different distributions – in maximum $M(M+1)/2$. However, one can also take less distributions.
How to continue is obvious, and in the extreme case, one can use one function of all variables as distribution,

$$f_j(x_1, \ldots, x_M) \ , \qquad j = 1, \ldots N \ .$$

Distributions of one and more dimensions even can be combined. For a clearer view, we summarize the variables into a vector $\vec{x} = (x_1, \ldots, x_M)^T$. We assume K distributions $f_{j,k}(\vec{x})$, where $k = 1, \ldots, K$ and j is the particle index. The functions $f_{j,k}$ depend on one

or more of the variables in $\vec{x}$ and are normalized with respect to the integral over the volume spanned by the variables f depends on.
The single probability to have the particle i under the assumption that $\vec{x}$ is inside a volume $\prod_{i=1}^{M} dX_i$ around $\vec{X}$ is given by

$$P_k(i|\vec{X}) = \frac{f_{i,k}(\vec{X})}{\sum_{j=1}^{N} f_{j,k}(\vec{X})} \,. \tag{A.5}$$

The total probability of having the particle i if $\vec{x}$ is inside a volume $\prod_{i=1}^{M} dX_i$ around $\vec{X}$ is then the normalized product

$$P(i|\vec{X}) = \frac{\prod_{k=1}^{K} P_k(i|\vec{X})}{\sum_{j=1}^{N} \prod_{k=1}^{K} P_k(j|\vec{X})} \,. \tag{A.6}$$

A.3 Notes for Application

The variables can be out of a finite range, but also out of a infinite range. To be useful for computer applications the range must be necessarily restricted to a finite range. In this case, a bin must be added with describes the probability to be outside this range. Important is also that the distributions are nowhere close to zero, because then the computer precision might not be sufficient to give a good separation in at this location. If the distribution is too close to zero, also the division-by-zero error could occur in Equation (A.6).
Usually the distributions are also not known analytically. One has to use histograms instead. Samples of distributions are generated using Monte-Carlo simulations, and the histograms are filled and normalized. The same remarks as for the distributions also hold for histograms.

Appendix B

Documentation of PFOID

PFOID is a MARLINRECO sub-package and provides processors for particle identification and creation of probability density functions (PDF) needed for the identification. The particle identification is based on a likelihood method as described in Appendix A. In the following the general usage of the processors is described, followed by a detailed description of the class hierarchy used.

B.1 Usage of the Processors

There are currently two processors in this package. PFOID performs the particle identification and CREATEPDFS creates one-dimensional probability functions needed by PFOID.

B.1.1 PFOID

The PFOID processor reads PDF files of a certain format. This format is that general, that in principle arbitrary combinations of the variables can be used in the histograms. That is, one could also combine one and more-dimensional histograms. The PDF file just describes the variables and the corresponding histograms in a header, and finally specifies the histogram entries.
The PFOID processor has four parameters (three after the last modification by A. Raspiereza):

RecoParticleCollection
the collection containing the reconstructed particle flow objects, to which a particle identity should be assigned.

NewRecoParticleCollection
the collection, in which the reconstructed particles with a particle ID should be written (obsolete now)

FilePDFName
the name of the PDF file containing the PDF histograms for the charged particles

neutralFilePDFName
the name of the PDF file containing the PDF histograms for the neutral particles

There are two big classes – charged and neutral particles – the particles are subdivided in. They are distinguished by whether they have a track or not. For both classes different variables and distributions give optimal results. That is why two different PDF files are necessary.
Currently identified particle types are electrons, muons and pions in the charged particle class, and photons and neutral hadrons (K_L^0) in the neutral particle class. Other particles than these are assigned to one of these particle types according to their probability.

B.1.2 CreatePDFs

The CreatePDFs processor shall create the PDF files. This is currently a bit inconvenient, since no way was found to split the task for each particle type. That is, all particle type samples must be available are processes at once.
CreatePDFs also provides only one-dimensional PDFs out of the following variables (see also Section 3.3): $E_{\mathrm{ECAL}}/N_{\mathrm{ECAL}}$, $E_{\mathrm{HCAL}}/N_{\mathrm{HCAL}}$, $\epsilon_{\mathrm{cluster}}$ (1-excentricity), $\langle d_{\mathrm{hit-track}} \rangle$ (mean hit-track distance), $L1$ (last layer of HCAL with a hit), $L2$ and $L3$ (next-to-last and next-to-next-to-last layer of HCAL with a hit), $E_{\mathrm{ECAL}}/E_{\mathrm{total}}$, E_{ECAL}, E_{HCAL}, $\langle E d_{\mathrm{hit-track}} \rangle$ (energy weighted mean hit-track distance), N_{ECAL}, N_{HCAL}, $EL1$ (first ECAL layer with a hit), $EL2$ and $EL3$ (second and third ECAL layer with a hit). Only these are also known by Pfoid!
For each of these variables ranges have to be specified, which are currently hard-coded in the *include/Configure.h*.
The following variables are used for the charged particle class: $E_{\mathrm{ECAL}}/N_{\mathrm{ECAL}}$, $E_{\mathrm{HCAL}}/N_{\mathrm{HCAL}}$, $\varepsilon_{\mathrm{cluster}}$, $\langle d_{\mathrm{hit-track}} \rangle$, $L1$, and $E_{\mathrm{ECAL}}/E_{\mathrm{total}}$.
For the neutral particle class, the following variables are used: $E_{\mathrm{ECAL}}/N_{\mathrm{ECAL}}$, $E_{\mathrm{HCAL}}/N_{\mathrm{HCAL}}$, $\varepsilon_{\mathrm{cluster}}$, $\langle d_{\mathrm{hit-track}} \rangle$, $L1$, $E_{\mathrm{ECAL}}/E_{\mathrm{total}}$ and $EL1$.
The parameters of the CreatePDFs processor are:

MCParticleCollection
collection containing the MC information of the reconstructed particles

RecoParticleCollection
the collection containing the reconstructed particle flow objects

ChargedPDFfilename
name of the output PDF file for the charged particle class

NeutralPDFfilename
name of the output PDF file for the charged particles

ChargedRunStart
array of run numbers at which a new charged particle sample starts in the sclio-input files

NeutralRunStart
array of run numbers at which a new neutral particle sample starts in the sclio-input files

PIDCollection
array of numbers containing the PIDs (particle identities), which shall be accepted in the calibration procedure (for neutral hadrons 130 (K_L^0) and 2112 (n) are used)

PIDnumbers
array of numbers of PIDs used per particle type (2 for neutral hadrons, see above)

RelCollection
name of the relation collection for the calorimeter hits (MC info relation)

MCTracksRelCollection
name of the relation collection for the tracker hits (MC info relation)

The sclio files must be specified in the order: first charged particles then neutral particles! It is in the responsibility of the user to provide the correct samples (single particle events) of the correct type and the correct order!

B.2 Description of the PDF Class Hierarchy

Both processors PFOID and CREATEPDFS use an object called *PDF* (corresponding to PDF.h and PDF.cc). This class contains the histograms, i.e. the distributions for each particle type, for example.
The PDF object is a general framework for likelihood based separation procedures of events. It was used for the particle identification as well as for the signal-background separation in the Higgs recoil mass analysis. A simple handling and a convenient extension to higher-dimensional probability density functions were the primary design guide lines.
This class contains a *VObject* (corresponding to VObject.h and VObject.cc), which contains the variables in a dynamic way. It contains further *Category* objects (which represent, for example, the particle types; corresponding to Category.h and Category.cc), and each category contains *Histogram* objects (corresponding to Histogram.h and Histogram.cc)
The *PDF* class contains methods to create and fill the histograms for each category, to read histograms from or to write them to a PDF file for each category with a consistency check, and to calculate the likelihood for a variable set (inside the *VObject*) of being one of the categories (e.g. particle types).
The *VObject* and the *Category* classes are just containers for bookkeeping. The actual work is done in the *Histogram* class. Methods for filling, reading, normalizing, ... the histogram are available, similar to the histogram class of ROOT. However, ROOT just provides at most three-dimensional histograms. Therefore, it was necessary to create an own histogram class. The filling of the histograms is not optimized with respect to the speed, yet. Just

a simple search algorithm is used. Here is space for optimization e.g. by using a binary search algorithm.
Table B.1 shows the format of the PDF file, which are currently ASCII files. Figure B.1 shows the class diagrams and hierarchy of the PDF object.

> PDF name
> Number of Categories = K
> Name of Category 1 > Name of Category 2 > .... > Name of Category K
> Number of Variables = M
> Name of Variable 1 > Name of Variable 2 > .... > Name of Variable M
> Number of Histograms = N
> Dimension of histogram 1 > Dimension of histogram 2 > .... > Dimension of histogram N
> Name of histogram 1 > Name of histogram 2 > .... > Name of histogram N
> Name of Variable 1 in histogram 1 > start1 > bin width 1 > Number of bins 1 > Name of Variable 2 in histogram 1 > start2 > bin width 2 > Number of bins 2 > .... > Name of Variable Dim. 1 in histogram 1 > start Dim > bin width Dim > Number of bins Dim
> Name of Variable 1 in histogram 2 > start1 > bin width 1 > Number of bins 1 > .... > .... > Name of Variable Dim. N in histogram N > start Dim > bin width Dim > Number of bins Dim
> content of histogram 1 in category 1 > content of histogram 2 in category 1 > .... > content of histogram N in category 1
> content of histogram 1 in category 2 > .... > .... > content of histogram N in category K

Table B.1: The PDF file format

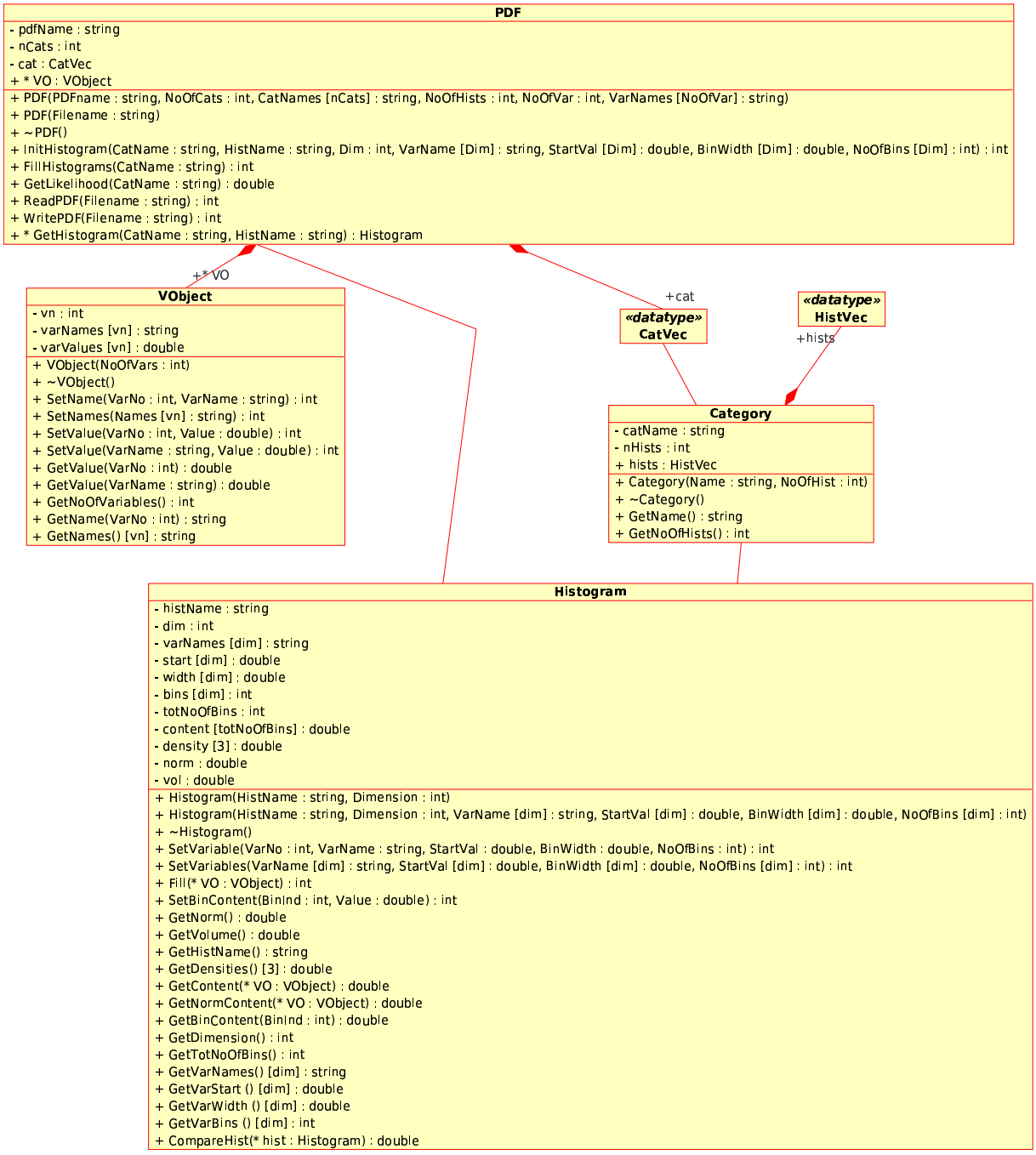

Figure B.1: Class hierarchy for the PDF object.

Appendix C

Kinematic of the Higgs-Strahlung Process

C.1 Relation between Z Boson and Lepton Momenta

As described in Section 4.1 for the on-shell situation where the recoiled Higgs and Z bosons have their pole masses, M_h and M_Z, respectively, the energy of the Z boson is given by

$$E_Z = \frac{s + M_Z^2 - M_h^2}{2\sqrt{s}} \, .$$

If the polar and azimuthal angles of the Z boson are given, also the momentum of the Higgs boson is completely determined by the energy-momentum conservation on the hZZ-vertex. However, the Z boson momentum direction is not fix. Using the coss-section in the Standard Model the Z prefers to be recoiled perpendicular to the beam pipe at the ILC, but any other polar angle is also possible. For the azimuthal angle there is no preference at all.

We therefore assume the Z boson moves into the positive z-direction, index 0 in this frame, i.e. its four-momentum is given by

$$p_Z^0 = (E_Z, 0, 0, p_Z)^T \equiv (E_Z, 0, 0, \beta_Z E_Z) \, ,$$

where $\beta_Z^2 = 1 - 1/\gamma_Z^2$ and $\gamma_Z = E_Z/M_Z$. Any other direction can be achieved by rotation of the three-momentum vector,

$$p_Z = R p_Z^0 \, , \quad R = \begin{pmatrix} 1 & 0 & 0 & 0 \\ 0 & & & \\ 0 & & \mathcal{R} & \\ 0 & & & \end{pmatrix} \, ,$$

and $\mathcal{R}$ being a three-dimensional rotation matrix. The Lorentz transformation matrix

$$\Lambda(-\beta_Z) = \begin{pmatrix} \gamma_Z & 0 & 0 & -\beta_Z\gamma_Z \\ 0 & 1 & 0 & 0 \\ 0 & 0 & 1 & 0 \\ -\beta_Z\gamma_Z & 0 & 0 & \gamma_Z \end{pmatrix}$$

transforms p_Z^μ in the Z boson rest frame, i.e.

$$\Lambda(-\beta_Z)p_Z^\mu = (M_Z, 0, 0, 0)^T \ .$$

$\Lambda(\beta_Z)$ is the back transformation.
The Z boson boost direction is taken as the z-axis also in the Z boson rest frame. The x- and y-axes are maintained. The Z boson decays into leptons, which obtain in the Z boson ret frame the equal amount of energy, $M_Z/2$, and fly in mutually opposite directions. Neglecting the lepton masses, their four-momenta can be parametrized by

$$p_\pm^r = \frac{M_Z}{2}(1, \pm\sin\vartheta^r\cos\varphi^r, \pm\sin\vartheta^r\sin\varphi^r, \pm\cos\vartheta^r)^T \ ,$$

where ϑ^r and φ^r are the polar and azimuthal angles, respectively, of the positive lepton, index r denoting quantities in the Z boson rest frame. By transforming these vectors into the ILC frame, i.e. applying $\Lambda(\beta_Z)$ results in

$$p_\pm^0 = \frac{M_Z}{2}(\gamma_Z(1 \pm \beta_Z\cos\vartheta^r), \pm\sin\vartheta^r\cos\varphi^r, \pm\sin\vartheta^r\sin\varphi^r, \gamma_Z(\beta_Z \pm \cos\vartheta^r))^T \ .$$

The three-momentum absolute value is

$$|\vec{p}_\pm^{\,0}| = \frac{M_Z}{2}\left(\sin^2\vartheta^r + \gamma_Z^2(\beta_Z \pm \cos\vartheta^r)^2\right)^{1/2} \ .$$

The cosine of the acollinearity is then obtained as

$$\cos\alpha_{\text{acoll}} = \frac{\vec{p}_-^{\,0}\cdot\vec{p}_+^{\,0}}{|\vec{p}_-^{\,0}|\,|\vec{p}_+^{\,0}|} = \frac{\gamma_Z^2(\beta_Z^2 - \cos^2\vartheta^r) - \sin^2\vartheta^r}{\left[\left(\sin^2\vartheta^r + \gamma_Z^2(\beta_Z + \cos\vartheta^r)^2\right)\left(\sin^2\vartheta^r + \gamma_Z^2(\beta_Z - \cos\vartheta^r)^2\right)\right]^{1/2}} \ ,$$

which results for $\vartheta^r = \pi/2$, i.e. the leptons move perpendicular to the Z boson momentum direction in the Z boson rest frame,

$$\cos\alpha_{\text{acoll}} = 1 - \frac{2}{\gamma_Z^2} = \frac{2M_Z^2}{E_Z^2} = 1 - \frac{4M_Z^2 s}{(s + M_Z^2 - M_h^2)^2} \ . \tag{C.1}$$

For $M_h = 120$ GeV and $\sqrt{s} = 250$ GeV, we obtain, thus, an acollinearity of about 108°. Furthermore, $|\vec{p}_\pm^{\,0}| = \frac{M_Z\gamma_Z}{2} = \frac{E_Z}{2}$, as it must be.
The rotation matrix $\mathcal{R}$ can be written as a product of the rotation about the x-axis with the Z boson polar angle, ϑ_Z, and the rotation about the z-axis with the Z boson azimuthal angle, φ_Z,

$$\mathcal{R} = \mathcal{R}_z(\varphi_Z) \circ \mathcal{R}_x(\vartheta_Z) \ ,$$

where

$$\mathcal{R}_z(\varphi_Z) = \begin{pmatrix} \cos\varphi_Z & -\sin\varphi_Z & 0 \\ \sin\varphi_Z & \cos\varphi_Z & 0 \\ 0 & 0 & 1 \end{pmatrix} , \qquad \mathcal{R}_x(\vartheta_Z) = \begin{pmatrix} 1 & 0 & 0 \\ 0 & \cos\vartheta_Z & -\sin\vartheta_Z \\ 0 & \sin\vartheta_Z & \cos\vartheta_Z \end{pmatrix} .$$

Then the relation to the lepton momenta in the ILC cms frame are

$$\vec{p}_\pm = \mathcal{R}\vec{p}^{\,0}_\pm = \frac{M_Z}{2} \begin{pmatrix} \pm\sin\vartheta^r\cos\varphi^r\cos\varphi_Z - \sin\varphi_Z\,(\pm\sin\vartheta^r\sin\varphi^r\cos\vartheta_Z - \gamma_Z(\beta_Z \pm \cos\vartheta^r)\sin\vartheta_Z) \\ \pm\sin\vartheta^r\cos\varphi^r\sin\varphi_Z + \cos\varphi_Z\,(\pm\sin\vartheta^r\sin\varphi^r\cos\vartheta_Z - \gamma_Z(\beta_Z \pm \cos\vartheta^r)\sin\vartheta_Z) \\ \pm\sin\vartheta^r\cos\varphi^r\sin\vartheta_Z + \gamma_Z(\beta_Z \pm \cos\vartheta^r)\cos\vartheta_Z \end{pmatrix} .$$

In a specific case we choose $\varphi_Z = 0$, $\vartheta_Z = \pi/2$, and the above expression simplifies

$$\vec{p}_\pm = \frac{M_Z}{2}(\pm\sin\vartheta^r\cos\varphi^r, -\gamma_Z(\beta_Z \pm \cos\vartheta^r), \pm\sin\vartheta^r\sin\varphi^r)^T .$$

Assuming further $\varphi^r = 0$, $\vartheta^r = \pi/2$, then this reduces to

$$\vec{p}_\pm = \frac{M_Z}{2}(\pm 1, -\beta_Z\gamma_Z, 0)^T .$$

C.2 Momentum Parametrizations and Relations

A three-momentum can be parametrized in spherical coordinates as

$$\vec{p} = p(\sin\vartheta\cos\varphi, \sin\vartheta\sin\varphi, \cos\vartheta) , \tag{C.2}$$

with p the absolute value, i.e. $|\vec{p}| = p$, and ϑ and φ the polar and azimuthal angles, respectively. In cylindrical coordinates it looks like

$$\vec{p} = p_\perp(\cos\varphi, \sin\varphi, \mathrm{ctg}\vartheta) ,$$

where ctg is the cotangent ($\cos\vartheta/\sin\vartheta$), $p_\perp$ is the transverse momentum. The absolute value is then

$$|\vec{p}| = p\sqrt{1 - \mathrm{ctg}^2\vartheta} = \frac{p_\perp}{\sin\vartheta} .$$

We define the acoplanarity as

$$\alpha_{\mathrm{acopl}} = |\varphi_+ - \varphi_-| \mod \pi , \tag{C.3}$$

which represents the angle between the two planes spanned each by the unit vector in z-direction and the respective momentum vector of the leptons.
In the final example of the previous section we obtain therefore

$$p_\pm = \frac{E_Z}{2} , \quad \vartheta_\pm = \frac{\pi}{2} , \qquad p_\perp \equiv p .$$

In this special case, acollinearity and acoplanarity are the same, but to calculate $\varphi_\pm$ one has to solve simultaneously

$$\cos\varphi_\pm = \pm\frac{1}{\gamma_Z} , \qquad \sin\varphi_\pm = -\beta_Z .$$

C.3 Summary of Event-specific Variables

The invariant di-lepton mass, $m_{\mathrm{di-lepton}}$ were introduced in Equation (4.6) in Section 4.1.3. The cosine of the polar angle of the lepton momenta in the ILC laboratory frame, $\cos\vartheta_{\ell^\pm}$, are also introduced there and were used for the process identification.
The acollinearity, i.e. the angle between the momenta of a lepton-antilepton pair, and the acoplanarity were introduced in Section 4.1.4 in Equation (4.9) and in Equation (C.3), respectively. Figure C.1 illustrates amongst others the acollinearity and the acoplanarity. Additionally, we define the di-lepton polar angle by

$$\cos\vartheta_{\mathrm{di-lepton}} = \frac{p_{\ell^+,z} + p_{\ell^-,z}}{|\vec{p}_{\ell^+} + \vec{p}_{\ell^-}|} \tag{C.4}$$

and the missing transverse momentum,

$$p_\perp^{\mathrm{miss}} = \sqrt{(p_{\ell^+,x} + p_{\ell^-,x})^2 + (p_{\ell^+,y} + p_{\ell^-,y})^2}\,, \tag{C.5}$$

$p_{\ell^\pm,x}$, $p_{\ell^\pm,y}$ and $p_{\ell^\pm,z}$ denoting the components of the lepton momenta in the ILC laboratory frame. $p_\perp^{\mathrm{miss}}$ characterizes the transverse momentum imbalance due to the not reconstructed recoiled Higgs boson.
All of the seven variables, $m_{\mathrm{di-lepton}}$, $\cos\vartheta_{\mathrm{di-lepton}}$, $\cos\vartheta_{\ell^\pm}$, α_{acoll}, α_{acopl}, and $p_\perp^{\mathrm{miss}}$, are distributed over a certain range. For the Higgs-strahlung process, all variables except the polar angles exhibit pronounced peaks in their distributions. Specifically, the peak of the Z boson resonance appears in the $m_{\mathrm{di-lepton}}$ spectrum at M_Z, and the acollinearity has a peak around 108° for $\sqrt{s} = 250$ GeV and $M_h = 120$ GeV.

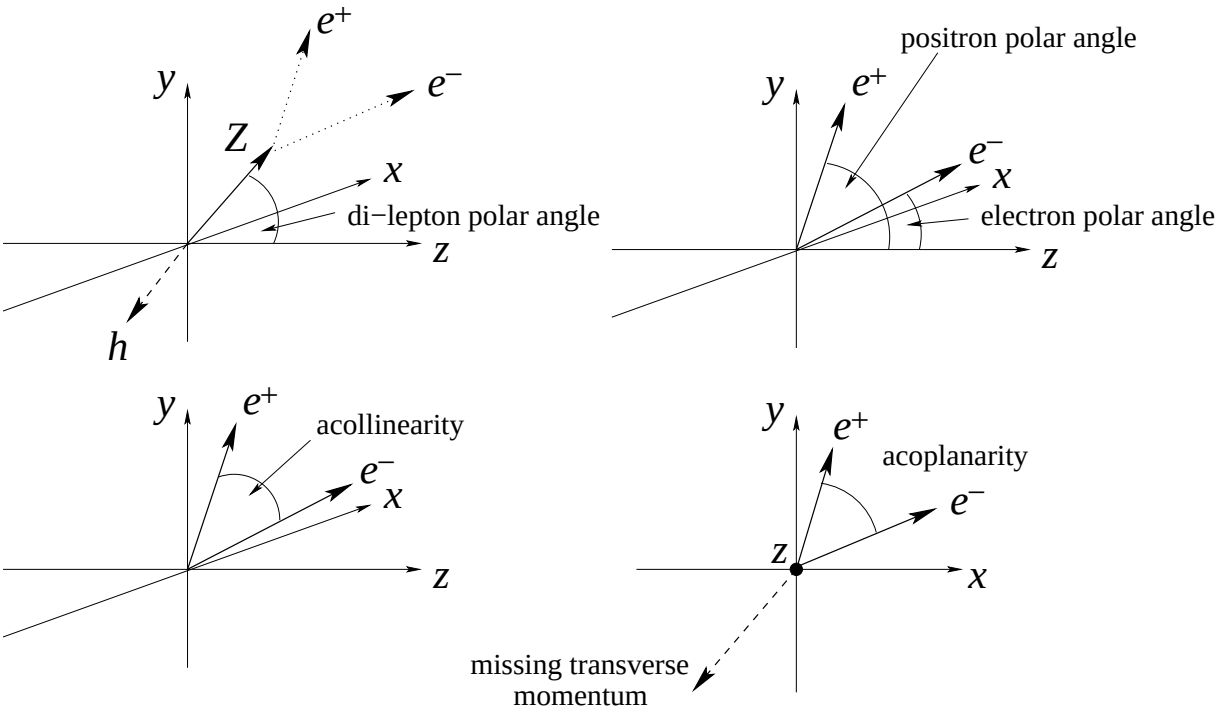

Figure C.1: Illustration of the variables characterizing the process signature, which are used by the case distinction procedure.

Appendix D

Properties of the Gauss-Landau Convolution

Definitions

The Landau distribution, $\varphi(\lambda)$, as defined in Equation (1.43) does not contain any free parameter. However, by a simple transformation of λ one can introduce two parameters, MPV and σ_{L}, characterizing the most probable value position and the width[1] by

$$\lambda = \frac{x - \mathrm{MPV}}{\sigma_{\mathrm{L}}} + \lambda_{\mathrm{MPV}} \ ,$$

where $\lambda_{\mathrm{MPV}} = -0.22278299...$ is the actual MPV position of the intrinsic Landau distribution $\varphi(\lambda)$. The new distribution $L(x; \mathrm{MPV}, \sigma_{\mathrm{L}})$,

$$L(x; \mathrm{MPV}, \sigma_{\mathrm{L}}) = \frac{1}{\sigma_{\mathrm{L}}} \varphi \left(\frac{x - \mathrm{MPV}}{\sigma_{\mathrm{L}}} + \lambda_{\mathrm{MPV}} \right) \ , \tag{D.1}$$

is then normalized if φ is,

$$\begin{aligned} \int_{-\infty}^{\infty} L(x; \mathrm{MPV}, \sigma_{\mathrm{L}}) \, dx &= \int_{-\infty}^{\infty} \frac{1}{\sigma_{\mathrm{L}}} \varphi \left(\frac{x - \mathrm{MPV}}{\sigma_{\mathrm{L}}} + \lambda_{\mathrm{MPV}} \right) \, dx \\ &= \int_{-\infty}^{\infty} \varphi(\lambda) \, d\lambda = 1 \ . \end{aligned}$$

In the last line $d\lambda = \frac{dx}{\sigma_{\mathrm{L}}}$ was used.

The Gaussian distribution is defined as

$$G(x; \mu, \sigma_{\mathrm{G}}) = \frac{1}{2\pi\sigma_{\mathrm{G}}^2} \exp \left(-\frac{(x - \mu)^2}{2\sigma_{\mathrm{G}}^2} \right) \ , \tag{D.2}$$

[1] It is not a standard deviation! Moments do not exist!

which is also normalized on $[-\infty, \infty]$. The two parameters, μ and σ_{G}, are the mean value and the standard deviation.

The convolution of the Landau and the Gaussian distributions is defined as

$$GL(z; \mathrm{MPV}, \sigma_{\mathrm{L}}, \sigma_{\mathrm{G}}) = \int_{-\infty}^{\infty} L(x; \mathrm{MPV}, \sigma_{\mathrm{L}})\, G(x; z, \sigma_{\mathrm{G}})\, dx\ . \tag{D.3}$$

MPV of L and GL are different

First we show that GL, Equation (D.3), is normalized, if L, Equation (D.1), is normalized:

$$\begin{aligned}
\int_{-\infty}^{+\infty} GL(z)\, dz &= \int_{-\infty}^{+\infty} \int_{-\infty}^{+\infty} L(x; \mathrm{MPV}, \sigma_{\mathrm{L}})\, G(x; z, \sigma_{\mathrm{G}})\, dx\, dz \\
&= \int_{-\infty}^{+\infty} L(x; \mathrm{MPV}, \sigma_{\mathrm{L}}) \underbrace{\int_{-\infty}^{+\infty} G(x; z, \sigma_{\mathrm{G}})\, dz}_{=1}\, dx \\
&= \int_{-\infty}^{+\infty} L(x; \mathrm{MPV}, \sigma_{\mathrm{L}})\, dx \\
&= 1\ .
\end{aligned}$$

In general are the most probable values of GL and L different. To show this, we use $G(x; z, \sigma_{\mathrm{G}}) = G(z; x, \sigma_{\mathrm{G}})$ and $\frac{d}{dz} G(z; x, \sigma_{\mathrm{G}}) = -\frac{z-x}{\sigma_{\mathrm{G}}^2} G(z; x, \sigma_{\mathrm{G}})$ and calculate:

$$\begin{aligned}
0 \stackrel{!}{=} \frac{d\, GL(z)}{dz} &= \int_{-\infty}^{+\infty} L(x; \mathrm{MPV}, \sigma_{\mathrm{L}})\, \frac{d\, G(z; x, \sigma_{\mathrm{G}})}{dz}\, dx \\
&= \int_{-\infty}^{+\infty} L(x'; 0, \sigma_{\mathrm{L}})\, \frac{d\, G(z; x' + \mathrm{MPV}, \sigma_{\mathrm{G}})}{dz}\, dx'\ , \quad \text{with } x' = x - \mathrm{MPV} \\
&= -\int_{-\infty}^{+\infty} L(x'; 0, \sigma_{\mathrm{L}})\, \frac{z - x' - \mathrm{MPV}}{\sigma_{\mathrm{G}}^2} G(z; x' + \mathrm{MPV}, \sigma_{\mathrm{G}})\, dx'\ .
\end{aligned}$$

Multiplication by σ_{G}^2 leads finally to

$$0 \stackrel{!}{=} f(z) + (\mathrm{MPV} - z) GL(z)\ ,$$

where $f(z) = \int_{-\infty}^{+\infty} x'\, L(x'; 0, \sigma_{\mathrm{L}})\, G(z; x' + \mathrm{MPV}, \sigma_{\mathrm{G}})\, dx'$. If we assume, that $z = \mathrm{MPV}$, then it would be necessary that $f(\mathrm{MPV}) = 0$. This is generally wrong, since $L(x'; 0, \sigma_{\mathrm{L}})$ in the integrand of $f(\mathrm{MPV})$ is positive and not symmetric with respect to $x' \to -x'$ – the area under L for $x' < 0$ is smaller than that for $x' > 0$ (most probable value is not equal to the median of the Landau distribution). The Gaussian in the integrand of $f(\mathrm{MPV})$, i.e. $G(x'; 0, \sigma_{\mathrm{G}})$ is symmetric under $x' \to -x'$, and x' is antisymmetric! Hence, $f(\mathrm{MPV}) \neq 0$, and the most probable values of L and GL are different.

Appendix E

The Charge Collection Distance

E.1 The CCD in Terms of a mean drift distance

An electrically charged particle is drifting in a material if an electric field is applied. We assume a process where a particle starts at some point z_0, drifts to the point z, i.e. it drifted the distance $z - z_0$. In a semiconductor electrons can be excited to the conduction band, where they are free to drift, and finally they are recombined with a hole.
Lets assume, that the distance $z - z_0$ is exponentially distributed with the mean drift distance λ,

$$(z - z_0) \sim \frac{1}{\lambda} e^{-(z-z_0)\lambda} \ ,$$

where $z \in [z_0, \infty]$.
In a measurement process is z, of course, limited. That is, $z_0 < z < d_\mathrm{s}$, if an electron drifts in positive direction. The electron (or hole) drifts the path length, $z - z_0$, and induces on the electrodes a mirror charge according to the Ramo-Shockley Theorem [194, 195, 153, 196, 197],

$$\frac{z - z_0}{d_\mathrm{s}} e = q_\mathrm{coll} \ ,$$

where q_coll is the charge collected as mirror charge at the electrode. e is in this terminology the induced charge. The maximum signal charge, that can be collected at the electrode is equal to $q_\mathrm{coll} = e$, if the electron started at $z_0 = 0$ and drifted until $z = d_\mathrm{s}$.
To find the averaged drift distance, we have to account for that $z < d_\mathrm{s}$. If $z > d_\mathrm{s}$ we would still measure $z = d_\mathrm{s}$, i.e. we average $(z - z_0)$ over $[z_0, d_\mathrm{s}]$ and add $d_\mathrm{s} - z_0$ times the probability, that z is larger than d_s,

$$\langle z - z_0 \rangle_\lambda = \int_{z_0}^{d_\mathrm{s}} \frac{z - z_0}{\lambda} e^{-(z-z_0)/\lambda} \, dz + (d_\mathrm{s} - z_0) \int_{d_\mathrm{s}}^{\infty} \frac{1}{\lambda} e^{-(z-z_0)/\lambda} \, dz \ .$$

We assume, that the ionization locations are uniformly distributed along the path of the ionizing particles, i.e. z_0 is uniformly distributed between $[0, d_\mathrm{s}]$. If we average $\langle z - z_0 \rangle_\lambda$

according to this uniform distribution, we obtain after the execution of the integrals

$$\langle z - z_0 \rangle := \frac{1}{d_\mathrm{s}} \int_0^{d_\mathrm{s}} \langle z - z_0 \rangle_\lambda \, dz_0 = \lambda \left[1 - \frac{\lambda}{d_\mathrm{s}} \left(1 - e^{-d_\mathrm{s}/\lambda} \right) \right] \ .$$

We identify this with the CCD for an ensemble of particles with uniformly distributed start values $z_0 \in [0, d_\mathrm{s}]$. The charge collection efficiency is just

$$\mathrm{CCE} = \frac{\mathrm{CCD}}{d_\mathrm{s}} \ .$$

λ is than the real material property and independent of the geometry, i.e. d_s. λ can be expressed in terms of a drift time, which we call *relaxation time*, and a drift speed,

$$\lambda = \tau_\mathrm{relax} v_\mathrm{drift} \ .$$

The drift speed can be written as $v_\mathrm{drift} = \mu \mathcal{E}$, i.e. it is proportional to the driving electric field.

E.2 Mathematical Properties of the CCE

The above introduced λ can depend on the space-coordinate, z, through the electric field, $\mathcal{E}$. We define the mean drift length in terms of the sensor thickness.

$$y = \frac{\lambda}{d_\mathrm{s}} \ .$$

The the CCE is

$$\mathrm{CCE}\big(y(z)\big) = y(z) \left[1 - y(z) \left(1 - e^{-1/y(z)} \right) \right] \ ,$$

where we now assume, that y is a function of the space-coordinate, z. We want to show, that it holds

$$\big\langle \mathrm{CCE}(y) \big\rangle \leq \mathrm{CCE}\big(\langle y \rangle \big) \ . \tag{E.1}$$

For this we only need to show, that $\mathrm{CCE}(y)$ is concave, i.e. $\frac{d^2\mathrm{CCE}}{dy^2} < 0$. The derivatives of the CCE are

$$\begin{aligned}
\frac{d\mathrm{CCE}}{dy} &= (1 - 2y) + (1 + 2y) e^{-1/y} \\
\frac{d^2\mathrm{CCE}}{dy^2} &= -2 + e^{-1/y} (2 + 2/y + 1/y^2) \\
\frac{d^3\mathrm{CCE}}{dy^3} &= y^{-4} e^{-1/y}
\end{aligned}$$

The third derivative is larger than zero, except at $y = 0$ and $y = \infty$, where this derivative is zero. That is, the second derivative monotonously increasing with y. Together with the

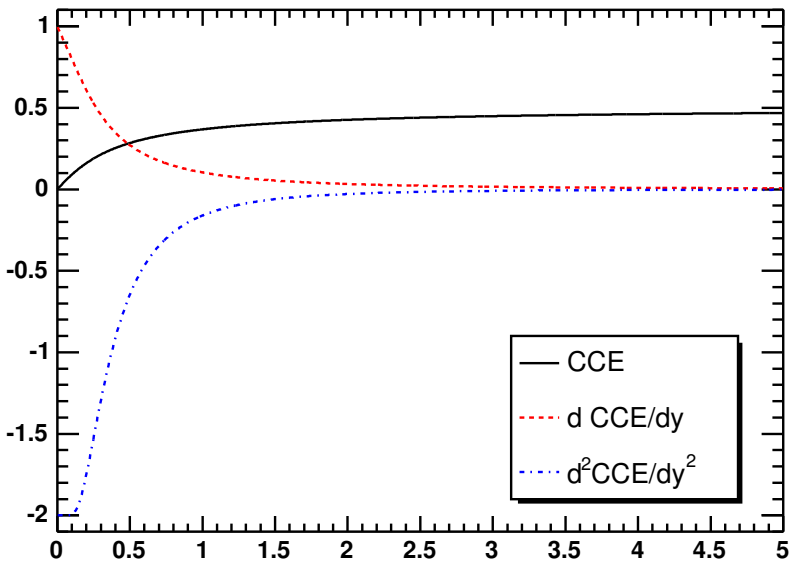

Figure E.1: The CCE as function of y and its first and second derivatives.

fact, that the second derivative is zero at $y = \infty$, which is the maximum, proves, that the second derivative of the CCE is negative for any finite y. Figure E.1 shows the CCE as function of y and its first two derivatives.
Therefore, the CCE as function of y is concave, and we can employ the Jensen's inequality, which directly gives (E.1) for the above assumptions. We use the standard representation for concavity,

$$\mathrm{CCE}\big(\xi y_1 + (1-\xi)y_2\big) \geq \xi \mathrm{CCE}(y_1) + (1-\xi)\mathrm{CCE}(y_2) \;,$$

with $0 \leq \xi \leq 1$, and quite arbitrary y_1 and $y_2 > y_1$. We choose, $\xi y_1 + (1-\xi)y_2 = \langle\lambda\rangle$, $y_2 = \lambda(z)$, and y_1 an arbitrary number. We obtain, therefore,

$$\xi = \frac{\langle\lambda\rangle - \lambda}{y_1 - \lambda} \;.$$

Inserting this into the above concavity inequality and multiplying by $(y_1 - \lambda)$ yields

$$(y_1 - \langle\lambda\rangle)\mathrm{CCE}\big(\langle\lambda\rangle\big) \geq (\langle\lambda\rangle - \lambda)\mathrm{CCE}(y_1) + (y_1 - \langle\lambda\rangle)\mathrm{CCE}(\lambda) \;.$$

Applying the averaging procedure to this inequality gives

$$(y_1 - \langle\lambda\rangle)\mathrm{CCE}\big(\langle\lambda\rangle\big) \geq (\langle\lambda\rangle - \langle\lambda\rangle)\mathrm{CCE}(y_1) + (y_1 - \langle\lambda\rangle)\big\langle\mathrm{CCE}(\lambda)\big\rangle \;,$$

where immediately the first term on the right-hand side vanishes. Finally, dividing by $(y_1 - \langle\lambda\rangle)$, we obtain (E.1).

Bibliography

[1] E. Rutherford. The Scattering of α and β Particles by Matter and the Structure of the Atom. *Philos. Mag.*, 6:22, 1909.

[2] Einstein, Albert. Zur Elektrodynamik bewegter Körper. *Annalen der Physik*, 4(17):891–921, 1905.

[3] Einstein, Albert. Prinzipielles zur allgemeinen Relativitätstheorie. *Annalen der Physik*, 55:241–244, 1918.

[4] W. Heisenberg. Über den anschaulichen Inhalt der quantentheoretischen Kinematik und Mechanik. *Zeitschrift für Physik*, 43:172–198, 1927.

[5] Hagiwara et al. Review of Particle Physics. *Physical Review D*, 66:010001+, 2002.

[6] D. J. Gross and F. Wilczek. Ultraviolet Behaviour of non-abelian Gauge Theories. *Phys. Rev. Let.*, 30:1343–1346, 1973.

[7] Frank Wilczek. Asymptotic freedom: From paradox to paradigm. *Proc. Nat. Acad. Sci.*, 102:8403–8413, 2005.

[8] Greiner, W. and Reinhardt, J. *Theoretische Physik: Feldquantisierung.* Verlag Harri Deutsch, 1993.

[9] Franz Schwabl. *Quantenmechanik für Fortgeschrittene.* Springer Verlag, 1997.

[10] F. Halzen and A.D. Martin. *Quarks & Lepton: An Inductory Course in Modern Particle Physiks.* John Wiley & Sons, 1984.

[11] T. Kugo. *Eichtheorie.* Springer Verlag, Berlin/Heidelberg/New York, 1997.

[12] Noether, Emmy. Invarianten beliebiger Differentialausdrücke. *Gött. Nachr.*, pages 37–44, 1918.

[13] Noether, Emmy. Invariante Variationsprobleme. *Gött. Nachr.*, pages 235–257, 1918.

[14] Peter W. Higgs. Broken Symmetries and the Masses of Gauge Bosons. *Phys. Rev. Lett.*, 13(16):508–509, Oct 1964.

[15] F. Englert and R. Brout. Broken symmetry and the mass of gauge vector mesons. *Phys. Rev. Lett.*, 13(9):321–323, Aug 1964.

[16] V. Trimble. Proceedings of the First International Symposium on Sources of Dark Matter in the Universe, Bel Air, California, 1994.

[17] G. Bertone, D. Hooper, and J. Silk. Particle dark matter: evidence, candidates and constraints. *Phys. Rep.*, 405:279–390, 2005.

[18] T. D. Lee and Chen-Ning Yang. Question of Parity Conservation in Weak Interactions. *Phys. Rev.*, 104:254–258, 1956.

[19] Wu, C. S. and Ambler, E. and Hayward, R. W. and Hoppes, D. D. and Hudson, R. P. Experimental test of parity conservation in beta decay. *Phys. Rev.*, 105(4):1413–1415, Feb 1957.

[20] M. Gell-Mann. Isotopic Spin and New Unstable Particles. *Phys. Rev.*, 92:833–834, 1953.

[21] K. Nishijima. Some Remarks on the Even-odd Rule. *Progress in Theoretical Physics*, 12(1):107–108, 1954.

[22] O. Nachtmann. *Phänomene und Konzepte der Elementarteilchenphysik.* Friedr. Vieweg & Sohn, Braunschweig / Wiesbaden, 1986.

[23] N. Cabibbo. Unitary Symmetry and Leptonic Decays. *Phys. Rev. Lett.*, 10(12):531–533, 1963.

[24] M. Kobayashi and T. Maskawa. CP-Violation in the Renormalizable Theory of Weak Interaction. *Progress of Theoretical Physics*, 49(2):652–657, 1973.

[25] Abdus Salam and John Clive Ward. Weak and electromagnetic interactions. *Nuovo Cim.*, 11:568–577, 1959.

[26] Glashow, S. L. Partial-Symmetries of Weak Interactions. *Nucl. Phys.*, 22(4):579–588, February 1961.

[27] Steven Weinberg. Elementary particle theory of composite particles. *Phys. Rev.*, 130(2):776–783, April 1963.

[28] Abdus Salam. Universal weak interaction Lagrangian. *Phys. Lett.*, 8:216–217, 1964.

[29] Abdus Salam and John Clive Ward. Electromagnetic and weak interactions. *Phys. Lett.*, 13:168–171, 1964.

[30] Weinberg, Steven. A Model of Leptons. *Phys. Rev. Lett.*, 19(21):1264–1266, 1967.

[31] A. Salam. Elementary particle physics: Relativistic groups and analyticity. -, page 367, 1968.

[32] M. Veltman. Perturbation theory of massive yang-mills fields. *Nuclear Physics B*, 7(5):637 – 650, 1968.

[33] G. 't Hooft. Renormalizable lagrangians for massive yang-mills fields. *Nuclear Physics B*, 35(1):167 – 188, 1971.

[34] G. 't Hooft and M. Veltman. Regularization and renormalization of gauge fields. *Nuclear Physics B*, 44(1):189 – 213, 1972.

[35] G. 't Hooft and M. Veltman. Combinatorics of gauge fields. *Nuclear Physics B*, 50(1):318 – 353, 1972.

[36] Jeffrey Goldstone, Abdus Salam, and Steven Weinberg. Broken Symmetries. *Phys. Rev.*, 127:965–970, 1962.

[37] LEP Electroweak Working Group. http://lepewwg.web.cern.ch/LEPEWWG/.

[38] Tevatron Electroweak Working Group. http://tevewwg.fnal.gov/higgs/.

[39] J. F. Gunion. *The Higgs hunter's guide.* Addison-Wesley Publishing Company, Amsterdam, 1990.

[40] CDF collaboration. Combined CDF and DZero Upper Limits on Standard Model Higgs-Boson Production with up to 4.2 fb-1 of Data. *arXiv*, 2009.

[41] M. Spira. HDECAY. http://people.web.psi.ch/spira/hdecay/.

[42] R. P. Feynman, R. B. Leighton, and M. Sands. *Feynman Lectures.* Addison-Wesley Longman, Amsterdam, 1966.

[43] Eldad Gildener. Gauge-symmetry hierarchies. *Phys. Rev. D*, 14(6):1667–1672, Sep 1976.

[44] Yu.A Golfand and E.P Likhtman. Extension of the Algebra of Poincare Group Generators and Violation of P invariance. *Sov. Phys. JETP*, 13:323, 1971.

[45] D.V. Volkhov and V.P. Akulov. -. *Nucl. Phys. B*, 46(109), 1973.

[46] J. Wess and B. Zumino. Supergauge Transformations in four Dimensions. *Nucl. Phys. B*, 70(1):39–50, feb 1974.

[47] A. Salam and J. Strathdee. Super-symmetry and non-Abelian gauges. *Physics Letters B*, 51(4):353–355, August 1974.

[48] P. Fayet and S. Ferrara. Supersymmetry. *Physics Reports*, 32(5):249 – 334, 1977.

[49] Lyndon Evans et al. Lhc machine. *JINST*, 3, 2008.

[50] Stephen P. Martin. A Supersymmetry Primer. *arXiv*, 1997.

[51] H. Bethe. Zur Theorie des Durchgangs schneller Korpuskularstrahlen durch Materie. *Annalen der Physik*, 397(3):325–400, 1930.

[52] F. Bloch. Bremsvermögen von Atomen mit mehreren Elektronen. *Zeitschrift für Physik A Hadrons and Nuclei*, 81:363–376, May 1933.

[53] W.R. Leo. *Techniques for Nuclear and Particle Physics Experiments. A How-to Approach.* Springer-Verlag, Berlin, second edition, 1994.

[54] L. Landau. On the energy loss of fast particles by ionization. *J. Phys. (U.S.S.R)*, 8(4):201 – 205, 1944.

[55] P. V. Vavilov. Ionization losses of high-energy heavy particles. *J. Exptl. Theoret. Phys. (U.S.S.R)*, 5(4):749 – 751, 1957.

[56] H. Bichsel. Straggling in thin Silicon Detectors. *Rev. Mod. Phys.*, 60:663–699, 1988.

[57] H. Bichsel. Approximation methods to calculate straggling functions. *Nucl. Instrum. Meth.*, A566:1–4, 2006.

[58] H. Bichsel. Comparison of Bethe-Bloch and Bichsel functions, 2007. STAR Note SN0439.

[59] S. Agostinelli et al. [GEANT4 Collaboration]. GEANT4 — a simulation toolkit. *Nuclear Instruments and Methods in Physics Research A*, 506(3):250–303, July 2003. SLAC-PUB-9350.

[60] Geant 4 – A Toolkit for the Simulation of the Passage of Particles through Matter. http://geant4.web.cern.ch/geant4/.

[61] Egidio Longo and Ignazio Sestili. Monte Carlo Calculation of photon-initiated electromagnetic Showers in Lead Glass. *Nuclear Instruments and Methods*, 128(2):283 – 307, 1975.

[62] Bock, Rudolf K. http://ikpe1101.ikp.kfa-juelich.de/briefbook_part_detectors/node58.html.

[63] H. A. Bethe. Molière's Theory of Multiple Scattering. *Phys. Rev.*, 89(6):1256–1266, Mar 1953.

[64] Walter R. Nelson, Theodore M. Jenkins, Richard C. McCall, and Joseph K. Cobb. Electron-induced cascade showers in copper and lead at 1 gev. *Phys. Rev.*, 149(1):201–208, Sep 1966.

[65] G. Bathow, E. Freytag, M. Köbberling, K. Tesch, and R. Kajikawa. Measurements of the longitudinal and lateral development of electromagnetic cascades in lead, copper and aluminum at 6 gev. *Nuclear Physics B*, 20(3):592 – 602, 1970.

[66] C.W. Fabjan and T.Ludlam. Calorimetry in High-Energy Physics. *Ann. Rev. Nucl. Part. Sci.*, 32, 1982.

[67] K. Grupen. *Teilchendetektoren.* Wissenschaftsverlag, Bibliographisches Institut & F.A. Brockhaus AG, Mannheim, 1993.

[68] C. Leroy and P.-G. Rancoita. *Physics of cascading shower generation and propagation in matter: principles of high-energy, ultrahigh-energy and compensating calorimetry. Rep. Prog. Phys.*, 63:505–606, 2000.

[69] Spieler, H. Lectures on Semiconductor Detectors and Electronics. http://www-physics.lbl.gov/ spieler/.

[70] U. Fano. On the Theory of Ionization Yield of Radiations in Different Substances. *Phys. Rev.*, 70(1-2):44–52, Jul 1946.

[71] U. Fano. Ionization Yield of Radiations. II. The Fluctuations of the Number of Ions. *Phys. Rev.*, 72(1):26–29, Jul 1947.

[72] H. R. Zulliger and D. W. Aitken. Fano Factor Fact and Fallacy. *IEEE Trans. Nucl. Science*, 17(3):187 – 195, June 1970.

[73] M.N. Mazziotta. Electron-hole pair creation energy and Fano factor temperature dependence in silicon. *Nucl. Instrum. Meth. A: Accelerators, Spectrometers, Detectors and Associated Equipment*, 584(2-3):436 – 439, 2008.

[74] R. C. Alig, S. Bloom, and C. W. Struck. Scattering by Ionization and Phonon Emission in Semiconductors. *Phys. Rev. B*, 22(12):5565–5582, Dec 1980.

[75] LHC TDR. http://ab-div.web.cern.ch/ab-div/publications/LHC-DesignReport.html.

[76] P. M. Zerwas. Physics with an e+ e- linear collider at high luminosity. *arXiv*, 2000.

[77] Wolfgang Lohmann. e^+e^- physics at LEP and a future linear collider. *arXiv*, 2001.

[78] Sally Dawson and Mark Oreglia. Physics Opportunities with a TeV Linear Collider. *Annual Review of Nuclear and Particle Science*, 54:269, 2004.

[79] ILC GDE and WWS. *International Linear Collider - Reference Design Report.* ILC Report 2007-001, 2007. http://lcdev.kek.jp/RDR/.

[80] D. V. Schroeder. *Beamstrahlung and QED Backgrounds at Future Linear Colliders.* PhD thesis, Stanford University., 1990.

[81] Kaoru Yokoya and Pisin Chen. Beam-beam phenomena in linear colliders. *Lect. Notes Phys.*, 400:415–445, 1992.

[82] Pisin Chen. Beamstrahlung and the QED, QCD backgrounds in linear colliders. *SLAC Note*, 1992. Presented at 9th International Workshop on Photon-Photon Collisions (PHOTON-PHOTON '92), San Diego, CA, 22-26 Mar 1992.

[83] C. Adolphsen et al. Design of the ILC Crab Cavity System. EUROTeV-Report-2007-010, SLAC-PUB-12751, 2007.

[84] G. Burt et al. Crab cavities for linear colliders. http://www.citebase.org/abstract?id=oai:arXiv.org:0810.2880, 2008.

[85] K. Yokoya and P. Chen. Beam-beam phenomena in linear colliders. In M. Dienes, M. Month, and S. Turner, editors, *Frontiers of Particle Beams: Intensity Limitations*, volume 400 of *Lecture Notes in Physics, Berlin Springer Verlag*, pages 415–445, 1992.

[86] K. Yokoya and P. Chen. *Beam-Beam phenomena in linear colliders. KEK Preprint*, 91-2, April 1995.
Guinea-Pig homepage at Slac.

[87] M. Alabau Pons, P. Bambade, and A. Faus-Golfe. Luminosity, beamstrahlung energy loss and beam-beam deflection for e^+e^- and e^-e^- collisions at the ILC with 500 GeV and varying transverse beam sizes. *CARE note*, 2005.

[88] Bob Siemann. *Introduction to Accelerator Physics – Luminosity and Beam-Beam Effects.*
http://www-group.slac.stanford.edu/sluo/Lectures/Accel-Lectures.html, 1998.
Lectures.

[89] A. W. Chao and Yukihide Kamiya. Bunch Shape at IP and the Pinch Effect. *SLAC Note*, 1983. SLAC-CN-218.

[90] Daniel Schulte. *Study of Electromagnetic and Hadronic Background in the Interaction Region of the TESLA Collider.* PhD thesis, Universität Hamburg, 1996.

[91] Rimbault, C. and Bambade, P. and Monig, K. and Schulte, D. Incoherent pair generation in a beam-beam interaction simulation. *Phys. Rev. ST Accel. Beams*, 9:034402, 2006.

[92] Chen, Pisin and Telnov, Valery I. Coherent Pair Creation in Linear Colliders. *Phys. Rev. Lett.*, 63:1796, 1989.

[93] Ringo S. Schmidt. *Optimisation of a Testbeam Setup and Background Estimates for Detectors at the ILC using Monte Carlo Simulations.* Diploma, Brandenburgische Technische Universität, Cottbus, 2007.

[94] Adrian Vogel. *Beam-Induced Backgrounds in Detectors at the ILC.* PhD thesis, Universität Hamburg, 2008.

[95] TPC R&D for an ILC Detector, report to the "ILC Tracking Review Committee, Beijing, 2007.

[96] H. Abramowicz et al. Instrumentation of the very forward region of a linear collider detector. *Nuclear Science, IEEE Transactions on*, 51(6):2983–2989, Dec. 2004.

[97] Forward Calorimetry Group (FCAL). *R&D for the ILC-Detector: Instrumentation of the Very Forward Region. http://www.desy.de/prc*, 2006.
Contact: Wolfgang Lohmann, wlo@ifh.de.

[98] Karsten Büsser. Instrumentation of the forward region of the TESLA detector. *The European Physical Journal C - Particles and Fields*, 33(0):1029–1031, July 2004.

[99] K. Buesser and A. Stahl. Detector concept of the forward regions. *LC note*, 2004. LC-DET-2004-034.

[100] W. Lohmann. Instrumentation of the very forward region of a linear collider detector, 2005. DESY-05-142.

[101] H. J. Bhabha. The Scattering of Positrons by Electrons with Exchange on Dirac's Theory of the Positron. *Royal Society of London Proceedings Series A*, 154:195–206, March 1936.

[102] R. Ingbir. *A Luminosity Detector for the International Linear Collider.* Diploma, Tel Aviv University, 2006.

[103] T. Tauchi and K. Yokoya. Nanometer beam size measurement during collisions at linear colliders. *Phys. Rev.*, E51:6119–6126, 1995.

[104] N. Delerue and T. Tauchi. *Beamstrahlung monitoring of the beam beam effects at the Linear Collider. arXiv:physics*, 0408132, September 2004.

[105] A. Stahl. Diagnostics of colliding bunches from pair production and beam-strahlung at the IP. *LC note*, 2005. LC-DET-2005-003.

[106] G. White. Reconstruction of IP beam parameters at the ILC from beamstrahlung. *SLAC publication*, 2005. SLAC-PUB-11341.

[107] L. Hendrickson, S. Bes, P. Grossberg, D. Mccormick, N. Phinney, P. Raimondi, and M. Ross. Luminosity Optimization Feedback in the SLC, 1997.

[108] L. Hendrickson, T. Himel, T. O. Raubenheimer, A. Seryi, P. Tenenbaum, M. Woodley, and D. Schulte. Implementation of dynamic misalignments and luminosity stabilization. In *Proceedings of the 2003 IEEE Particle Accelerator Conference (PAC*

03). 12-16 May 2003, Portland, Oregon. 20th IEEE Particle Accelerator Conference., p.2757, pages 2757–+, 2003.

[109] Grah, C. and Sapronov, A. Fast Luminosity Measurement and Beam Parameter Determination. EUROTeV Report 2007-006, 2007.

[110] Christian Grah and A. Sapronov. Beam parameter determination using beamstrahlung photons and incoherent pairs. *JINST*, 3:P10004, 2008.

[111] P. Bambade, .V Drugakov, and W. Lohmann. The Impact of BeamCal performance at different ILC beam parameters and crossing angles on stau searches. In *LAL-06-145*. Pramana 69:1123-1128,2007, October 2006. Talk given at International Linear Collider Workshop (LCWS06), Bangalore, India, 9-13 Mar 2006.

[112] Investigations and Private Communication with Bill Morse.

[113] GuineaPig – Beam Beam Interaction Simulator.
http://flc.web.lal.in2p3.fr/mdi/BBSIM/bbsim.html
http://www-sldnt.slac.stanford.edu/nlc/programs/guinea_pig/gp_index.html.

[114] PRC Meeting FAL Collaboration. Report for the ILC Detector R&D Panel Instrumentation of the Very Forward Region, 2007.
http://www.desy.de/prc/docs_rd/prc_rd_02_01_update_05_07.pdf.

[115] GamCal – A Beam-strahlung Gamma Detector for Beam Diagnostics. LCWS, 2007.
www-zeuthen.desy.de/ILC/lcws07/pdf/MDI/morse_bill.pdf.

[116] A. Sapronov. LCWS, 2007.

[117] A. Elagin. The Optimized Sensor Segmentation for the Very Forward Calorimeter. *SNOWMASS-2005-ALCPG0719*, page 3, 2005.

[118] Sherpa – MC Event Generator. http://www.sherpa-mc.de.

[119] Pythia – MC Event Generator. http://home.thep.lu.se/~torbjorn/Pythia.html.

[120] BHWide – MC Event Generator. http://placzek.home.cern.ch/placzek/bhwide.

[121] ILC Simulation and Reconstruction Software. http://ilcsoft.desy.de/portal.

[122] A. Raspereza. Tracking in LDC Detector, including VXD, FTD, SIT & TPC Implementation within MarlinReco package, 2006. ILC Workshop - ECFA and GDE Joint Meeting.

[123] Fujii Keisuke. Extended Kalman Filter.
www-jlc.kek.jp/subg/offl/kaltest/doc/ReferenceManual.pdf.

[124] ROOT – An Object-Oriented Data Analysis Framework. http://root.cern.ch/.

[125] T. Kraemer. Track parameters. Technical report, ILC LC-DET-2006-004, 2006.

[126] K. R. Bock, H. Grote, D. Notz, and M. Regler. *Data analysis techniques for high-energy physics experiments*. Cambridge University Press, Cambridge, 1990.

[127] H. A. Bethe. Multiple Scattering and the Mass of the Meson. *Phys. Rev.*, 70(11-12):821–831, Dec 1946.

[128] U. Fano. Inelastic Collisions and the Molière Theory of Multiple Scattering. *Phys. Rev.*, 93(1):117–120, Jan 1954.

[129] *Particle Idetification at STAR-TPC with Ionization Measurements*, 2003.

[130] M. Brigida et al. Particle identification with the Silicon Transition Radiation Detector (SiTRD): State of art and future perspectives. *Nucl. Instrum. Meth. A: Accelerators, Spectrometers, Detectors and Associated Equipment*, 563(2):388 – 391, 2006.

[131] Pablo Garcia-Abia and Wolfgang Lohmann. Measurement of the Higgs Cross Section and Mass with Linear Colliders. *Eur. Phys. J. direct*, C2:2, 2000.

[132] A. V. Raspereza. *Search for neutral Higgs bosons in e^+e^- collisions*. PhD thesis, Humboldt Univ., 2002. Presented on Sep 2002.

[133] P. Garcia-Abia, W. Lohmann, and A. Raspereza. Measuring the Higgs mass at TESLA. *Proceedings for the LCWS 2000*, 2000. Prepared for 5th International Linear Collider Workshop (LCWS 2000), Fermilab, Batavia, Illinois, 24-28 Oct 2000.

[134] P. Garcia-Abia and W. Lohmann. *Measurement of the Higgs Cross Section and Mass with Linear Colliders. LC-PHSM*, 2000-063, March 2000.
tesla.desy.de/new_pages/TDR_CD/PartIII/references/hmass1.pdf.

[135] Higgs Working Group at Snowmass 05. *Higgs Physics at International Linear e^+e^- Collider*. In *Snowmass*, 2005.
Summary of current status of Higgs boson studies at future linear e^+e^- collider.

[136] P. Garcia-Abia, W. Lohmann, and A. Raspereza. Prospects for the measurement of the Higgs boson mass with a linear e+ e- collider. *Eur. Phys. J.*, C44:481–488, 2005.

[137] Francois Richard and Philip Bambade. Strategy to measure the Higgs mass, width and invisible decays at ILC. *arXiv*, 2007.

[138] M. Ohlerich, A. Raspereza, A. Schälicke, and W. Lohmann. Prospects to Measure the Higgs Boson Mass and Cross Section in ee–>ZH Using the Recoil Mass Spectrum. *arXiv, Proceedings for LCWS 2007*, 2007.

[139] D. J. Miller. Proving Higgs bosons are scalars at a linear collider. *arXiv*, 2001.

[140] D. J. Miller, S. Y. Choi, B. Eberle, M. M. Muhlleitner, and P. M. Zerwas. Measuring the spin of the Higgs boson. *Phys. Lett.*, B505:149–154, 2001.

[141] M. T. Dova, P. Garcia-Abia, and W. Lohmann. Determination of the Higgs boson spin with a linear e^+e^- collider. *Internal DESY LC Note*, 2001. LC-PHSM-2001-055.

[142] M. T. Dova, P. Garcia-Abia, and W. Lohmann. Determination of the Higgs boson spin with a linear e^+e^- collider. *arXiv*, 2003.

[143] Maria Teresa Dova and Sergio Ferrari. On the determination of CP-even and CP-odd components of a mixed CP Higgs boson at e+ e- linear colliders. *Phys. Lett.*, B605:376–383, 2005.

[144] M. Carena and P. Zerwas et al. Higgs Physics at LEP2, 1996.

[145] A. Schälicke. Initial State Radiation. Master's thesis, Technische Universität Dresden, 2002.

[146] Andrei Seryi et al. ILC Beam parameters including 250 GeV ILC. http://ilcphys.kek.jp/soft/ILCBeam/BeamParameter.html.

[147] D. M. Schmidt, R. J. Morrison, and Michael S. Witherell. A General method of estimating physical parameters from a distribution with acceptance and smearing effects. *Nucl. Instrum. Meth.*, A328:547–552, 1993.

[148] G. Bohm and G. Zech. Einführung in die Statistik und Messwertanalyse für Physiker. Verlag Deutsches Elektronen-Synchrotron.

[149] C. Canali, E. Gatti, S.F. Kozlov, P.F. Manfredi, C. Manfredotti, F. Nava, and A. Quirini. Electrical properties and performances of natural diamond nuclear radiation detectors. *Nucl. Instrum. Meth. A*, 160(1):73 – 77, 1979.

[150] C. Canali, M. Martini, G. Ottaviani, and A. Alberigi Quaranta. Measurements of the average energy per electron-hole pair generation in silicon between 5-320 k. *IEEE Trans. Nucl. Science*, 19(4):9 – 19, August 1972.

[151] R. C. Alig and S. Bloom. Electron-hole-pair creation energies in semiconductors. *Phys. Rev. Lett.*, 35(22):1522–1525, Dec 1975.

[152] C. Bussolati, A. Fiorentini, and G. Fabri. Energy for Electron-Hole Pair Generation in Silicon by Electrons and α Particles. *Physical Review*, 136:1756–1758, December 1964.

[153] W. Shockley. Problems related to p-n-Junctions in Silicon. *Czech. J. Phys.*, B11(81), 1961.

[154] C. A. Klein. Bandgap Dependence and Related Features of Radiation Ionization Energies in Semiconductors. *Journal of Applied Physics*, 39:2029–2038, March 1968.

[155] S. Zhao. *Characterization of the Electrical Properties of Polycrystalline Diamond Films*. PhD thesis, The Ohio State University., 1994.

[156] Alexander Sinclair Howard. *Diamond detectors for particle physics*. PhD thesis, University of London, 1998.

[157] A. Oh. *CVD Diamant als Material für Teilchendetektoren*. PhD thesis, Universität Hamburg, 1999. http://www-flc.desy.de/thesis/doctor.1999.oh.ps.gz.

[158] L. Fernandez Hernando et al. Development of a CVD diamond beam condition monitor for CMS at the Large Hadron Collider. *Nucl. Instrum. Meth.*, A552:183–188, 2005.

[159] Chong et al. Validation of Synthetic Diamond for a Beam Condition Monitor for the Compact Muon Solenoid Experiment. *IEEE Trans. Nucl. Science*, 54(1):182–185, 2007.

[160] L. Perera. Simulation of a Small Angle Pixel Telescope Luminosity Monitor.

[161] E. Halkiadakis. A proposed luminosity monitor for cms based on small angle diamond pixel telescopes. *Nuclear Instruments and Methods in Physics Research Section A: Accelerators, Spectrometers, Detectors and Associated Equipment*, 565(1):284 – 289, 2006. Proceedings of the International Workshop on Semiconductor Pixel Detectors for Particles and Imaging - PIXEL 2005.

[162] E. Kuznetsova. *Design studies and sensor tests for the beam calorimeter of the ILC detector*. PhD thesis, Humboldt Univ., 2006. [Online: Stand 2008-12-03T16:25:40Z].

[163] P. Gonon, S. Prawer, and D. Jamieson. Thermally stimulated currents in polycrystalline diamond films: Application to radiation dosimetry. *Applied Physics Letters*, 70(22):2996–2998, 1997.

[164] T. Behnke, M. Doucet, N. Ghodbane, and A. Imhof. Radiation Hardness and Linearity Studies for a Diamond Luminosity Calorimeter. *LC note*, 2002. LC-DET-2002-001.

[165] Gerhard Lutz. *Semiconductor Radiation Detectors: Device Physics*. Springer, 1999.

[166] L. Reggiani, S. Bosi, C. Canali, F. Nava, and S. F. Kozlov. Hole-drift velocity in natural diamond. *Phys. Rev. B*, 23(6):3050–3057, Mar 1981.

[167] FCAL Sensor Properties Webpage.
http://www.ifh.de/ chgrah/diamondproperties.html.

[168] NSM archive - physical properties of semiconductors.
http://www.ioffe.rssi.ru/SVA/NSM/Semicond/index.html.

[169] K. L. Choy. Chemical vapour deposition of coatings. *Progress in Materials Science*, 48(2):57 – 170, 2003. and references herein.

[170] Element Six, E6 Hard Materials; Staedeweg 12 - 24, 36151 Burghaun, Germany.

[171] E. Berdermann, M. Ciobanu, S. H. Connell, A. M. O. D. da Costa, L. Fernandez-Hernando, A. Oh, and J. P. F. Sellschopdagger. Charged particle detectors made of single-crystal diamond. *physica status solidi (a)*, 201(11):2521–2528, 2004.

[172] Wim de Boer, Johannes Bol, Alex Furgeri, Steffen Müller, Christian Sander, Eleni Berdermann, Michal Pomorski, and Mika Huhtinen. Radiation hardness of diamond and silicon sensors compared. *physica status solidi (a)*, 204(9):3004–3010, 2007.

[173] C. Grah, K. Afanaciev, I. Emeliantchek, U. Harder, H. Henschel, A. Ignatenko, E. Kouznetsova, W. Lange, W. Lohmann, M. Ohlerich, and R. Schmidt. Polycrystalline cvd diamonds for the beam calorimeter of the ilc. In *Nuclear Science Symposium Conference Record, 2006. IEEE*, volume 2, pages 721–724, 29 2006-Nov. 1 2006.

[174] Yoshihiro Imamura and Jiro Osaka. Deep electron traps in undoped semi-insulating gaas grown by the liquid encapsulated czochralski method. *Japanese Journal of Applied Physics*, 22(Part 2, No. 6):L333–L335, 1983.

[175] G. I. Ayzenshtat, N. N. Bakin, D. L. Budnitsky, E. P. Drugova, V. P. Germogenov, S. S. Khludkov, O. B. Koretskaya, L. S. Okaevich, L. P. Porokhovnichenko, A. I. Potapov, K. M. Smith, O. P. Tolbanov, A. V. Tyazhev, M. D. Vilisova, and A. P. Vorobiev. Gaas structures for x-ray imaging detectors. *Nuclear Instruments and Methods in Physics Research Section A: Accelerators, Spectrometers, Detectors and Associated Equipment*, 466(1):25 – 32, 2001.

[176] G. I. Ayzenshtat, D. L. Budnitsky, O. B. Koretskaya, V. A. Novikov, L. S. Okaevich, A. I. Potapov, O. P. Tolbanov, A. V. Tyazhev, and A. P. Vorobiev. Gaas resistor structures for x-ray imaging detectors. *Nuclear Instruments and Methods in Physics Research Section A: Accelerators, Spectrometers, Detectors and Associated Equipment*, 487(1-2):96 – 101, 2002.

[177] A. I. Ayzenshtat, D. L. Budnitsky, O. B. Koretskaya, L. S. Okaevich, V. A. Novikov, A. I. Potapov, O. P. Tolbanov, A. V. Tyazhev, and A. P. Vorobiev. Gaas as a material for particle detectors. *Nuclear Instruments and Methods in Physics Research Section A: Accelerators, Spectrometers, Detectors and Associated Equipment*, 494(1-3):120 – 127, 2002.

[178] A. V. Tyazhev, D. L. Budnitsky, O. B. Koretskay, V. A. Novikov, L. S. Okaevich, A. I. Potapov, O. P. Tolbanov, and A. P. Vorobiev. Gaas radiation imaging detectors with an active layer thickness up to 1ămm. *Nuclear Instruments and Methods in Physics Research Section A: Accelerators, Spectrometers, Detectors and Associated*

Equipment, 509(1-3):34 – 39, 2003. Proceedings of the 4th Internatonal Workshop on Radiation Imaging Detectors.

[179] G. I. Ayzenshtat, D. L. Budnitsky, O. B. Koretskaya, V. A. Novikov, D. Y. Mokeev, L. S. Okaevich, O. P. Tolbanov, and A. V. Tyazhev. Gaas detector material made from 3-inch wafers. *Nuclear Instruments and Methods in Physics Research Section A: Accelerators, Spectrometers, Detectors and Associated Equipment*, 531(1-2):121 – 124, 2004. Proceedings of the 5th International Workshop on Radiation Imaging Detectors.

[180] Valery Chmill. *Radiation tests of semiconductor detectors*. PhD thesis, KTH, Physics, 2006.

[181] Brookhaven National Lab, P.O. Box 5000, Upton, NY 11973-5000.

[182] H. D. Gräh and H. Miska and E. Spamer and O. Titze and Th. Walcher. High resolution electron scattering facility at the darmstadt linear accelerator (dalinac): I. accelerator. *Nucl. Instrum. Meth.*, 153(1):9 – 15, 1978.

[183] S-DALINAC, Darmstadt Linear Accelerator. "http://www.ikp.physik.tu-darmstadt.de/richter/s-dalinac/".

[184] C. Bauer, I. Baumann, C. Colledani, J. Conway, P. Delpierre, F. Djama, and et al. Recent results from the RD42 Diamond Detector Collaboration. *Nucl. Instrum. Meth.*, A383:64–74, 1996.

[185] Bügel et al. *Bergmann - Schaefer: Lehrbuch der Experimentalphysik: Festkörper*. Walter de Gruyter, Berlin/New York, 2005.

[186] Gerd Czycholl. *Theoretische Festkörperphysik*. Vieweg Verlag, 2000.

[187] Ibach, H. and Lüth, H. *Festkörperphysik: Einführung in die Grundlagen*. Springer Verlag, 5. edition, 1999.

[188] A. Einstein. Über die von der molekularkinetischen Theorie der Wärme geforderte Bewegung von in ruhenden Flüssigkeiten suspendierten Teilchen. *Annalen der Physik*, 17:549–560, 1905.

[189] M. Smoluchowski. Zur kinetischen Theorie der brownschen Molekularbewegung und der Suspensionen. *Annalen der Physik*, 21(756-780), 1906.

[190] V. K. Arora. Drift diffusion and Einstein relation for electrons in silicon subjected to a high electric field. *Applied Physics Letters*, 80:3763–+, May 2002.

[191] Drude, Paul. Zur Elektronentheorie der Metalle. *Annalen der Physik*, 306(3):566–613, 1900.

[192] M. Sotoodeh, A. H. Khalid, and A. A. Rezazadeh. Empirical low-field mobility model for III-V compounds applicable in device simulation codes. *Journal of Applied Physics*, 87:2890–2900, March 2000.

[193] T. Bayes. An Essay towards solving a Problem in the Doctrine of Chance. http://www.stat.ucla.edu/history/essay.pdf, 1763.

[194] S. Ramo. Currents Induced by Electron Motion. *Proc. IRE*, 27:584–585, September 1939.

[195] W. Shockley. Currents to Conductors Induced by a Moving Point Charge. *Journal of Applied Physics*, 9:635–636, October 1938.

[196] Zhong He. Review of the Shockley-Ramo theorem and its application in semiconductor gamma-ray detectors. *Nucl. Instrum. Meth. A: Accelerators,Spectrometers,Detectors and Associated Equipment*, 463(1-2):250 – 267, 2001.

[197] E. Gatti and A. Geraci. Considerations about Ramo's theorem extension to conductor media with variable dielectric constant. *Nucl. Instrum. Meth. A: Accelerators, Spectrometers, Detectors and Associated Equipment*, 525(3):623 – 625, 2004.

Index